Dynamics in the Magnetospheres of Compact Objects

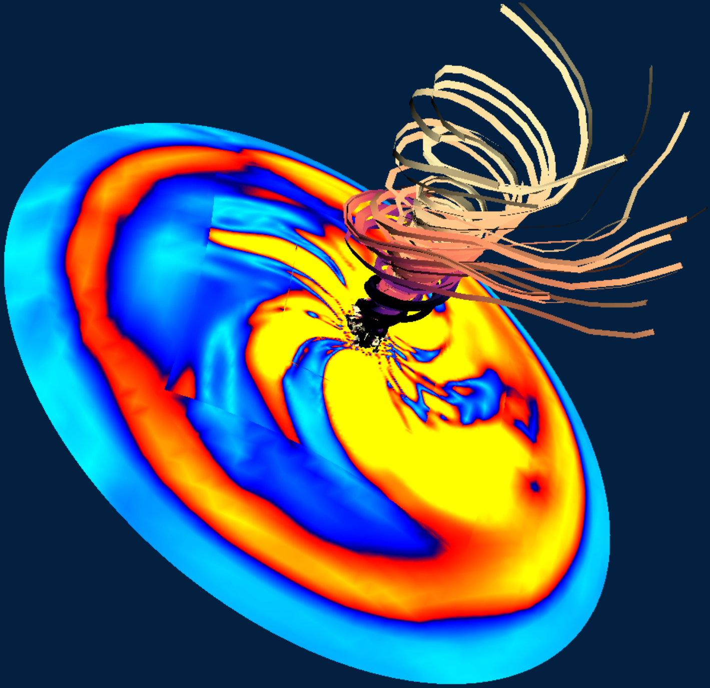

Jens Florian Mahlmann

Miguel Ángel Aloy Torás, Pablo Cerdá-Durán

Departament d'Astronomia i Astrofísica
Programa de Doctorat en Física
Universitat de València

TESI DOCTORAL, Maig 2020

Dynamics in the Magnetospheres of Compact Objects

Jens Florian Mahlmann

Departament d'Astronomia i Astrofísica
Programa de Doctorat en Física
Universitat de València

TESI DOCTORAL

Miguel Ángel Aloy Torás, Pablo Cerdá-Durán

Maig 2020

To my grandfather Henning, who taught me how to drill holes.
To my mother Manuela, who allowed me to study them.

Acknowledgements

We thank all the people who many days deserve the greatest credit. Between them are Felicidad, Guadalupe, and Manel, managing in our department's administration. Alejandro Soriano and Josep Vicent Sala, maintaining our simulations and results safe at the *Servei d'Informàtica*. Christine Schade being always available for our requests at the *Studienstiftung des Deutschen Volkes*. Manolo and Amparo, who know our needs during the 11 o'clock *café con leche*.

I thank Dimitrios Giannios for being my first teacher of astrophysics and the catalyst for my first contact with Miguel Angel Aloy as a graduate student. Exceptional gratitude for good teachers is ever-present, like for Albrecht Sievers, Monika Gerdemann, Jörg Peters, and Glen Langemeyer. Likewise, the great lectures by Knut Smoczyk, exploring all flavors of differential geometry, as well as several years of the best exercises in theoretical physics by Michael Flohr and Thomas Brockt, are a constant guide field in the right direction.

I profoundly thank Miguel Angel Aloy. First, for replying to my first message. Second, for allowing science to become a discussion. Third, for sharing his extraordinary intuition about simulations and theory, potentials, and possibilities. His supervision and determination exceed all standards. They are a masterclass to understand the workings of astrophysics and its modeling beyond the boundaries of knowledge or expectation. Likewise, no part of this thesis would have advanced without Pablo Cerdá-Durán and his realistic view on the balance between feasibility and astrophysical relevance of our project. I am exceptionally lucky with my supervisors. The work shared between the three of us, and our co-authors has been a great success. There is eternal gratitude for this experience and always eagerness to explore the next question together.

Amir Levinson has sparked motivation for exploring big questions that I have not known before. I truly enjoy working with him and have the fondest memories of our time in Tel Aviv. Thank you for this inspiration and my first of many weekends in Israel with dinner in the old harbor of Jaffa.

Chronically missed, but still not judging me are Thomas, Julian, Till, Thomas, Milena, Julian, Kai, Apostolos, and Antonia. I cannot wait to be closer to you all, and until then I am already looking forward to toasting with you.

The reason for not loosing my calm and sanity, believe in science and humanity is always one. Lorena.

No words of thank can be sufficient for our family, the grandparents Henning and Sylke, former single mother Manuela, and fortunately not single stepfather Günter. Insisting on homework before playing outside, and covering in red our mediocre essays in English and German. We can only explore our world because we know that somewhere there is the home and love you built, every day. Thank you, Jan, for being my best friend. We are unbelievably lucky. First academics in the family. One became a real doctor, the other one is studying holes.

I thank our original team at the University of Valencia, for accepting me as a student even though I did not have the slightest idea about modeling astrophysical plasma. José Adsuara, Carlos Cuesta, Petar Mimica, and Jesús Rueda-Becerril, you helped me to arrive in our science and in Spain. Martin Obergaulinger is a font of knowledge and my favorite office colleague; thank you for letting me have a glimpse of scientific codes which are bullet trains rather than crocodiles. Without Vassilios Mewes' relentless help in all questions around the EINSTEIN TOOLKIT, this thesis would not have moved past its introduction. The latter is also true for the sharpened numerical intuition of Tomasz Rembiasz. The guidance by Isabel Cordero, José Font, José María Ibáñez, Antonio Marquina, José María Martí, Juan Antonio Miralles, Manel Perucho, and Vicent Quilis, directly - or through their channels - will be recognizable throughout this work.

I thank the University of Valencia, for signing the latest talent, José. You made the second half of my Ph.D. in Valencia more enjoyable. This is also true for our colleagues Nico and Alejandro, but the first half. And Fabrizio, Sergio, Miquel, and Francisco in general.

We are grateful to the members of the Ph.D. committee for evaluating our project in turbulent times. Finally, our thanks go to two entities, without which we would not do our work. First, the agencies that pay us: The *Studienstiftung des Deutschen Volkes* with their generous Ph.D. grant, the *Spanish Ministry of Science and Education* with the grants AYA2015-66899-C2-1-P, and PGC2018-095984-B-I00, the *Valencian Regional Government* through the funding GRISOLIAP/2016/097, and PROMETEO-II-2014-069, and the *Barcelona Supercomputing Center* with their competitive high-performance computing resources. Second, the people who read our work and ask questions.

Gracias.

Abstract

This Ph.D. thesis explores the modeling of dynamics in magnetospheres around compact objects (black holes and neutron stars), and their implications in the formation of high energy phenomena such as magnetar flares and the highly-variable teraelectron Volt (TeV) emission of some active galactic nuclei, by means of numerical simulations. The amazing images of black hole (BH) shadows from the galactic center and the M87 galaxy provide a first direct glimpse into the physics of accretion flows in the most extreme environments of the universe. The efficient extraction of energy in the form of collimated outflows or jets from a rotating BH is directly linked to the topology of the surrounding magnetic field.

General Relativistic force-free electrodynamics (GRFFE) is one possible plasma-limit employed to analyze energetic outflows in which strong magnetic fields are dominant over all inertial phenomena. In this work, we present numerical strategies capable of modeling both, stationary, and fully dynamic force-free magnetospheres of compact objects. The latter is provided by an implementation of GRFFE on the infrastructure of the EINSTEIN TOOLKIT. This Ph.D. thesis reviews the methodology behind this newly developed code package and its application to magnetars and rapidly spinning BHs in detail.

Scientific results of this project are presented by a series of publications. We improved the numerical techniques used to solve for equilibrium magnetospheres of Kerr BHs across their singular surfaces and provide a first detailed review of convergence properties. Furthermore, we identified instabilities in the high energy branches of twisted magnetar magnetospheres which may act as the triggering mechanism of the most powerful soft-gamma repeaters (SGRs). Finally, we confirmed the possibility of energy extraction by the Blandford/Znajek mechanism from rapidly spinning BHs in 3D dynamical magnetospheres induced by the accretion of small scale magnetic structures.

Key words: accretion, accretion discs – black hole physics – magnetic fields – methods: numerical – stars: magnetars – stars: neutron – X-rays: bursts

Resumen

Introducción

La astronomía moderna del siglo XXI es capaz de observar fenómenos que proceden del espacio mucho más allá de nuestro propio sistema solar o nuestra galaxia local. Actualmente disponemos de una espectacular red de telescopios que proporciona datos en todas las longitudes de onda del espectro electromagnético (p.e. Acero et al., 2015; de Naurois, 2017; Reinacher et al., 2018; Sanna et al., 2018; Aghanim et al., 2019; Benneke et al., 2019; Di Mascolo et al., 2019; Marcote et al., 2020) y permite observar los fenómenos más extremos del universo con cada vez mayor precisión. Operando con esfuerzos internacionales y de varias disciplinas, estos telescopios han permitido incluso obtener las primeras imágenes de la sombra de un agujero negro (Event Horizon Telescope Collaboration et al., 2019a) y combinar estas observaciones con datos de los observatorios de rayos cósmicos (IceCube Collaboration et al., 2019) y de detectores de ondas gravitatorias (Abbott et al., 2017). Es por eso por lo que comúnmente hablamos del advenimiento de la era de la astronomía multi-mensajero, ya que combina distintos canales de observación (mensajes) más allá de los estrictamente electromagnéticos.

El estado más abundante de masa (bariónica) del universo es el de plasma. Por derecho propio, el de plasma ha sido calificado como el *cuarto estado de materia* (p.e. Chiuderi and Velli, 2015; Piel, 2017). De forma más precisa, un plasma consta tanto de partículas cargadas como de los campos electromagnéticos generados por las mismas y que dan lugar a una interacción de largo alcance. Ambos ingredientes (cargas y campos) interactúan tanto consigo mismo como recíprocamente entre ellos. En un plasma, las partículas tienden a colocarse de una manera que se supriman (en parte) los potenciales electrostáticos de las cargas involucradas dentro de una distancia característica, quedando el plasma apantallado y electro-neutral. Perturbaciones locales de la cuasi-neutralidad inducen movimientos regulares y periódicos, limitados por la frecuencia característica resultante.

En la Tierra, el plasma altamente magnetizado se encuentra en algunos de los fenómenos más misteriosos y extremadamente desafiantes. Tales condiciones superan los límites de los experimentos y las simulaciones. La bola de rayos (*ball lightening*) consiste en una bola de fuego que aparece *cerca de la descarga de [...] rayos normales, manteniendo su brillo, forma y tamaño hasta 10 segundos o más* (Rañada et al., 2000). Dichas bolas de rayos están en un equilibrio de presión entre sus campos magnéticos y la tensión atmosférica (Tsui, 2003), posiblemente disipándose gradualmente o en una explosión rápida. Los notables procesos desencadenados por los campos eléctricos de relámpagos y tormentas eléctricas se han observado como destellos de rayos gamma terrestres a bordo de la Estación Espacial Internacional (Neubert et al., 2020). En una nota más práctica, el emocionante avance de los dispositivos de fusión nuclear y su reciente vuelta a la atención (Clery, 2006; Holtkamp et al., 2007; Milch, 2019) han llevado los desafíos técnicos y teóricos restantes a los regímenes de plasma más extremos en el planeta. Los eventos disruptivos durante las llamadas inestabilidades de enfriamiento encontrados en las paredes de los reactores de fusión potencialmente pueden describirse en el límite de alta magnetización (Kiramov and Breizman, 2018) y necesitan ser comprendidos de forma urgente.

Más allá de los límites de la Tierra, la fascinante proximidad del sol como laboratorio de plasma es una oportunidad excepcional para sondear directamente los modelos en los límites más extremos para obtener un rico registro de observaciones. Los campos magnéticos, que a menudo dominan la dinámica, están detrás de casi todas las manifestaciones de la actividad solar, desde las manchas solares hasta las eyecciones coronales, así como el viento solar (Babcock, 1963; Parker, 1970). La difusión de los campos magnéticos en la atmósfera del sol causada por el movimiento relativo entre los componentes neutros e ionizados del plasma (p. ej., Pandey and Wardle, 2008; Khomenko and Collados, 2012), así como los rápidos cambios en la topología de los campos magnéticos que dan lugar a eyecciones colimadas (p. ej., Alexander and Fletcher, 1999; Savcheva et al., 2007; Moreno-Insertis and Galsgaard, 2013) constituyen ambas, una visión asombrosa del funcionamiento solar, así como pistas inestimables para el modelado de astrofísica de alta energía. La medición in situ del plasma interplanetario y su dinámica en nuestro sistema solar es un esfuerzo continuo (Bandyopadhyay et al., 2018; Nakamura et al., 2018; Liu et al., 2019). La misión Voyager de 1977 ya estaba equipada con un instrumento que medía los parámetros de plasma locales a lo largo de su trayectoria, tales como la densidad, la velocidad y la presión

(Bridge et al., 1977). La misión del *Interstellar Boundary Explorer* (IBEX) de la NASA ha ido más allá que las misiones Voyager. Su objetivo es descubrir la naturaleza de las interacciones entre el viento solar y el medio interestelar en el borde de nuestro sistema solar (McComas et al., 2004). En el mismo ámbito, Europa Clipper de la NASA (Phillips and Pappalardo, 2014) medirá las características del plasma de la luna de Júpiter, que está incrustada en un *complejo plasma magnetosférico joviano* (Grey et al., 2018). Esta sonda opera a sensibilidades suficientes para analizar la estructura y el océano de Europa explotando las corrientes inducidas en su interior. La Tierra misma está sujeta al plasma interplanetario por su exposición a los vientos solares. Ambos, el origen de estos vientos en impresionantes eyecciones de masa coronal del sol (Chen, 2011; Lyutikov and Gourgouliatos, 2011; Webb and Howard, 2012), y su destino en asombrosos flujos de plasma auroral a lo largo del campo magnético de la tierra (Chaston et al., 2015; Hull et al., 2016; Damiano et al., 2018; Sun et al., 2019), están dominados o guiados por efectos magnéticos.

El papel de los campos magnéticos y los efectos secundarios no ideales, así como la emisión no térmica de plasma magnetizado, es de suma importancia para desentrañar la física de las fuentes astrofísicas. Todos estos problemas son lo suficientemente complejos como para alentar la elección de un enfoque computacional. Suponiendo que estas fuentes pueden modelarse como plasma diluido relativista, la respuesta teórica a los fenómenos en el régimen altamente magnetizado puede abordarse a través de la electrodinámica libre de fuerzas en relatividad general (GRFFE por sus siglas en inglés), empleando simulaciones numéricas de campos electromagnéticos en espacio-tiempo en evolución dinámica. El objetivo de este proyecto de investigación es nada menos que contribuir a las respuestas deseadas desde hace mucho tiempo a la pregunta de cómo los objetos astrofísicos compactos transportan enormes reservas de energía en el seno de plasma magnetizado.

Para los plasmas que están dominados por fenómenos magnéticos (alta magnetización) como los que esperamos encontrar en las atmósferas rarificadas alrededor de objetos compactos (especialmente estrellas de neutrones y agujeros negros), *la inercia de partículas es insignificante, por lo que la fuerza electromagnética (Lorentz) sobre cada partícula tiene que ser cero* (Znajek, 1977). Para que la conductividad eléctrica de un plasma sea infinita, condición necesaria para poder tratar el plasma en el seno de la magnetohidrodinámica (MHD) *ideal*, el plasma debe poseer campos magnéticos más intensos que los eléctricos. Esta situación se conoce como *dominancia magnética* (Uchida, 1997; Paschalidis and Shapiro, 2013, p.e.). Por otro lado, cuando se desprecia la influencia dinámica de la inercia de las partículas que constituyen el plasma, no se puede encontrar un sistema de referencia *comóvil* con dichas partículas. Por lo tanto, no se puede definir la velocidad física del plasma (Shibata, 2015) y el producto de las cargas y la velocidad que aparecen en la fuerza de Lorentz debe ser reemplazado por la llamada corriente de la electrodinámica libre de fuerzas. La desaparición de la fuerza de Lorentz en sí misma (en combinación con la existencia de una corriente de la electrodinámica libre de fuerza, ver Paschalidis and Shapiro, 2013) implica que el campo eléctrico no tiene componentes a lo largo del campo magnético. Llamamos plasma libre de fuerzas a aquel en el que estas dos condiciones (conductividad infinita e inercia despreciable de las partículas constituyentes) se mantienen. El plasma libre de fuerza (astro)físico se considera además como *no derivable de un potencial* (Marsh, 1996) exclusivamente. Es decir, en general, estamos interesados en sistemas en que existe una densidad de la corriente en contraste con el electrovacío. Este plasma está gobernado por las ecuaciones de Maxwell (también llamadas ecuaciones de la electrodinámica *clásica*, e.d. no cuántica).

El término *magnetosfera* fue acuñado para la posteridad por Gold (1959) como la *región sobre la ionosfera en la que el campo magnético de la tierra tiene un control dominante sobre los movimientos del gas y las partículas cargadas rápidas*. Dichas regiones también existen alrededor de objetos astrofísicos compactos; son de gran importancia para nuestra investigación por una variedad de razones: i) Los fenómenos magnetosféricos son más fáciles de observar en el espectro electromagnético que los procesos en el interior del objeto compacto. Por lo tanto, nos proporcionan medios para sondear nuestros modelos teóricos con datos astronómicos. ii) Las magnetosferas son tan diluidas que el campo magnético domina la dinámica, haciendo que la inercia del plasma sea insignificante en la mayoría de los casos. iii) Las magnetosferas alrededor de las estrellas de neutrones se pueden conectar a la estructura magnética interior de la estrella. Sin embargo, la escala de tiempo característica de estas regiones puede ser muy diferente, permitiendo una variedad de dinámicas inducidas electromagnéticamente. iv) Las magnetosferas alrededor de agujeros negros son radicalmente diferentes de aquellas alrededor de estrellas de neutrones porque un agujero negro no está dotado de una superficie (perfectamente conductora, bien definida). Aún así, en la vecindad de un agujero negro, los efectos de relatividad general tienen una gran influencia en los flujos de energía electromagnética. En esta tesis, proporcionamos un estudio detallado sobre los mecanismos dinámicos utilizados para construir procesos de emisión de alta energía asociados con las magnetosferas de objetos compactos, específicamente de agujero negros y magnetares.

La existencia de los llamados campos eléctricos no ideales, que tienen una componente a lo largo del campo magnético, se considera una condición para los procesos de alta energía y prestan un enlace prometedor a las signaturas observacionales. Nuestra investigación tiene como objetivo identificar posibles ubicaciones de tales campos no ideales y sitios de disipación para allanar el camino para futuros modelos que no se limitan necesariamente al régimen altamente magnetizado. La reconexión de líneas del campo magnético, es decir, la ruptura y el nuevo ensamblaje de campos magnéticos, generalmente induce campos eléctricos no ideales. La relajación de ciertas condiciones de simetría (por ejemplo, simetría axial) en magnetosferas de equilibrio alrededor de objetos compactos, afecta profundamente a la dinámica que conduce a tales eventos de reconexión y láminas de fuertes corrientes. Las cadenas de plasmoides, por lo tanto, tubos de campos magnéticos rizados a lo largo de los sitios de reconexión, pueden acelerar las partículas a velocidades relativistas. Sin embargo, es probable que su topología 3D sea muy diferente de las estructuras 2D (axialmente simétricas) idealizadas que se han estudiado en toda la literatura. Argumentos similares son válidos para la formación de estructuras magnéticas a pequeña escala de tipo turbulento; de modo que las restricciones de simetría suprimen en gran medida su desarrollo. Para estas regiones, las simulaciones 3D son la clave para dibujar una imagen más completa de la dinámica magnetosférica.

Objetivos

Las magnetosferas alrededor de magnetares (estrellas de neutrones altamente magnetizadas y típicamente con rotación lenta) son especialmente adecuadas para el análisis en el límite de la electrodinámica libre de fuerzas. Debido a su lenta velocidad de rotación, su cilindro-luz (puesto que la inercia del plasma es despreciable, dicho cilindro es también una superficie de Alfvén), donde la velocidad de rotación de las líneas de campo magnético se hace igual a la de la luz, está lejos del objeto central y toda la región contenida en su seno (hasta la superficie estelar) se puede considerar dominada por efectos magnéticos. A lo largo de la literatura, uno encuentra una amplia variedad de soluciones analíticas y numéricas a la ecuación de equilibrio transversal del campo en magnetosferas de magnetares (por ejemplo Akgün et al., 2017, 2018). Para las magnetosferas de agujeros negros en rotación, se han utilizado técnicas de perturbación para explicar la extracción de masa/energía reducible del objeto central (Blandford and Znajek, 1977). Debido a los efectos gravitacionales, las magnetosferas de agujeros negros de Kerr poseen un cilindro-luz adicional comparado con el caso de magnetares (es decir, una segunda superficie de Alfvén) dentro de la ergosfera. Más allá de esta superficie, el flujo está, nuevamente, dominado por efectos inerciales (Beskin, 1997; Punsly, 2001). Al imponer condiciones de regularidad a través de los cilindros-luz como superficies singulares de la ecuación de Grad-Shafranov, y suponiendo un flujo bien comportado en la región de inyección intermedia, la ecuación de equilibrio transversal del campo se puede resolver numéricamente (como se ha hecho, por ejemplo, en Contopoulos et al., 2013; Nathanail and Contopoulos, 2014; Yuan et al., 2019), siendo éste uno de los objetivos de esta tesis (véase más abajo) y que ha resultado en la publicación Mahlmann et al. (2018).

Las escalas temporales breves de variabilidad observadas en la radiación TeV de M87 (Acciari et al., 2009; Aharonian et al., 2003) sugieren que el *motor central* que la produce debe ser no estacionario en escalas de tiempo tan pequeñas como unos pocos milisegundos. Dado que ni la masa del agujero negro ni su momento angular pueden cambiar en tan poco tiempo, esta variabilidad debe proceder de otras fuentes, entre las que cambios en el campo magnético cerca del horizonte de sucesos es una de las posibilidades. Si el campo magnético del disco es regular en escalas mucho más grandes que la altura del disco de acreción, el flujo magnético del agujero negro puede cambiar significativamente solo si la parte interna del disco de acreción colapsa de vez en cuando. Luego, el campo magnético del agujero negro se escapa hacia la abertura creada entre el horizonte y el borde interno del disco truncado, que típicamente se encuentra a la distancia correspondiente al radio de la última órbita estable. Recientemente, Parfrey et al. (2015) sugirió que los chorros relativistas pueden crearse mediante sistemas de flujo magnético a pequeña escala, que se amplifican y sostienen naturalmente en un disco de acreción turbulento. En tales modelos, no se requiere flujo a gran escala. Los bucles de campo magnético que conectan el agujero negro al disco interno pueden abrirse (debido a la acción de la rotación diferencial), lo que resulta en episodios de chorros del tipo Blandford/Znajek (BZ) impulsado por un agujero negro. En los modelos electrodinámicos libres de fuerza de la evolución de la magnetosfera realizados por Parfrey et al. (2015), la polaridad del campo poloidal (perpendicular al plano ecuatorial) cambia con el tiempo, siendo coherente en escalas de tiempo suficientemente largas para sostener chorros episódicos por la acción del mecanismo BZ.

La investigación del lanzamiento de chorros relativistas de agujeros negros, tanto como de la disipación magnetosférica alrededor de agujeros negros y magnetares requiere simulaciones dinámicas en 3D para: i) El análisis de la validez de estudios realizados previamente con éxito en 2D (Beckwith et al., 2009;

Parfrey et al., 2015) en 3D, y ii) la prueba de la estabilidad de magnetosferas obtenidas bajo las hipótesis de independencia temporal y simetría axial. A tales configuraciones se atribuye gran importancia como datos iniciales de simulaciones dinámicas y como modelo para entender la dinámica energética de estados (momentáneos) semejante a estructuras de equilibrio que aparecen en el curso de evoluciones en el tiempo en 3D. Con objeto de comprender en profundidad las inestabilidades desarrolladas en configuraciones simétricas de equilibrio, queremos diferenciar entre fluctuaciones, cuyo origen se encuentra en la dependencia del tiempo, e inestabilidades introducidas por la carencia de simetrías espaciales. Con el objeto de desarrollar una argumentación extensa alrededor de las magnetosferas que circundan objetos compactos, nuestra investigación se establece a lo largo de los temas siguientes:

1. **Flujos de energía en magnetosferas calculadas suponiendo equilibrio y simetría axial.** La así llamada ecuación de Grad-Shafranov (GSE por sus siglas en inglés) prescribe los campos electromagnéticos en magnetosferas estacionarias, libres de fuerzas, y con simetría axial alrededor de agujeros negros de Kerr. En la literatura, dos topologías magnéticas son las más frecuentemente consideradas a efectos de estimar la extracción de energía de un agujero negro en rotación: la topología del monopolo dividido (consistente en un campo puramente radial) y la topología de campo parabólico. Las soluciones numéricas a la GSE pueden usarse como datos iniciales para simulaciones 3D. Además, se pretende entender mejor la conexión magnética (*magnetic link*) entre el disco de acreción y el agujero negro por medio de líneas de campo cerradas. Esta conexión se ha visto que puede darse incluso en magnetosferas de agujeros negros estacionarios (Uzdensky, 2004) y es clave para entender procesos de interacción magnética entre el disco de acreción y el agujero negro. Se estima que la región del disco más alejada que sigue conectada magnéticamente con el agujero negro (digamos a una distancia $r_{\rm link}$) es susceptible de experimentar enormes procesos de disipación magnética. Entre nuestros objetivos en se encuentra primero reproducir la estructura de la conexión magnética agujero negro/disco de acreción en magnetosferas estacionarias. Esto se ha hecho (entre otras cosas) en Mahlmann et al. (2018). Posteriormente, en Mahlmann et al. (2020) exploramos con más detalle esta conexión en entornos dinámicos (véase el tercer objetivo, más abajo).

2. **Inestabilidades de magnetosferas retorcidas de magnetares con alta energía.** Los datos iniciales de las soluciones degeneradas de la GSE

(con las mismas condiciones de contorno, pero de diferente energía magnetosférica) para las magnetosferas de magnetares (Akgün et al., 2018) son potencialmente inestables y pueden liberar grandes cantidades de energía en las inmediaciones de la superficie del magnetar. Dichas inestabilidades actúan como el mecanismo desencadenante de los repetidores de rayos gamma suaves (*soft gamma repeaters*) más potentes, especialmente de sus picos de luminosidad iniciales (donde las energías son mayores). En un artículo recientemente publicado (Mahlmann et al., 2019), y que constituye parte de esta tesis, examinamos en detalle el mecanismo de liberación de energía y, de forma aproximada, la emisión térmica (bolométrica) esperada. Así mismo, pretendemos estimar las consecuencias que la liberación de esta (potencialmente) enorme cantidad de energía podría tener sobre la corteza del magnetar. Ya que es conocido que tales energías pueden dar lugar a gigantescos seísmos en la superficie del magnetar, de tal magnitud que es posible que lleguen a fracturar la corteza del mismo. En este ámbito, nos planteamos también estimar la evolución de la profundidad óptica de la magnetosfera a medida que se libera la energía contenida en el campo magnético retorcido. Un estudio así puede permitir acotar los valores típicos de la multiplicidad de leptones y su factor de Lorentz típico para que la radiación bolométrica producida por nuestros modelos sea semejante a la observada. Para ello se planea seguir una versión simplificada de la metodología descrita en Beloborodov (2013).

3. **Chorros del tipo Blandford/Znajek producidos por la acreción de estructuras magnéticas de pequeña escala.** Una de las objeciones típicamente atribuida al mecanismo BZ es la necesidad de tener un campo magnético poloidal a gran escala (ordenado), cuyo flujo no debe ser cero en ninguno de los dos hemisferios del horizonte del agujero negro. Parfrey et al. (2015) sugirió que la extracción de energía podría llevarse a cabo si el agujero negro central acreta bucles magnéticos de polaridad alterna (incluso de flujo magnético neto cero). En nuestro artículo (Mahlmann et al., 2020), que también forma parte de esta tesis, generalizamos la propuesta de Parfrey et al. (2015) a 3D al considerar la producción de energía electromagnética resultante de la activación del proceso BZ de forma transitoria, debido a la acreción de estructuras de pequeña escala (bucles magnéticos) sobre un agujero negro que gira rápidamente (spin $a = 0.9$). Más allá de verificar la factibilidad del proceso descrito por Parfrey et al. (2015) sin restricciones de simetría, una de los objetivos básicos que se plantean es si el entorno (enormemente) magnetizado del agujero negro

será estable frente a este proceso. Es bien conocido que las regiones con polaridad magnética alterna, si son muy pequeñas, forman láminas o capas de corriente (*current sheets*). Las capas de corriente son tremendamente delicadas desde el punto de vista numérico en la aproximación libre de fuerzas. Ello se debe a que en el centro de esas capas de corriente se disipa energía magnética y, en la naturaleza, esta energía es reconvertida en otras formas dinámicas como, por ejemplo, en energía térmica o cinética. Sin embargo, dado que tanto la inercia del plasma como su energía térmica son despreciadas en la aproximación libre de fuerzas, el tratamiento numérico de las capas de corriente supone un enorme reto. Independientemente de esta dificultad numérica, las topologías tridimensionales generan más oportunidades para que se den procesos como la reconexión magnética e inestabilidades varias. Estos procesos son una fuente de variabilidad muy significativa en escalas de tiempo muy pequeñas y que pueden ayudar a explicar ciertas fenomenologías observadas en agujeros negros supermasivos en núcleos de galaxias activas.

Metodología

La investigación presentada pretende encontrar respuestas a preguntas relacionadas con un plasma astrofísico altamente magnetizado (y en el que, por tanto, la aproximación de la electrodinámica libre de fuerzas es aceptable) utilizando técnicas numéricas. Para ser exactos, durante este proyecto se han desarrollado dos códigos distintos para enfrentarse a los retos definidos en las secciones previas:

1. Un resolvedor numérico de la GSE en la geometría de un agujero del tipo Kerr tratando con especial cuidado sus superficies singulares (Mahlmann et al., 2018).
2. Un conjunto de códigos numéricos para la evolución en el tiempo de campos electromagnéticos libres de fuerzas en geometrías arbitrarias (Mahlmann et al., 2019, 2020).

Debido a las enormes necesidades computacionales demandadas por las simulaciones 3D, y al hecho de que las instalaciones computacionales más avanzadas están compuestas por miles de núcleos de cálculo, necesitamos recurrir a códigos numéricos que sean paralelos y altamente escalables. El Einstein Toolkit (ET; Löffler et al., 2012; Etienne et al., 2017) proporciona un marco excelente para el desarrollo de rutinas específicas (conocidas como `thorns`) que aprovechan la infraestructura computacional del ET para ser ejecutados en las instalaciones informáticas más grandes disponibles. Además, el ET permite la evolución del espacio-tiempo en Relatividad General. Se ha implementado una *thorn* evolutiva para la electrodinámica libre de fuerzas (basándose en Baumgarte and Shapiro, 2003; Komissarov, 2004; McKinney, 2006; Paschalidis and Shapiro, 2013) y aplicado a una variedad de aplicaciones astrofísicas. Los desarrollos recientes en el campo (Baumgarte et al., 2013; Montero et al., 2014) enfatizan la necesidad de códigos numéricos que se adapten a la geometría del problema en cuestión, especialmente cuando se consideran los argumentos numéricos de estabilidad y la influencia de los efectos 3D. Hemos extendido la versión actual (cartesiana) de nuestro código a un esquema de volúmenes finitos en coordenadas esféricas y sobre bases ortonormales de vectores en espacios-tiempos que evolucionan dinámicamente.

Conclusiones

El estudio de la electrodinámica de las magnetosferas de agujeros negros de Kerr estáticas, axisimétricas y libres de fuerzas se basa en gran medida en soluciones de la GSE. Por esa razón, se han introducido diferentes enfoques numéricos para la solución del GSE en la literatura, pero ninguno de ellos se ha evaluado completamente desde el punto de vista numérico en términos de eficiencia y calidad de las soluciones encontradas. Presentamos una generalización de estos algoritmos y ofrecemos informaciones adicionales sobre la implementación algorítmica en Mahlmann et al. (2018) (incluido en esta tesis). Evaluamos la estabilidad numérica de los algoritmos implementados y cuantificamos la convergencia de la metodología presentada para las configuraciones más establecidas (monopolo dividido, paraboloidal, híbrida disco-agujero negro, uniforme). En nuestra comparación con diferentes implementaciones, logramos una mejora de la precisión numérica de más de diez órdenes de magnitud mediante el uso de discretización de las derivadas parciales con fórmulas sesgadas a través de los cilindros-luz. Hemos confirmado las correcciones a la aproximación de la potencia de Blandford/Znajek para agujeros negros de espín extremo, previamente deducidas por Tchekhovskoy et al. (2010).

En Mahlmann et al. (2019) (parte de esta tesis), presentamos simulaciones electrodinámicas libres de fuerzas en 3D de magnetosferas de magnetares que demuestran la inestabilidad de ciertas soluciones de equilibrio con degeneraciones (de alta energía) de la GSE. Este resultado indica la existencia de una rama inestable de soluciones magnetosféricas de campo retorcido y permite formular un criterio de inestabilidad. La reorganización de las líneas del campo magnético como consecuencia de esta inestabilidad desencadena la disipación de hasta un 30% de la energía magnetosférica en una capa delgada sobre la superficie del magnetar. Durante este proceso, predecimos un aumento de las tensiones mecánicas en la corteza estelar, lo que puede resultar en una falla mecánica global de una fracción significativa de la misma. Encontramos que la liberación de energía estimada y las propiedades de emisión son compatibles con eventos observados de llamaradas gigantes. La inestabilidad recientemente identificada es un candidato para la disipación de energía recurrente, lo que podría explicar parte de la fenomenología observada en los magnetares.

Los sistemas de agujeros negros con discos de acreción son los motores centrales de los chorros relativistas desde las escalas estelares a las escalas galácticas. Cuantificamos numéricamente el flujo de Poynting saliente a través del horizonte de un agujero negro que gira rápidamente y que está dotado de un disco de acreción giratorio. El disco admite tubos de flujo concéntricos de pequeña escala con el flujo magnético total siendo cero. Nuestras simulaciones de electrodinámica libre de fuerzas en Relatividad General siguen la dinámica de la magnetosfera del agujero negro durante varios cientos de escalas de tiempo dinámicas en 3D. Para el caso de los discos de acreción retrógrados, la eficiencia promedio del proceso alcanza hasta $\langle \epsilon \rangle \approx 0.43$, en comparación con una extracción de energía estacionaria por el proceso Blandford/Znajek. La eficiencia del proceso depende del área de la sección transversal de los bucles, es decir, del producto $l \times h$, donde l es la longitud radial del bucle y h su altura de escala vertical. Identificamos una fuerte correlación entre la extracción eficiente de energía electromagnética y el ajuste cuasi estacionario de las condiciones ideales para la operación del proceso Blandford/Znajek (por ejemplo, la velocidad angular de las líneas de campo óptima y el cumplimiento de la llamada *condición de Znajek*). Sorprendentemente, la extracción de energía opera de manera intermitente (episodios alternos de alta y baja eficiencia) sin imponer ningún campo magnético a gran escala que atraviese la ergosfera del agujero negro central. Escalando nuestros resultados a agujeros negros supermasivos, estimamos que la escala de tiempo de variabilidad típica del sistema es del orden de días a meses. Tales escalas de tiempo pueden explicar las escalas de variabilidad más largas de emisión de TeV observadas, por ejemplo en la galaxia M87.

Publications

- **Mahlmann, J. F.**, Cerdá-Durán, P., & Aloy, M. A. (2018).
  Numerically solving the relativistic Grad–Shafranov equation in Kerr spacetimes: numerical techniques.
  Monthly Notices of the Royal Astronomical Society, 477(3), 3927-3944.

- **Mahlmann, J. F.**, Akgün, T., Pons, J. A., Aloy, M. A., & Cerdá-Durán, P. (2019).
  Instability of twisted magnetar magnetospheres.
  Monthly Notices of the Royal Astronomical Society, 490(4), 4858-4876.

- **Mahlmann, J. F.**, Levinson, A., & Aloy, M. A. (2020).
  Striped Blandford/Znajek jets from advection of small scale magnetic field.
  Monthly Notices of the Royal Astronomical Society, 494(3), 4203–4225.

- **Mahlmann, J. F.**, Aloy, M. A., Mewes, V., & Cerdá-Durán, P. (2020)
  Computational General Relativistic Force-Free Electrodynamics: I. Multi-Coordinate Implementation and Testing
  Submission to Astronomy & Astrophysics in preparation.

- **Mahlmann, J. F.**, Aloy, M. A., Mewes, V., & Cerdá-Durán, P. (2020)
  Computational General Relativistic Force-Free Electrodynamics: II. Characterization of Numerical Diffusivity
  Submission to Astronomy & Astrophysics in preparation.

Contents

Part I

Summary

Chapter 1

Introduction

1.1 Motivation

Plasma is the most abundant state of (baryonic) matter in the universe. Besides the directly tangible states of solid, liquid, and gaseous matter, ionized particles in a quasi-neutral ensemble form plasma as the *fourth state of matter* (e.g., Chiuderi and Velli, 2015; Piel, 2017). Plasma ensembles consist of freely moving charged and neutral particles and their associated, self-consistent long-range electromagnetic fields. Such long-range fields are generated by the charge carriers and the respective currents in the plasma, regardless of external sources. Both of these ingredients interact with themselves (i.e., particle-particle and field-field interactions) and each other (i.e., particle-field interactions), providing us with a rich ensemble of highly energetic phenomena. Within plasma, particles can rearrange in a way that the electrostatic potentials of the contributing charges nearly vanish at some characteristic distance; clouds of positive charges are paired with their negative counterpart. Local perturbations of this quasi-neutrality yield orderly periodical motions bound by the resulting characteristic plasma frequency. Plasma constituents do not need to be bound by electrostatic forces, which leads to additional collisions among them, very much like in a gas or a liquid. The fourth state of matter is very different from its firstborn namesake of blood plasma, which is the liquid part of the sanguine fluid. The latter acts as the mere carrier of the blood's molded constituents.

On earth, highly magnetized plasma is found somewhere in between mysterious and extremely challenging phenomena, pushing the boundaries of experiments and simulations. Ball lightning is a fireball that appears *near the discharge of [...] normal lightning, maintaining their brilliance, shape, and size up to 10s or* *even more* (Rañada et al., 2000). They are in a pressure balance between their magnetic fields and the atmospheric strain (Tsui, 2003), possibly dissipating gradually or in a prompt explosion. The remarkable processes unleashed by the electric fields of lightnings and thunderstorms have been observed as terrestrial gamma-ray flashes on board of the International Space Station (Neubert et al., 2020). On a more practical note, the exciting advance of nuclear fusion devices and their recent shift back into the spotlight (Clery, 2006; Holtkamp et al., 2007; Milch, 2019) have brought the remaining technical and theoretical challenges to the most extreme plasma regimes on the planet. Disruptive events during so-called current quench instabilities at the walls of fusion reactors can potentially be described in the high-magnetization limit (Kiramov and Breizman, 2018) and need urgent closure.

Beyond the earth's boundaries, the fascinating proximity of the sun as a plasma laboratory is an exceptional opportunity to directly probe models in the most extreme limits to a rich record of observations. Magnetic fields, often dominating the dynamics, are behind nearly all of the manifestations of the solar activity, from sunspots to coronal ejections, as well as the solar wind (Babcock, 1963; Parker, 1970). The diffusion of magnetic fields in the sun's atmosphere caused by the relative motion between neutral and ionized components of the plasma (e.g., Pandey and Wardle, 2008; Khomenko and Collados, 2012) as well as rapid changes in the topology of magnetic fields, e.g., resulting into collimated ejections (e.g., Alexander and Fletcher, 1999; Savcheva et al., 2007; Moreno-Insertis and Galsgaard, 2013) are both, an amazing insight into the solar workings as well as blueprints for the modeling of astrophysical high-energy processes. The in situ measurement of interplanetary plasma and its dynamics in our solar system is an ongoing endeavor (Bandyopadhyay et al., 2018; Nakamura et al., 2018; Liu et al., 2019). Already the 1977 Voyager mission was equipped with an instrument measuring local plasma parameters along its path, like density, velocity, and pressure (Bridge et al., 1977). The Interstellar Boundary Explorer (IBEX) mission of the NASA has gone further than the Voyager missions. It aims at discovering the nature of the interactions between the solar wind and the interstellar medium at the edge of our solar system (McComas et al., 2004). On the same footing, NASA's Europa Clipper (Phillips and Pappalardo, 2014) will measure the plasma characteristics of Jupiter's moon, which is embedded in a *complex Jovian magnetospheric plasma* (Grey et al., 2018). It operates at sensitivities sufficient to analyze the structure and ocean of Europa by exploiting the currents induced in its interior. Earth itself is subject to interplanetary plasma by its exposure to solar winds. Both, the origin of these winds in impressive coronal-mass-ejections of the sun (Chen, 2011; Lyutikov and Gourgouliatos, 2011; Webb and Howard, 2012), and their destination in staggering auroral plasma flows along the earth's magnetic field (e.g., Chaston et al., 2015; Hull et al., 2016; Damiano et al., 2018; Sun et al., 2019), are dominated or guided by magnetic effects.

Modern astronomy of the 21^{st} century is observing phenomena emerging from space well beyond our solar system or galaxy. A spectacular, well-established set of telescopes is providing data across the electromagnetic spectrum[1] and paves the way for increasingly accurate windows into the most extreme phenomena of the universe. In combined international efforts across disciplines, these telescopes operate in large networks with astonishing accuracy, combining electromagnetic observations (e.g., in radio wavelengths, Event Horizon Telescope Collaboration et al., 2019a) with cosmic-rays (IceCube Collaboration et al., 2019) and gravitational wave detectors (Abbott et al., 2017). This is the era of multi-messenger astronomy. Astrophysical plasma around black holes (BHs) or neutron stars, as well as the emitted high-energy radiation, are one key messenger in this exciting epoch.

The role of magnetic fields and non-ideal side effects, as well as the non-thermal emission of magnetized plasma, is of paramount importance to disentangle the physics of astrophysical sources. All these problems are sufficiently complex to encourage the choice of a computational approach. Assuming that these sources can be modeled as relativistic, dilute plasma, the theoretical answer to phenomena in the highly magnetized regime can be approached through General Relativistic force-free electrodynamics (GRFFE) - numerical simulations of electromagnetic fields in dynamically evolving spacetimes. The goal of this research project is nothing less than contributing to long-desired answers to the question of how compact astrophysical objects transport huge energy reservoirs in magnetized plasma.

The term *magnetosphere* was coined for years to come by Gold (1959) as the *region above the ionosphere in which the magnetic field of the earth has dominant control over the motions of gas and fast charged particles*. Such regions also exist around astrophysical compact objects; they are of outstanding importance for our research for a variety of reasons: i) Magnetospheric phenomena are easier to

---

[1] An incomplete sample of observatories across the electromagnetic spectrum is: FERMI and HESS for gamma-rays (Acero et al., 2015; de Naurois, 2017), NuSTAR for X-Rays (Sanna et al., 2018), KEPLER for visible light (Benneke et al., 2019), SOFIA for infrared (Reinacher et al., 2018), PLANCK for microwave (Aghanim et al., 2019), ALMA and CHIME for radio waves (Di Mascolo et al., 2019; Marcote et al., 2020), HUBBLE SPACE TELESCOPE for near-infrared, visible light, and ultraviolet (see Spitzer, 1979, for a historical review).

observe in the electromagnetic spectrum than processes in the interior of the compact object. They, hence, provide us with means to probe our theoretical models with astronomical data. ii) Magnetospheres are so dilute that the magnetic field dominates the dynamics, rendering plasma inertia negligible in most cases. iii) Magnetospheres around neutron stars can be connected to the interior magnetic structure of the star. However, the characteristic time scale of these regions can be very different, allowing for a variety of electromagnetically induced dynamics. iv) Magnetospheres around BHs are radically different from those around neutron stars (NSs) because a BH is not endowed with a (perfectly conducting, well defined) surface. Still, in the vicinity of a BH, General Relativistic effects have a great influence on the electromagnetic energy flows. In this thesis, we provide insight into the dynamical mechanisms used to build up high-energy emission processes associated with the magnetospheres of compact objects, specifically of BHs and magnetars.

So-called non-ideal electric fields, which have a component along the magnetic field, are regarded as a condition for high-energy processes and lend a promising link to observational signatures. Our research aims at identifying possible locations of such non-ideal fields and dissipation sites to pave the way for future models which are not necessarily limited to the highly magnetized regime. Reconnection of magnetic field lines, i.e., the breaking-up and new assembly of magnetic fields, generally induces non-ideal electric fields. The relaxation of certain symmetry conditions (e.g., axial symmetry) in equilibrium magnetospheres around compact objects, profoundly affects the dynamics leading up to such reconnection events and sheets of strong currents. Chains of plasmoids, thus, tubes of curled magnetic fields along reconnection sites, can accelerate particles to relativistic speeds. However, their 3D topology is likely to be very different from the idealized 2D (axially symmetric) structures that have been studied throughout the literature. Similar arguments hold for the formation of turbulent-like, small-scale magnetic structures; so that symmetry restrictions greatly suppress their development. For these regions, 3D simulations are the key to paint a more complete picture of magnetospheric dynamics.

1.2 Force-Free Astrophysical Plasma

Theoretically, the dynamics of plasma can be encoded in the so-called kinetic description, where the number of particles per phase-space volume is given by a distribution function, separately for each species (such as electrons, ions, neutral particles, etc.). The particle number density is conserved along a trajectory (Liouville's theorem) for the collective movement of all the constituents and only altered by their collisions. Such movements are ultimately governed by the plasma *kinetic equation* (e.g., Chiuderi and Velli, 2015), also known as Boltzmann equation. In the limit of rarefied plasma - found for example in the solar wind or magnetospheres around compact objects - collisions are replaced by long-range aggregated interactions (e.g., those produced by electromagnetic fields). In this case, the distribution function of each plasma constituent follows the simpler case of the Vlasov equation (cf. Vlasov, 1968). The particle distribution function itself may depend on several quantities (not necessarily linearly) and is different for each particle species. Thus, the kinetic description of plasma may result in a very large and complicated system of equations. If the electromagnetic fields are derived self-consistently from the moving charges, the complete description is highly non-linear and not practical to solve analytically. So-called particle-in-cell (PIC) approaches can model plasma kinetics by carefully integrating all elements of the kinetic plasma description, i.e., particle motion, field dynamics, and their mutual interference (e.g., Tskhakaya, 2008, for an overview).

Another possible remedy consists in taking (a finite number of) moments of the kinetic equation, which are obtained by first multiplying each of the terms in the equation by powers of the velocity and then integrating over velocity space. With this procedure, one gives up information on the velocity fluctuations of phase-space at the benefit of integrability in ordinary space. Such an approximation entails the assumption that the particle velocities do not significantly deviate from the average speed. Each of the moments of the kinetic equation represents a separate evolutionary equation for the respective moment of the distribution function itself. For practical reasons, the number of moments of the kinetic equation which one solves must be rather limited. Typically, only the zeroth (number density), first (momentum density), and second (energy density) order moments are considered, which leaves us with the multi-fluid approximation of the plasma in form of a system of partial differential equations (PDEs). The PDEs can be simultaneously solved (including all charged species in the plasma).

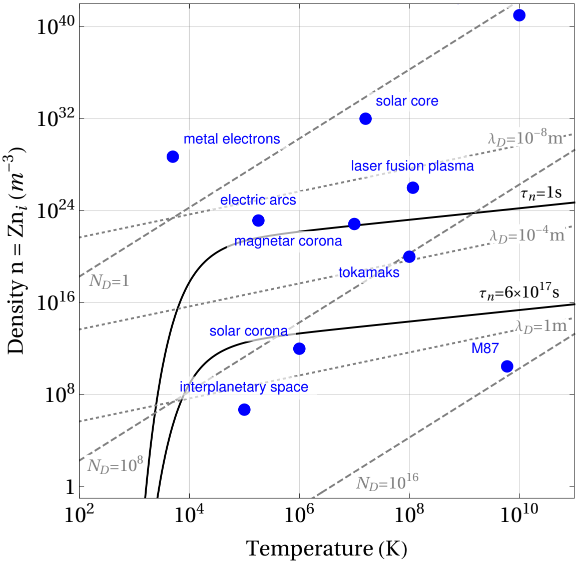

(a) The mean time between collisions of charged plasma particles with neutrals; n_n is the number density of neutrals and T its temperature:

$$\tau_n \approx 10^{17} n_n^{-1} T^{-1/2} \tag{1.1}$$

(b) Debye length, λ_{D}, as the typical size of a region in which charge imbalance may occur due to thermal fluctuations:

$$\lambda_D \approx 7 \times 10^{3} n^{-1/2} T^{1/2} \tag{1.2}$$

n is the number density of electrons, n_i the number density of ions and Z the ion charge number, such that $n \equiv Z n_i$.

(c) Number of particles in a Debye sphere with radius λ_{D}:

$$N_D \approx 1.4 \times 10^{6} n^{-1/2} T^{3/2} \tag{1.3}$$

Box 1.1: Conditions that illustrate the different collisional regimes in a plasma, in terms of the number density of electrons n and the temperature, T. *Graph panel:* The solid lines coincide with conditions in the (n, T)-plane with the same typical charge-neutral collision time (equation 1.1). The lower τ_n-isoline corresponds to a collision time of the order of one age of the universe. The short-dashed, straight lines indicate the length scales necessary for the condition of quasi-neutrality to hold (equation 1.2). Long-dashed, straight lines represent the number of particles enclosed in a Debye sphere (equation 1.3). *Graph panel* and *definitions* according to section 1.4.1 in Goedbloed and Poedts (2004), and section 2.3. in Piel (2017). The different conditions met in various environments with terrestrial or astrophysical plasma are labeled in blue.

The multi-fluid approximation may be restricted further to a two-fluid system (consisting of electrons and ions) if the positive and negative charge carriers undergo frequent collisions, and, thus, clearly establish the separated electron and ion fluids. Assuming that the plasma is electrically neutral over sufficiently large ensembles of particles (with particle numbers which are significantly smaller than the ones contained in the whole - macroscopic - system size), the multitude of particle species can be steamed down to a single fluid described by the center of mass and total charge density of the particle distribution. In other words, the so-called single-fluid regime corresponds to the two-fluid theory of plasma in the limit of sufficiently large scales: Fluctuations of the microscopic density distribution and the quasi-neutral charge distribution average out.

Once a single-fluid description has been obtained, one simplifies further by assuming a comparable order of magnitude for the *typical speeds* (defined as the ratio of typical length and time scale, Chiuderi and Velli, 2015) of electromagnetic and hydrodynamic phenomena. For the limit of low plasma frequencies, one dismisses the contributions of the Hall effect and the electron pressure (Chiuderi and Velli, 2015), as well as any plasma oscillations (or Langmuir waves) resulting from microscopic charge imbalances. This regime is the intermediate case of maximum mutual dynamical interaction between electromagnetic (magneto) and inertial (hydro) contributions and as such it is called magnetohydrodynamics (MHD). Closure relations in form of equations of state and a suitable Ohm's law constrain the remaining free variables and make the equations of MHD accessible to both analytical and numerical analysis.

Two different regimes of MHD are the classical regime, in which the macroscopic (and thermal) motion is restricted to be non-relativistic, and the relativistic regime. The confinement to the low-frequency regime of electromagnetic interactions implies that one neglects contributions of the electromagnetic fields which vary rapidly in time. As such, in the limit of classical MHD, the so-called displacement current can be disregarded, which simplifies the equations. Further regimes of magnetohydrodynamics are also distinguished, depending on the speed of magnetic dissipation. Magnetic fields in the MHD formulation may be destroyed as a result of Ohmic dissipation on diffusivity time scales which become shorter with increasing resistivity (i.e., decreasing conductivity). If the diffusivity time scale is much larger than the typical dynamical time scale, resistive effects can be safely neglected. This is the so-called *ideal* MHD regime. In the opposite case, Ohmic resistivity plays a central role in the dynamics and, the system must be treated with the *resistive* MHD equations. A basic difference between both regimes is that magnetic field lines, which are subjected to resistivity may drag along with a different velocity than the flow velocity of plasma particles. In the ideal regime, the plasma is a perfect conductor and all field lines are frozen into the moving plasma particles. In astrophysical plasma, the diffusivity time scale is typically extremely large because of the huge characteristic length scales of astrophysical systems (actually, it is often a major problem to find fast enough dissipation mechanisms to observe such violent reconnection phenomena as solar flares). Hence, oftentimes the ideal MHD regime is an excellent description of astrophysical systems. Therefore, it justifies that the starting point for our investigation of magnetized astrophysical plasma is the limit of (General) Relativistic ideal MHD.

Axially symmetric plasma configurations in equilibrium and neglecting gravitational forces have been studied extensively in the early second half of the past century, mainly nourished by the perspective of using them for plasma confinement in tokamak nuclear fusion devices (Lüst and Schlüter, 1957; Shafranov, 1958; Grad and Rubin, 1958). Several authors identified that under the constraints of axial symmetry and stationarity, the meridional projection of magnetic field lines coincides with the respective projection of the electric currents if the plasma resistivity is negligible. In this case, electromagnetic fields do not exert forces on the matter and the plasma is dubbed *force-free* plasma. In axial symmetry the electromagnetic field can be decomposed into poloidal (perpendicular to the equatorial plane) and toroidal (along the direction of equatorial revolution) components. Their equilibrium configuration can be computed with the time-independent (ideal) MHD equations. If there is no flow motion (zero velocity), only the momentum and circuital Ampère's law (and the zero divergence constraint of the magnetic field) are non-trivial. Indeed, Ampère's law can be inserted into the momentum equation to express the force balance between the pressure gradient and the Lorentz force. The resulting equation is known as the Grad-Shafranov equation (GSE). Nowadays, the GSE has been the seed for a whole class of equations well beyond its original application to toroidally symmetric terrestrial plasma. The ones relevant for this thesis are the extensions of the GSE, which describe equilibrium magnetic field configurations for various geometries and arbitrary spacetimes (e.g., Blandford and Znajek, 1977; Uzdensky, 2004, 2005; Nathanail and Contopoulos, 2014; Contopoulos et al., 2013; Akgün et al., 2017, 2018; Mahlmann et al., 2018; Yuan et al., 2019, and references therein). These extensions have been driven by the growing interest in the exploration of magnetically dominated plasma for astrophysical scenarios. Such dominant magnetic fields prescribe all movements of the plasma (Lüst and Schlüter, 1954): *Either, this movement will be in a way that* *the Lorentz force transforms magnetic into mechanic energy until their energy densities are comparable and the action of matter onto the magnetic field becomes considerable. Or, the movements change the magnetic fields by induction such that the currents are everywhere (almost) parallel to the magnetic fields, and therefore no force is exerted on the matter.*[2]

In our research of force-free astrophysical plasma, we assume that magnetic dominance implies that *particle inertia is negligible so that the electromagnetic (Lorentz) force on each particle has to be zero* (Znajek, 1977). Requiring the perfect conductivity of the plasma (ideal MHD condition) amounts to demanding that the magnetic field be always greater than its electric counterpart (Uchida, 1997; Paschalidis and Shapiro, 2013). As particle inertia is neglected, no proper rest frame of the plasma can be found. Hence, no physical plasma velocity can be defined (Shibata, 2015) and the product of charges and velocity appearing in the Lorentz force must be replaced by the so-called force-free current. The vanishing Lorentz force itself (in combination with a non-vanishing force-free current, Paschalidis and Shapiro, 2013) evokes that the electric field has no component along the magnetic field. We call a plasma in which these two conditions hold, i.e., perfect conductivity and negligible particle inertia, force-free plasma. The magnetic fields of (astro)physical force-free plasma are further considered to be *not derivable from a potential* alone (Marsh, 1996), i.e., in general, we are interested in the existence of a current density as contrasted with electrovacuum (where the electromagnetic field is not supported by currents).

Compact objects, e.g., white dwarfs, neutron stars, or BHs, are self-gravitating stellar bodies whose compactness parameter (defined as the ratio of the object's mass to its radius) is much smaller than in ordinary stars or planets. Often, compact objects are endowed with rarefied, magnetically dominated atmospheres, commonly dubbed magnetospheres (cf. Camenzind, 2007). The high-energy phenomena associated to transitory events in the magnetospheres of magnetized, isolated neutron stars and spinning BHs are the primary target of this thesis. Magnetic fields in stellar magnetospheres are supported by interior currents flowing through the stellar surface. For both, stellar and BH magnetospheres, charges are supplied by discharges close to the inner magnetospheric boundary (cf. Blandford and Znajek, 1977). It is essential to ensure the presence of a

---

[2] Translated by the author: *Diese [Bewegung] wird dann entweder so klein sein, daß das Magnetfeld durch die Lorentzkraft magnetische Energie in mechanische verwandelt, solange bis ihre Dichten vergleichbar werden und damit die Wirkung der Materie auf das Magnetfeld wesentlich wird; oder aber die Bewegung verändert durch Induktion das Magnetfeld so, daß der Strom überall (fast) parallel zum Magnetfeld fließt, daß also keine Kraft auf das Magnetfeld ausgeübt wird.*

sufficiently large charge density for the shielding of non-ideal electric fields, i.e., to fulfill the force-free condition of perpendicular electric and magnetic fields. Since the Poynting flux amply surmounts the kinetic flux and the magnetic diffusion time scale is typically much longer than the dynamical time scale of the magnetosphere, the force-free approximation is valid in the entirety of the immediate surrounding of the compact object.

Nevertheless, BHs would annihilate magnetic fields by themselves within dynamical time scales of the horizon crossing time, typically around thousands of seconds for AGNs (Thorne et al., 1986). Thus, magnetic fields and sufficient electron-positron-pairs must be supplied and supported by external sources. In practice, this is not a problem in accreting BHs, where the currents which are threading the accretion disc (AD) may provide the magnetic fields and charges, needed to sustain the magnetosphere (Beskin, 1997). The structure of the supporting disc results from a very complex interplay of different physical mechanisms such as radiative vs. advective transport, the mass accretion rate, the type of accreting compact object, and non-ideal effects. Hence, it is common to address magnetospheric problems around BHs incorporating a simplified model for the AD. For instance, it may be a thin boundary layer (Blandford and Znajek, 1977) or a non-force-free region within the domain. The latter is key in allowing for non-trivial field line configuration like the coupling between black holes and their accretion discs (BH/AD) or other closed magnetic flux structures (MacDonald and Thorne, 1982; Gralla and Jacobson, 2014).

Flows along axisymmetric, stationary magnetic fields around compact astrophysical objects were studied analytically employing the so-called MHD wind equations (e.g., Camenzind, 1986; Takahashi et al., 1990; Beskin, 1997; Punsly, 2001). These consist of the balance laws of (i) plasma momentum, (ii) mass conservation, (iii) Maxwell's equations, and (iv) the perfect conductivity condition. As such, they yield five integrals of motion (Takahashi et al., 1990) along magnetic flux tubes: The angular velocity of a magnetic field line, the entropy, the (normalized) mass flux per flux tube, the total energy, and the total angular momentum. When these constants of motion are *injected* (Punsly, 2001) into a flow as boundary conditions, equations (i), (ii) and (iii) specify the local plasma dynamics, while (iii) and (iv) determine the structure of the electromagnetic fields prescribed by the so-called transfield equation. Of note is that the transfield equation is a generalization of the aforementioned GSE, but allows the possibility of non-vanishing (stationary) flows. Very often, the transfield equation is also dubbed as GSE in the literature. Following this convention, we use the terms GSE, generalized GSE, or transfield equation indistinctly to refer to the most general equation allowing for the calculation of magneto-stationary configurations. Indeed, the transfield equation has been worked out for general stationary and axisymmetric spacetimes in Gourgoulhon et al. (2011), and for the case without the requisite of stationarity in Park (2002).

The analysis of the characteristic structure of the MHD wind equations, i.e., the propagation speeds of plasma waves, have proven exceptionally valuable for the understanding of wind dynamics and magnetospheric energy transport (e.g., Camenzind, 1986; Takahashi et al., 1990; Beskin, 1997; Punsly, 2001; Komissarov, 2002). Especially in the case of high magnetization and intermediate to high field line angular velocity (for field lines connecting to the central object), large regions of the magnetosphere for both, pulsars and BHs result to be sub-Alfvénic. This is because the magnetic energy dominates and gas is forced to flow along the field lines. Only well beyond the so-called Alfvén surface, which in this case approaches the light cylinder (LC, i.e., singular surfaces of the generalized GSE, which correspond to the location of points in the magnetosphere where the speed of rotation equals the light speed), the opposite is true. With the entropy having a subdominant contribution in plasma which is not relativistically hot (Punsly, 2001), all inertial contributions to the system are dominated by magnetic pressure. Hence, this class of winds may be approximately treated in the force-free limit (see also discussion of Lyutikov, 2003; Yuan et al., 2019).

In the force-free limit, the aforementioned axially symmetric, stationary MHD wind problem reduces to the analysis of the generalized GSE. The dynamics can be described by only two integrals of motion, namely the field line angular velocity and the current along a flux tube (Beskin, 1997). This is the case, e.g., in the extended magnetospheres of magnetars (highly magnetized, isolated neutron stars). Due to the slow rotational speed of most observed magnetars (e.g., Mereghetti et al., 2015; Turolla et al., 2015; Kaspi and Beloborodov, 2017; Pons and Viganò, 2019), their Alfvén surface (and, thus, their LC) is far away from the central object and their magnetosphere is essentially force-free. Throughout the literature, one finds a broad variety of analytical and numerical solutions to the transfield equation in magnetar magnetospheres (e.g., Glampedakis et al., 2014; Pili et al., 2015; Akgün et al., 2017, 2018; Kojima and Okamoto, 2018). Due to gravitational effects, the magnetospheres of spinning BHs possess an additional light cylinder (i.e., a second Alfvén surface) inside of the ergosphere. Beyond this surface, the flow is, again, inertially dominated (Beskin, 1997; Punsly, 2001). By imposing regularity conditions across the LCs as singular surfaces of the GSE, and assuming a well-behaved flow in the intermediate injection region, the transfield equation can be solved numerically (as has been done, e.g., by

Contopoulos et al., 2013; Nathanail and Contopoulos, 2014; Mahlmann et al., 2018; Yuan et al., 2019).

The described assumption of axial symmetry and stationarity is highly idealized and lacks (3D) dynamical effects, which possibly leads to energy dissipation for astrophysically (and astronomically) relevant radiative processes. The linking of the insights drawn from equilibrium solutions of the GSE to the dynamical evolution of electromagnetic fields is essential to avoid that *physical reality renders the discussion of the Grad–Shafranov equation probably no more than a mere pedantic exercise* (Punsly, 2001).

1.2.1 (Global) Energy Flows in BH Magnetospheres

Blandford and Znajek (1977) exploited the reduction of conserved quantities in the force-free limit of axisymmetric, stationary winds around Kerr BHs. In their seminal work, they theoretically analyze the extraction of reducible mass/energy from slowly spinning BHs, potentially able to power luminous outflows in the form of jets. The BZ process has later been identified as the electromagnetic analogy to the Penrose process (e.g., Beskin, 1997; Punsly, 2001; Komissarov, 2009). The braking of BH rotation and its conversion into energy flowing across the BH horizon works most efficiently for a field line angular velocity corresponding to half of the BH rotational velocity (i.e., half of the rotational velocity of its outer event horizon; see equation 3 of Mahlmann et al., 2018). Furthermore, in axially symmetric equilibrium configurations, the so-called Znajek condition (Znajek, 1977) holds, restricting the toroidal field at the BH horizon (see section 3.4 of Mahlmann et al., 2018). As such, it is a regularity condition (e.g., the extensive analysis by Beskin, 1997) rather than a boundary condition.

The treatment of the BH horizon as an actual (boundary) surface for analysis purposes was promoted, e.g., by Thorne et al. (1986); MacDonald and Thorne (1982). The so-called membrane paradigm equips the BH with a surface of physical properties, such as a surface resistivity (dragging along magnetic field lines during BH rotation). Until today, the membrane analogy has provided a great deal of intuitive understanding of magnetospheric processes, as has been recently demonstrated by the numerical experiments of Yuan et al. (2019). There, magnetic field lines are twisted by differentially rotating membranes, mimicking both the effects of a rotating BH and a thin AD extending over the equatorial plane (see also appendix B of Mahlmann et al., 2020). Penna et al. (2013) show a good agreement between jet parameters (torques, dissipation, and electromagnetic fields) derived from long-duration General Relativistic

Magnetohydrodynamics (GRMHD) simulations and the membrane paradigm locally, i.e., at the location of the BH horizon. At the same time, however, they demonstrate a large deviation from the approximated ideal BZ power due to the field geometry (see also Tchekhovskoy et al., 2010; Mahlmann et al., 2018) and the presence of an AD. The membrane paradigm endows an intuitive interpretation to field lines that connect to the central object. However, it is inapt to describe the dynamics (and their consequence for the BZ process) of general electromagnetic fields which are subject to frame-dragging of the spacetime or non-axisymmetric effects in extended regions of the magnetosphere (Mahlmann et al., 2020).

In its typical application, the BZ process requires that the BH ergosphere is threaded by large-scale magnetic fields connecting it to infinity and that the net magnetic flux supplied to the BH be non-zero. Neither of these conditions is trivially satisfied. In this context, *large-scale* denotes that, ab initio, magnetic field lines that cross the outer LC exist. Hence, there must be magnetic field lines with a typical radius of curvature that is already much greater than the BH's gravitational radius. An extensive effort to simulate ADs and jets produced by BH/AD systems (e.g., Koide et al., 2000; McKinney and Gammie, 2004; Hawley and Krolik, 2006; Tchekhovskoy et al., 2010; Palenzuela et al., 2011; Sądowski and Narayan, 2016; Chatterjee et al., 2019; Liska et al., 2019; Vourellis et al., 2019) has generally found that large-scale fields are required or preferred for jet production. However, Beckwith et al. (2008, 2009) point out the role of small scale structures emerging from these fields.

The short variability time scales observed in the TeV radiation of M87 (Acciari et al., 2009; Aharonian et al., 2003) suggest a strong non-stationarity of the central engine on time scales down to milliseconds. Since neither the BH mass nor its spin can change in such a short time, this variability can more reliably be related to the changes in the magnetosphere (and relatively close to the BH). Despite this, the origin of the observed variability is not yet understood and one can only speculate on the possible mechanisms driving it. Generally speaking, if the disc's magnetic field is ordered on scales much larger than the AD height, the magnetic flux of BH can change significantly only if the inner part of the AD collapses from time to time. Recently, Parfrey et al. (2015) have suggested that jets can be created by small-scale magnetic flux systems, which are naturally amplified and sustained in a turbulent AD. In such models, no large-scale flux is required. Magnetic field loops that connect the BH to the inner disc can open up, resulting in BH-powered BZ jet episodes. In the force-free, axisymmetric, electrodynamic models of the magnetosphere's evolution performed by Parfrey et al. (2015), the polarity of the poloidal field changes with time, being coherent over sufficiently long time scales to sustain episodic jets by the action of the BZ mechanism. As we shall show in this thesis, the mechanism described in Parfrey et al. (2015) also works efficiently when abolishing the restriction of axial symmetry (Mahlmann et al., 2020).

Blandford and Payne (1982, BP) devised a process in which *energy and angular momentum are removed magnetically from accretion discs, by field lines that leave the disc surface and extend to large distances*. Such magneto-centrifugal (MC; Krasnopolsky et al., 1999, and references therein) jet launching relies on the possibility of forming large-scale structured magnetic fields in the AD (e.g., by the action of turbulent dynamos Pudritz, 1981a,b). Historically, the extraction of mass and angular momentum from ADs forming in collapsing stars (Bisnovatyi-Kogan and Ruzmaikin, 1976) was considered in environments that naturally provided large-scale magnetic fields (e.g., the preexisting, large-scale stellar magnetic field). If field lines have an adequate inclination below a critical angle from the disc towards the vertical direction (Blandford and Payne, 1982; Lyutikov, 2009), sufficient thrust for a centrifugally driven flow is released. At large distances and with increasing toroidal dominance of the magnetic field, the flow is collimated in its motion away from the central system (but see Spruit et al., 1997). Over the lifetime of a BH/AD system, a combination of the BZ and BP process may be acting in the unification of both or developing the dominant contribution of one (cf. Garofalo et al., 2018).

In the realms of GRBs, active galactic nuclei (AGN), and X-ray binaries, the immediate vicinity of BHs is usually treated as a magnetosphere (cf. McKinney, 2005, 2006; Alic et al., 2012). In these astrophysical environments, a Poynting dominated flow in a baryon poor environment carries energy from either the BH or the AD (or both) into the jet launching region, in an interplay between the BZ and BP process. Given the extremely high magnetization of both the magnetosphere and the outflow, conventional GRMHD modeling is prone to severe numerical difficulties. Instead, GRFFE can be a suitable approximation in studying the dynamics of these energy flows in the vicinity of BHs and has been applied in this context by different groups (e.g., Komissarov, 2004; McKinney, 2006; Palenzuela et al., 2010; Alic et al., 2012; Paschalidis and Shapiro, 2013; Etienne et al., 2017). AGNs of the local universe, such as the Galactic Center or M87, are well suited to be modeled also by GRFFE in studies of the BZ process, due to their relatively low mass accretion rates (cf. Blandford and Begelman, 1999). The energy extraction by the BZ process (e.g., Thorne et al., 1986; Lee et al., 2000; Uzdensky, 2004; McKinney and Gammie, 2004; Komissarov, 2004; Tanabe and Nagataki, 2008; Tchekhovskoy et al., 2010; Penna et al., 2013; Mahlmann et al., 2018; Pan, 2018; Grignani et al., 2018, 2019; Huang et al., 2019) scales quadratically with the BH mass M as well as the strength of the magnetic field B threading the BH horizon. With typical masses of $\sim 10^6 - 10^9\, M_\odot$ they are, hence, likely to launch powerful outflows by the BZ mechanism.

1.3 (General Relativistic) Force-Free Simulations of Magnetospheres

The task of studying force-free electrodynamics as axisymmetric, stationary solutions to the (generalized) GSE around neutron stars and BHs has been conducted up to the limits of numerical accuracy in the recent years (e.g., Contopoulos et al., 1999, 2013; Nathanail and Contopoulos, 2014; Mahlmann et al., 2018; Yuan et al., 2019). Also, the workings of the BZ mechanism under ideal conditions have been thoroughly assessed and opened up to our intuition by the membrane paradigm (Thorne et al., 1986; MacDonald and Thorne, 1982). The seminal work by Blandford and Znajek (1977) is nowadays one of the preferred models in attempting to explain jet launching in magnetically dominated astrophysical environments. But only in recent years, due to the ever-increasing computational power, the scientific community has been able to start the necessary steps in order to include dissipative and 3D (non-axisymmetric) effects into a dynamical modeling of force-free magnetospheres. A major part of this thesis aims to be a contribution towards these efforts.

Simulations of physical processes require the modeling of relevant quantities discretized on numerical meshes and the solution of PDEs. These models can be numerically discretized (locally) in a Eulerian grid, attributing physical (local) quantities to every grid cell and evolving them by integrating conservative fluxes across cell interfaces in finite volume and finite difference methods (e.g., LeVeque, 2007; Rezzolla and Zanotti, 2013; Thomas, 2013; Toro, 2013, for a general review). An alternative approach is the choice of global representations of physical quantities in the coefficients of basic functions by spectral methods (e.g., Gottlieb and Orszag, 1977; Canuto et al., 2007). During this research, we have developed a finite volume simulation numerical code for GRFFE. Since this is the key tool in our research, we dedicate chapters 2 and 3 to thoroughly report on the numerical methods, validation and testing we have employed in it.

Two principal formulations to evolve force-free electromagnetic fields in time have emerged in recent years (see a detailed review in Paschalidis and Shapiro, 2013). Komissarov (2004) suggests the time-evolution of the full set of Maxwell's equations, where the magnetic induction and displacement elegantly encode the General Relativistic geometry as non-vacuum effects. Thus, in the formulation of Komissarov, there are six fundamental evolutionary variables, namely, the components of the electric and magnetic fields (extensive details can be found in section 2.2.2). This formulation has also been employed in an implementation relying on spectral methods (Phedra, Parfrey et al., 2015, 2017). Furthermore, Palenzuela et al. (2010); Carrasco and Reula (2017) carried out simulations in spherical geometries and higher-order finite difference approximations. McKinney (2006) introduces a formulation that is based on an adaptation of GRMHD to evolve the magnetic field (3 fundamental variables) as well as Poynting fluxes in time (three vector components; see further details in Section 2.2.4). As such, it was implemented, for example, in the GRMHD code HARM (Gammie et al., 2003), and in the GIRAFFE code provided in the frame of the EINSTEIN TOOLKIT[3] (Löffler et al., 2012) by Etienne et al. (2017). For this project, we have implemented the Maxwell's equations evolution system in General Relativity on the infrastructure of the EINSTEIN TOOLKIT (see a detailed review and motivation for our choice of formulation in chapter 2).

1.3.1 Magnetospheric Dissipation

Though they are not explicitly included in the single-fluid MHD and force-free limits, charged particles must still be present to i) shield the longitudinal electric field (Beskin, 1997), and ii) support magnetic fields by electrical currents. In other words, it is assumed that the currents of charge carriers required by the field dynamics exist, but do not carry inertia (Lyutikov, 2003). Suitable currents which ensure the so-called force-free conditions of magnetic dominance and zero longitudinal electric fields are employed throughout the literature (e.g., Lyutikov, 2003; Komissarov, 2004; Palenzuela et al., 2010; Alic et al., 2012; Paschalidis and Shapiro, 2013; Carrasco and Reula, 2017; Parfrey et al., 2017, see also section 2.2.2). All of them aim to introduce a well-behaved numerical dissipation of the electric field to maintain the *physicality* (McKinney, 2006) of the force-free fields, i.e., the restoring of configurations which fulfill the force-free constraints.

In practice, the force-free conditions reduce the number of independent fundamental variables in the system. So far, in all the numerical methods employed to deal with the force-free regime, the number of evolutionary variables is larger than allowed by the constraints. Hence, the fulfillment of the force-free conditions is not guaranteed during the time evolution, even if the initial conditions satisfy them. But besides numerical reasons, physically, the development of strong magnetic field gradients or current sheets (see below) in the borders of regions having different magnetic field polarity is a natural outcome of the evolution, impairing the fulfillment of the force-free constraints. Guided by the fact that regions, where force-free constraints are violated, are natural sites of magnetic dissipation (e.g., Komissarov, 2004), current numerical methods

---

[3] http://www.einsteintoolkit.org

introduce a resistivity, often of numerical origin (see section 1.3.1). Certainly, that methodology is contradictory to the very nature of force-free plasma (cf. Lyutikov, 2003) since: i) A non-zero resistivity yields an extra force acting on the charges (along the direction of the magnetic field while the Lorentz force is perpendicular to it). ii) Resistivity is defined through a suitable Ohm's law in the plasma rest frame[4] (e.g., Palenzuela, 2013); such a frame within the plasma is not uniquely defined in the force-free approximation. Any dissipation of field energy must, hence, be linked to a breakdown of ideal force-free conditions or be of numerical origin (Li et al., 2019).

Current sheets, *thin current-carrying layers across which the magnetic field changes either direction or magnitude* (Harra and Mason, 2004), are an exceptional challenge in force-free electrodynamics. Such locations may violate the perfect conductivity condition and require a model of (physical) resistivity (cf. Lyutikov, 2003; Komissarov, 2004). The magnetic diffusivity appears in the resistive (GR)MHD equations in combination with gradients of the (electro-)magnetic field (see, e.g., section 4.4.1 in Goedbloed and Poedts, 2004). Thus, when (very) small-scale perturbations or turbulences occur, the associated resistive terms may become dynamically important. This fact is challenging in general for numerical calculations because of the huge requirements on the necessary spatial resolution. At the same time, they are potential spots of singular importance for the acceleration of charged particles to relativistic speeds. So-called X-points in reconnecting highly magnetized plasmas are closely linked to the formation of magnetic islands (plasmoids), which are of paramount importance for the aforementioned acceleration mechanisms in general (e.g., Priest and Forbes, 2000), and specifically in the context of relativistic outflows (e.g., Ball et al., 2019; Petropoulou et al., 2019). Lyutikov (2003) points out that *one cannot construct a non-trivial (current-carrying) X-type point configuration of a force-free field.* However, in a numerical comparability study between force-free electrodynamics and particle-in-cell simulations, Lyutikov et al. (2017) found that the reconnection in a collapsing X-point is accurately described by force-free electrodynamics (augmented by suitable resistive currents) as long as the charge-starved electric fields do not become dominant.

Though the discussion of reconnection regions is often limited to 2D models due to their huge computational demands, turbulences, and small scale perturbations triggered by resistive instabilities (e.g., tearing modes, Furth et al., 1963) are intrinsically 3D effects. Magnetic dissipation is an intrinsically 3D

---

[4] I.e., the frame in which an observer comoves with the flow, perceiving the plasma in its immediate surroundings to be at rest.

phenomenon. Many features of reconnection are quite different in three dimensions (Hesse and Schindler, 1988; Schindler et al., 1988; Priest and Forbes, 2000), requiring a profound understanding of field line topology in order to correctly classify zero points (X-points) and bifurcations (Y-points). In 3D, one classifies reconnection according to the induced changes in field line topology. This justifies a genuine 3D modeling of magnetic dissipation in astrophysical plasma which we have employed for different astrophysical applications in Mahlmann et al. (2019, 2020).

As stated above, magnetar magnetospheres are an exceptionally well-suited laboratory for force-free electrodynamics due to the slow rotational periods of the central object (the Alfvén surface is far away from the stellar surface), the large magnetic fields provided by strong currents in the stellar surface, and the strong observational evidence of extreme processes in their vicinity (Beloborodov, 2017). Twisted configurations in such magnetospheres resulting from the *shearing of the stellar crust by internal magnetic stresses* (Parfrey et al., 2013) have been subject of research for several years (also Beloborodov and Thompson, 2007; Beloborodov, 2009). The sudden twisting at the footpoints of magnetic field lines or rapid rearrangement in the extended magnetospheres excites strong Alfvén waves which can catalyze the dissipation of magnetic energy either by mutual interaction or by deposition into the stellar crust (Howes and Nielson, 2013; Nielson et al., 2013; Li and Beloborodov, 2015; Li et al., 2019). In Mahlmann et al. (2019), we apply our GRFFE code to magnetar magnetospheres with a strong twist. When evolving (high-energy) solutions to the generalized GSE in time, instabilities develop and deposit a significant fraction of energy on the stellar surface, also resulting in notable stresses at the footpoints of magnetic field lines.

The consideration of non-symmetric force-free fields in 3D time-dependent simulations can produce current sheets whose effective size is much larger than their axially symmetric counterparts. In the context of BH/AD systems, Yuan et al. (2019) elaborate on the possibility of dissipation in elongated magnetic structures with significant (poloidal) kink, emerging vertically due to differential rotation of field lines. This argument can also be extended to toroidal structures by considering a helical component and, hence, an additional periodicity of dissipative regions. Bromberg et al. (2019) identify dissipation by magnetic reconnection due to the compression and merging of so-called kink lobes, recurring structures developing in the nonrotating plasma column of high magnetization.

Understanding the location and nature of dissipative mechanisms of BH magnetospheres is key to explain the so-called lamppost radiation produced in AGNs (e.g., Martocchia et al., 2000; Wilkins and Fabian, 2012). Lamppost radiation is assumed to be generated at a relatively low distance from the AD, reflected over it, and then observed on the earth. Signatures of this process are found as additional features in the observed spectral data emerging from relativistic accretion flows around BHs (George and Fabian, 1991; Tanaka et al., 1995). Martocchia et al. (2000) trace the origin of the reflected radiation to spots at only a few to a few tens of dynamical length scales (i.e., a few gravitational radii) above the BH. This shifts the center of attention to processes near the central object, which can not be explained by dissipation processes extending along large scales, often invoked to drive efficient energy extraction from the BH/AD system (for example in the Magnetically Arrested Disc - MAD - regime, Narayan et al., 2003).

Alternatively, the time scale restriction associated with the magnetic dissipation in large-scale field structures might be circumvented if there exist charge-starved regions in the vicinity of the central BH. These so-called spark gaps (as known in pulsar theory; Ruderman and Sutherland, 1975) are locations at which the electric field has a component parallel to its magnetic counterpart. Since in a pulsar magnetosphere, currents are parallel to the magnetic field, the existence of electric fields parallel to the currents yields Ohmic dissipation, i.e., they induce a significant voltage drop (a gap) along magnetic field lines. Gaps can also exist in the vicinity of BHs, such that particles can be accelerated to ultra-high energies and radiate in the TeV band (potentially with short variability, as observed in nearby galaxies, e.g., Acciari et al., 2009; Aharonian et al., 2003; Aleksić et al., 2014) by *inverse Compton scattering of ambient photons by electrons (positrons) accelerating in the gap* (Levinson and Rieger, 2011). The existence of conditions associated to such charge-starved regions can be inferred from both, very long baseline array (VLBA) observations and MHD simulations (Walker et al., 2008; Acciari et al., 2009), though one-fluid descriptions are not sufficient to account for charge separation. Levinson and Cerutti (2018) elaborate on this possibility in the case of the jet launching region of M87 by employing a kinetic description in their 1D particle-in-cell (PIC) code. In order to set on the mission of interpreting the limits of observable radiation emitted by (force-free) astrophysical plasma, it is crucial to - at least - differentiate the physical breakdown of electrical field screening in force-free simulations from numerically induced inaccuracies (since both effects develop electric fields with components parallel to the magnetic field). Our research of the accretion of small magnetic field structures onto rapidly spinning BHs (Mahlmann et al., 2020) paves the way for detailed analysis of magnetospheric dissipation in General Relativistic BH magnetospheres with GRFFE (and fully kinetic models in future).

Numerical errors in the discretization of continuum physics in space and time can be interpreted as a (numerical) resistivity, as has been discussed in depth for Eulerian MHD codes by Rembiasz et al. (2017). In the context of force-free electrodynamics, and since all numerical simulations are limited by finite resolution, the force-free conditions are expected to be repeatedly violated by numerical resistivity (see section 2.3.3 on constraint preservation in GRFFE codes). Besides, there are locations in the computational domain where it is natural to expect the breakdown of the force-free nature of the modeled plasma and the action of physical resistivity (necessary, but absent in GRFFE). The latter may be rather large in current sheets, kinked structures, or charge-starved regions. Magnetospheric dissipation in highly magnetized plasma is a topic of great relevance because it connects the physics of dynamical astrophysical environments to signals, which we can observe by current and future generation telescopes. Evaluating and controlling the dissipation in numerical (in our case, force-free) methods is, hence, of paramount importance.

1.4 Thesis Goals and Outline

With the methods and results presented in this thesis, we achieved the following goals:

1. Building accurate, non-trivial magnetic field configurations of stationary magnetospheres around Kerr BHs by solving the (generalized) GSE. Some of these configurations should include a magnetic connection between the BH and an idealized, equatorial accretion discs. These models are of key importance, both as initial data for dynamical simulations, and as blueprints for the energetics of (transient) states resembling those of the equilibrium structures during time-dependent 3D GRFFE evolution.

2. Assessing the stability of high-energy, twisted magnetospheres of non-rotating magnetars as the twist (thus, the magnetospheric energy) rises.

3. Obtaining an understanding of whether the instabilities that may disturb the energetic equilibrium of the magnetar magnetosphere arise from the relaxation of the axial symmetry restriction, hence, if the perturbations are 3D instabilities.

4. Grasping the observational signature that the transition from a high-energy (high-twist) state to a low-energy state of magnetar magnetospheres implies by applying simple theoretical models.

5. Extending the existing 2D axisymmetric studies (e.g., Beckwith et al., 2009; Parfrey et al., 2015) by full 3D modeling. In this way, we intend to understand the dynamics of magnetospheres around BHs when small-scale magnetic field structures (i.e., configurations in which magnetic field lines do not connect the BH to infinity) are accreted.

6. Assessing if efficient energy extraction from rapidly spinning BHs is possible under the circumstances stated in item 3 (above).

7. Seeking to link the fast TeV variability observed in some AGNs to instabilities in the magnetosphere surrounding a Kerr BH.

As we have laid out in the motivation of section 1.1 of this thesis, the tenuous atmospheres surrounding BHs and neutron stars are expected to be magnetically dominated and, hence, the net force acting on the plasma is very close to zero. Furthermore, General Relativistic gravitational fields are inherent to the aforementioned compact objects (especially in the case of BHs). Thereby, GRFFE modeling aiming to understand their general dynamics seems to be a sound (at least, low-order) approximation. The complex dynamics of the magnetospheres of compact objects are of genuine 3D nature. For instance, the modes of instability that disturb most of the outflows generated in BHs are non-axisymmetric. Perturbations are induced, for example, due to the kink instability in the high-magnetization regime, or due to the Kelvin-Helmholtz instability in the low-magnetization regime.

The lowest energy state of the magnetosphere around a magnetar is typically axisymmetric. However, as a matter of empirical fact, we observe energetic flares in soft gamma-ray repeaters (SGRs). Regardless of the origin of these flares (see the introduction of Mahlmann et al., 2019, included in appendix A) the possibility that they are associated - or motivated - by the transition from unstable, generically 3D, magnetospheres with high energies into a ground state of lower energy is extremely appealing. These points, like many other facts that are introduced in the three publications supporting the contents of this thesis (appendix A), justify our methodological choice for studying the dynamics of magnetospheres of compact objects utilizing 3D (GR)FFE numerical simulations. Our endeavor to build a suitable numerical tool is broadly described in chapter 2 and tested in chapter 3. Since this thesis is presented as a compendium of refereed publications, we discuss our main results and the connections to the new algorithmic developments we have undertaken in our code in chapter 4. This regards to all increments and add-ons in our code since Mahlmann et al. (2019) was published. We also deepen the discussion on the so-called critical loop length beyond the models included in Mahlmann et al. (2020).

Chapter 2

Methodology

2.1 Intermezzo

While elliptic differential equations, in general, correspond to physical states of equilibrium, oscillations, and propagation processes are expressed by hyperbolic differential equations [1] (Courant and Hilbert, 1968). An integral curve is called characteristic of a hyperbolic PDE, if the solution of the PDE along that curve can be computed by propagating the initial data forward along it. The meaning of characteristics is paramount in propagation processes, in which a quantity evolves in time along the very same. For example, in case of hydrodynamics, the characteristics of the Euler equations are given by two sets of curves: (a) The streamlines generated by the velocity fields and (b) a family of functions defined for the case that the propagation velocity is larger than the speed of sound. It can be shown that a regular solution to a hyperbolic equation exists and is unique, and that the *region of dependence of a point P is cut from the initial curve C by the [...] characteristics which meet point P* [2] (Courant and Hilbert, 1968). In other words, the finite speed of propagation along characteristics specifies a region of causal connection, providing solutions to a hyperbolic system of PDEs by propagating the initial data along characteristic curves.

As Lax (1973) elegantly elaborates, *a conservation law asserts that the rate of change of the total amount of a substance contained in a fixed domain G is equal to the flux of that substance across the boundary of G.* In hyperbolic

---

[1] Translated by the author. *Während elliptische Differentialgleichungen im allgemeinen physikalischen Gleichgewichtszuständen entsprechen, werden Schwingungen und Ausbreitungsvorgänge durch hyperbolische Differentialgleichungen dargestellt.*

[2] Translated by the author. *Das Abhängigkeitsgebiet eines Punktes P wird aus der Anfangskurve C durch die [...] P treffenden Charakteristiken ausgeschnitten.*

systems of PDEs *the formula which yields the [...] speed of propagation of one movement within another is [...] established without the need to be concerned about the form of the integrals* [3] (Hugoniot, 1887) of the underlying differential laws. These speeds correspond with the eigenvalues of the Jacobian matrices associated with the system of hyperbolic PDEs expressed in its quasi-linear form. A system is called strictly hyperbolic, if the eigenvalues (also called characteristic values) of its Jacobian matrix are distinct and real (Lax, 1973).

Hugoniot (1889) further analyzes the discontinuities which can arise in the movement of a fluid. Among those discontinuities introduced in the initial state and those arising from the boundaries (by external forces), he lays out the understanding that *discontinuities can arise within the movement, even though the initial conditions imposed at the boundaries are perfectly smooth* [4] (Hugoniot, 1889). With the work of Rankine (1870), conditions on the propagating quantities described by hyperbolic systems emerged. Arising from the weak (integral) solution of the corresponding conservation law (cf. Lax, 1973) the so-called Rankine-Hugoniot jump relations hold *for any type of disturbance, continuous or discontinuous, gradual or abrupt* (Rankine, 1870). In the case of the occurrence of discontinuous or non-differential regions in the domain, many generalized solutions to the same initial data can be found (Lax, 1973). *The task is to give a criterion for selecting the right one. A class of such criteria [...] are called entropy conditions, for in the gas dynamical case, they amount to requiring the increase of entropy of particles crossing the shock front. [...] A discontinuity satisfying the jump relation and the entropy condition is called a shock* (Lax, 1973). Besides shocks, there can be other discontinuities in a fluid dubbed *contact discontinuities*. From a mathematical viewpoint, while shocks are associated with genuinely non-linear characteristic fields, contact discontinuities may arise in linearly degenerate eigenfields (e.g., Lax, 1973). The physical difference among them (in fluid dynamics) is whether or not a flux of mass across the discontinuity is present.

The theory of systems of hyperbolic PDEs derived from conservation laws is exceptionally profound. Its historical development, gradually building up the techniques employed in the simulation of the most extreme regions of our universe is in itself a fascinating endeavor. In the following, we will use this

---

[3] Translated by the author. *La formule qui donne la vitesse [...] de propagation d'un mouvement dans un autre, se trouve [...] établie sans qu'il y ait eu lieu de se préoccuper de la forme des intégrals.*

[4] Translated by the author. *[...] des discontinuités peuvent prendre naissance dans le mouvement, même lorsque les conditions initiales et celles qui sont imposées aux extrémités sont parfaitement continues.*

theory to formulate a conservative time evolution scheme for the Maxwell's equations in General Relativity and augmented by the constraints of force-free electrodynamics. Historically, Maxwell's equations are closely related to the analysis of causal dependency in General Relativistic spacetimes (Courant and Hilbert, 1968).

Their force-free limit, namely the case were the inertially negligible *electrical masses [are] free, i.e., under the sole influence of the electromagnetic field* [5] (Einstein, 1916), is not strictly hyperbolic. Due to the constraint of a vanishing Lorentz force, the eigenvalues of the studied system of PDEs under consideration have a multiplicity larger than one and all waves are linearly degenerate (Komissarov, 2002). Though no shocks can be produced in the domain by steepening waves, *discontinuities may be introduced via discontinuous initial data and/or boundary conditions.* Numerical time evolution methods prescribed by hyperbolic PDEs derived from conservation laws rely heavily on the accurate discretization of continuous quantities in containers of finite extension (a computational mesh). Numerical truncation errors can drive the electromagnetic fields into a regime where the force-free conditions are violated and the system loses its hyperbolicity since some of its eigenvalues may become complex-valued (Komissarov, 2002). In the following sections, we present our formulation and implementation of GRFFE and discuss some of its subtleties.

---

[5] Translated by the author. *[...] die elektrischen Massen [sind] frei, d.h. unter dem alleinigen Einfluß des elekromagnetischen Feldes, [...]*

2.2 GRFFE as a Conservative Scheme

The following sections as well as the code implementation in the Einstein Toolkit employ units where $M_\odot = G = c = 1$, which sets the respective time and length scales to be $1M_\odot \equiv 4.93 \times 10^{-6}$ s $\equiv 1477.98$ m. This unit system is a variation of the so-called system of *geometrized units* (as introduced in appendix F of Wald, 2010), with the additional normalization of the mass to $1M_\odot$ (see also Mahlmann et al., 2019, on unit conversion in the Einstein Toolkit).

2.2.1 The $3+1$ Decomposition of Spacetime

To solve initial value boundary problems in General Relativity, a fully covariant formulation is not optimal. Instead, it is common to resort to a $3+1$ splitting of the space-time quantities when analyzing (tangible) physical quantities in General Relativity. Such foliations (Gourgoulhon, 2012; Tondeur, 2012) single out a time variable with respect to the remaining spatial coordinate (e.g., Arnowitt et al., 1959; Brown et al., 2009; Reisswig et al., 2011; Baumgarte et al., 2013, and references therein). It allows specifying initial conditions (i.e., initial values) on hypersurfaces of the spacetime that are isochrone. These initial values may be evolved forward in time exploiting the hyperbolic character of PDEs, governing most physical systems (e.g., the equations of GRFFE; see section 2.2.2). The four-dimensional space described by the metric $g_{\mu\nu}$ is foliated into non-intersecting timelike hypersurfaces Σ_t, i.e., level surfaces of the scalar field t. n_μ is defined as the future-pointing, timelike normal to Σ_t through the constituting relation

$$\alpha\, n_\mu \nabla^\mu t = 1\,. \tag{2.1}$$

Hereafter, ∇ denotes the spacetime covariant derivative. We adopt the convention that Greek indices stand for arbitrary spacetime quantities, while Latin indices will refer to the spatial coordinate directions of a $3+1$ spacetime decomposition. The lapse function α (Wheeler, 1964) indicates the separation in proper time between two hypersurfaces (measured in the direction normal to the extrinsic curvature at the base point). Trajectories of constant spatial coordinates across different hypersurfaces Σ_t define the time vector along them:

$$t^\mu = \alpha n^\mu + \beta^\mu \tag{2.2}$$

$\boldsymbol{\beta}$ is the shift vector, which denotes the spacelike displacement in the direction perpendicular to n^μ, required to reach the original base coordinate in a hypersurface $\Sigma_{t'}$ after leaving Σ_t. Hence, $\boldsymbol{\beta}$ is the spatial shift of coordinates between two time-slices (Wheeler, 1964). The shift vector satisfies by definition that $\beta^\mu n_\mu = 0$, but it is otherwise arbitrary, as the lapse function. Both together (lapse and shift) constitute gauge potentials (cf. Baumgarte et al., 2013). Choosing the time coordinate such that $t^\mu = (1, 0, 0, 0)$, the components of the normal vector n^μ and its (metric) dual n_μ are (assuming the metric signature is $+1$[6])

$$n^\mu = \left(\frac{1}{\alpha}, -\frac{\beta^i}{\alpha}\right) \qquad\qquad n_\mu = (-\alpha, 0, 0, 0)\,. \tag{2.3}$$

The line element of the spacetime may be written in the form (Arnowitt et al., 1959)

$$ds^2 = -\alpha^2 dt^2 + \gamma_{ij}\left(dx^i + \beta^i dt\right)\left(dx^j + \beta^j dt\right). \tag{2.4}$$

The level surfaces Σ_t are then three-dimensional slices of spacetime endowed with the projected three-metric

$$\gamma_{\mu\nu} = g_{\mu\nu} + n_\mu n_\nu. \tag{2.5}$$

The determinants of the metric tensors will be denoted by g or γ, respectively. Central to the numerical implementation of multi-coordinate methods in General Relativity is the conformally related spatial metric,

$$\bar{\gamma}_{ij} = e^{-4\phi}\gamma_{ij} \qquad\qquad \sqrt{\bar{\gamma}} = e^{-6\phi}\sqrt{\gamma}, \tag{2.6}$$

where $\bar{\gamma}$ denotes the determinant of the conformally related metric, and $e^{-6\phi}$ is the conformal factor. For practical purposes, we choose the gauge (the so-called Lagrangian choice, Brown, 2005),

$$\partial_t \bar{\gamma} = 0. \tag{2.7}$$

In other words, $\bar{\gamma}$ does not change during any spacetime evolution. This choice simplifies time-marching numerical algorithms and their theoretical foundation (effectively simplifying the derivation of covariant derivatives). We follow Alcubierre (2008) in defining the spacetime Christoffel symbols with respect to

---

[6] We note that in Mahlmann et al. (2018) we employ a signature $(+---)$, which is the usual one (historically) to deal with stationary problems, such as the evaluation of magnetospheric equilibria around compact objects. However, for dynamical problems, the alternative signature $(-+++)$ is more widespread. Hence, we have adopted it in Mahlmann et al. (2020).

components of the decomposed metric (2.4):

$$\begin{aligned}
\Gamma^0_{00} &= \left(\partial_t\alpha + \beta^m\partial_m\alpha - \beta^m\beta^n K_{mn}\right)/\alpha \\
\Gamma^0_{i0} &= \left(\partial_i\alpha - \beta^m K_{im}\right)/\alpha \\
\Gamma^0_{ij} &= -K_{ij}/\alpha \\
\Gamma^l_{00} &= \alpha\partial^l\alpha - 2\alpha\beta^m K^l_m - \beta^l\left(\partial_t\alpha + \beta^m\partial_m\alpha - \beta^m\beta^n K_{mn}\right) \\
&\quad + \partial_t\beta^l + \beta^m\nabla^{(3)}_m\beta^l \\
\Gamma^l_{m0} &= -\beta^l\left(\partial_m\alpha - \beta^n K_{mn}\right)/\alpha - \alpha K^l_m + \nabla^{(3)}_m\beta^l \\
\Gamma^l_{ij} &= {}^{(3)}\Gamma^l_{ij} + \beta^l K_{ij}/\alpha
\end{aligned} \tag{2.8}$$

Here, K_{mn} denotes the components of the extrinsic curvature (cf. Alcubierre, 2008) and one uses the contractions $\partial^l = \gamma^{lm}\partial_m$ as well as $K^l_m = \gamma^{ln}K_{nm}$. $\nabla^{(3)}$ and ${}^{(3)}\Gamma^l_{ij}$ are the covariant derivative and the Christoffel symbols with respect to the three-metric γ, respectively.

2.2.2 Maxwell's Equations in Conservative Form

The evolution of the full set of Maxwell's equations is one possibility[7] to deal with electrodynamics in General Relativity (Komissarov, 2004):

$$\nabla_\nu F^{\mu\nu} = I^\mu \tag{2.9}$$

$$\nabla_\nu {}^*F^{\mu\nu} = 0 \tag{2.10}$$

$F^{\mu\nu}$, and ${}^*F^{\mu\nu}$ are the Maxwell tensor and its dual, respectively. The dual of the Maxwell tensor is defined as

$$^*F^{\mu\nu} \equiv \frac{1}{2}\eta^{\mu\nu\lambda\zeta}F_{\lambda\zeta}, \tag{2.11}$$

where

$$\eta^{\mu\nu\lambda\zeta} = -(-g)^{-1/2}[\mu\nu\lambda\zeta], \qquad \eta_{\mu\nu\lambda\zeta} = (-g)^{1/2}[\mu\nu\lambda\zeta]. \tag{2.12}$$

$[\mu\nu\lambda\zeta]$ is the completely antisymmetric Levi-Civita symbol. I^μ is the electric current four-vector associated with the charge density $\rho = -n_\mu I^\mu = \alpha I^t$, and the current three vector $J^i = \alpha I^i$ measured by the normal observer n^μ. A covariant definition of the current four-vector is (Komissarov, 2004)

$$J^\mu = 2I^{[\nu}t^{\mu]}n_\nu, \tag{2.13}$$

where we use the standard terminology $I^{[\nu}t^{\mu]} = \frac{1}{2}(I^\nu t^\mu - I^\mu t^\nu)$. Komissarov (2004) introduces a set of vector fields which are analog to the electric and

---

[7] Another evolution scheme, developing energy fluxes rather than electric fields, was employed by e.g., McKinney (2006) or Etienne et al. (2017), see also section 2.2.4.

magnetic fields, **E** and **B**, and electric displacement and magnetic induction, **D** and **H**, of the electrodynamic theory of continuous media (see, e.g., Jackson, 1999, §I.4). They have the following spatial components in a $3+1$ decomposition of spacetime:

$$E_i = F_{it} \tag{2.14}$$

$$B^i = \frac{1}{2} e^{ijk} F_{jk} \tag{2.15}$$

$$D^i = \frac{1}{2} e^{ijk} {}^*F_{jk} \tag{2.16}$$

$$H_i = {}^*F_{ti} \tag{2.17}$$

Using the definitions (2.16) and (2.15) into in the time components of equations (2.9) and 2.10, one obtains the familiar constraints

$$\mathrm{div}\mathbf{D} = \rho, \tag{2.18}$$

$$\mathrm{div}\mathbf{B} = 0. \tag{2.19}$$

We separately evolve the charge continuity equation, which is straightforwardly obtained by taking the covariant derivative of (2.9),

$$\nabla_\nu I^\nu = 0\,, \tag{2.20}$$

to ensure the conservation of the (total) electric charge in the computational domain, as well as the compatibility of the charge distribution obtained numerically, with the currents that they generate. If this is not done, the difference $|\mathrm{div}\,\mathbf{D} - \rho|$ may grow unbounded with time due to the accumulation of numerical errors (Munz et al., 1999).

Following the convention in, e.g., Baumgarte and Shapiro (2003), the four-dimensional volume element induces a volume element over the hypersurfaces of the foliation

$$e^{abc} = n_\mu \eta^{\mu abc} = -\alpha \eta^{0abc}. \tag{2.21}$$

In the previous expression $e^{abc} \neq 0$ only for spatial indices, thus, we can write $e^{ijk} = -\alpha\eta^{0ijk} = [ijk]/\sqrt{\gamma}$. These equivalents to the classical electric field and magnetic induction as well as the electric displacement and the magnetic field, encode the geometry of spacetime (i.e., the lapse in time and frame-dragging of space) as non-vacuum effects in the full set of Maxwell equations. Embodied in the definitions (2.14) to (2.17) one has the following vacuum constitutive relations (Komissarov, 2004):

$$\mathbf{E} = \alpha\mathbf{D} + \boldsymbol{\beta} \times \mathbf{B} \tag{2.22}$$

$$\mathbf{H} = \alpha\mathbf{B} - \boldsymbol{\beta}\times\mathbf{D} \tag{2.23}$$

We may now write the Maxwell tensor as measured by the Eulerian observer (coincides with the zero angular momentum observer, ZAMO, in axisymmetric space times) in terms of the macroscopic field quantities (cf. McKinney, 2006):

$$F^{\mu\nu} = n^\mu D^\nu - D^\mu n^\nu - \eta^{\mu\nu\lambda\zeta} B_\lambda n_\zeta \tag{2.24}$$

$$^*F^{\mu\nu} = -n^\mu B^\nu + B^\mu n^\nu - \eta^{\mu\nu\lambda\zeta} D_\lambda n_\zeta \tag{2.25}$$

In the previous expressions, the electric and magnetic four-vectors are given by

$$D^\mu = F^{\mu\nu} n_\nu. \tag{2.26}$$

$$B^\mu = {}^*F^{\nu\mu} n_\nu, \tag{2.27}$$

For later reference, we provide two Lorentz invariants of the Faraday tensor, namely:

$$^*F^{\mu\nu} F_{\mu\nu} = 4 D^\mu B_\mu \tag{2.28}$$

$$F^{\mu\nu} F_{\mu\nu} = 2(\mathbf{B}^2 - \mathbf{D}^2) \tag{2.29}$$

If the electromagnetic field is the only source of stress-energy, the stress-energy tensor reads

$$T^{\mu\nu} = F^{\mu}{}_{\lambda} F^{\nu\lambda} - \frac{1}{4} g^{\mu\nu} F^{\lambda\kappa} F_{\lambda\kappa} \tag{2.30}$$

$$\begin{aligned} &= \frac{B^2 + D^2}{2}(\gamma^{\mu\nu} + n^\mu n^\nu) - s(B^\mu B^\nu + D^\mu D^\nu) \\ &- D_\lambda B_\kappa n_\delta (n^\mu \eta^{\nu\lambda\kappa\delta} + n^\nu \eta^{\mu\lambda\kappa\delta}), \end{aligned} \tag{2.31}$$

and the energy and momentum densities are defined as in, e.g., Gourgoulhon (2012), respectively:

$$e \equiv T^{\mu\nu} n_\mu n_\nu = \frac{1}{2}\left(B^2 + D^2\right), \tag{2.32}$$

$$S_\alpha \equiv -T_{\mu\nu} \gamma^{\mu}{}_{\alpha} n^\nu = \frac{B^2 + D^2}{2} n_\alpha - \eta_{\alpha\delta\lambda\kappa} n^\delta D^\lambda B^\kappa \tag{2.33}$$

Here, we use the projector $\gamma^{\mu}{}_{\alpha} = \delta^{\mu}{}_{\alpha} + n^\mu n_\alpha$, with $\delta^{\mu}{}_{\alpha}$ being the Kronecker delta, onto the hypersurfaces of the foliation. The components of the stress-energy tensor as a function of the vector fields $\{\mathbf{B}, \mathbf{D}, \mathbf{H}, \mathbf{E}\}$ are (Komissarov, 2004):

$$T^{t}{}_{t} = -\frac{1}{2\alpha}\left(\mathbf{E}\cdot\mathbf{D} + \mathbf{B}\cdot\mathbf{H}\right) \tag{2.34}$$

$$T^{i}{}_{t} = -\frac{1}{\alpha} e^{ijk} E_j H_k \tag{2.35}$$

$$T^{t}{}_{i} = \frac{1}{\alpha} e_{ijk} D^j B^k \tag{2.36}$$

$$T^i{}_j = -\frac{1}{\alpha}\left(D^i E_j + B^i H_j\right) + \frac{1}{2\alpha}\left(\mathbf{E}\cdot\mathbf{D} + \mathbf{B}\cdot\mathbf{H}\right)\delta^i{}_j \tag{2.37}$$

In the following, we make use of the algebraic relation

$$\frac{1}{2\alpha}\left(\mathbf{E}\cdot\mathbf{D} + \mathbf{B}\cdot\mathbf{H}\right) = \frac{1}{2}\left(\mathbf{D}^2 + \mathbf{B}^2\right) + \frac{1}{\alpha}e_{klm}D^k\beta^l B^m. \tag{2.38}$$

In order to build up a stationary magnetic configuration (as, e.g., in the magnetosphere around a compact object), it is necessary to guarantee that there are either no forces acting on the system or, more generally, that the forces of the system are in equilibrium. Except along current sheets the latter condition implies that the electric four-current I^μ satisfies the force-free condition (Blandford and Znajek, 1977):

$$F_{\mu\nu}I^\nu = 0 \tag{2.39}$$

Equation (2.39) is equivalent to a vanishing Lorentz force density f_μ on the charges measured by the ZAMO:

$$\nabla_\nu T^\nu{}_\mu = -F_{\mu\nu}I^\nu = -f_\mu \equiv 0 \tag{2.40}$$

Also, equation (2.39) can be seen as a system of linear equations, the non-trivial solution of which demands that the determinant of $F_{\mu\nu}$ vanishes. Since $\det F_{\mu\nu} = ({}^*F_{\mu\nu}F^{\mu\nu})^2/16 = (D^\mu B_\mu)^2$, the force-free condition (2.39) reduces to

$${}^*F_{\mu\nu}F^{\mu\nu} = 0, \tag{2.41}$$

or, equivalently (see 2.28)

$$D^\mu B_\mu = 0. \tag{2.42}$$

Hence, the component of the electric field parallel to the magnetic one always vanishes. Since $\det F_{\mu\nu} = 0$, the rank of $F_{\mu\nu}$ is two, provided $F_{\mu\nu}$ has non-vanishing components. If a^μ is a zero eigenvector of $F_{\mu\nu}$, i.e., $F_{\mu\nu}a^\mu = 0$, then another null eigenvector orthogonal to a^μ is $b^\mu = {}^*F^{\mu\nu}a_\nu$, and the Faraday tensor can be expressed as $F_{\mu\nu} = \eta_{\mu\nu\lambda\delta}a^\lambda b^\delta$ (cf. Komissarov, 2002). Hence, it admits a two-dimensional space of eigenvectors associated with the null eigenvalue (cf. Uchida, 1997). These zero eigenvectors are time-like if the Lorentz invariant $F_{\mu\nu}F^{\mu\nu}$ is positive (Uchida, 1997). The sign of the invariant $F_{\mu\nu}F^{\mu\nu}$ is not unanimously defined for generic electromagnetic four-vectors B^μ and D^μ. To choose the sign of the invariant, it is useful to consider the force-free approximation as a low inertia limit of relativistic MHD. This means that a physical force-free electromagnetic field should be compatible with the existence of a velocity field of the plasma. Recalling that the plasma four-velocity u^μ is a unit time-like vector ($u^\mu u_\mu = -1$), and that the Lorentz force is $f_\mu \propto F_{\mu\nu}u^\nu$, a physical force-free electromagnetic field ($f_\mu = 0$) should satisfy $F_{\mu\nu}u^\nu = 0$ (note that this is also required by the ideal MHD condition). Hence, the sign of the Lorentz invariant $F_{\mu\nu}F^{\mu\nu}$ (see equation 2.29) should consistently be positive, i.e.,

$$F_{\mu\nu}F^{\mu\nu} = 2(B^2 - D^2) > 0. \tag{2.43}$$

In the introduced language of the full system of Maxwell's equations in $3+1$ decomposition, expressions (2.42), and (2.43) respectively read

$$\mathbf{D}\cdot\mathbf{B} = 0\,, \tag{2.44}$$

$$\mathbf{B}^2 - \mathbf{D}^2 \geq 0. \tag{2.45}$$

Condition (2.45) implies that the magnetic field is always stronger than the electric field. Equivalently, one can classify the degenerate electromagnetic tensor as magnetic, since condition (2.43) guarantees that there exists a frame in which an observer at rest measures zero electric field (cf. Uchida, 1997). This observer is the comoving observer with four-velocity u^μ in the ideal MHD limit.

The challenge of maintaining the physical constraints of $\operatorname{div}\mathbf{B} = 0$ and $\operatorname{div}\mathbf{D} = \rho$ in numerical simulations (see section 2.3.3) has been reviewed throughout the literature (e.g., Dedner et al., 2002; Mignone and Tzeferacos, 2010), and applied to GRFFE, e.g., by Komissarov (2004) and the relativistic MHD regime, e.g., by Palenzuela et al. (2009); Miranda-Aranguren et al. (2018). Following Palenzuela et al. (2009, 2010) as well as Mignone and Tzeferacos (2010), we suggest to modify the system of Maxwell's equations (2.9), (2.10) in the following way (cf. Alic et al., 2012):

$$\nabla_\nu\left(F^{\mu\nu} + g^{\mu\nu}\Phi\right) = I^\mu + t^\mu \kappa_\Phi \Phi \tag{2.46}$$

$$\nabla_\nu\left({}^*F^{\mu\nu} + s^{\mu\nu}\Psi\right) = t^\mu \kappa_\Psi \Psi \tag{2.47}$$

Here, the definition of t^μ is given in (2.2), and we define $s^{\mu\nu} \equiv c_h^2\gamma^{\mu\nu} - n^\mu n^\nu$. c_h corresponds to a speed of propagation of the divergence cleaning errors; κ_Φ and κ_Ψ are adjustable constants that control the parabolic damping of the aforementioned numerical errors. The scalar potentials Ψ and Φ are ancillary variables employed to control the errors in the elliptic constraints $\operatorname{div}\mathbf{B} = 0$ and $\operatorname{div}\mathbf{D} = \rho$, respectively (see section 2.3.4, for details, and Dedner et al., 2002; Palenzuela et al., 2009; Mignone and Tzeferacos, 2010).

The augmented system of Maxwell equations (2.46, 2.47), can be written as a system of balance laws of the form

$$\partial_t\,\mathcal{C} + \bar{\nabla}_j\,\mathcal{F}^j = \mathcal{S}_n + \mathcal{S}_s\,, \tag{2.48}$$

where $\bar{\nabla}$ is the covariant derivative with respect to the conformally related metric, $\bar{\gamma}$ (2.6). $\mathcal{C}$ denotes the vector of conserved variables, $\mathcal{F}^j$ the flux vectors, $\mathcal{S}_n$ the geometrical and current-induced source terms, and finally $\mathcal{S}_s$ are the potentially stiff source terms (cf. Komissarov, 2004, App. C2). Note that each of these quantities consists of elements in a multidimensional space. In general, the conserved variables are derived from the so-called primitive variables; primitive variables are usually the physically measurable quantities, namely ρ, $\mathbf{B}$, and $\mathbf{D}$, as well as the numerical cleaning potentials Ψ and Φ. Adapting the notation used by Cerdá-Durán et al. (2008) and Montero et al. (2014), we specify the components of equation (2.48) in terms of the determinant of a reference metric $\hat{\gamma}$. We define the conserved variables as

$$\mathcal{C} \equiv \begin{pmatrix} \mathcal{L} \\ \mathcal{Q} \\ \mathcal{P} \\ b^i \\ d^i \end{pmatrix} = e^{6\phi}\sqrt{\frac{\bar{\gamma}}{\hat{\gamma}}} \begin{pmatrix} \rho \\ \frac{\Psi}{\alpha} \\ \frac{\Phi}{\alpha} \\ B^i + \frac{\Psi}{\alpha}\beta^i \\ D^i - \frac{\Phi}{\alpha}\beta^i \end{pmatrix}, \tag{2.49}$$

with their corresponding fluxes

$$\mathcal{F}^j \equiv e^{6\phi}\sqrt{\frac{\bar{\gamma}}{\hat{\gamma}}} \begin{pmatrix} \alpha J^j \\ B^j - \frac{\Psi}{\alpha}\beta^j \\ -\left(D^j + \frac{\Phi}{\alpha}\beta^j\right) \\ e^{ijk}E_k + \alpha\left(c_h^2\gamma^{ij} - n^i n^j\right)\Psi \\ -\left(e^{ijk}H_k + \alpha g^{ij}\Phi\right) \end{pmatrix}. \tag{2.50}$$

For the source terms, the split according to equation (2.48) yields the source terms $\mathcal{S}_n$, and the potentially stiff source terms $\mathcal{S}_s$:

$$\mathcal{S}_n \equiv e^{6\phi}\sqrt{\frac{\bar{\gamma}}{\hat{\gamma}}} \begin{pmatrix} 0 \\ \alpha\Psi\Gamma^t_{\mu\nu}s^{\mu\nu} \\ \alpha\Phi\Gamma^t_{\mu\nu}g^{\mu\nu} - \rho \\ -\alpha\Psi\Gamma^i_{\mu\nu}s^{\mu\nu} \\ \alpha\Phi\Gamma^i_{\mu\nu}g^{\mu\nu} - J^i \end{pmatrix} \qquad \mathcal{S}_s \equiv e^{6\phi}\sqrt{\frac{\bar{\gamma}}{\hat{\gamma}}} \begin{pmatrix} 0 \\ -\alpha\kappa_\Psi\Psi \\ -\alpha\kappa_\Phi\Phi \\ 0 \\ 0 \end{pmatrix} \tag{2.51}$$

2.2.3 The Force-Free Current

In force-free electrodynamics there is no uniquely defined rest frame for the fluid motion (e.g., Uchida, 1997; McKinney, 2006; Paschalidis and Shapiro, 2013; Shibata, 2015); the electromagnetic current I^{μ} cannot be determined by tracking the velocity of charges throughout the domain. Rather, the enforcement of the force-free conditions (2.44) and (2.45) determines a suitable current. Conditions (2.44) and (2.45), as well as the conservation condition (implicitly embodied in Maxwell's equations)

$$\partial_t \left(\mathbf{D} \cdot \mathbf{B}\right) = 0 \tag{2.52}$$

can be combined to obtain an explicit expression for the so-called force-free current I^{μ}_{FF} (cf. McKinney, 2006; Komissarov, 2011; Parfrey et al., 2017):

$$\begin{aligned} I^{\mu}_{\mathrm{FF}} = \rho n^{\mu} &+ \frac{\rho}{\mathbf{B}^2} \eta^{\nu\mu\alpha\beta} n_{\nu} D_{\alpha} B_{\beta} \\ &+ \frac{B^{\mu}}{\mathbf{B}^2}\, \eta^{\alpha\beta\lambda\sigma} n_{\sigma} \left(B_{\lambda;\beta} B_{\alpha} - D_{\lambda;\beta} D_{\alpha}\right) \end{aligned} \tag{2.53}$$

In practice, the combination of the force-free current (2.53) as a source-term to equation (2.9) - or equation (2.46) if we consider the augmented system of equations - with numerically enforcing conditions (2.44) and (2.45) restricts the evolution to the force-free regime. The discussion of techniques to ensure a *physical* (cf. McKinney, 2006) evolution of numerical force-free codes is a recurrent topic that can be found throughout the literature (e.g., Lyutikov, 2003; Komissarov, 2004; Palenzuela et al., 2010; Alic et al., 2012; Paschalidis and Shapiro, 2013; Carrasco and Reula, 2017; Parfrey et al., 2017; Mahlmann et al., 2019). We review one of these techniques in section 2.3.3.

2.2.4 Energy Balance Laws in GRFFE

The set of Maxwell's equations (2.9, 2.10) provides a numerically efficient way to directly evolving force-free electromagnetic fields. They form a system of eight PDEs; the constrains $\operatorname{div}\mathbf{B} = 0$ and $\operatorname{div}\mathbf{D} = \rho$ limit the number of independent variables to six (i.e., the three spatial components of B^{μ} and of D^{μ}). The force-free condition expressed in (2.42) limits the number of independent variables further to five. In order to prevent the accumulation of numerical errors in one particular component of the electromagnetic field, it is methodologically convenient to keep the six evolutionary equations and reset, e.g., the electric field component parallel to the magnetic field (e.g., Komissarov, 2002; McKinney, 2006, and section 2.3.3). However, if the electromagnetic field is the only source of stress-energy, then Maxwell's equations are equivalent to the conservation of the stress-energy tensor (Komissarov, 2002; McKinney, 2006), as shown in (2.40). The last equivalence in (2.40) is strictly valid under force-free conditions (i.e., if 2.39 holds). It is, thus, possible to use (all or part of) the four equations of energy-momentum conservation (2.40) in place of an equivalent number of Maxwell equations. Komissarov (2002) takes three spatial components of the magnetic field along with the three spatial components of the momentum density covector (2.33), which coincide with the covariant components of the Poynting vector,

$$S_i = e_{ijk} D^j B^k = \alpha T^t{}_i. \tag{2.54}$$

Here, the last equality follows from (2.36). The momentum density four-vector (2.33) is orthogonal to the magnetic field four-vector ($S_\mu B^\mu = 0$). Hence, not all components of S_μ are independent. Furthermore, the electric field four-vector can be obtained from S_μ and B_μ explicitly, using the fact that $D^\mu B_\mu = 0$ (i.e., assuming force-free conditions, see Paschalidis and Shapiro, 2013):

$$D^\mu \equiv -\frac{\eta^{\mu\delta\lambda\kappa} B_\delta S_\lambda n_\kappa}{B^2} \tag{2.55}$$

Thus, the evolution and constraint equations for the electric field (obtained from the inhomogeneous Maxwell equations, 2.9) become redundant. Paschalidis and Shapiro (2013) further show that the energy equation, associated with the time-component of the Poynting four-vector, is redundant under strict attainment of the force-free conditions, i.e., in the absence of dissipation (see appendix B in Paschalidis and Shapiro, 2013). Because of the choice of dynamical variables, we will refer to this set of evolutionary equations (following Paschalidis and Shapiro, 2013) as the **BS** formulation of GRFFE (to differentiate it from the **BE** formalism, where Maxwell's equations are evolved). However, excluding the inhomogeneous Maxwell equation (2.9) implies that I^μ does not explicitly appear in the equations of the **BS** formulation. Komissarov (2007) noted that the charge conservation equation (2.20) must be supplemented to the Maxwell's equations in the **BE** formalism. Otherwise, *there would be no guarantee that its numerical implementation would keep the electric charge distribution consistent with the evolution of the electric current* (Komissarov, 2007). We point out that neither McKinney (2006) nor Paschalidis and Shapiro (2013) include equation (2.20) in their implementation of the **BS** formalism.

In the remainder of this section, we obtain the evolution equations of the Poynting four-vector (2.33). As it is customary (e.g., Komissarov, 2004), we split these equations into their spatial components S_i (2.54) and the scalar S_t. We note that the derivation of these equations starting from the original Maxwell equations (2.9 and 2.10) has been done before (e.g., Komissarov, 2002, 2004; McKinney, 2006; Paschalidis and Shapiro, 2013). In that case, the derivation is relatively simple from the conservation (2.40) of the electromagnetic stress-energy tensor (2.30). However, when considering the augmented system of Maxwell equations (2.46 and 2.47), one does not usually have an explicit stress-energy tensor that incorporates the stress, energy, and momentum as well as the potential contribution of additional scalar potentials. Dedner et al. (2002) already considers several variants of parabolic/hyperbolic divergence cleaning techniques, in particular, the so-called extended generalized Lagrangian multipliers MHD formulation. This formulation yields source terms in the momentum and energy equations of classical ideal MHD which are directly related to the scalar potential Ψ. We may, thus, proceed to obtain the energy-momentum equations assuming that the conserved variables are still the energy and momentum densities corresponding to the standard electromagnetic stress-energy tensor (2.30). We further - momentarily - relax the force-free current constraint (2.39) since we aim to identify the sources of energy dissipation in the resulting equations. We will analyze the following products of the spatial components of the evolution equations (2.46) and (2.47), corresponding to the augmented system of Maxwell equations:

$$[\text{ eq. } 2.46 \ ] \times \mathbf{B} \tag{2.56}$$

$$\mathbf{D} \times [\text{ eq. } 2.47 \ ] \tag{2.57}$$

$$[\text{ eq. } 2.46 \ ] \cdot \mathbf{E} \tag{2.58}$$

$$[\text{ eq. } 2.47 \ ] \cdot \mathbf{H} \tag{2.59}$$

Equation (2.56) yields:

$$\begin{aligned} & e_{ijk}\sqrt{\gamma}\alpha\Gamma^j_{\mu\nu}g^{\mu\nu}B^k\Phi - \sqrt{\gamma}e_{ijk}J^jB^k \\ = & \, e_{ijk}\left(\sqrt{\gamma}D^j\right)_{,t}B^k - e_{ijk}\left(\sqrt{\gamma}\frac{\beta^j}{\alpha}\Phi\right)_{,t}B^k - e_{ijk}\left(\sqrt{\gamma}e^{jlm}H_m\right)_{,l}B^k \\ & - e_{ijk}\left(\sqrt{\gamma}\alpha g^{jl}\Phi\right)_{,l}B^k \end{aligned} \tag{2.60}$$

Analogously, from equation (2.57) one finds:

$$\begin{aligned} & - e_{ikj}\sqrt{\gamma}\alpha\Gamma^j_{\mu\nu}s^{\mu\nu}D^k\Psi \\ = & \, e_{ikj}\left(\sqrt{\gamma}B^j\right)_{,t}D^k + e_{ikj}\left(\sqrt{\gamma}\frac{\beta^j}{\alpha}\Psi\right)_{,t}D^k + e_{ikj}\left(\sqrt{\gamma}e^{jlm}E_m\right)_{,l}D^k \\ & + e_{ikj}\left(\sqrt{\gamma}\alpha s^{jl}\Psi\right)_{,l}D^k \end{aligned} \tag{2.61}$$

In order to derive an evolution equation for the Poynting flux, we will study the sum of equations (2.60) and (2.61) by its constituents:

$$e_{ijk}\left(\sqrt{\gamma}D^j\right)_{,t}B^k + e_{ikj}\left(\sqrt{\gamma}B^j\right)_{,t}D^k = \left(e_{ijk}\sqrt{\gamma}D^jB^k\right)_{,t} \tag{2.62}$$

$$\begin{aligned}
&- e_{ijk}\left(\sqrt{\gamma}e^{jlm}H_m\right)_{,l}B^k + e_{ikj}\left(\sqrt{\gamma}e^{jlm}E_m\right)_{,l}D^k \\
&= \sqrt{\gamma}H_{k,i}B^k - \sqrt{\gamma}H_{i,k}B^k + \sqrt{\gamma}E_{k,i}D^k - \sqrt{\gamma}E_{i,k}D^k \\
&= -\left(\sqrt{\gamma}\left(H_iB^k + D^kE_i\right)\right)_{,k} + \sqrt{\gamma}B^kH_{k,i} + \sqrt{\gamma}D^kE_{k,i} \\
&\quad + \sqrt{\gamma}E_i\mathrm{div}\mathbf{D} + \sqrt{\gamma}H_i\mathrm{div}\mathbf{B}
\end{aligned} \tag{2.63}$$

The simplification of the remaining terms makes use of the spacetime identities shown in section 2.2.1:

$$\begin{aligned}
&- e_{ijk}\left(\sqrt{\gamma}\frac{\beta^j}{\alpha}\Phi\right)_{,t}B^k - e_{ijk}\left(\sqrt{\gamma}\alpha g^{jl}\Phi\right)_{,l}B^k - e_{ijk}\sqrt{\gamma}\alpha\Gamma^j_{\mu\nu}g^{\mu\nu}B^k\Phi \\
&+ e_{ikj}\left(\sqrt{\gamma}\frac{\beta^j}{\alpha}\Psi\right)_{,t}D^k + e_{ikj}\left(\sqrt{\gamma}\alpha s^{jl}\Psi\right)_{,l}D^k + e_{ikj}\sqrt{\gamma}\alpha\Gamma^j_{\mu\nu}s^{\mu\nu}D^k\Psi \\
= &- e_{ijk}\sqrt{\gamma}\alpha\left[B^k\nabla_\mu\left(g^{\mu j}\Phi\right) + D^k\nabla_\mu\left(s^{\mu j}\Psi\right)\right]
\end{aligned} \tag{2.64}$$

All in all, the combination of equations (2.60) and (2.61) leaves us with the following evolution equation for the Poynting flux:

$$\begin{aligned}
&\left(\sqrt{\gamma}S_i\right)_{,t} - \left[\sqrt{\gamma}\left(H_iB^k + E_iD^k\right)\right]_{,k} \\
= &- \sqrt{\gamma}E_i\mathrm{div}\mathbf{D} - \sqrt{\gamma}H_i\mathrm{div}\mathbf{B} - \sqrt{\gamma}e_{ijk}J^jB^k - \sqrt{\gamma}B^kH_{k,i} - \sqrt{\gamma}D^kE_{k,i} \\
&+ e_{ijk}\alpha\sqrt{\gamma}\left[B^k\nabla_\mu\left(g^{\mu j}\Phi\right) + D^k\nabla_\mu\left(s^{\mu j}\Psi\right)\right]
\end{aligned} \tag{2.65}$$

Here, we have used equation (2.54). Employing the constitutive relations (2.22) and (2.23) this equation may be further simplified. For that, we obtain the following intermediate results:

$$\begin{aligned}
&\sqrt{\gamma}\left(B^kH_{k,i} + D^kE_{k,i}\right) \\
&= \frac{1}{2}\left[\sqrt{\gamma}\left(\mathbf{E}\cdot\mathbf{D} + \mathbf{B}\cdot\mathbf{H}\right)\right]_{,i} - \sqrt{\gamma}e_{klm}B^lD^m\beta^k_{,i} - e\alpha^2\left(\frac{\sqrt{\gamma}}{\alpha}\right)_{,i}
\end{aligned} \tag{2.66}$$

Inserted into equation (2.65) and using (2.37) for the mixed stress-energy tensor components results in the final equation of the Poynting flux balance:

$$\begin{aligned}
&\left(\sqrt{\gamma}S_i\right)_{,t} + \left(\sqrt{\gamma}\alpha T^k{}_i\right)_{,k} \\
&\quad = -\sqrt{\gamma}E_i \mathrm{div}\mathbf{D} - \sqrt{\gamma}H_i \mathrm{div}\mathbf{B} - \sqrt{\gamma}e_{ijk}J^j B^k \\
&\qquad + \sqrt{\gamma}e_{klm}B^l D^m \beta^k_{,i} + \frac{\alpha^2}{2} e \left(\frac{\sqrt{\gamma}}{\alpha}\right)_{,i} \\
&\qquad + e_{ijk}\alpha\sqrt{\gamma}\left[B^k \nabla_\mu \left(g^{\mu j}\Phi\right) + D^k \nabla_\mu \left(s^{\mu j}\Psi\right)\right]
\end{aligned} \tag{2.67}$$

The energy balance equation emerges from the analysis of equations (2.58) and (2.59):

$$\begin{aligned}
-\sqrt{\gamma}E_i J^i = {} & E_i \left(\sqrt{\gamma}D^i\right)_{,t} - E_i \left(\sqrt{\gamma}\frac{\beta^i}{\alpha}\Phi\right)_{,t} - E_i \left(\sqrt{\gamma}e^{ijk}H_k\right)_{,j} \\
& - E_i \left(\sqrt{\gamma}\alpha g^{ij}\Phi\right)_{,j} - \sqrt{\gamma}\alpha E_i \Gamma^i_{\mu\nu} g^{\mu\nu}\Phi
\end{aligned} \tag{2.68}$$

$$\begin{aligned}
0 = {} & H_i \left(\sqrt{\gamma}B^i\right)_{,t} + H_i \left(\sqrt{\gamma}\frac{\beta^i}{\alpha}\Psi\right)_{,t} + H_i \left(\sqrt{\gamma}e^{ijk}E_k\right)_{,j} \\
& + H_i \left(\sqrt{\gamma}\alpha s^{ij}\Psi\right)_{,j} + \sqrt{\gamma}\alpha H_i \Gamma^i_{\mu\nu} s^{\mu\nu}\Psi
\end{aligned} \tag{2.69}$$

We explicitly point out that the left-hand side of (2.68) is zero in the force-free regime, but this condition has been relaxed in this derivation. Adding up equations (2.68) and (2.69) by its constituents yields the following intermediate result:

$$\begin{aligned}
&E_i \left(\sqrt{\gamma}D^i\right)_{,t} + H_i \left(\sqrt{\gamma}B^i\right)_{,t} \\
&\quad = \frac{1}{2}\left[\sqrt{\gamma}\left(\mathbf{E}\cdot\mathbf{D} + \mathbf{B}\cdot\mathbf{H}\right)\right]_{,t} - \sqrt{\gamma}e_{klm}B^l D^m \beta^k_{,t} - e\gamma\left(\frac{\alpha}{\sqrt{\gamma}}\right)_{,t}
\end{aligned} \tag{2.70}$$

$$E_k \left(\sqrt{\gamma}e^{ijk}H_i\right)_{,j} + H_i \left(\sqrt{\gamma}e^{ijk}E_k\right)_{,j} = \left(\sqrt{\gamma}e^{ijk}H_i E_k\right)_{,j} \tag{2.71}$$

The simplification of the remaining terms makes use, again, of the spacetime identities shown in section 2.2.1:

$$\begin{aligned}
& - E_i \left(\sqrt{\gamma}\frac{\beta^i}{\alpha}\Phi\right)_{,t} - E_i \left(\sqrt{\gamma}\alpha g^{ij}\Phi\right)_{,j} - \sqrt{\gamma}\alpha E_i \Gamma^i_{\mu\nu} g^{\mu\nu}\Phi \\
& + H_i \left(\sqrt{\gamma}\frac{\beta^i}{\alpha}\Psi\right)_{,t} + H_i \left(\sqrt{\gamma}\alpha s^{ij}\Psi\right)_{,j} + \sqrt{\gamma}\alpha H_i \Gamma^i_{\mu\nu} s^{\mu\nu}\Psi \\
& = \alpha\sqrt{\gamma}\left[H_i \nabla_\mu \left(s^{\mu i}\Psi\right) - E_i \nabla_\mu \left(g^{\mu i}\Phi\right)\right]
\end{aligned} \tag{2.72}$$

Altogether, the combination of equations (2.70) to (2.72) leaves us with the following scalar balance law for the energy, accounting for the contributions of the scalar potentials and the possibility of breached force-free conditions:

$$\begin{aligned} &\left(\sqrt{\gamma}\alpha T^{t}{}_{t}\right)_{,t} + \left(\sqrt{\gamma}\alpha T^{k}{}_{t}\right)_{,k} \\ &= \sqrt{\gamma}E_iJ^i - \sqrt{\gamma}e_{klm}B^lD^m\beta^k_{,t} - e\frac{\gamma}{2}\left(\frac{\alpha}{\sqrt{\gamma}}\right)_{,t} \\ &+ \alpha\sqrt{\gamma}\left[H_i\nabla_\mu\left(s^{\mu i}\Psi\right) - E_i\nabla_\mu\left(g^{\mu i}\Phi\right)\right] \end{aligned} \tag{2.73}$$

A detailed understanding of the developed evolution equations for the electromagnetic energy density and the corresponding fluxes has a specific value in two different ways: i) It tracks and explains (physical) dissipation of electromagnetic energy. ii) It is a way to coherently separate electromagnetic contributions from the overall (fluid) stress-energy tensor. During this research, we focus on the implications of the first of these points. Besides the contributions induced by the spacetime geometry and numerical cleaning potentials, two terms in equations (2.67) and (2.73) are of paramount importance for the interpretation of physical dissipation:

$$\sqrt{\gamma}E_i\rho + \sqrt{\gamma}e_{ijk}J^jB^k = -\sqrt{\gamma}\alpha f_i \tag{2.74}$$

$$E_iJ^i = \mathbf{E}\cdot\mathbf{J} \tag{2.75}$$

Equation (2.74) includes the Lorentz force, f_i, which vanishes in GRFFE (2.40). Expression (2.75) is known as Joule's law (Landau et al., 2013) and measures the work done by an electric field on current-carrying particles. This work is dissipated into heat in the conducting medium. In GRFFE, condition (2.44) in general prevents both, Ohmic heating, and the action of a Lorentz force. Violations to ideal force-free conditions, or non-force-free regions within the domain may introduce physical dissipation through the channels identified in (2.74) and (2.75). We have applied this analysis for a tangible interpretation of the instability of closed loops in GRFFE in our recently published work Mahlmann et al. (2020).

2.3 Einstein Toolkit GRFFE Implementation

During this Ph.D. project, we have implemented a General Relativistic force-free electrodynamics (GRFFE) time-evolution code in Cartesian coordinates (Cartesian version, hereafter) for 3D simulations on the infrastructure of the Einstein Toolkit. In chapter 3, we present a suite of numerical and astrophysical tests to calibrate and validate the new code. The Cartesian version of our GRFFE tool has been used to set up numerical laboratories which produced data for dynamical magnetospheres of magnetars and rapidly spinning black holes within two publications (see appendix A, Mahlmann et al., 2019, 2020). In another branch of this project, we have started to implement a finite volume evolution scheme for GRFFE in spherical coordinates (spherical version, hereafter), including recent developments in the infrastructures adapting to curvilinear geometries (Baumgarte et al., 2013; Montero et al., 2014; Mewes et al., 2018, 2020). In section 2.3.6 we present a short overview (work-in-progress) of the envisioned spherical GRFFE scheme, though all the presented tests and results focus on the well established Cartesian version of our code.

Our GRFFE method uses the framework of the Einstein Toolkit (Löffler et al., 2012). The Einstein Toolkit is an open-source software package utilizing the modularity of the Cactus[8] code (Goodale et al., 2003), which enables the user to specify so-called thorns in order to set up customized simulations. The spacetime is integrated in time using the ML_BSSN[9] implementation of the BSSN formalism (Brown et al., 2009). Recently, extensive support of spherical grids has been successfully tested on the traditionally Cartesian Carpet mesh by the new implementation of Spherical_BSSN (Mewes et al., 2018). We make use of a variety of open-source software, such as the event horizon finder AHFinderDirect (Thornburg, 2004), the extraction of quasilocal quantities QuasiLocalMeasures (Dreyer et al., 2003), and the efficient SummationByParts (Diener et al., 2007).

To ensure the conservation properties of the algorithm, it is critical to employ *refluxing* techniques correcting numerical fluxes across different levels of mesh refinement (e.g., Collins et al., 2010). Specifically, we make use of the thorn Refluxing[10] in combination with a cell-centered refinement structure (cf. Shibata, 2015). We highlight the fact that employing the refluxing algorithm makes the numerical code $2-4$ times slower for the benefit of enforcing the

---

[8] http://www.cactuscode.org

[9] http://www.cct.lsu.edu/~eschnett/McLachlan/

[10] Refluxing at mesh refinement interfaces by Erik Schnetter: https://svn.cct.lsu.edu/repos/numrel/LSUThorns/Refluxing/trunk

conservation properties of the numerical method (especially of the charge). Refluxing also reduces the numerical instabilities, which tend to develop at mesh refinement boundaries.

This section reviews the techniques which are inherently important components of GRFFE in detail. Apart from these, we use a wide range of numerical recipes, such as higher-order monotonicity preserving (MP) reconstruction at cell interfaces (Suresh and Huynh, 1997) and the cleaning of numerically induced divergence and charges, respectively (cf. Dedner et al., 2002; Palenzuela et al., 2009; Mignone and Tzeferacos, 2010). For a comprehensive review of numerical strategies for GR fluid simulations, including the employed HLL Riemann solver and slope limiters we refer to Rezzolla and Zanotti (2013).

2.3.1 Finite Volume Integration

We solve equation (2.48) by discretizing its integral over the volume V of a cell of our numerical mesh (cf. LeVeque, 2007; Mignone, 2014; Martí and Müller, 2003),

$$\partial_t \langle \mathcal{C} \rangle + \frac{1}{V} \int_{\partial V} \mathrm{d}\mathbf{A} \cdot \mathbf{F} = \langle \mathcal{S}_n \rangle + \langle \mathcal{S}_s \rangle \,. \tag{2.76}$$

Here, $\langle\rangle$ denotes the volume average of a quantity. The divergence term $\bar{\nabla}_j \, \mathcal{F}^j$ appearing in equation (2.48) is integrated by applying Stoke's theorem and summing up the reconstructed fluxes $\mathbf{F}$ through the cell interfaces with respective area elements $\mathrm{d}\mathbf{A}$. In practice, we approximate volume averages by cell-centered values for the respective grid element. We name each cell-centered grid element by the indices (i, j, k) which correspond to the locations $x_i = x_0 + i\Delta x$, $y_j = y_0 + j\Delta y$, and $z_k = z_0 + k\Delta x$. Δx, Δy, and Δz represent the (uniform) numerical grid spacing in each coordinate direction. The quantities (x_0, y_0, z_0) denote the coordinates of an arbitrary reference point in 3D. Face-centered quantities are indicated by the subscript of a half-step added to the respective index, i.e., the subscript $i + 1/2$ denotes the value located at the face between the two elements (i, j, k) and $(i + 1, j, k)$. If no subscript is provided, we refer to the cell-centered values. The system of equations (2.49) to (2.51) is specified to its application in Cartesian coordinate systems (x, y, z) by setting $\sqrt{\bar{\gamma}} = 1$. In this case, the (*exact*) cell volume is

$$V = \Delta x \times \Delta y \times \Delta z \,, \tag{2.77}$$

and the (*exact*) area elements are denoted by

$$\mathrm{d}\mathbf{A} = (\Delta y \times \Delta z, \Delta x \times \Delta z, \Delta x \times \Delta y) \,. \tag{2.78}$$

Equation (2.76) is *approximated* by evaluating the fluxes $\mathbf{F}$ as reconstructed averages at cell interfaces:

$$\begin{aligned}\frac{1}{V}\int_{\partial V} \mathrm{d}\mathbf{A}\cdot\mathbf{F} \approx &\frac{F^x_{i+1/2}-F^x_{i-1/2}}{\Delta x}+\frac{F^y_{j+1/2}-F^y_{j-1/2}}{\Delta y}\\ &+\frac{F^z_{k+1/2}-F^z_{k-1/2}}{\Delta z}\end{aligned} \tag{2.79}$$

2.3.2 Numerical Fluxes Across Cell Interfaces

One central ingredient of conservative evolution schemes as formulated in equation (2.48) is the knowledge of the wave speeds, $\mathbf{w}$, and the corresponding directions, by which signals propagate through the domain. These speeds are then used for the setup of approximate Riemann solvers. The determination of characteristic speeds from the conserved fluxes $\mathcal{F}^j$ is well established (e.g., LeVeque, 2007; Toro, 2013, and references therein) and proceeds through the calculation of the eigenvalues of the Jacobian matrices of fluxes with respect to the conserved (or primitive) variables. Characteristic speeds of the force-free electrodynamics equations have been obtained, e.g., by Komissarov (2002) and Carrasco and Reula (2016). For the GRFFE system as defined in equations (2.49) to (2.51), the characteristic speeds $\mathbf{w}$ are

$$\mathbf{w}=\begin{bmatrix} -\beta^i\pm\alpha\sqrt{\gamma^{ii}} & m=3 & \text{(EVI)}\\ -\beta^i\pm c_h\alpha\sqrt{\gamma^{ii}} & m=1 & \text{(EVII)}\\ w_q & m=1 & \text{(EVIII)}\end{bmatrix}. \tag{2.80}$$

Here, we do not employ the sum convention; by m we denote the multiplicity of the respective eigenvalues. The speeds EVI correspond to the coordinate velocity of light as defined by Cordero-Carrión et al. (2008). The other two eigenspeeds (EVII) account for the propagation of the divergence cleaning potentials at speed c_h. Finally, EVIII corresponds to the wavespeed induced by the continuity equation of charge conservation, which is at most the coordinate velocity of light (EVI). We employ an approximate (HLL) Riemann solver (e.g., Rezzolla and Zanotti, 2013) to derive the numerical fluxes at the cell interfaces:

$$\mathbf{F}^j=\frac{\lambda_+\mathcal{F}^j\left(\mathbf{U}^-\right)-\lambda_-\mathcal{F}^j\left(\mathbf{U}^+\right)+\lambda_+\lambda_-\left(\mathbf{U}^+-\mathbf{U}^-\right)}{\lambda_+-\lambda_-} \tag{2.81}$$

$\mathbf{U}^{+}$ and $\mathbf{U}^{-}$ correspond to the reconstructed (conserved) variables at the cell interfaces. $\lambda_{\pm}$ are given by the minimal or maximal wave speeds:

$$\lambda_{+} = \max\left(0, \mathbf{w}\right) \qquad \lambda_{-} = \min\left(0, \mathbf{w}\right) \tag{2.82}$$

In flat space, the propagation speeds for the conservative scheme derived from equations (2.9) and (2.10) reduce to $\lambda_{+} = 1$ and $\lambda_{-} = -1$.

The characteristic decomposition for the alternative evolution system of energy fluxes (McKinney, 2006; Paschalidis and Shapiro, 2013; Etienne et al., 2017) is different from the one presented in this section. There, the necessary recuperation of electric fields from the Poynting fluxes requires $\mathbf{D} \cdot \mathbf{B} = 0$. Hence, the conservation law itself is augmented by one further condition (cf. Komissarov, 2002), resulting in an additional wavespeed with delicate degeneracies. The evolution of the full set of Maxwell's equations allows us to treat the force-free conditions as constraints that are decoupled from the numerical integration of equation (2.48).

2.3.3 Force-Free Constraint Preservation

Across the literature (e.g., Komissarov, 2004; Alic et al., 2012; Parfrey et al., 2017) we find various modifications in the definition of I^{μ} to drive the numerical solution of the system of PDEs (2.9) and (2.10) towards a state which fulfills equation (2.45) by introducing a suitable cross-field conductivity. This effectively augments the condition (2.52) used to determine expression (2.53) by a recipe to avoid (numerically) building up violations of $\mathbf{D} \cdot \mathbf{B} = 0$. We have presented a comprehensive summary of force-free constraint preservation in Mahlmann et al. (2019) and specify one of these techniques further in the following.

A straightforward way to guarantee the preservation of the $\mathbf{D} \cdot \mathbf{B} = 0$ constraint (equation 2.44) is the introduction of a numerical correction to the electric field after every step (and in each intermediate step) of the time evolution. As for this, the electric field ($\mathbf{D}$) is projected onto the direction perpendicular to the magnetic field ($\mathbf{B}$) in every point of the numerical mesh (e.g., Palenzuela et al., 2010):

$$D^{i} \rightarrow D^{k}\left({\delta^{i}}_{k} - B_{k}\frac{B^{i}}{\mathbf{B}^{2}}\right) \tag{2.83}$$

Alternatively, dissipative currents (induced by so-called driver terms) may ensure the evolution of the electromagnetic fields towards physically allowed (force-free) configurations. Using driver terms, the numerical evolution does not guarantee that the electromagnetic fields are exactly force-free after every time-step. However, force-free constraint violations are significantly reduced. While Komissarov (2004, 2011), and Alic et al. (2012) introduce a modified Ohm's law with a suitably chosen cross-field dissipation, Parfrey et al. (2017) modify the force-free currents (2.53) with additional dissipation driving the evolution towards a target ($\mathbf{D}\cdot\mathbf{B}=0$) configuration without further models for cross-field dissipation. They further generalize the conservation of equation (2.44) by introducing a target current fulfilling the following equation:

$$n^{\lambda}\nabla_{\lambda}\left({}^{*}F_{\mu\nu}F^{\mu\nu}\right)=\kappa_{I}\left(\eta I^{\mu}B_{\mu}-{}^{*}F_{\mu\nu}F^{\mu\nu}\right) \tag{2.84}$$

Here, κ_I is the decay rate driving the left-hand side of (2.52) towards the target value and η is a dissipation coefficient for the electric field which is parallel to the current.

As for the preservation of the $\mathbf{B}^2-\mathbf{D}^2\geq 0$ constraint (2.45), one can also employ an algebraic correction of the electric field after every step of the time evolution. Following Palenzuela et al. (2010), the electric field ($\mathbf{D}$) is rescaled in every point of the numerical mesh to the length of the magnetic field ($\mathbf{B}$) in a qualitatively similar manner as in (2.83):

$$D^{i}\rightarrow D^{i}\left(1-\Theta\left(\chi\right)+\frac{|\mathbf{B}|}{|\mathbf{D}|}\Theta\left(\chi\right)\right) \tag{2.85}$$

Here, Θ is the Heaviside function, and $\chi=\ \mathbf{D}^2-\mathbf{B}^2$. Again, an alternative is employed by Komissarov (2011), and Alic et al. (2012), introducing driver terms for additional dissipative currents, also for the conservation of the $\mathbf{B}^2-\mathbf{D}^2\geq 0$ constraint.

Our GRFFE scheme employs, by default, the algebraic correction of electric fields in every (intermediate) step of the time evolution as given by equations (2.83) and (2.85). However, in Mahlmann et al. (2019) we resorted to a suitably chosen resistivity model (in analogy to Komissarov, 2004) replacing the instant algebraic cutback of the electric displacement field by a gradual relaxation of force-free violations. For a review on the interpretation of constraint violations in GRFFE, we refer to Mahlmann et al. (2019).

2.3.4 Cleaning of Numerical Errors

We extend the augmented evolution equations by a hyperbolic/parabolic divergence error cleaning with the possibility of having a hyperbolic advection speed, $c_h>1$ (see below), as suggested by Mignone and Tzeferacos (2010). Contracting (2.47) with ∇_μ yields for the simplified case of stationary spacetimes (cf.

Komissarov, 2004):

$$\begin{aligned} -\kappa_\Psi \nabla_t \Psi &= \nabla_\mu \nabla_\nu \left({}^*F^{\mu\nu} + \left(c_h^2 \gamma^{\mu\nu} - n^\mu n^\nu \right) \Psi \right) \\ &= \nabla_\mu \nabla_\nu \left(c_h^2 \gamma^{\mu\nu} - n^\mu n^\nu \right) \Psi \\ &= c_h^2 \nabla_i \nabla^i \Psi - \nabla_\mu \nabla_\nu n^\mu g^{\nu\alpha} n_\alpha \Psi \\ &= c_h^2 \nabla_i \nabla^i \Psi + \nabla_t \nabla^t \Psi \end{aligned} \tag{2.86}$$

This compares to telegrapher equations, used for example to describe signal propagation in lossy wires. In this analogy, κ_Ψ, and c_h are the parameters controlling the damping and advection of numerical errors (Mignone and Tzeferacos, 2010). We stress the correspondence of c_h with a finite propagation speed for divergence errors (Mignone and Tzeferacos, 2010) and their decay according to the damping factor κ_Ψ. For c_h chosen equal to the speed of light, equation (2.10) reduces to the evolution system given in Palenzuela et al. (2009). In order to minimize violations of div$\mathbf{B} = 0$ in GR spacetimes of BHs, we find it beneficial to employ $c_h = 2$. In practice, this larger propagation speed does not limit the time step strongly, since BH spacetimes usually demand CFL factors (Courant et al., 1928) significantly smaller than unity (say $f_{\text{CFL}} \sim 0.1 - 0.3$) and, often, choosing $c_h > 1$ allows somewhat larger values of the same. Hence, we choose to advect numerical errors of this constraint with a speed faster than the speed of light to significantly reduce the numerical noise. We employ the same scheme with $c_h = 1$ for the cleaning of numerically induced errors in charge conservation by the scalar potential Ψ.

κ_Ψ and κ_Φ are damping rates, introducing time scales which act in addition to the advection time scales of the hyperbolic conservation law of the augmented GRFFE system (equations 2.49 to 2.51). Following the remarks by Miranda-Aranguren (2018) we consider that *a system of conservation laws is stiff when at least one of its relaxation times is small compared to the time scale determined by the frozen characteristic speeds of the system and some appropriate length scale.* Stiffness goes hand in hand with large damping factors (i.e., small timescales). At the same time, there is no unique and obvious choice for the calibration of the parameters driving the parabolic/hyperbolic cleaning; the ideal choice of constants can differ between implementations and boundary conditions, and also depends weakly on resolution (Mignone and Tzeferacos, 2010). To account for this juxtaposition of stiffness versus numerical composition we deem the damping contribution on the right-hand sides of equations (2.46) and (2.47) as potentially stiff, resulting in equation (2.51).

In order to deal with the potential stiffness introduced by the parabolic damping numerically, we employ a time-step splitting technique (Strang splitting, see, e.g., LeVeque, 2007), which has been applied previously to GRFFE by Komissarov (2004). Prior to and after the method-of-lines time integration[11] of the EINSTEIN TOOLKIT thorn MOL we evaluate the equations

$$\mathcal{P}\left(t\right)=\mathcal{P}_0\exp\left[-\alpha^2\kappa_\Phi c_h t\right]\ , \tag{2.87}$$

$$\mathcal{Q}\left(t\right)=\mathcal{Q}_0\exp\left[-\alpha^2\kappa_\Psi t\right]\ , \tag{2.88}$$

for a time $t=\Delta t/2$. We find it beneficial to choose a large value for κ_Φ, effectively dissipating charge conservation errors on very short time scales (and justifying the time-splitting approach). As for the divergence cleaning, we conducted a series of tests, optimizing κ_Ψ to yield stable and converging evolution for all shown resolutions, ultimately resorting to $\kappa_\Psi=0.125-0.25$ (see also Mahlmann et al., 2019). It may be interesting in the future to refine the described implementation of splitting techniques in the EINSTEIN TOOLKIT (embracing the MOL routines) by compiling a tailor-made time integrator for the system at hand.

2.3.5 Spacetime-Field-Spacetime Coupling

We employ the KRANC (Husa et al., 2006) generated MCLACHLAN code (Brown et al., 2009; Reisswig et al., 2011) to evolve the Einstein equations of spacetime evolution. We follow Löffler et al. (2012) and Mewes et al. (2016) in their numerical setup, evolving stably a single puncture for several light crossing times with the $1+\log$ and $\tilde{\Gamma}$-driver gauge conditions (cf. Baumgarte et al., 2009). We choose to employ the numerical evolution of BH geometries in two different simulation strategies: i) Decoupled (Cowling) evolution of a vacuum spacetime, employing the metric quantities in the time development of force-free equations. ii) Coupled evolution, employing both the metric quantities in the force-free equations and the field energy as a source-term to the Einstein equations (non-vacuum). Strategy ii) is used in currently ongoing projects of our GRFFE code, though the results presented in this thesis (specifically in appendix A, but see also Mahlmann et al., 2019, 2020) exclusively employ strategy i) or a flat background. In this section, we discuss some (numerical) subtleties of these strategies, especially relevant for the simulations in Mahlmann et al. (2020).

For both of these strategies (i and ii), we need to make use of the following prescriptions. GRFFE is naturally coupled to the (dynamical) properties of spacetime (spacetime-field coupling), which becomes manifest through metric terms appearing in the conservation laws (2.49 to 2.51). In their fully General

---

[11] Specifically, we add the exact evaluation of stiff source terms before the scheduling bin MOL_STEP and before MOL_POSTSTEP. The latter has to be restricted to the last intermediate step of the method-of-lines integration.

Relativistic formulation, equations (2.46) and (2.47) are singular at spacetime singularities. It has been shown that for hyperbolic formulations of spacetime evolution, no information can cross the BH horizon in the outwards direction (Etienne et al., 2007; Brown et al., 2007; Alcubierre, 2008; Brown et al., 2009). In the same context of BH spacetimes in the puncture gauge, all characteristics of General Relativistic hydrodynamics point inwards within a region (deep) inside of the BH horizon (Faber et al., 2007). This reasoning is applied in GR hydrodynamics and magnetohydrodynamics simulations, e.g., by Reisswig et al. (2013) and Mewes et al. (2016), to justify a reset of fluid variables in the causally disconnected numerical interior of the BH. We follow this strategy of cleaning the evolved quantities deep inside the BH horizon by an analogous implementation of a HORIZONCLEANER. In practice, this routine resets all fields and potentials (numerical and physical) to the initial value or zero after every step (and intermediate step) of the time evolution. Thus, we are ensuring a regular time development by correcting strong numerical errors induced by spacetime singularities in causally disconnected regions.

When resorting to the full spacetime-field-spacetime coupling encoded in strategy ii), we perform the feedback from the GRFFE fields onto the spacetime metric (field-spacetime coupling) by including the respective stress-energy-tensor (equations 2.34 to 2.37) as source terms of the Einstein equations in the spacetime evolution. In our simulations, electromagnetic and spacetime initial data is not self-consistently derived. Especially, the Hamiltonian and momentum constraints (cf. Gourgoulhon, 2012) are not necessarily fulfilled by default. In fully coupled evolutions we, hence, need to ensure that the total field energy is no more than a fraction of the BH rest mass-energy. Also, we make sure that the spacetime can adjust to the prescribed non-vacuum energy content by gradually building up electromagnetic fields from a vacuum (cf. Mahlmann et al., 2020).

During evolution, the BH is analyzed by a variety of routines. AHFINDER DIRECT (Thornburg, 2004) provides run-time measurements of the BH horizon radius and its reducible mass. QUASILOCALMEASURES (Dreyer et al., 2003; Schnetter et al., 2006) provides the (Bondi) mass and spin (aligned with the z-axis of the 3D coordinate box) of the central object. PUNCTURETRACKER determines the (potentially) time-dependent location of the BH singularity. Gravitational waves (GWs) are extracted by a multipole expansion (MULTIPOLE) of the Weyl scalar Ψ_4 (WEYLSCAL4, Hinder et al., 2011; Löffler et al., 2012). Finally, we monitor the accuracy of the spacetime evolution by evaluating the Hamiltonian and momentum constraints as derived by the thorn ML_ADMCONSTRAINTS.

2.3.6 Outlook: Spherical Finite Volume GRFFE

The traditionally Cartesian numerical Carpet mesh of the Einstein Toolkit has been adapted recently to support spherical coordinates (Mewes et al., 2018). For certain applications in the realm of astrophysical compact objects, it is beneficial to exploit the system's geometric and/or symmetric properties. One resorts to a decomposition in spherical coordinates in order to enhance the accuracy of the employed method. Starting from the reference metric formulation presented in section 2.2.2, there are two possible strategies for the numerical implementation of an evolution scheme in spherical coordinates:

i) Employ a Cartesian (flat) finite volume integrator (cf. section 2.3.1, as implemented in the thorn GRHydro, Mösta et al., 2013) to derive the right-hand side for method-of-lines time integration.

ii) Employ a spherical (curved) finite volume integrator (as implemented by Cerdá-Durán et al., 2008) to derive the right-hand side for method-of-lines time integration.

Option i) has been followed recently by various authors (Montero et al., 2014; Mewes et al., 2018) in order to use existing code infrastructure (for example in the Einstein Toolkit) without internal modifications. The fact that we have developed our GRFFE scheme from scratch has made it much more straightforward to employ option ii) by providing two different finite volume integration schemes (flat and curved, see sections 2.3.1 and 2.3.6.1). By construction, option ii) reserves the possibility to improve numerical accuracy by further adaptations, e.g., of the employed reconstruction algorithms (Mignone, 2014), which will be a subject of interest for future revisions of our GRFFE code.

2.3.6.1 Finite Volume Integration

The system of equations (2.49) to (2.51) is specified to its application in spherical geometries (r, θ, ϕ) by setting $\sqrt{\hat{\gamma}} = r^2 \sin\theta$. In this case, the (*exact*) cell volume is

$$V = -\frac{\Delta r^3}{3} \times \Delta \cos\theta \times \Delta\phi, \tag{2.89}$$

where we employ $\Delta r^3 = r^3_{i+1/2} - r^3_{i-1/2}$, $\Delta \cos\theta = \cos\theta_{j+1/2} - \cos\theta_{j-1/2}$. The numerical stability of the spacetime integral in equation (2.76) critically depends on the balancing of coordinate singularities, e.g., at the rotation axis. We guarantee an *exact* evaluation of metric contributions at the location of the cell-interfaces by transforming the reconstructed fluxes $\mathbf{F}$ to an orthonormal basis. The (*exact*) area elements in an orthonormal basis are denoted by

$$\mathrm{d}\hat{\mathbf{A}} = \left(r^2 \sin\theta \times \Delta\theta \times \Delta\phi, r\sin\theta \times \Delta r \times \Delta\phi, r \times \Delta r \times \Delta\theta\right). \tag{2.90}$$

Equation (2.76) is *approximated* by evaluating the fluxes $\mathbf{F}$ as reconstructed averages in an orthonormal basis at cell interfaces:

$$\begin{aligned}\frac{1}{V}\int_{\partial V} \mathrm{d}\hat{\mathbf{A}} \cdot \hat{F} \approx 3\,&\frac{r^2_{i+1/2}\,\hat{F}^r_{i+1/2} - r^2_{i-1/2}\,\hat{F}^r_{i-1/2}}{\Delta r^3} \\ &- \frac{3\Delta r^2}{2\Delta r^3}\,\frac{\sin\theta_{j+1/2}\,\hat{F}^\theta_{j+1/2} - \sin\theta_{j-1/2}\,\hat{F}^\theta_{j-1/2}}{\Delta\cos\theta} \\ &- \frac{3\Delta r^2}{2\Delta r^3}\,\frac{\Delta\theta}{\Delta\cos\theta}\,\frac{\hat{F}^\phi_{k+1/2} - \hat{F}^\phi_{k-1/2}}{\Delta\phi}\end{aligned} \tag{2.91}$$

In analogy to the above, we use $\Delta r^2 = r^2_{i+1/2} - r^2_{i-1/2}$. The reconstructed fluxes $\mathbf{F}$ (coordinate basis) are related to their orthonormal counterparts $\hat{\mathbf{F}}$ by the following relations:

$$\hat{F}^r = F^r \tag{2.92}$$

$$\hat{F}^\theta = r \times F^\theta \tag{2.93}$$

$$\hat{F}^\phi = r \times \sin\theta \times F^\phi \tag{2.94}$$

Chapter 3

Numerical Tests

This chapter aims to test the Cartesian GRFFE code which we have developed. For this purpose, we present several tests whose results specifically depend on the various numerical methods (e.g., reconstruction, cleaning of numerical errors) available in the new tool. Since the code is genuinely 3D, in 1D and 2D simulations, the surplus dimensions are condensed to the extension of one cell by applying appropriate boundary conditions to them. Section 3.1 reviews the 1D tests of signal propagation and stability in GRFFE following the work by Komissarov (2004) and Yu (2011) closely. In 3.2 we extend parts of the analysis of numerical resistivity in Eulerian MHD codes conducted by Rembiasz et al. (2017) to the implemented GRFFE scheme and quantify its numerical resistivity. In section 3.3 we probe the correct representation of force-free plasma waves by reproducing key results by Punsly (2003) and Li et al. (2019). Section 3.4 compiles selected tests with an astrophysical application, also including force-free electrodynamics on General Relativistic spacetimes of rotating Kerr black holes. We do not elaborate on the details of numerical spacetime evolution within the Einstein Toolkit, for which we refer the reader to Löffler et al. (2012) as well as section 2.3. We provide the cornerstones of our test setups in information boxes throughout this chapter. They contain some basic information about the Carpet grid specifications, especially including the requirements of the thorn CoordBase[1].

---

[1] http://einsteintoolkit.org/thornguide/CactusBase/CoordBase/documentation.html

3.1 Testing the 1D Reconstruction Methods

GRFFE allows two modes of plasma waves (Komissarov, 2002; Punsly, 2003; Li and Beloborodov, 2015; Li et al., 2019): Alfvén waves which transport energy along magnetic field lines and fast waves which correspond to the linearly polarized waves of vacuum electrodynamics (see also section 2.3.2). The following set of 1D problems is selected to demonstrate (a) the correct propagation of fast waves, (b) the formation of a current-sheet when magnetic dominance breaks down and (c) the correct modeling of stationary Alfvén waves which do not transport energy across magnetic field lines (cf. Li et al., 2019). The latter can only diffuse due to a finite numerical resistivity if the force-free constraints are not preserved (see section 3.2). The numerical solution to all these problems critically depends on the employed reconstruction algorithms. Since our code employs numerical reconstruction in 1D sweeps across all dimensions, we consider the following suite of 1D tests a fundamental measure for the performance of our GRFFE scheme. We verify (in the sense of Roache, 1997) the correct implementation of the reconstruction methods evaluating the convergence order from several data-sets with increasingly high-resolution. Specifically, we evaluate the (global) difference measure (cf. Antón et al., 2010)

$$\epsilon^{ab} = \frac{1}{N} \times \sum_i \left| u_i^a - u_i^b \right| , \tag{3.1}$$

where u^a and u^b are the one-dimensional vectors (of N elements) of the considered evolved quantity at different levels of resolution, $a, b \in [1, 2, 3]$. We denote the resolution on each of these levels by Δx_1, Δx_2, Δx_3, where $\Delta x_3/\Delta x_2 = \Delta x_2/\Delta x_1$. With level 1 being the level with the finest resolution, the (empirical) order of convergence is then defined as

$$\mathcal{O} = \frac{\log_n \left(\epsilon^{23}/\epsilon^{12}\right)}{\log_n \left(\Delta x_3/\Delta x_2\right)}. \tag{3.2}$$

3.1.1 (Degenerate) Current Sheet Test

Komissarov (2004) examines two variations of a current sheet problem, one of which has a solution in force-free electrodynamics, while the other violates the force-free constraints (equations 2.44, and 2.45). The tests for physical current sheets (figure 3.1) and degenerate current sheets (figure 3.2) is initialized by the

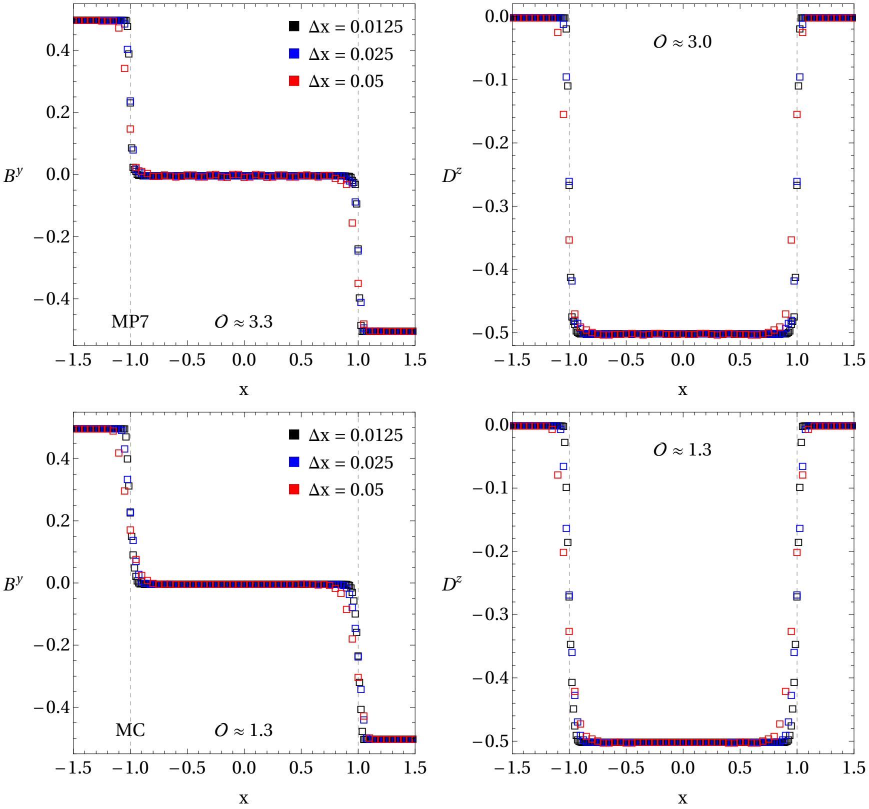

Figure 3.1: Current sheet test (Komissarov, 2004; Yu, 2011) as described by the initial data in equation (3.3) on a $x \in [-2, 2]$ grid ($f_{\text{CFL}} = 0.25$) at $t = 1.0$ for $B_0 = 0.5$ and different resolutions. Two fast waves emerge from the original discontinuity and propagate outwards with the speed of light (analytical position of the waves are indicated by dashed vertical lines). The order of convergence, $\mathcal{O}$ is indicated according to equation (3.2). *Top:* MP7 reconstruction. *Bottom:* MC reconstruction.

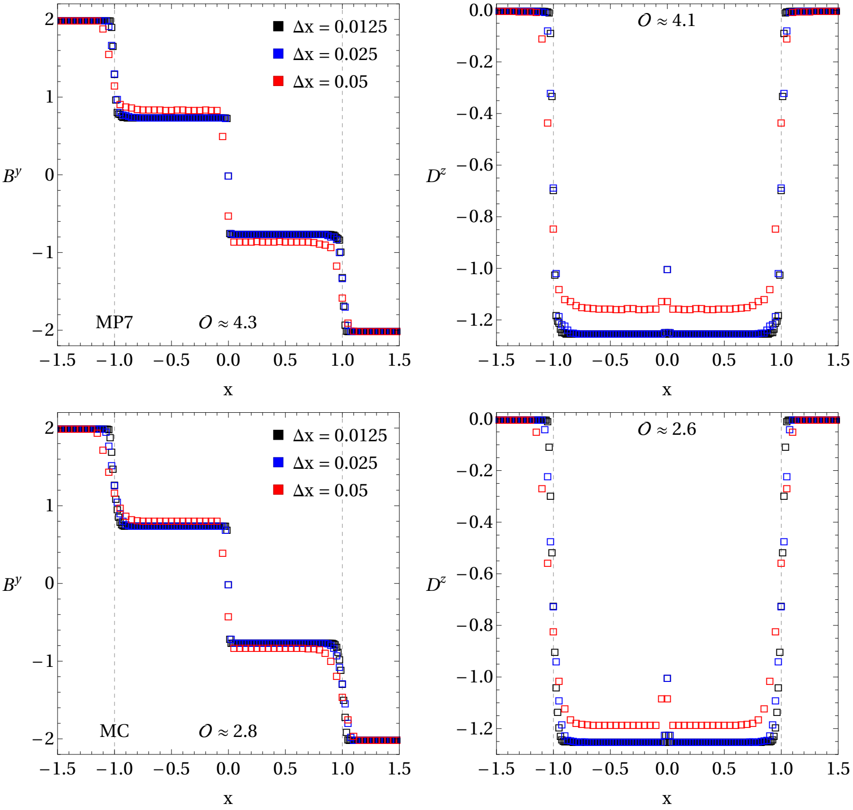

Figure 3.2: Degenerate current sheet test (Komissarov, 2004; Yu, 2011) as described by the initial data (3.3) with $B_0 = 2.0$. Two fast waves emerge from the original discontinuity and propagate outwards with the speed of light. The cross-field conductivity induced by conserving conditions (cf. equation 2.44, and 2.45) terminates the fast waves in the breakdown-zone. *Top:* MP7 reconstruction. *Bottom:* MC reconstruction.

following set of data:

$$\begin{aligned} \mathbf{D} = 0 \qquad B_x = 1.0 \qquad B_z = 0.0 \\ B_y = \begin{cases} B_0 & x < 0 \\ -B_0 & x > 0 \end{cases} \end{aligned} \tag{3.3}$$

If $B_0 < 1$, there exists a force-free solution given by two fast waves traveling at the speed of light (see figure 3.1, also figure C2 in Komissarov, 2004). For $B_0 > 1$ the solution is dominated by an increasing cross-field conductivity that locks $\mathbf{B}^2 - \mathbf{D}^2$ to zero in a current sheet located at $x = 0$. At this location, the conservation of the force-free constraints (sec. 2.3.3) becomes important for the field dynamics, i.e., it changes the structure of the propagating waves. The states bounded by the fast waves are terminated at the current sheet and a standing field reversal remains (see figure 3.2, cf. figure C2 in Komissarov, 2004). We take advantage of this test to compare the performance of two different reconstruction schemes: the second-order accurate, monotonized central (MC, van Leer, 1997) reconstruction and the seventh-order accurate monotonicity-preserving (MP7, Suresh and Huynh, 1997) reconstruction. From the results of the presented tests (figures 3.1 and 3.2), we draw the following conclusions:

- Fast electromagnetic waves propagate correctly with the speed of light.
- For a resolution similar to the one employed in Komissarov (2004), where $\Delta x = 0.015$, the time evolution of the (degenerate) current sheet is in good qualitative agreement with the literature (Komissarov, 2004; Yu, 2011).
- For resolutions below the lowest presented resolution (i.e., for $\Delta x > 0.05$) the wave structure of the presented test quickly smears out.
- Conservation of force-free constraints in the degenerate current sheet test is working well and agrees with similar tests throughout the literature.
- While monotonicity preserving reconstruction is slightly more oscillatory than, e.g., monotonized central flux limiters, the higher-order schemes allow a steeper resolution of wave-fronts and current sheets. While the order of convergence of the (more diffusive) MC reconstruction approaches the formal theoretical order of convergence ($\mathcal{O} = 2$), the order of convergence degrades below its theoretical value for MP7.
- Although some degradation of the order of convergence is expected in non-smooth regions of the flow (e.g., the discontinuities associated with fast or Alfvén waves), the algebraic enforcement of the violated force-free

constraints seems to have a large impact on the computed value of $\mathcal{O}$. Very likely, the latter procedure is the main source of deviation from the theoretical expectations regarding the order of convergence.

Given the previous statements, the developed GRFFE code passes the 1D (degenerate) current sheet test.

3.1.2 Three-Wave and Stationary Alfvén Wave Test

Komissarov (2002), Yu (2011) and Paschalidis and Shapiro (2013) suggest the three-wave problem (or a variant of the same, see figure 3.3) as a test for force-free electrodynamics. The initial discontinuity at $x = 0$ splits into two fast discontinuities and one stationary Alfvén wave. This effectively combines the previously introduced test of section 3.1.1 with the standing Alfvén wave test which was also employed by Komissarov (2004). The initial electromagnetic field reads (Paschalidis and Shapiro, 2013):

$$\begin{aligned} &\mathbf{B} = (1.0, 1.5, 3.5) \qquad \mathbf{D} = (-1.0, -0.5, 0.5) \qquad \text{if } x < 0 \\ &\mathbf{B} = (1.0, 3.0, 3.0) \qquad \mathbf{D} = (-1.5, 2.0, -1.5) \qquad \text{if } x > 0 \end{aligned} \tag{3.4}$$

We evolve this setup in time and present the results for different resolutions and reconstruction schemes in figures 3.3 and 3.4. Around the standing Alfvén wave at $x = 0$, high-order reconstructions tend to develop small-scale oscillations, especially visible in the plots of D^x, restricted to the region delimited by the fast waves (at $x = \pm 1$ for $t = 1$). Oscillations around this discontinuity can also be observed (for higher resolutions) in part of the literature (specifically, figure 4 in Yu, 2011). The order of convergence is slightly reduced when compared to the results shown in the previous section, probably due to the specific challenges of resolving stationary Alfvén waves, not only in GRFFE but also in relativistic MHD (see, e.g. Antón et al., 2010).

Komissarov (2004) achieves high accuracy maintaining a single standing Alfvén wave stationary during evolution for resolutions comparable to the highest one shown in figures 3.3 and 3.4. The numerical techniques of Komissarov (2004) are slightly different from ours, employing, for example, a linear Riemann solver which makes use of the full spectral decomposition of the FFE equations. The latter distinguishes all physical, and non-physical wave speeds and may provide additional accuracy at critical locations (in the context of GRFFE, e.g., current sheets). Additionally, Komissarov (2004) employs a different form of the current in Faraday's equation (2.9) based on a specific (numerical) resistivity model to drive electromagnetic fields towards a force-free state throughout the evolution.

Although one could suspect that this different treatment of the currents may alter the numerical solution significantly in this test (dominated by the numerical diffusivity of the standing wave), we find that our results are quite similar to the ones of Komissarov (2004). We consider the analytical solution of a standing Alfvén wave as initial data in the following:

$$\mathbf{B} = (1, 1, B^z) \qquad \mathbf{D} = (-B^z, 0, 1)$$
$$B^z = \begin{cases} 1 & x \leq 0 \\ 1 + 0.15\,[1 + \sin[5\pi\,(x - 0.1)]] & 0 < x \leq 0.2 \\ 1.3 & x > 0.2 \end{cases} \tag{3.5}$$

We present the results of the Alfvén stationarity test in figure 3.5. With resolutions comparable to the one employed in Komissarov (2004), i.e., $\Delta x \approx 0.015$, the artifacts around the wave-front diminish with an order of convergence of ≈ 2 for the MP7 reconstruction. As mentioned in the previous tests, standing Alfvén waves seem to introduce severe degradation of the order of convergence in MP methods (we have also tested these results with, e.g., MP5). This is very likely related to the preservation of the $\mathbf{D} \cdot \mathbf{B} = 0$ constraint, in the extended region $0 \leq x \leq 0.2$ where B^z is not uniform (3.5). In that region, the cutback of the electric displacement generates numerical errors which accumulate mostly close to its lower boundary (see the behavior of D^x in $-0.5 \lesssim x \lesssim 0$ in figure 3.3).

The presented three-wave and stationary Alfvén wave tests confirm our code's ability to correctly reproduce all possible plasma waves of GRFFE. However, our comparison shows that accurate results depend heavily on large resolutions around critical regions of GRFFE, like current sheets and stationary waves. Otherwise, numerical violations of the force-free conditions are likely to reduce the order of the scheme at hand. We therefore find it necessary to quantify our code's numerical resistivity in section 3.2. With the presented tests and their broad comparability to their counterparts in the literature (Komissarov, 2004; Yu, 2011), we conclude that our GRFFE tool passes the three-wave and standing Alfvén test.

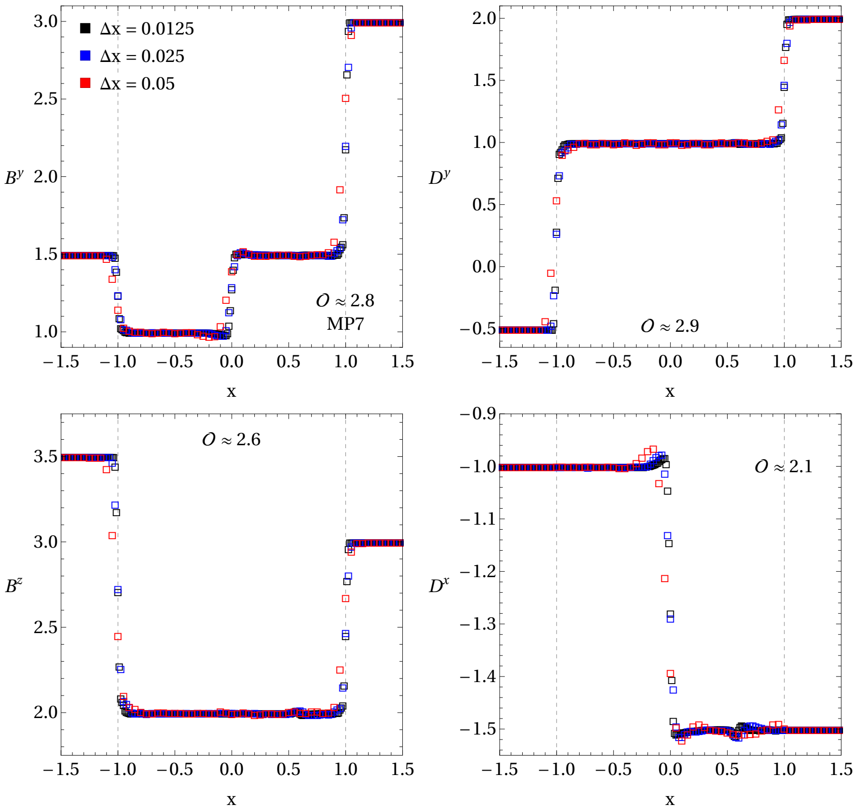

Figure 3.3: Three-wave problem (Paschalidis and Shapiro, 2013) as described by the setup in equation (3.4). The numerical setup and labels are the same as in figure 3.1. The initial discontinuity at $x = 0$ splits into two fast discontinuities and one stationary Alfvén wave. MP7 reconstruction.

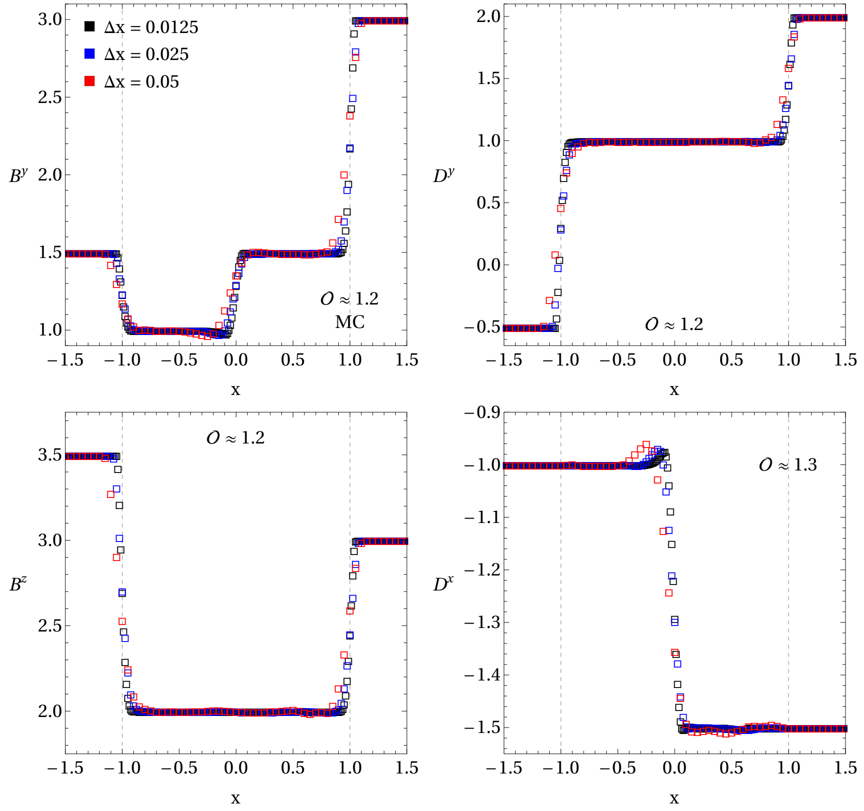

Figure 3.4: As figure 3.3 but employing MC reconstruction.

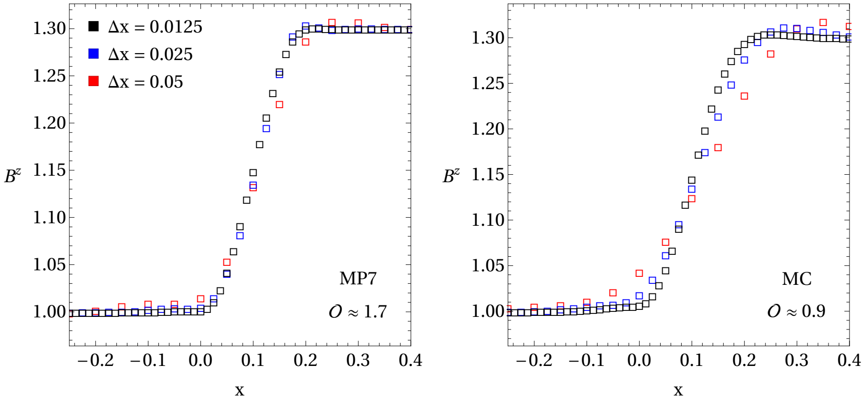

Figure 3.5: Stationary Alfvén wave problem (Komissarov, 2004), numerical setup as in figure 3.1.

3.2 Tearing Modes and Numerical Resistivity

Any conventional numerical method to solve hyperbolic systems of PDEs adds different (method dependent) amounts of numerical diffusivity which is necessary to stabilize the solution across discontinuities. Furthermore, the process of discretizing the PDEs for their numerical treatment introduces some numerical diffusivity. The hyperbolic system of conservation laws of GRFFE described in chapter 2 is no exception to this general rule and, thus, their numerical evolution also adds numerical diffusivity. Conventionally, this numerical diffusivity acting on the magnetic field is called *numerical resistivity*. Calibrating the amount of numerical resistivity in a numerical code that aims to implement the equations of ideal GRFFE is very important. It allows us to understand whether the modeled dynamics are dominated by physical effects or by an (excessive) numerical dissipation. However, a complete characterization and measure of the amount of numerical resistivity in a Eulerian code as ours is not an easy task. It would require an extensive suite of calibration tests (e.g., Rembiasz et al., 2017, and references therein), something which is beyond the scope of this thesis but will be subject of future work. Nevertheless, we may obtain some preliminary characterization of the code's numerical resistivity measuring the growth rate of well known resistive instabilities such as tearing mode (TM) instabilities. A similar strategy has been followed in Miranda-Aranguren et al. (2018) in resistive relativistic MHD. Since the development of TMs requires, at least, a longitudinal current sheet in 2D (though, obviously, they can also develop in 3D), the study of the growth rate of resistive TMs allows us to test our code in more than one dimension.

TM instabilities are resistive instabilities which can develop in current sheets and dissipate magnetic energy into kinetic energy if a plasma fluid is considered. Note, however, that in a pure force-free approximation, the only existing energy is that of the electromagnetic field and, thus, the dissipation of magnetic energy may

- Numerical mesh ($[x_{\min}, y_{\min}, z_{\min}] \times [x_{\max}, y_{\max}, z_{\max}]\,; [\Delta x, \Delta y, \Delta z]$):
  $\left[-2-\frac{\Delta x}{2}, -\frac{\Delta x}{2}, -\frac{\Delta x}{2}\right] \times \left[2+\frac{\Delta x}{2}, \frac{\Delta x}{2}, \frac{\Delta x}{2}\right]; [\Delta x, \Delta x, \Delta x]$,
  where $\Delta x \in [0.05, 0.025, 0.0125]$
- Boundaries: Staggered boundaries, periodic in y and z.
- CFL-factor: $f_{\text{CFL}} = 0.25$ (4^{th} order Runge-Kutta time integration)
- Parabolic/hyperbolic cleaning: $k_\Psi = 0.25$, $k_\Phi = 250$, $c_h = 1$.

Box 3.1: Code parameters; testing the 1D Reconstruction Methods (3.1).

simply result in a sink of the latter. Layers of reconnecting (i.e., disconnecting and rejoining) magnetic field lines are a potential site of (astrophysically relevant) relativistic particle acceleration (Ball et al., 2019; Guo et al., 2019; Petropoulou et al., 2019). In GRFFE, besides the standard sources of numerical diffusivity, there is yet another one, namely, the numerical resistivity induced by the algorithms used to control the violations of conditions (2.44) and (2.45). As we shall see, both, the standard sources of numerical resistivity as well as the resistivity produced by the violation of the force-free constraints are especially sensitive to the resolution of the numerical mesh.

Following the setup of a force-free current sheet in relativistic resistive MHD adapted from Del Zanna et al. (2016), we examine TMs along the x-axis on a two-dimensional domain of $[-20a, 20a] \times [-L/2, L/2]$, where $a = 0.05$, and $L = 2\pi/k$. In magnetically dominated plasma, the theoretical growth rate of TMs is the same as in incompressible MHD (e.g., Komissarov et al., 2007). In this test, we employ $k = \pi$. Furthermore, we use periodic boundary conditions in the x and y directions. Our models run on a numerical grid consisting of $N_x \times N_z$ zones, which are uniform in each of the x and y directions. In order to trigger TM instabilities, the initial magnetic field

$$\begin{aligned} B_{0x} &= B_0 \tanh\left(z/a\right), \\ B_{0y} &= B_0 \operatorname{sech}\left(z/a\right), \end{aligned} \tag{3.6}$$

is perturbed by

$$\begin{aligned} B_{1x} &= \epsilon\left(ak\right)^{-1} B_0 \sin\left(kx\right) \tanh\left(z/a\right) \operatorname{sech}\left(z/a\right), \\ B_{1z} &= \epsilon B_0 \cos\left(kx\right) \operatorname{sech}\left(z/a\right). \end{aligned} \tag{3.7}$$

We set $B_0 = 1$ and the perturbation amplitude parameter $\epsilon = 10^{-4}$. Note that a represents the width of the current sheet, compared to its length, L. We assume that the initial electric field is zero. The growth rate of the TMs, $\gamma_{\rm TM}$, may be traced, e.g., by examining the growth of the magnetic field component B_z. After a (numerical) transient phase, one should have a theoretical growth according to

$$B_z\left(t, x, y, z\right) = B_{1z}(x, y, z) e^{\gamma_{\rm TM} t}, \tag{3.8}$$

where B_{1z} is a time-independent eigenfunction of the TM. To obtain a globally and positively defined quantity for the growth rate, we study the integral of B_z^2 over a suitably chosen patch of the computational domain (covering the entire length of the current sheet):

$$\ln \int B_z^2 \mathrm{d}S = 2\gamma_{\rm TM} t + \ln \int B_{1z}^2 \mathrm{d}S \tag{3.9}$$

Figure 3.6 shows the time evolution of (3.9) for different mesh resolutions and reconstruction schemes. The slope $2\gamma_{\rm TM}$ of the linear relation (3.9) may be derived by a suitable fit which disregards the initial (numerically dominated) adjustment phase. We aim to provide an estimate of the numerical resistivity as a function of the numerical resolution based on two different approximations. The first one (model A) assumes that the plasma is inviscid. In this case, the growth rate of the TM mode (for a given mode k) depends on the physical resistivity, η, as (Rembiasz et al., 2017, equation 147)

$$\gamma_{\rm TM} = 1.82\eta^{3/5} v_A^{2/5} a^{-8/5} (ak)^{2/5} \left(\frac{1}{ak} - ak\right)^{4/5}. \tag{3.10}$$

Here, v_A denotes the Alfvén speed, which in our GRFFE code is $v_A = 1$. For the specific choice of k and a employed in our setup, we can write (3.10) as

$$\gamma_{\rm TM}(k = \pi, a = 0.05) \approx 451\eta^{3/5}. \tag{3.11}$$

Alternatively, in the so-called long-wavelength approximation (model B, characterized by $ka \ll 1$), the maximum growth rate (i.e., the growth rate of the fastest-growing mode) can be evaluated from figure 3 of Furth et al. (1963), resulting in

$$\gamma_{\rm TM,max} \approx 0.6 a^{-3/2} v_A^{1/2} \eta^{1/2}, \tag{3.12}$$

or, equivalently,

$$\gamma_{\rm TM,max}(a = 0.05) \approx 53.7\eta^{1/2}. \tag{3.13}$$

The force-free models we run do not include any physical resistivity. Hence, the growth of TM modes is induced by the action of resolution-dependent, numerical resistivity, η_*. Thus, we may replace η in equations (3.11) and (3.13) by η_*. Once the TM growth rate is obtained for each resolution and reconstruction method, we can express the corresponding numerical resistivity following Rembiasz et al. (2017, section 4.3.3), namely using

$$\eta_* = \mathfrak{N} \times \mathcal{V} \times \mathcal{L} \times \left(\frac{\Delta x}{\mathcal{L}}\right)^r, \tag{3.14}$$

where $\Delta x = 40a/N_x$ is the resolution at which the growth rate is measured, and $\mathfrak{N}$ is a (resolution-independent) numerical coefficient. Expression (3.14) together with the estimates of the growth rate (equations 3.11 and 3.13) allow to compute the resolution-independent coefficient $\mathfrak{N}$ and the exponent r that characterize the numerical method used to perform the simulation. $\mathcal{V}$ and $\mathcal{L}$ are the characteristic velocity and length scale of the process. Having neglected the plasma inertia, the light speed ($\mathcal{V} = 1$) is the only possible choice in the

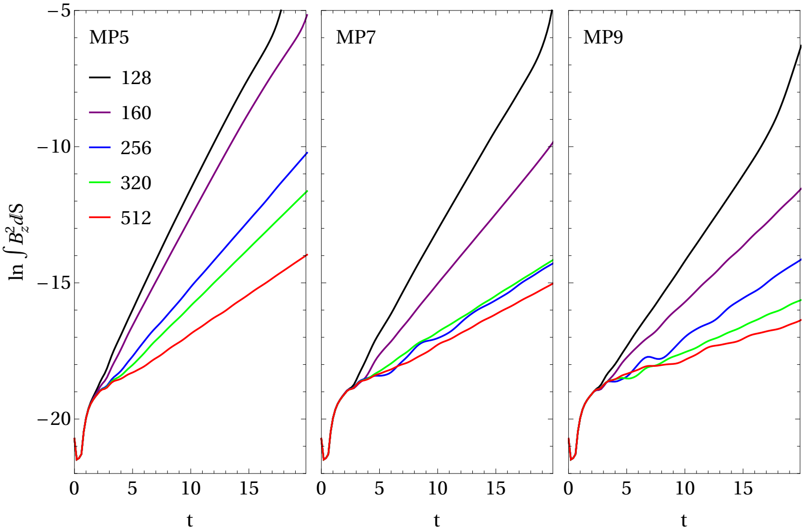

Figure 3.6: 2D Tearing mode (TM) test conducted for different numerical reconstruction schemes (MP5, MP7, MP9) on numerical grids of varying resolutions (indicated by different colors) during the linear phase of the growth of the TM.

force-free regime. The selection of $\mathcal{L}$ is much more involved (see Rembiasz et al., 2017, for a detailed discussion) and prone to accuracy restrictions since typically $\mathcal{L} \ll a$, which makes that the numerical resolution needed to reliably measure it becomes prohibitive. To obtain an order of magnitude estimate, we may assume that

$$\mathcal{L} \sim (ka)^2 a \approx 0.1a. \tag{3.15}$$

We cautiously note that assuming that $\mathcal{L}$ is constant, i.e. resolution-independent, and not fully accurate (Rembiasz et al., 2017). In future work, we will improve upon this simplifying hypothesis. $\mathfrak{N}$ and r are computed from the coefficients of the linear fit

$$\log \gamma_{\rm TM} = A \log \Delta x + B. \tag{3.16}$$

Using higher-order reconstruction is found to decrease the numerical resistivity (as we show in table 3.1 and visualize in figure 3.7). Such an increase of the order of reconstruction naturally goes hand in hand with additional boundary zones and, hence, comes at the cost of additional computational time.

As we emphasized in section 3.1, higher-order MP reconstruction is susceptible to small oscillations around discontinuities, though steep discontinuities across linearly degenerated characteristic fields are very well conserved. Such oscillations

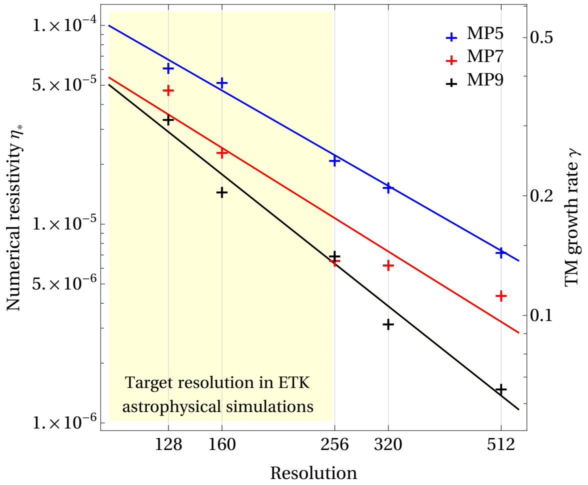

Figure 3.7: Estimates for the numerical resistivity, closely following Rembiasz et al. (2017). We display the empirical values of growth rates (see figure 3.6) and add the fit functions (model A, 3.13) as solid lines. Within the target resolution of the Einstein Toolkit in astrophysical simulations (yellow shaded region), an augmentation of the reconstruction order from MP5 to MP7 notably decreases the estimated numerical resistivity.

Table 3.1: Estimates of the reference numerical resistivity ($\mathfrak{N}$) and its dependence on the resolution (r) according to the limits defined by equations (3.11) and (3.13). The parameters are obtained by the linear fit given by equation (3.14).

Limit	Reconstruction	$\mathfrak{N} \times \mathcal{V} \times \mathcal{L}$	r
Model A	MP5	2.11×10^{-6}	1.32
	MP7	1.10×10^{-6}	1.44
	MP9	3.90×10^{-7}	1.84
Model B	MP5	1.09×10^{-5}	1.60
	MP7	1.73×10^{-6}	1.73
	MP9	2.20×10^{-6}	2.20

are also imprinted on the surface integrals which correspond to the intermediate resolution and high-order reconstruction cases of this test, depicted in figure 3.6. Oscillations are especially apparent in the blue curves ($N_z = 256$) of the mid and right panels. These oscillations decrease significantly in amplitude for finer resolutions (corresponding to $N_z \geq 320$). In our derivation of the numerical resistivity, there is a turning point for the slope of higher-order (MP7 and MP9) resistivity curves at an intermediate resolution ($N_z = 256$). Beyond this point, the accuracy gained by higher-order reconstruction is somewhat reduced (more significantly from the MP7 reconstruction). The source of this behavior is, at least in part, connected to the less accurate determination of the growth rate from the slope of the relation (3.9), which results from the oscillations observed in figure 3.6. It is also explained by the feedback of the boundary conditions on the solution. The growth rate of TMs obtained analytically explicitly depends on the boundary conditions set at infinite distance (Furth et al., 1963). Hence, the influence of the (open) boundaries set at a finite distance in the x-direction (precisely at $x = \pm 20a$) may manifest more prominently in simulations performed with the methods having formally higher accuracy and for the smallest growth rates (in our case directly linked to the smaller resistivity of the method).

In practical applications, this is, however, not a matter of concern. We developed our GRFFE routines on the infrastructure of the EINSTEIN TOOLKIT to conduct 3D simulations of astrophysical plasma on supercomputing resources. The sheer nature of global 3D simulations, i.e., simulations of complete systems and not small parts of them (which is the target of local simulations), limits our numerical analysis to the compromise of the highest possible numerical resolution which can be evolved for a sufficiently long time on the available computational resources. In the available computational resources, employing much more than ~ 10 points to resolve wavelengths of interest is, normally, the best one can afford in global models. In this section, we are presenting tests with up to a few hundred zones per wavelength of the computed TMs (i.e., much more than we may aim to resolve in actual models). We have indicated a crude approximation of this resolution by a yellow background color in figure 3.7. We find that within this region, an increase of the reconstruction order from MP5 to MP7 significantly decreases the numerical resistivity of our method, with a reasonable additional computational cost ($\sim 10\%$). Based on this test, we typically choose MP7 reconstruction for our production simulations.

Our GRFFE code produces the growth rates of TMs, which are expected if physical resistivity is present. They grow in our simulations because of the existence of numerical resistivity. Their growth rate decreases with numerical methods of higher-order (i.e., methods that decrease the effective numerical diffusion). The calculated approximations of the numerical resistivity are an important measure for the benchmarking of our code prior to large-scale production simulations.

- Numerical mesh ($[x_{\min}, y_{\min}, z_{\min}] \times [x_{\max}, y_{\max}, z_{\max}]\,; [\Delta x, \Delta y, \Delta z]$):
  $\left[-1.0, -\frac{\Delta y}{2}, -1.0\right] \times \left[1.0, \frac{\Delta y}{2}, 1.0\right]; [\Delta y, \Delta y, \Delta z]$,
  where $\Delta y = 0.03125$, and
  $\Delta z \in [0.015625, 0.0125, 0.0078125, 0.00625, 0.00390625]$
- Boundaries: Staggered boundaries, periodic.
- CFL-factor: $f_{\text{CFL}} = 0.2$ (4^{th} order Runge-Kutta time integration)
- Parabolic/hyperbolic cleaning: $k_\Psi = 0.25$, $k_\Phi = 250$, $c_h = 1$.

Box 3.2: Code parameters; tearing modes and numerical resistivity in 2D (3.2).

3.3 FFE Wave Propagation and Interaction

In the following, we demonstrate the correct conservation of the mode structure of force-free waves and probe the energy conservation during their collisions. Howes and Nielson (2013) and Nielson et al. (2013) extensively analyze the interaction of counter-propagating Alfvén waves and their energy cascading from their initial scales to (much smaller) ones. Such interactions are of potential importance for astrophysical applications in magnetar (Li and Beloborodov, 2015) and BH (Punsly, 2003) magnetospheres. We observed rapid cascades of dissipating energy in the context of twisted magnetar magnetospheres in Mahlmann et al. (2019), where the complex dynamics of their non-linear 3D interaction is a promising starting point for future analyses.

3.3.1 Mode Conservation (2D)

We perform this test building up on the mode decomposition into Alfvén and fast modes of force-free electrodynamics by Punsly (2003). In this section, we perturb a guide field by both, fast and Alfvén waves of different wavenumbers; probing their stability and superposition. Fast waves traveling in the direction of the guide field $B^y = B_0$ in the y-direction are excited by the following 2D Cartesian initial setup:

$$\begin{aligned}\mathbf{B} &= (B_0\epsilon\cos ky, B_0, 0)\\ \mathbf{D} &= (0, 0, B_0\epsilon\cos ky)\end{aligned} \tag{3.17}$$

We denote the strength of the imposed perturbation by ϵ with k being a suitably chosen wavenumber. On a similar note, Alfvén waves traveling in the x-direction at an angle $\theta = \pi/4$ to the guide field are excited by these initial conditions:

$$\begin{aligned}\mathbf{B} &= \left(B_0/\sqrt{2}, B_0\epsilon\cos kx, B_0/\sqrt{2}\right)\\ \mathbf{D} &= (B_0\epsilon\cos kx, 0, -B_0\epsilon\cos kx)\end{aligned} \tag{3.18}$$

We evolve the initial data presented in equations (3.17) and (3.18) in time for $B_0 = 1$ and different excitation modes $k = 2\pi n/L$. Here, $n \in [1, 2, 3]$ stands for the number of the excited mode and L the excitation length, which we fix equal to the domain length of the 2D plane (see box below). Figure 3.8 shows the time evolution of the perturbation amplitude $B^z_{\text{ref}} = B^z(0, 0)$ of the initial data provided in (3.17). We further analyze the variation of the perturbation amplitudes for both, Alfvén and fast waves, in its respective Fourier spectrum (figure 3.9). Over several light crossing times, the mode structure is well conserved, even in the case of superposition of different modes. The

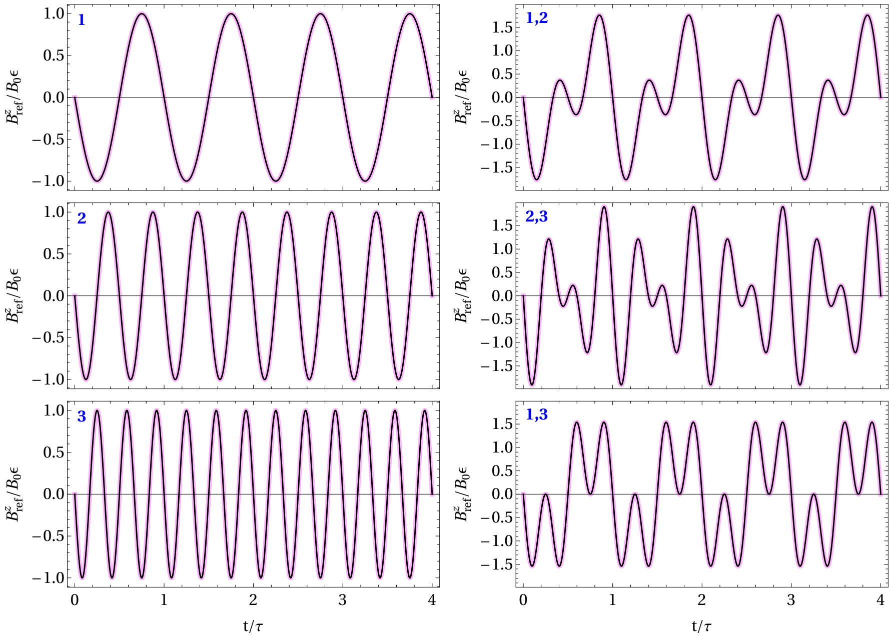

Figure 3.8: Time evolution of their perturbation amplitude B^z_{ref}, normalized to $B_0\epsilon$ of wave modes on a 2D numerical mesh (128^2) during the evolution of 4 light-crossing times t/τ. We present exemplary data for the setup of single fast wave modes according to equation (3.17) in the left column and of two simultaneous modes in the right column. The blue numbers coined in the upper left corners of each panel correspond to the values of n employed for each test case. The analytical solution of the wave propagation is included in the background (magenta).

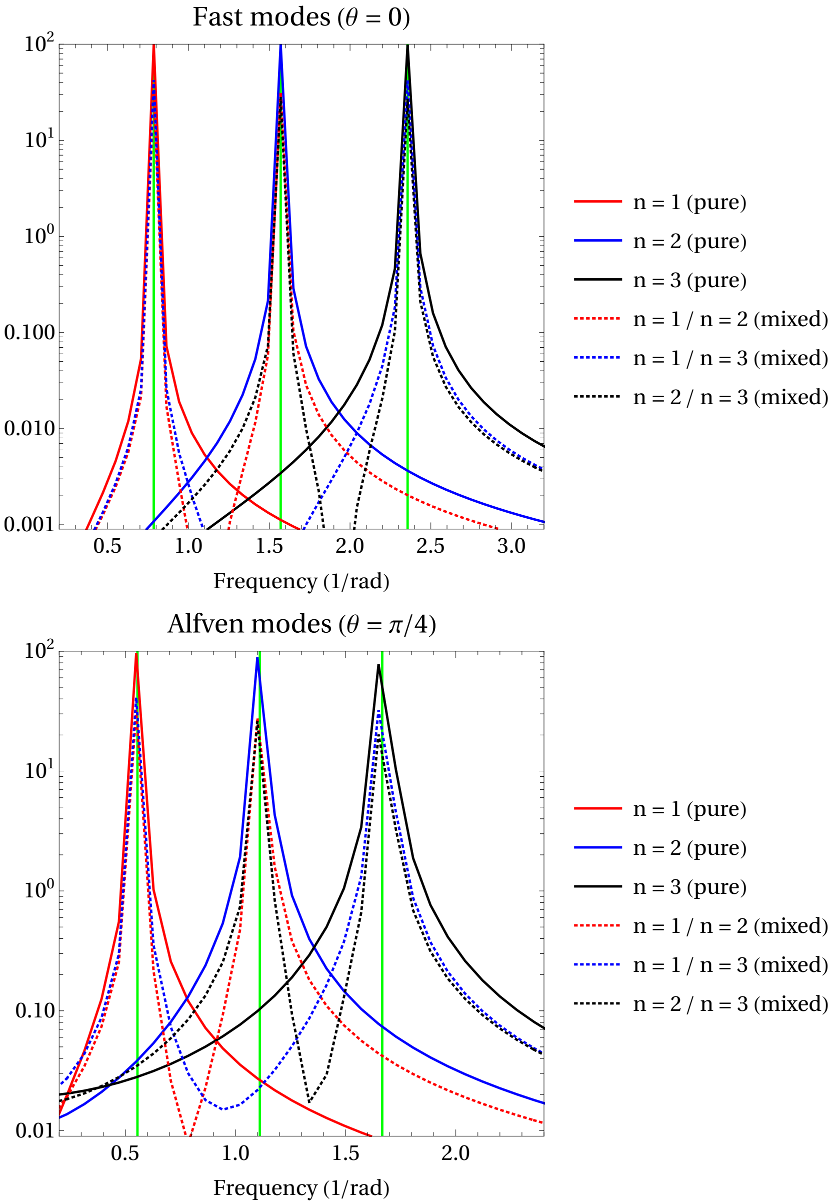

Figure 3.9: Fourier spectrum of the perturbation amplitude (as shown in figure 3.8 for the case of fast waves). The frequency spectrum for fast waves (*top* panel) and Alfvén waves (*bottom* panel) is presented for the evolution of 10 light-crossing times along the vertical size, L, of the computational box. The initial states are set up according to (3.17) and (3.18) for fast and Alfvén waves, respectively. The analytical values of the employed excitation frequencies are indicated by green (vertical) lines.

total electromagnetic energy and charge is conserved exactly (up to round-off errors) during the presented time interval of ten light-crossing times of the computational box in the direction of the guide field. In all simulations, the difference with the analytical solution is $\lesssim 10^{-5} B_0 \epsilon$, with no significant increase over time. Our code correctly preserves the frequency structure of force-free electromagnetic waves and passes this test.

3.3.2 Wave Interaction (2D/3D)

We perform a test (explored in extensive detail and high-resolution by Li et al., 2019) of the interaction between colliding Alfvén modes in suitably chosen 2D and 3D computational boxes. In this section, we intend to reproduce the most basic results of energy cascades from Alfvén wave interactions to show the ability of our GRFFE scheme to explore such phenomena in further detail in the future. However, such an exploration requires a rich numerical analysis and highly resolved 3D modeling (cf. Howes and Nielson, 2013; Nielson et al., 2013), which is beyond the scope of this thesis.

On the respective numerical meshes, one initializes counter-propagating Gaussian 2D or 3D wave packets traveling along a uniform guide field $B^y = B_0$. Periodic boundary conditions facilitate the recurring superpositions and interaction of the wave packets, eventually triggering an energy cascade of rapid dissipation due to the source terms appearing on the RHS of equations (2.65) and (2.73). The 3D Gaussian wave packets are initialized as

$$\mathbf{B} = B_0 \hat{\mathbf{y}} + B_0 \nabla \times (\phi \hat{\mathbf{y}}) \,, \tag{3.19}$$

where $\hat{\mathbf{y}}$ is the unit vector in the y-direction and the scalar field ϕ is

$$\phi(\mathbf{r}) = \xi \, l \sum_{i=1,2} \exp\left(-\frac{|\mathbf{r} - \mathbf{r}_i|^2}{l^2} \right) . \tag{3.20}$$

- Numerical mesh $([x_{\min}, y_{\min}, z_{\min}] \times [x_{\max}, y_{\max}, z_{\max}] \,; [\Delta x, \Delta y, \Delta z])$: $\left[-8.0, -8.0, -\frac{\Delta x}{2}\right] \times \left[8.0, 8.0, \frac{\Delta x}{2}\right] ; [\Delta x, \Delta x, \Delta x]$, where $\Delta x = 0.125$.
- Boundaries: Staggered boundaries, periodic.
- Reconstruction: MP7
- CFL-factor: $f_{\text{CFL}} = 0.2$ (4th order Runge-Kutta time integration)
- Parabolic/hyperbolic cleaning: $k_\Psi = 0.25$, $k_\Phi = 250$, $c_h = 1$.

Box 3.3: Code parameters; force-free wave mode conservation in 2D (3.3.1).

In this section, ξ denotes the perturbation strength, l the width of the wave packet, whose centers are located at $\mathbf{r}_1$ and $\mathbf{r}_2$. We follow Li et al. (2019) in choosing $\xi = 0.5$, $l = 0.1$, $\mathbf{r}_1 = (0.5, 0.25, 0.5)$ and $\mathbf{r}_2 = (0.5, 0.75, 0.5)$ for the 3D wave packet. With this setup, the field perturbation is purely azimuthal with respect to the y-axis. On a reduced 2D mesh, we initialize Gaussian wave packets with magnetic fields

$$\mathbf{B} = B_0\hat{\mathbf{y}} + B_z\hat{\mathbf{z}}, \tag{3.21}$$

where $\hat{\mathbf{z}}$ is the unit vector in the z-direction and

$$B_z = B_0\xi \sum_{i=1,2} \exp\left(-\frac{|\mathbf{r} - \mathbf{r}_i|^2}{l^2} \right). \tag{3.22}$$

We employ $\xi = 0.4$, $l = 0.1$, $\mathbf{r}_1 = (0.5, 0.25)$ and $\mathbf{r}_2 = (0.5, 0.75)$ for the 2D setup. The motion of the wave packets is induced with a drift speed $\mathbf{D} \times \mathbf{B}/B^2$, that results form an electric field

$$\mathbf{D} = \pm\hat{\mathbf{y}} \times \mathbf{B}, \tag{3.23}$$

with opposite signs for each wave packet. After initialization of the electromagnetic fields, the bounding box of length $L = 1$ and periodic boundaries are left to evolve for 200τ. τ is the light-crossing time of the box in the direction of the guide field, and t/τ the number of collisions. Following Li et al. (2019), we define the free energy U as the total electromagnetic energy of the system e_{tot} under removal of the background magnetic field B_0:

$$U = e_{\text{tot}} - \frac{1}{2}\int \mathrm{d}V B_0^2 \tag{3.24}$$

Figure 3.10 shows the free energy for the collision of the Alfvén wave packets defined in equations (3.20) and (3.22). The wave packets are spherical and - due to their curvature - prone to redistribute energy across wave modes (as one can see lucidly in figure 3.11) and rapid dissipation in cascade-like processes (see Howes and Nielson, 2013; Nielson et al., 2013, for an in-depth analysis of such phenomena). Such processes are likely to be found along curved guide-fields, for example in magnetar magnetospheres. They will be subject to future research.

We have visualized the progressing collisions of 2D Alfvén wave packets in figure 3.11. Such collisions excite higher frequency waves and eventually trigger the rapid decay of wave energy (see figure 3.12). Our GRFFE code is able to reproduce the dissipation patterns of free electromagnetic energy presented in figure 5 of Li et al. (2019) for the 2D setup of equation (3.22). For the case of two-dimensional simulations, our tests correspond to the lowest three

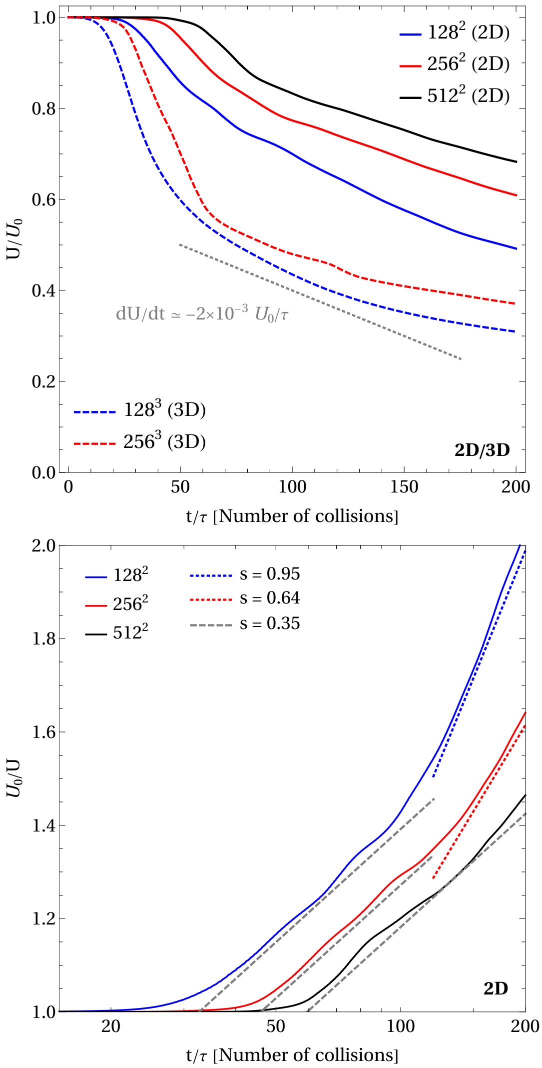

Figure 3.10: Free energy U (normalized to its initial value U_0) during the collision of Alfvén wave packets on numerical meshes (2D/3D) of various resolutions (indicated by different line styles). *Top:* Free-energy evolution comparing to figures 2 and 5 from Li et al. (2019). The asymptotic slope for 3D models found by Li et al. (2019) is indicated by a gray dashed line. *Bottom:* Evolution of U_0/U for the set of 2D models. Slopes for the asymptotic linear relation between U_0/U and $\ln t$ are indicated by dashed/dotted lines, comparing to figure 7 of Li et al. (2019).

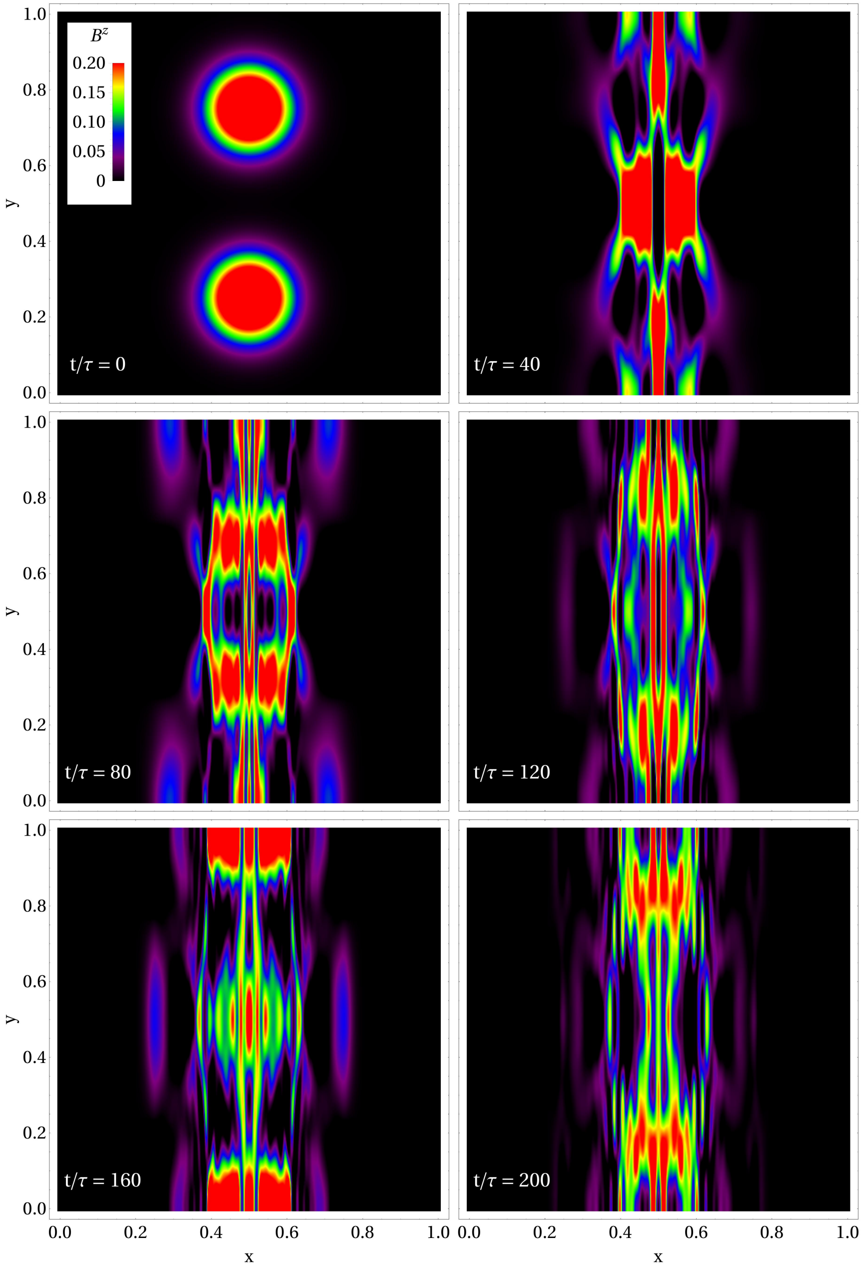

Figure 3.11: Perturbation amplitude during the 2D wave collision test for a selected resolution of 512^2. The initially clearly defined wave packets excite higher-order interference patterns (possibly of smaller scales) as the number of collisions increases.

mesh resolutions employed by Li et al. (2019). However, for the case of full 3D setups, we are limited to the lowest resolution (and below) of the corresponding reference case in Li et al. (2019) to stay within the computational costs which are reasonable for a test setup. While general features of the interactions of Alfvén waves in 3D remain, such as a very rapid onset of the energy cascade compared to 2D, we are not able to confirm the convergence to the same content of free energy which is shown for 3D setups in figure 2 of Li and Beloborodov (2015). However, we find comparable asymptotic slopes for energy decay, as we indicate in figure 3.10. In the bottom panel of figure 3.10, we present slopes for the decay of free energy. Contrasting the findings by Li et al. (2019), the decay of U initially proceeds at the same rate ($s \approx 0.35$) for all of the analyzed 2D models, independent of the chosen resolution. Only at later times, the slopes deviate and (roughly) approach the numerical values given in figure 7 of Li et al. (2019).

Howes and Nielson (2013) and Nielson et al. (2013) stress the genuine 3D nature of Alfvén waves. This observation is of paramount importance for the fully-fledged 3D simulations we envision. Due to the agreement of the presented results in 2D (figure 3.10) with the literature (Li et al., 2019), as well as the

- Numerical mesh ($[x_{\min}, y_{\min}, z_{\min}] \times [x_{\max}, y_{\max}, z_{\max}]\,; [\Delta x, \Delta y, \Delta z]$):
  $\left[0.0, 0.0, -\frac{\Delta x}{2}\right] \times \left[1.0, 1.0, \frac{\Delta x}{2}\right]; [\Delta x, \Delta x, \Delta x]$,
  where $\Delta x \in [0.0078125, 0.00390625, 0.00195313]$.
- Boundaries: Staggered boundaries, periodic.
- Reconstruction: MP7
- CFL-factor: $f_{\text{CFL}} = 0.2$ (4^{th} order Runge-Kutta time integration)
- Parabolic/hyperbolic cleaning: $k_\Psi = 0.25$, $k_\Phi = 250$, $c_h = 1$.

Box 3.4: Code parameters; force-free wave collisions in 2D (3.3.2).

- Numerical mesh ($[x_{\min}, y_{\min}, z_{\min}] \times [x_{\max}, y_{\max}, z_{\max}]\,; [\Delta x, \Delta y, \Delta z]$):
  $[0.0, 0.0, 0.0] \times [1.0, 1.0, 1.0]\,; [\Delta x, \Delta x, \Delta x]$,
  where $\Delta x \in [0.0078125, 0.00390625]$.
- Boundaries: Staggered boundaries, periodic.
- Reconstruction: MP7
- CFL-factor: $f_{\text{CFL}} = 0.2$ (4^{th} order Runge-Kutta time integration)
- Parabolic/hyperbolic cleaning: $k_\Psi = 0.25$, $k_\Phi = 250$, $c_h = 1$.

Box 3.5: Code parameters; force-free wave collisions in 3D (3.3.2).

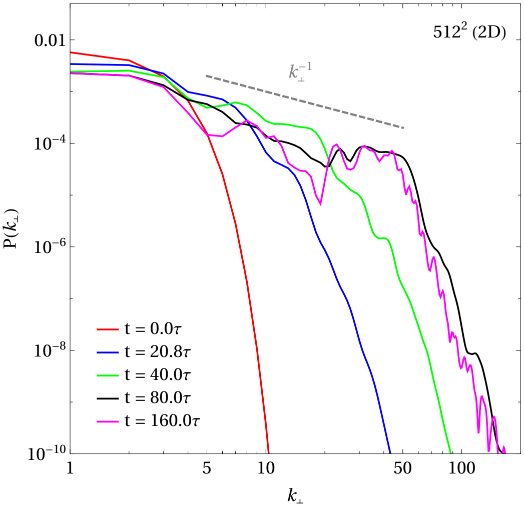

Figure 3.12: Spectrum evolution for the 2D simulation of resolution 512^2 (see figure 3.11, and compare to figure 6 in Li et al., 2019).

promising coincidence of rapid dissipation in 3D, we conclude that our GRFFE code passes this test. However, a thorough review of the interaction of Alfvén waves in 3D with high-resolution in GRFFE and kinetic models is required to provide data for a deep understanding of the rich and non-linear underlying physics.

3.4 Astrophysically Motivated Tests

3.4.1 Magnetar Magnetospheres

The magnetospheres of magnetars are a well-suited laboratory for numerical methods dealing with force-free plasma, and we have explored their dynamics (Mahlmann et al., 2019, included in appendix A). Prior to those numerical simulations of a potentially very dynamic scenario, we performed numerical tests to assess the ability of our GRFFE code to maintain the structural stability of a magnetosphere around a spherical, non-rotating neutron star with a dipolar magnetic field. We present all these tests, which are not part of Mahlmann et al. (2019) for reasons of space, in this thesis; they are fundamental to validate the GRFFE code. For reasons of simplicity, our model neglects the complications associated with the General Relativistic gravitational field. We use a spherical mask to cut out the neutron star interior to avoid dealing with the equation of state of nuclear matter, the different phases of matter which may occur inside of the neutron star, and the solid structure of the stellar crust. This is achieved by setting an internal boundary in a 3D Cartesian grid (i.e., stair-stepping along the spherical boundary mask) inside of which the evolution is frozen (see below). We note that 3D Cartesian coordinates are neither adapted to the spherical shape of the neutron star nor the axial symmetry of the magnetospheric dipole. Hence, even if one sets an equilibrium electromagnetic configuration, one may expect some degree of numerical evolution because there is a mismatch between the analytical solution provided as initial data and the actual solution in the discretized grid. This mismatch eventually separates the time-evolved configurations from the original conditions. We emphasize that both, the discretization error and the numerical dissipation in the code, may act as a driver for change in otherwise static configurations. Challenges associated with keeping a static or stationary configuration with a code devised for the dynamic evolution of the system are ameliorated employing sufficiently fine numerical resolution (i.e., sufficiently small grid spacing). In 3D, this can be a true challenge, since one could find that the required resolution to maintain stability is excessively large for practical applications. We shall see below that this is not the case for our code.

Although our models are all 3D and employ Cartesian coordinates, due to the axial symmetry of a dipolar field, it is easy to specify the employed initial data in spherical coordinates (r,θ,ϕ) and, subsequently, map it to the computational grid. The analytically derived equilibrium dipolar magnetic field

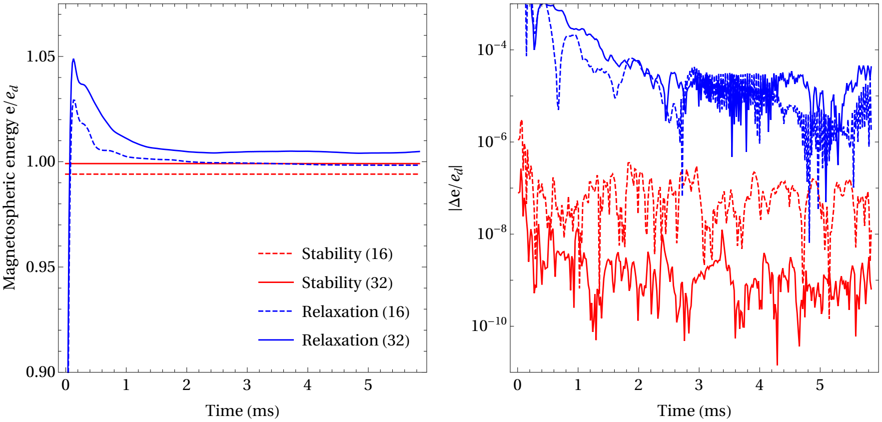

Figure 3.13: Stability and relaxation test of magnetar magnetospheres endowed with an analytic dipole field structure for different resolutions (16 and 32 points per stellar radius, 3D Cartesian CARPET grid with the same structure as in Mahlmann et al., 2019). *Left:* Evolution of total magnetospheric energy (in units of the dipole energy see equation (21) of Mahlmann et al., 2019). *Right:* Difference of the relative error between two consecutive time-steps of the evolution. The relaxation test has a transient spike in magnetospheric energy which gradually relaxes towards the dipole energy.

in (the orthogonal basis of) spherical coordinates reads:

$$\mathbf{B} = \left(\frac{2B_0\cos\theta}{r^3}, \frac{B_0\sin\theta}{r^4}, 0\right) \qquad \mathbf{D} = (0,0,0) \tag{3.25}$$

In analogy to the simulations shown in Mahlmann et al. (2019), our simplified magnetar model consists of a spherical region (mimicking the star) in which we fix the electromagnetic fields to their initial values. All shown simulations are conducted in a 3D box with dimensions $[4741.12M_\odot \times 4741.12M_\odot \times 4741.12M_\odot]$ with a grid spacing of $\Delta_{x,y,z} = 74.08M_\odot$ on the coarsest grid level. For the chosen magnetar model of radius $R_* = 9.26M_\odot$ this corresponds to a $[512R_* \times 512R_* \times 512R_*]$ box with a grid spacing of $\Delta_{x,y,z} = 8R_*$. For the low and high-resolution tests we employ seven and eight additional levels of mesh refinement, each increasing the resolution by a factor of two and encompassing the central object, respectively. This means that the finest resolution of our models (close to the magnetar surface) are $\Delta^{\mathrm{min}}_{x,y,z} = 0.0625 \times R_* = 0.5787M_\odot$ and $\Delta^{\mathrm{min}}_{x,y,z} = 0.03125 \times R_* = 0.2894M_\odot$ for the low and high-resolution models, or in other words 16 and 32 points per R_*, respectively. The setup is evolved for a period of $t = 1185.28M_\odot \simeq 5.84\,\mathrm{ms}$. We provide extensive details on the internal boundary conditions (frozen electromagnetic fields but balanced radial

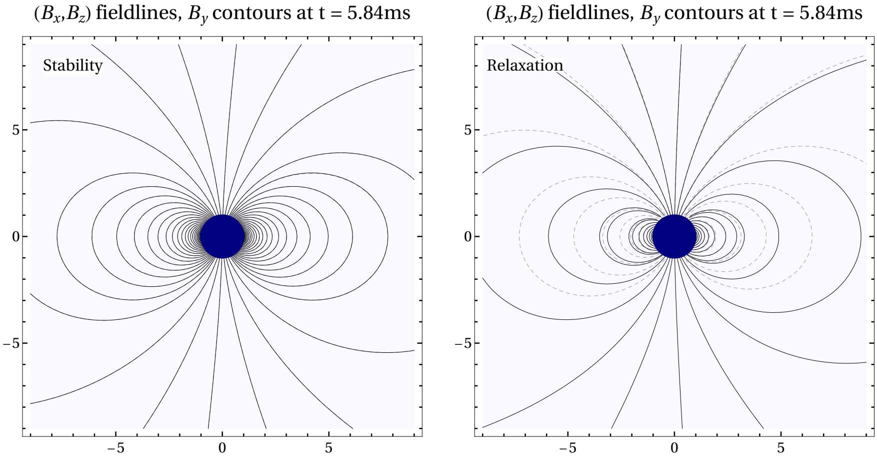

Figure 3.14: Same setup as for figure 3.13 but displaying the final states of the test simulation (32 points per stellar radius). The initial configuration of the stability test (*left*) is indicated by gray dashed lines in both panels.

current) in Mahlmann et al. (2019). Also, we expand vastly on the choice of simulation time which may appear short in physical units, but may be justified by the counteracting dynamical timescales.

Figure 3.13 shows stability and relaxation tests of the dipole magnetosphere as defined above for different resolutions. The stability test initializes the dipole structure throughout the entire computational domain and tracks the stability during a dynamical evolution. The relaxation test is even more challenging than the stability test since it requires the time evolution towards the physical topology set by the boundary conditions. Precisely, in a relaxation test we fix the dipolar structure inside of the star, but fill the magnetosphere with a purely radial field at the start of the simulation. Once initialized, the energy of the dipole magnetosphere (cf. Mahlmann et al., 2019) is well conserved (stability) or else gradually approaches the dipole energy (relaxation). Figure 3.14 shows the final field line distributions (in a 2D slice of the 3D domain) of the evolved states. Very lucidly, the right panel of figure 3.14 shows that the external radial field has evolved towards the dipolar structure imposed by the boundary conditions (which, ultimately, mimic the currents inside the neutron star that sustain the magnetospheric field). Even though the simulations are on 3D Cartesian grids, no notable toroidal fields build up at the magnetar surface. Hence, our code seems to conserve well the axial symmetric character of the problem at hand.

The initial spike of the relaxation model can be attributed to a surge of electromagnetic energy during a rapid rearrangement in the early phase. The excited energy pulses propagate as plasma waves through the magnetosphere. A part of these pulses is confined to closed field lines in the vicinity of the central object. The rest of this energy propagates outwards through the numerical grid. As the dissipation of electromagnetic energy in collisions of force-free waves strongly depends on the employed resolution (see section 3.3.2), the confined energy pulses remain within the domain longer for higher resolution. This is the case for the high-resolution relaxation test in figure 3.13. For different resolutions, the asymptotic energy differs by $< 1\%$. Complete relaxation of this energy will require longer simulation times (such that waves emerging from the initial relaxation can leave the domain) and accurate treatment of the interior boundary (and plasma waves in the region of closed field lines dissipate physically).

A similar gap in the magnetospheric energy is present in the stability test, in which the difference can safely be attributed to the coarser discretization of the dipole field. Due to its dependence on the radial distance (see equation 3.25), the largest contribution to the magnetospheric energy comes from regions close to the stellar surface. Cartesian stair-stepping along the spherical boundary explain the small difference in the measured magnetospheric energy for the stability test at each resolution, while for both resolutions the relative numerical error between two consecutive steps stays low throughout the evolution (left panel of figure 3.13).

Due to the very good coincidence of the evolution of the stable configuration with its analytical counterpart and the overall reproduction of the dipole model in the relaxation setup, our GRFFE code passes this astrophysically motivated test.

3.4.2 Black Hole Monopole Test

In this section, we present the first calibration tests for which General Relativistic effects are taken into account. A big difference between the modeling of BH magnetospheres and magnetar magnetospheres (see section 3.4.1) is the contrasting treatment of the internal boundary. As our choice of coordinates for BH spacetimes always employs horizon penetrating formulations (such as the puncture gauge), there is no need for a physical (or numerical) boundary at the location of the BH apparent horizon. Some additional challenges arising with the simulations of (dynamical) spacetimes and their coupling to GRFFE in the Einstein Toolkit can be found in section 2.3.5.

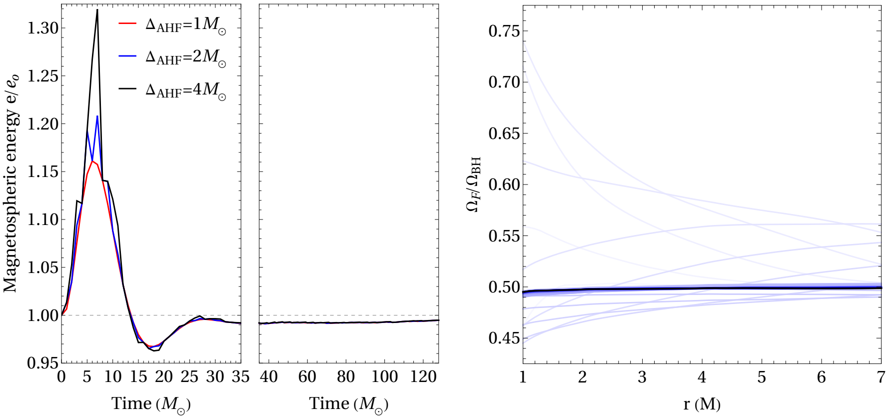

Figure 3.15: Time evolution of the Schwarzschild monopole ($\Omega_{\rm F} = \Omega_{\rm BH}/2$) of a slowly spinning Kerr BH ($a^* = 0.1, M = 1$). The spacetime metric is dynamically evolving (3D Cartesian CARPET grid with nine refinement levels, with the highest resolution of $0.03125 M_\odot$ completely enclosing the central object). *Left:* Evolution of the total magnetospheric (electromagnetic) energy normalized to the initial value, e_0. $\Delta_{\rm AHF}$ denotes the frequency of the update of the apparent horizon location, which is used to determine integration domains, e.g., for the magnetospheric energy. *Right:* Fieldline angular velocity along the equatorial plane. The final value is shown in a strong black color. Intermediate states throughout the simulation are depicted by light blue lines (strength of the color increasing with simulation time).

Blandford and Znajek (1977) presented analytic equilibrium solutions of BH magnetospheres by applying perturbation techniques to the GSE which match the Znajek condition (Znajek, 1977) at the BH horizon and the flat space solution of Michel (1973) at infinity. One of these results is a monopole-like magnetic field, which is often adapted to the so-called split monopole by mirroring the field quantities across the equatorial plane. The latter is a necessary step to avoid divergences of the magnetic field. In this section, however, we follow Komissarov (2004) in considering the monopole field structure to avoid the challenge of resolving a current sheet at the equator. The monopole electromagnetic fields for slowly spinning BHs ($a^* \ll 1$) as derived in Blandford and Znajek (1977) can be written in the spatial components of vectors in Boyer-Lindquist coordinates (r, θ, ϕ) as follows:

$$\mathbf{B} = \left(-\frac{\sin\theta}{2\sqrt{\gamma}}, 0, -\frac{a^* \sin^2\theta}{8\alpha g_{\phi\phi}}\right) \qquad \mathbf{D} = \left(0, -\frac{\Omega_\mathrm{F} + \beta^\phi}{2\alpha g_{\theta\theta}} \sin\theta, 0\right) \tag{3.26}$$

Here, Ω_F is the field line angular velocity as defined for axially symmetric equilibrium solutions (see Mahlmann et al., 2020, for a discussion of its validity in 3D time-dependent configurations). Figure 3.15 summarizes the time evolution of the monopole field for a dynamically evolving spacetime metric. We do not couple the field energy to the source terms of the BSSN equations. During a transient phase in which the metric terms relax to the chosen mesh and gauge, the electromagnetic fields can differ significantly from their initial state. This test demonstrates that, while the spacetime adjusts, they relax towards the equilibrium given by (3.26) concurrently. Though the energy evolution shown in figure 3.15 approaches the energy of the initial model rather well, such seemingly equilibrium results have to be taken with care. The evolution of dynamical spacetimes and corresponding GRFFE fields can be subject to the influence of small changes of the BH mass and spin (due to finite numerical resolution), as well as an involved array of source terms (defined in equations 2.73 and 2.65).

The geometric (i.e., spacetime) quantities determined by the initial data for spinning BHs presented in Liu et al. (2009) relax to their equilibrium state depending on the chosen numerical resolution of the mesh and specification of gauge quantities (i.e., the lapse and shift) during an initialization phase. The choice of these quantities is preferably done in a way which causes the least possible noise across all metric quantities during their evolution. As an example, instead of providing the spacetime data with the analytic lapse function defined in Boyer-Lindquist coordinates (Liu et al., 2019), we resort to the approximate lapse function (defined by Mewes et al., 2016, 2018)

$$\tilde{\alpha} = 2 \times \left[1 + \left(1 + \frac{M}{2r} \right)^4 \right]^{-1} . \tag{3.27}$$

With this initialization, the spacetime relaxes swiftly to its equilibrium state, at the obvious cost that the magnetic fields in equation (3.26) are not set up by employing the analytical expression of α. We employ the technique proposed in (3.27) for this test. In practice, the perturbation in the initial magnetospheric configuration introduced by the approximation of α is negligible. For the transient spacetime relaxation phase during the first $\Delta t_{\text{init}} \approx 20 M_\odot$, however, the choice of (3.27) significantly reduces the variability and quickly establishes a numerically stable spacetime setup. In order to visualize the strong, gauge-induced dynamics during the spacetime adjustment, we consider different frequencies Δ_{AHF} of applying the apparent horizon finder, i.e., restricting our domain for the integration of global quantities like the magnetospheric energy (figure 3.15). The update frequency of the apparent horizon location is important during Δt_{init} (left panel of figure 3.15). However, after this initialization phase, it ceases to have notable effects. By then, the spacetime has relaxed to its equilibrium on the numerical mesh and the position of the apparent horizon is almost constant. In practice, a less frequent execution of analysis routines like the apparent horizon finder is acceptable. The tests presented in this section give some important hints on the strategies chosen to set up BH magnetospheres for our future research. The goal of this test was to show that the magnetospheric data is conserved throughout the (dynamic) relaxation of the spacetime induced, e.g., by the BSSN algorithms of the EINSTEIN TOOLKIT. As both, the magnetospheric energy as well as the field line angular velocity at the equator, are recovered after Δt_{init}, our GRFFE code passes this test of spacetime-field coupling.

- Numerical mesh ($[x_{\text{min}}, y_{\text{min}}, z_{\text{min}}] \times [x_{\text{max}}, y_{\text{max}}, z_{\text{max}}]\,; [\Delta x, \Delta y, \Delta z]$): $[-256.0, -256.0, -256.0] \times [256.0, 256.0, 256.0]\,; [\Delta x, \Delta x, \Delta x]$, where $\Delta x = 8.0$. Eight additional levels of mesh refinement.
- Boundaries: Staggered boundaries, linear extrapolation boundary.
- Reconstruction: MP7
- CFL-factor: $f_{\text{CFL}} = 0.25$ (4^{th} order Runge-Kutta time integration)
- Parabolic/hyperbolic cleaning: $k_\Psi = 0.25$, $k_\Phi = 250$, $c_h = 2$.

Box 3.6: Code parameters; black hole monopole test (3.4.2).

3.4.2.1 Code Performance: Cleaning of Errors

We describe the hyperbolic/parabolic cleaning of numerical errors in detail in section 2.3.4 for both, numerical errors of div$\mathbf{B} = 0$ and div$\mathbf{D} = \rho$. This section explores the code performance for the black hole monopole test (with the setup from section 3.4.2) for different choices of the parameters governing the numerical cleaning of errors. We measure the numerical errors to the aforementioned conditions by considering the global measures:

$$\varepsilon_{\nabla\cdot\mathbf{B}}(t) = \int \left[\nabla\cdot\mathbf{B}(t)\right]\mathrm{d}V - \int \left[\nabla\cdot\mathbf{B}(t=0)\right]\mathrm{d}V \tag{3.28}$$

$$\varepsilon_{\nabla\cdot\mathbf{D}}(t) = \int \left[\nabla\cdot\mathbf{D}(t) - \rho(t)\right]\mathrm{d}V - \int \left[\nabla\cdot\mathbf{B}(t=0) - \rho(t=0)\right]\mathrm{d}V \tag{3.29}$$

Here, we employ the 3D region outside of the BH horizon as an integration region, and subtract the initially present discretization errors. Figures 3.16 and 3.17 show the evolution of numerical errors and the corresponding cleaning potentials for different combinations of the parameters κ_Φ, κ_Ψ, and c_h. The optimization of these parameters may differ for different applications and can be critical in highly dynamical processes where strong numerical violations of the divergence constraints occur (e.g., by strong violations of the force-free conditions, see also the discussion of Mahlmann et al., 2019). For the tests at hand, the exact calibration of the parameters of the cleaning method may have very small effects (the total magnetospheric energy presented in figure 3.15 is not notably changed by any of the different combinations shown in figures 3.16 and 3.17). However, their analysis provides crucial information about the code's performance and in other applications the proper calibration of the cleaning routines has a significant impact (Mahlmann et al., 2019).

As it is lucidly shown in figure 3.16, the introduction of the superluminal advection velocity c_h into the augmented system of equations (2.47) for divergence cleaning reduces the error $\varepsilon_{\nabla\cdot\mathbf{B}}$ (especially in the early and late phase of the evolution) significantly. Furthermore, the required maximum magnitude of the cleaning potential Ψ decreases by two orders of magnitude. Small variations in $\varepsilon_{\nabla\cdot\mathbf{B}}$ are also observed for stronger damping of errors by greater values for κ_Ψ. Though the presented tests in this chapter for flat background geometries employ $c_h = 1$, we conclude from the results in figure 3.16 that $c_h = 2$ improves the code performance (i.e., reducing the arising numerical errors) for General Relativistic spacetimes.

As for the errors in the consistency of (local) charge density, figure 3.17 shows an improvement in the error $\varepsilon_{\nabla\cdot\mathbf{D}}$ by a factor of ~ 4 when using a mild damping of $\kappa_\Phi = 1$, rather than strong damping (as we employed in a different context in

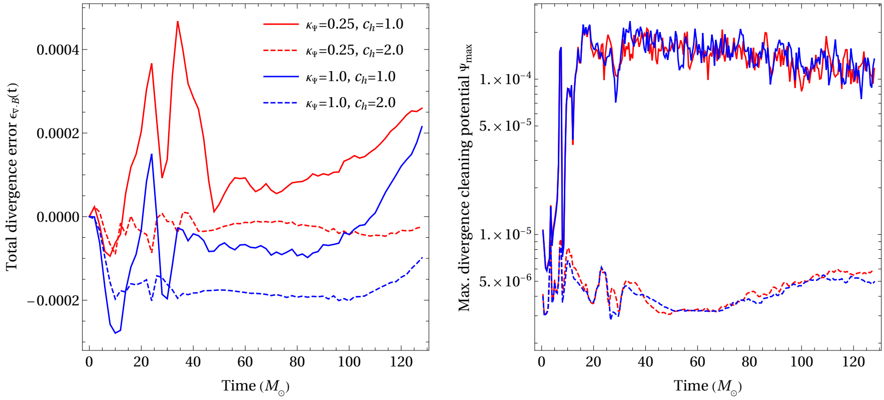

Figure 3.16: Time evolution of numerical errors (div**B** = 0, *left* panel) and the corresponding maximum cleaning potential Ψ (*right* panel). We present combinations of different κ_Ψ and c_h for a fixed $\kappa_\Phi = 1.0$.

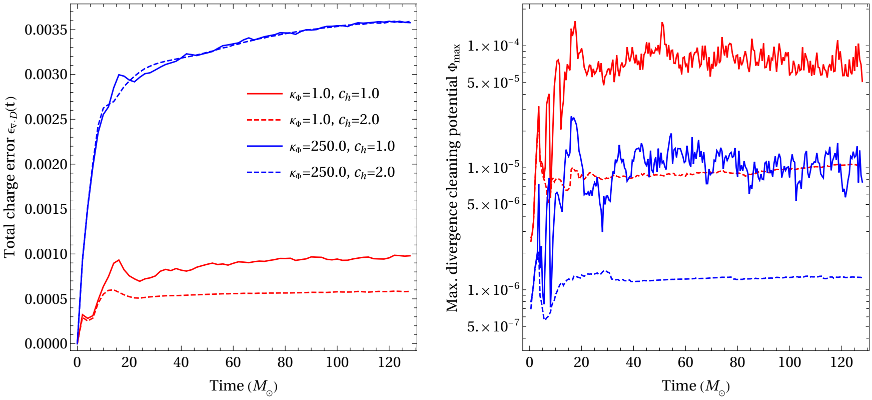

Figure 3.17: Time evolution of numerical errors (div**D** = ρ, *left* panel) and the corresponding maximum cleaning potential Φ (*right* panel). We present combinations of different κ_Φ and c_h for a fixed $\kappa_\Psi = 0.25$.

Mahlmann et al., 2019). However, the maximum value of the cleaning potential Φ increases by one order of magnitude. For the presented combinations of κ_Φ and c_h, the maximum deviation of total magnetospheric energy is $< 1\%$. Also, the maximum deviation of magnetospheric charge (from zero) is one order of magnitude smaller for strong damping ($\kappa_\Phi = 250$) and can be reduced further by choosing $c_h = 2$.

This comparison of parameters responsible for the cleaning of numerical errors emphasizes the strong need for diligent calibration for each setup (i.e., boundary conditions, geometry, etc.) at hand. The standard configurations employed for the hyperbolic/parabolic cleaning of numerical errors throughout this chapter, should and will be readjusted in the light of future applications of our GRFFE method.

3.4.3 The Wald Magnetosphere

The immersion of a BH into a magnetic field which is uniform at infinity was originally suggested by Wald (1974) and then explored throughout the literature, both as a test and as a laboratory for force-free plasma (Komissarov, 2004; Komissarov and McKinney, 2007; Carrasco and Reula, 2017; Parfrey et al., 2019). Komissarov (2004) dubbed this setup *an ultimate 'Rosetta Stone' for research into black hole electrodynamics*, i.e., a particularly well-suited laboratory to decipher the different ingredients of BH magnetospheres. In this section, we reproduce the initial data of the Wald magnetosphere of a Schwarzschild BH in Boyer-Lindquist coordinates (rescaled according to the prescription of Liu et al., 2009) and evolve it for different spins of the central object. We, therefore, extend the testing of GR capacities of our code to large (close to maximal) BH dimensionless rapidities (up to $a^* = 0.9$). The initial data proposed for this test (equation 3.30) embodies the limitation that a uniform magnetic field extending all over to infinity contains an infinite (nonphysical) energy. However, one may argue that this is a simple model for a situation where the uniform magnetic field extends sufficiently far away from the central BH and then suitably decays with distance at the appropriate rate.

The Wald magnetosphere of a Schwarzschild BH in the spatial components of Boyer-Lindquist coordinates (r, θ, ϕ) can be initialized as follows:

$$\mathbf{B} = \left(-\sqrt{\frac{r}{2+r}} \cos\theta, \frac{2\sin\theta}{\sqrt{r\,(2+r)}}, 0 \right) \qquad \mathbf{D} = (0, 0, 0) \tag{3.30}$$

Figure 3.18 shows the results from time evolution simulation of these fields in spacetimes of rotating BHs. The magnetic field lines connecting to the BH, which are initially not rotating, are gradually twisted in case of a spinning central object (e.g., Yuan et al., 2019; Mahlmann et al., 2020, for further exploration of twisting magnetic field lines by differential rotation). Also, current sheets form along the equatorial plane within the BH ergosphere, preventing the development of static magnetospheric conditions (cf. Komissarov, 2004). The overall topology of the magnetic field throughout the BH ergosphere broadly coincides with respective equilibrium solutions of Kerr magnetospheres (as derived, e.g., in Nathanail and Contopoulos, 2014; Mahlmann et al., 2018). In figure 3.19 we extract the field line angular velocity and toroidal magnetic field at different locations for comparison with figure 5 in Komissarov (2004). The chosen extraction location is slightly different from the literature in order to represent the complete range of BH spins. We find that our GRFFE code reproduces qualitatively the results in the literature, though some differences remain to be mentioned. Komissarov

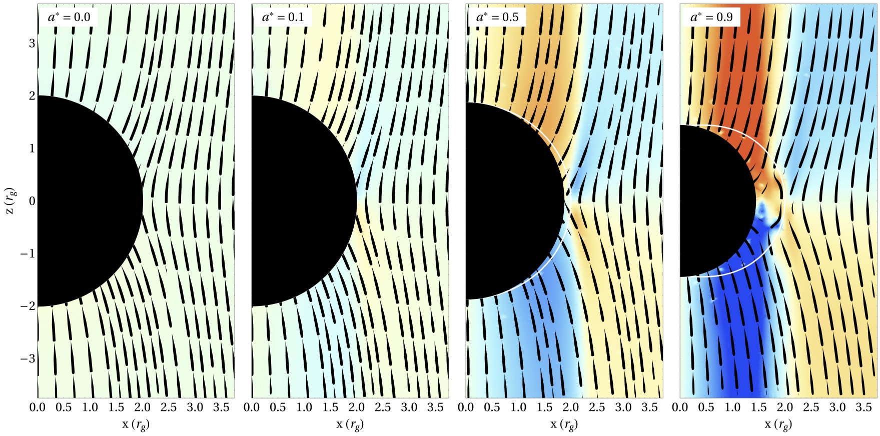

Figure 3.18: Final state ($t = 256M_\odot$) of the simulation of Wald magnetospheres (3D Cartesian Carpet grid with ten refinement levels, with the highest resolution of $0.03125M_\odot$ around the central object) for different BH dimensionless rapidities and a BH mass $M = 1$. The poloidal field is indicated by streamlines, the toroidal field by red and blue colors (color scale coincides for all panels) indicating whether the toroidal field leaves or enters into the displayed plane, respectively. The BH ergosphere is denoted by a solid white line, which coincides with the BH horizon for the case $a^* = 0$ and is hardly visible in the case $a^* = 0.1$ due to its proximity to the BH horizon.

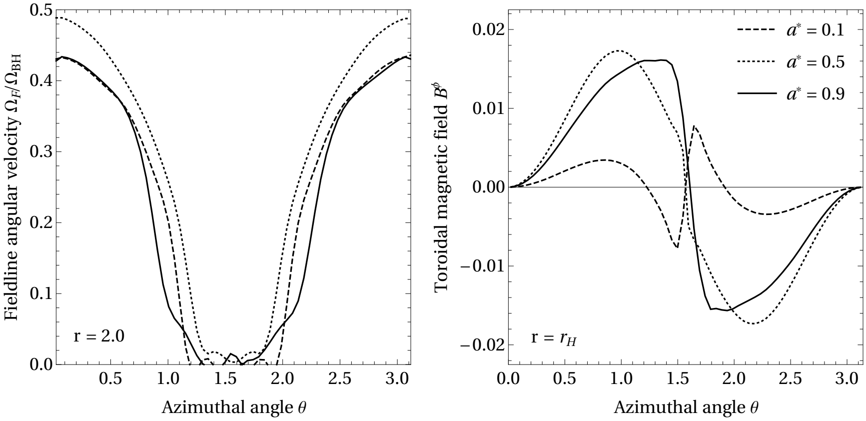

Figure 3.19: One-dimensional values of the field line angular velocity (*left*) and the toroidal magnetic field (*right*) for the Wald test using different BH dimensionless rapidities (see legends). The interpolation radius (for the extraction in a Cartesian grid) is indicated in the respective panel, corresponding to the ergosphere radius at the equator (*left*) or the BH horizon radius (*right*).

(2004) uses spherical coordinates and axial symmetry, as opposed to our 3D simulations with mesh refinement. More even, the angular resolution of 800 cells in the θ-direction is almost ten times the resolution which we have used on our finest refinement level (the resolution limit is simply imposed by the aim of running numerical tests that do not consume disproportionate computational resources). The quantitative difference in the shape of the angular velocity distribution (V-shape in figure 5 of Komissarov, 2004, vs. U-shape in figure 3.19) may, hence, be significantly improved by resorting to a GRFFE code in spherical coordinates (as we plan to do in the near future). Also, we point out that we show the toroidal component of the magnetic field $\mathbf{B}$ rather than $\mathbf{H}$. The overall form of the toroidal field for the rapidly rotating case ($a^* = 0.9$) corresponds well (up to a difference in sign) with figure 5 of Komissarov (2004). For a direct comparison of numerical data, comparable resolutions and exact convergence (longer simulations) are required; this is beyond the scope of the test presented here.

In conclusion, especially field lines threading the ergosphere are gradually twisted by the rotating BH. Due to the broad coincidence with Komissarov (2004), and the reproduction of magnetospheres which resemble respective equilibrium solutions of the GSE (Nathanail and Contopoulos, 2014; Mahlmann et al., 2018), the Wald magnetosphere test is passed.

- Numerical mesh ($[x_{\min}, y_{\min}, z_{\min}] \times [x_{\max}, y_{\max}, z_{\max}]\,; [\Delta x, \Delta y, \Delta z]$): $[-512.0, -512.0, -512.0] \times [512.0, 512.0, 512.0]\,; [\Delta x, \Delta x, \Delta x]$, where $\Delta x = 16.0$. Nine additional levels of mesh refinement.
- Boundaries: Staggered boundaries, linear extrapolation boundary.
- Reconstruction: MP7
- CFL-factor: $f_{\text{CFL}} = 0.25$ (4^{th} order Runge-Kutta time integration)
- Parabolic/hyperbolic cleaning: $k_\Psi = 0.25$, $k_\Phi = 250$, $c_h = 2$.

Box 3.7: Code parameters; Wald magnetosphere test (3.4.3).

Chapter 4

Discussion of results

We present the principal scientific results of this project in an assortment of published manuscripts in appendix A. Each of the attached manuscripts provides extensive discussions and conclusions of the respective scientific cases. This chapter serves three purposes: i) Outline the improvements and remaining numerical challenges in our scientific GRFFE code. ii) Give a summary of the published results from Mahlmann et al. (2018, 2019, 2020). iii) Present follow-up investigations extending our manuscripts and setting the stage for future projects.

4.1 A Multi-Coordinate GRFFE Code

We have implemented, tested, and applied a new tool for General Relativistic force-free electrodynamics on the infrastructure of the EINSTEIN TOOLKIT. For this purpose, we have distilled the extensive theoretical efforts which lead to the so-coined **BE** (cf. Komissarov, 2004; Paschalidis and Shapiro, 2013) and **BS** (McKinney, 2006; Paschalidis and Shapiro, 2013; Etienne et al., 2017) formulations of GRFFE. The **BE** system of equations is well-suited for a very efficient numerical implementation due to the possibility of expressing all characteristics in terms of the conserved variables (see section 2.3.2). As the current explicitly appears in equation (2.46), the **BE** formulation allows a straightforward inclusion of charge conservation and possible resistive currents into the underlying PDEs.

Different from other numerical schemes, we have augmented the GRFFE scheme (equations 2.49 to 2.51) by the conservation of charge. The local charge is consistently evolved (conserving total charge) and then used in our derivation of the force-free current (2.53). This contrasts other strategies, in which the local charge is derived in every time step by calculating div**D**. During the stages of development on the mesh-refinement capacities of Carpet, we identified this strategy to artificially load the domain with surplus charge, especially across refinement boundaries. On a more applied note, the strong gradients at the stellar surface in our models of magnetar instabilities were prone to introduce significant errors in charge conservation. Employing *refluxing* techniques and the conservative system consisting of nine evolution equations has greatly improved these artifacts and, hence, the physical validity of the GRFFE method.

Following the GRFFE implementation of Komissarov (2004), we employ the hyperbolic/parabolic cleaning of numerical errors in the solenoidal constraint $\mathrm{div}\mathbf{B} = 0$. We further augmented the system of equations of GRFFE by a second cleaning potential (as did, e.g., Palenzuela et al., 2009, in the context of relativistic resistive MHD), minimizing numerical errors in the constraint $\mathrm{div}\mathbf{D} = \rho$. In order to quantify the energy dissipation of these techniques theoretically, we present an extensive derivation of the expressions of the energy-momentum balance equations of our GRFFE scheme in section 1.2.1. This exploration extends the identification of dissipation channels which was employed in the context of the interaction of Alfvén waves by Li et al. (2019) to General Relativity. As such, they will be valuable assets in the identification of magnetospheric dissipation in future projects.

We extended the work by Mignone and Tzeferacos (2010) on hyperbolic/-parabolic cleaning to its application in GRFFE. Especially, our method allows for advection of numerical errors to the constraint $\mathrm{div}\mathbf{B} = 0$ with speeds that exceed the speed of light (as the fastest characteristic speeds of conventional GRFFE). For this purpose, we have introduced the tensor $s^{\mu\nu} = c_h^2 \gamma^{\mu\nu} - n^\mu n^\nu$ into our augmented evolution equation (2.47). This is one possibility of providing the advection speed c_h in a way that is consistent with the fully covariant underlying argument of error propagation following a telegrapher equation (see section 2.3.4). Especially when exploring the full GR capabilities of our method in its application to dynamical spacetimes of spinning BHs, we find the choice of $c_h = 2$ to reduce numerical errors significantly. At the same time, this value (larger than 1) does not limit excessively the time step size of our explicit, time-marching method (section 3.4.2.1).

We allow the values of the damping constants κ_Φ and κ_Ψ to be significantly larger than one. For that, it is necessary to account for the potential stiffness introduced into the system of PDEs by the cleaning potentials. With the employed Strang splitting techniques used to deal with the potential stiffness of the equations associated with the evolution of the scalar potentials Φ and

Ψ, we have fully incorporated the hyperbolic/parabolic cleaning procedures into GRFFE. Though cleaning potentials are perceived challenging in General Relativistic simulations (as opposed to other strategies, e.g., constraint transport), we have found them very versatile, and straightforward to incorporate into our methods. However, it should be emphasized again (see also sections 2.3.4 and 3.4.2.1), that their calibration requires fine-tuning for different applications.

Though we employ high-order reconstruction methods (MP5/7/9, Suresh and Huynh, 1997), we find that our method's order of convergence is below its formal value in a range of tests (chapter 3). This finding may be related to the algebraic enforcement of the force-free constraints (section 2.3.3) and, hence, be a general feature of GRFFE methods. During our development efforts, we have reviewed a range of techniques used to maintain the force-free character of all fields throughout the domain (Mahlmann et al., 2019, and references therein). Most of these methods achieve a stable evolution, often only resulting in very small changes to the physically measurable quantities. Thus, we could not identify a method of enforcing the force-free constraints which is preferable over all others. However, their impact on the order of convergence should be further reviewed in the future, and for every application individually.

With a view to these subtleties, the quantification of the numerical resistivity of scientific codes seems to be an insurmountable task; in our case, to assess the reliability of astrophysical simulations of force-free magnetospheres. Specifically, we aim to state to which extend the simulations we presented (Mahlmann et al., 2019, 2020) are driven by physics, and to which extend they are dominated by numerical artifacts (like the algebraic enforcement of force-free constraints or the hyperbolic/parabolic cleaning of errors). In this thesis, we present a preparatory exercise for the classification of our GRFFE method by analyzing the growth rates of tearing modes (section 3.2).

In our preliminary assessment, we find $\eta_* \sim 10^{-5} - 10^{-4}$ to be typical values of numerical resistivities for our GRFFE method (figure 3.7). This simplified estimate can also be used as a reference value for the astrophysical simulations presented in appendix A. In Mahlmann et al. (2020) we have introduced a resistive model into the domain to mimic the accretion of closed magnetic loops onto a rapidly spinning BH. For this accretion disc region, we use a resistivity of $\eta \sim 1$, which is well above our numerical resistivity. In future studies focusing on the interaction of Alfvén waves and their dissipation of energy in higher-order modes, the thresholds set by the numerical diffusion properties of the method itself will be a crucial part of information.

Finally, writing our GRFFE method from scratch, allowed us to adapt it to recent developments in the infrastructure of the Einstein Toolkit. With the spherical version of our code, we can simulate astrophysical scenarios with numerical routines that are aligned with the geometry of the specific problems at hand (see below). In its Cartesian version, our GRFFE code has completed several production cycles on Tier-1 supercomputing resources accumulating a total of around 5 Million CPU hours in production over the past 2 years. We are currently able to reach computational speeds between 10μs and 100μs per iteration, depending on the number of mesh refinement levels and boundary cells. Typical production simulations of high-resolution BH magnetospheres (like the ones shown in Mahlmann et al., 2020, but resolving the domain even better) use around 500 CPUs (though we have scaled our GRFFE up to 3072 CPUs) and require approximately 200.000 CPU hours.

4.2 Instabilities of Magnetar Magnetospheres

In our 3D Cartesian (special relativistic) experiments (appendix A, Mahlmann et al., 2019), we have identified the development of an instability whose ultimate nature was unspecified. It triggered the relaxation of a magnetar magnetosphere in a high energy state (degenerate solution to the GSE, as derived by Akgün et al., 2017, 2018) to a lower energy state. After the onset of the instability, strongly twisted magnetic field lines relax rapidly to a dipole-like structure, depositing a significant fraction of energy on the magnetar surface. There, strong shear-stresses and surface currents dissipate up to 30% of the magnetospheric energy. The currents which drive the rearrangement dynamics in the extended magnetosphere are likely to sustain an opaque region and, thus, a giant flare event with close similarities in its evolution to the so-called magnetically confined fireball model.

Though we observed the close to axially symmetric development of the instability in Mahlmann et al. (2019), we were not able to further constrain the 2D or 3D nature of the instability with the fully-fledged 3D simulations. Recently, we followed up the stability analysis in Mahlmann et al. (2019) with the additional constraint of axial symmetry. A possible strategy to mimic axial symmetry is provided in the Einstein Toolkit by the thorn Cartoon2D (Alcubierre et al., 2001). During testing of this strategy in the context of wave propagation in magnetar magnetospheres, we have encountered difficulties to properly develop the GRFFE equations in time at the symmetry axis with Cartoon2D.

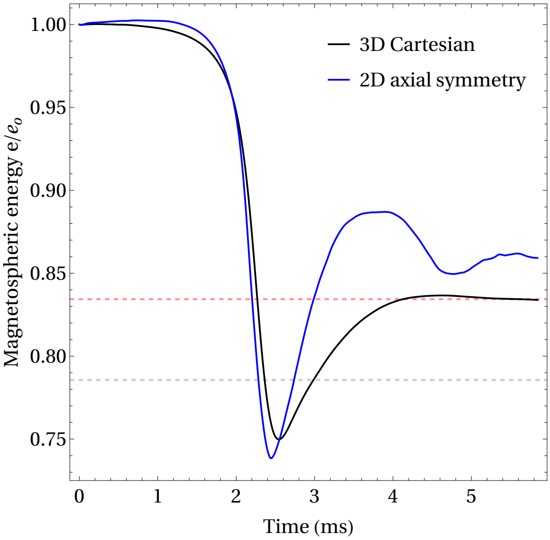

Figure 4.1: Comparison of the evolution of a selected (higher energy) degenerate solution to the GSE (model C2 from Mahlmann et al., 2019) in 3D and 2D axial symmetry. We show the onset of the instability and drop of magnetospheric energy for a Cartesian 3D mesh (with mesh refinement, *black line*) and the 2D axially symmetric mesh (uniform) of a development version of our GRFFE scheme in spherical coordinates. The resolution coincides with the highly resolved cases in Mahlmann et al. (2019), using 32 grid-points per stellar radius at the stellar surface. The energy of the reference case of an analytic dipole (lowest energy configuration, see section 3.4.1) is indicated by a *gray dashed* line, the energy of the low energy state of the respective degenerate model is represented by a *red dashed* line.

Instead, recently, we extended our GRFFE scheme for the time-evolution of equations (2.49) to (2.51) to spherical coordinates (see section 2.3.1). For this, we have used techniques implemented into the Einstein Toolkit by Mewes et al. (2018). They provide boundary conditions such that the conventionally Cartesian grid of Carpet can be used with spherical coordinates. In such a scheme, it is possible to reduce the polar direction to one single numerical cell, hence, to drastically decrease the computational demands of the model (which is effectively 2D and not 3D). Using such coordinates, which are better adapted to the symmetry of the surface of the neutron star and the essentially axisymmetric magnetosphere, we can directly compare axially symmetric dynamics to their full 3D counterpart. The final implementation and testing of this new code in full General Relativity is currently ongoing and will be subject to a subsequent publication highlighting the details of our GRFFE code package. In this section, we present preliminary results employing the full potential of the Cartesian/spherical implementation on a flat background.

Figure 4.1 compares the energy evolution of a selected high energy magnetar magnetosphere (model C2 from Mahlmann et al., 2019) in full 3D and 2D axial symmetry for the same numerical resolution at the stellar surface. We expected these curves to deviate, specifically the 2D axially symmetric simulation to conserve magnetospheric energy over longer time scales. However, the calculated evolution during the force-free evolution phase (up to $t \approx 2.5$ms) is almost congruent. This paramount coincidence of the different evolution schemes indicates two key findings that add up to our knowledge of the nature of the instability with respect to Mahlmann et al. (2019) and, thus, they are novelties of this thesis: i) The instability developing in our models is indeed axisymmetric. ii) Our Cartesian 3D code (as employed with adequate resolution in Mahlmann et al., 2019) resolves the axisymmetric instability well - it is not amplified significantly by Cartesian stair-stepping at the surface.

We attribute part of the energy decay (even below the energy of an analytic dipole solution) to the development of strong surface currents at the magnetar crust. In a 3D Cartesian mesh, the stellar surface is merely a pseudo-spherical discretization prone to effects by Cartesian stair-stepping. For the future, it will be important to correctly model the interior boundary associated with the magnetar surface. However, modeling a spherical boundary within the Cartesian grid structure of Carpet is a challenge and prone to numerical artifacts developing at the interior boundary. Only the step towards spherical coordinates and delicate treatment of plasma waves at the interior boundary may lead to a fully satisfactory numerical modeling (see also our extensive discussion in Mahlmann et al., 2019). In a spherical mesh, the location of the stellar surface is naturally well resolved due to the adaptation of the coordinates to the geometry of the boundary. Hence, one expects better accounting for the dissipation in this particular problem in spherical coordinates and more accurate confinement of force-free waves along closed field lines (due to the axially symmetric setup). Ultimately, these convergence properties require a physically sound treatment of wave propagation at the stellar surface (i.e., the exact modeling of reflection and absorption of plasma waves, cf. Carrasco and Reula, 2017), which will be addressed in future projects employing our newly developed spherical GRFFE code.

4.3 Striped BZ Jets by Accretion of Small Scale Flux Structures

We use our GRFFE thorn of the EinsteinToolkit in fully-fledged General Relativistic 3D simulations in our most recent publication (see appendix A Mahlmann et al., 2020). There, we investigate the energy flows in magnetospheres of a rapidly spinning BH ($a^* = 0.9$), which are induced by the accretion of small scale magnetic fields. We extended previous experiments in 2D axial symmetry by Parfrey et al. (2015) and show that efficient Blandford/Znajek type outflows can be produced from the accretion of magnetic flux tubes with zero net magnetic flux in 3D. The basic mechanism by which zero net magnetic flux tubes may activate the BZ mechanism is the inflation of magnetic field lines in the vertical direction. This is an unavoidable result of the differential rotation between footpoints located in the accretion disc and the plunging region surrounding the BH. However, to have an efficient energy outflow, vertical inflation of the lines must lift them up sufficiently far away from the BH, so that they behave as open field lines effectively connecting the BH ergosphere to infinity. As efficient energy outflow, we define an electromagnetic energy extraction as formulated in Blandford and Znajek (1977); we elaborate extensively on these processes in Mahlmann et al. (2020). We consider a set of different models (varying in the extension of the flux tubes, i.e., the width and length of the magnetic loops) and make a detailed account of the energy outflow across the horizon. We find that very small loop sizes fail to produce regular and efficient outflows.

In the discussion of Mahlmann et al. (2020) we propose that a drastic reduction in BZ energy output happens if field line structures extending to regions well above the central BH have a significant kink or fail to open up. In

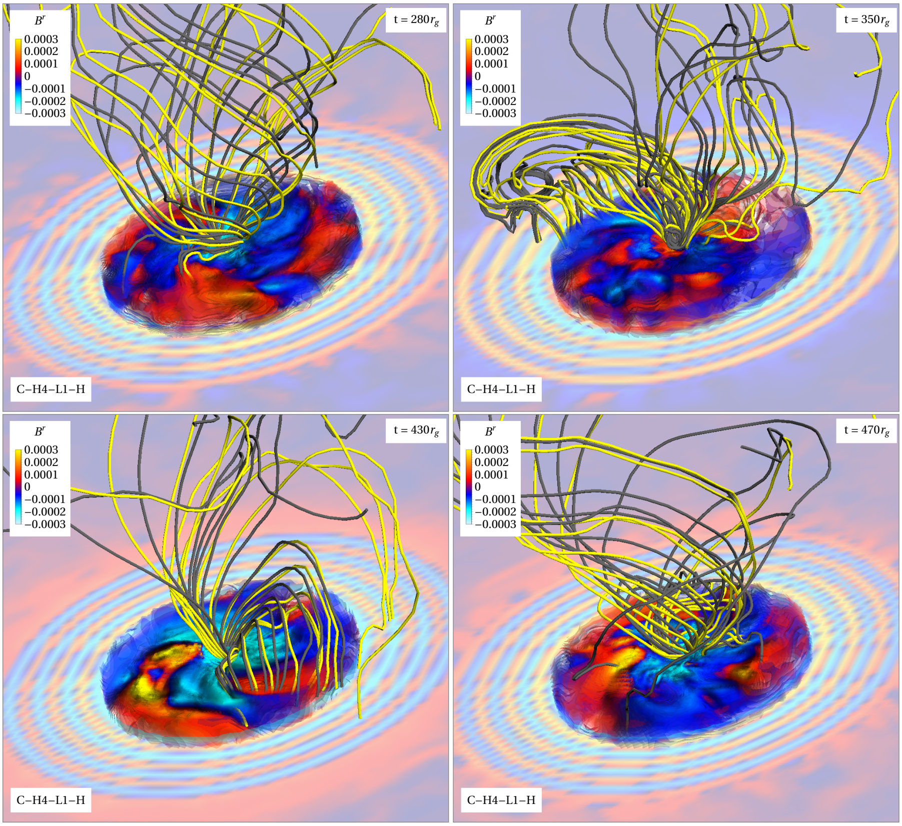

Figure 4.2: Magnetic flux in the accretion funnel and extended magnetic field line structure of a model with short diameters of the accreted loops in the equatorial direction (the loops, or more accurately, toroidal flux tubes, are noticeable by the alternated pattern - cyan/orange - of B^r in the equatorial plane). The visualized field lines emerge from two discs above the BH pole (of different radii, not larger than the horizon radius, distinguished by yellow and black color). The evolution has three different phases: *Top left panel:* Late phase of a structure which efficiently extracts energy by the BZ process. Field lines extend to far distances in a helical structure ($t = 280r_g$). *Top right panel:* Failed structure (no efficient BZ process). The field lines have tipped over onto the disc ($t = 350r_g$). *Bottom left panel:* Early phase of a BZ efficient structure. The 3D loop structure is closing; field lines are differentially rotated and their footpoints brought closer together ($t = 430r_g$). *Bottom right panel:* Later phase of a BZ efficient structure ($t = 470r_g$), similar to ($t = 280r_g$).

full 3D, this may happen due to tipping over a tower of magnetic field lines on the accretion disc. Following up on the published results, we have analyzed the 3D magnetic field structure of a model, in which counter-rotating magnetic loops of short extent in the equatorial direction are accreted onto a rapidly spinning BH. The presented data stems from ancillary simulations that we conducted in order to support the statements we made after our initial investigation in Mahlmann et al. (2020). It becomes clear in those images (figure 4.2), that the (costly) step to full 3D simulations is indeed necessary to understand the impaired BZ efficiency which goes hand in hand with such failed structures.

For the comparison to previously published results, it should be noted, that Parfrey et al. (2015, 2017) employ the pseudo-spectral code Phedra in 2D axial symmetry. In this endeavor, they have produced exceptionally well-behaved simulations (i.e., very ordered field structures and smooth, repeating episodes of efficient energy extraction) of dynamical magnetospheric processes that lay the basis for a deeper understanding of how global magnetospheric models can influence the local field dynamics. The models by Parfrey et al. (2015) do not seem to display the small scale dynamics which are characteristic of our 3D models (cf. Mahlmann et al., 2020). Such differences may be attributed to either the 2D axially symmetric modeling (intrinsically limiting one degree of freedom in the electromagnetic fields) or, possibly, the filtering techniques applied in their spectral methods.

One important finding of Parfrey et al. (2015) is the existence of a critical loop width, l_{crit}, below which accreting loop structures fail to open up to high vertical extensions in a certain time if the accretion disc is prograde (for retrograde discs there is no such limitation). The consequence of this failure is that the efficiency of the BZ process of energy extraction is severely diminished, if not destroyed. The results in Mahlmann et al. (2020) are broadly compatible with the existence of a minimum critical loop width, which depends on the spin of the BH. Nevertheless, the complications in the modeling of prograde discs in BHs with a^* close to 1, and the cost of the 3D models we deemed necessary, prevented us to assess quantitatively the value of l_{crit}. However, we have extended a model of stationary small scale structures (as presented by Yuan et al., 2019) to our fully General Relativistic framework (see also Mahlmann et al., 2020) and can identify three key aspects related to the opening of field lines to significant vertical heights:

1. Short loop lengths prevent the rapid opening of field lines, pointing towards the existence of a critical loop length $l_{\mathrm{crit}} \gtrsim 3.5 r_g$ for an $a^* = 0.9$ BH.

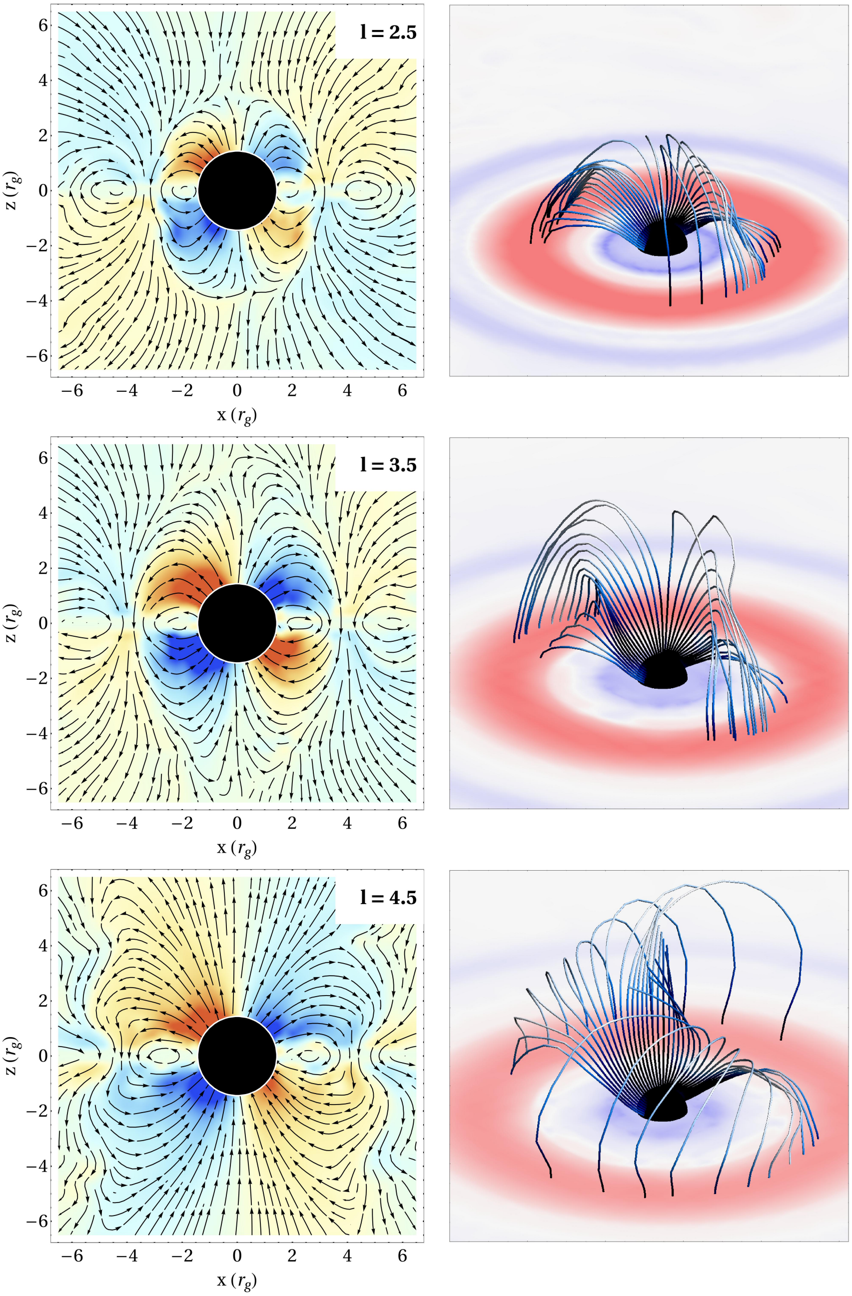

Figure 4.3: *Left:* Toroidal field B^T (*blue* negative, *red* positive) for selected tests of a co-rotating AD with $\alpha = 2$, $r_1 = r_{\rm ISCO}$, $v^r = 0$, and a completely force-free plunging region. We vary the loop length l (increasing from the top to the bottom panel) and overlay poloidal magnetic field lines. The presented snapshots are taken at ~ 9 revolutions of the BH ($\sim 180 r_g$). *Right:* A 3D impression of the corresponding model. Field lines are anchored on a circular ring around the BH horizon. We indicate the vertical magnetic flux in the equatorial plane by *red* and *blue* shades.

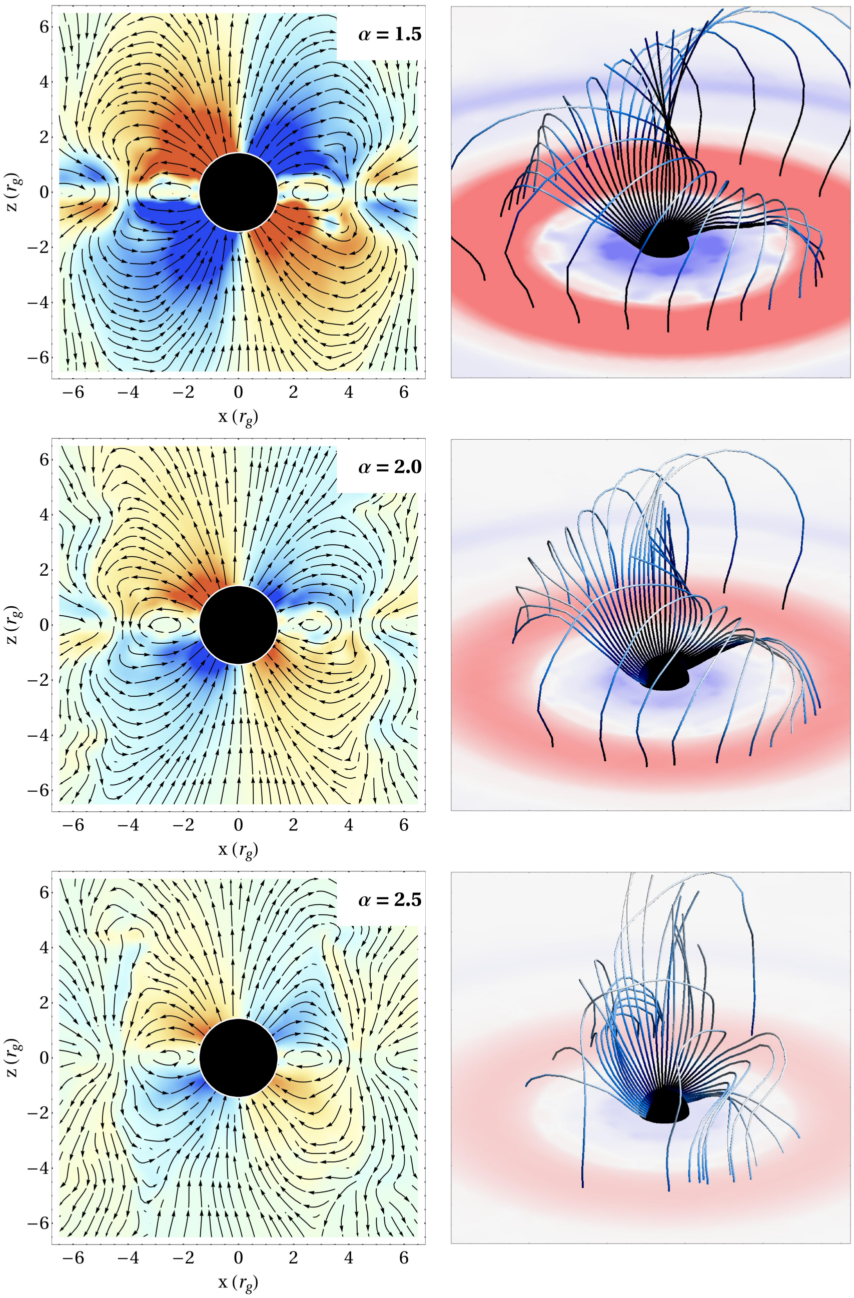

Figure 4.4: As Figure 4.3, but employing a fixed loop length ($l = 4.5$) and varying the parameter α. All configurations open up to large vertical elevations. However, for higher values of α, the inclination of field lines is much steeper and, hence, more prone to develop kinks.

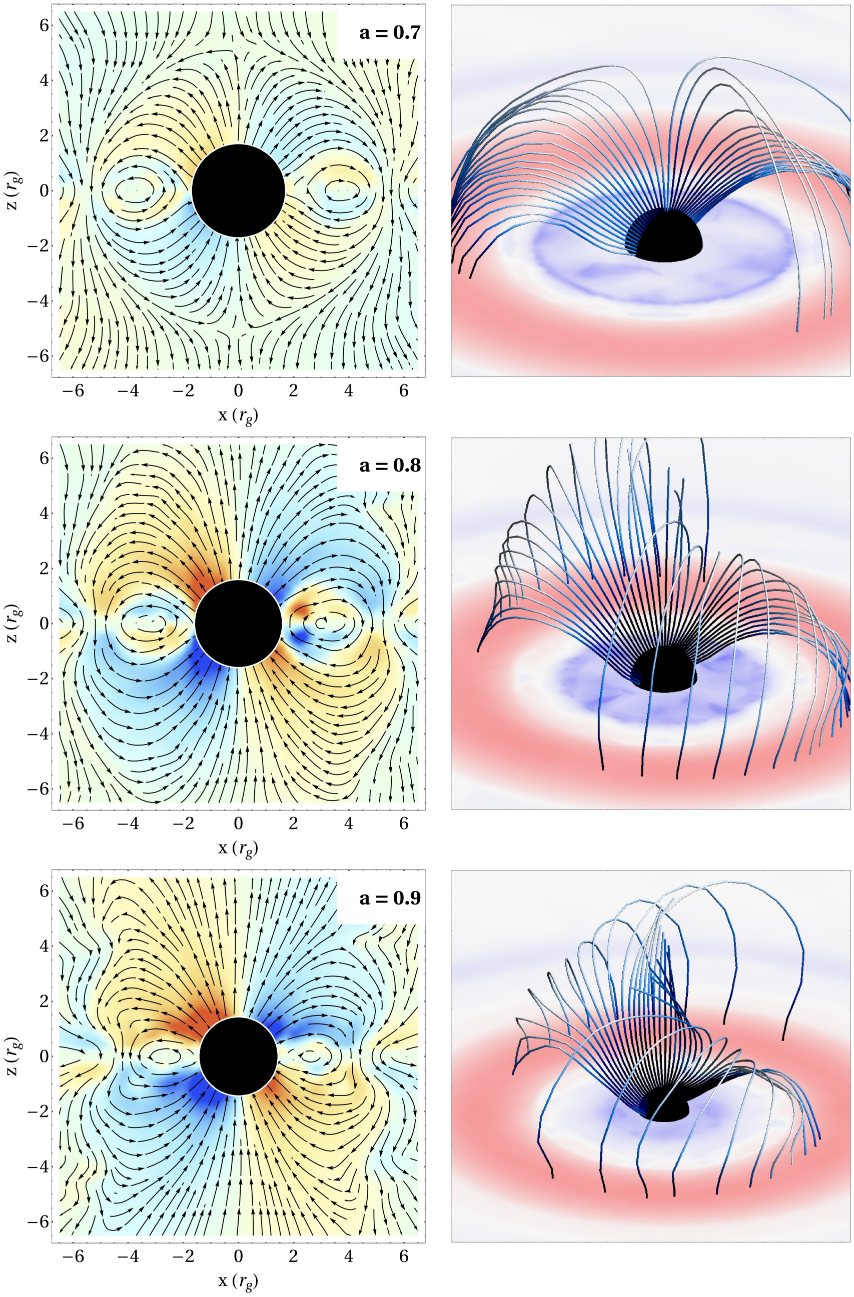

Figure 4.5: As Figure 4.3, but employing a fixed loop length ($l = 4.5$) as well as a fixed $\alpha = 2$ parameter and varying the BH spin. For lower BH spins, the configurations fail to open up to large vertical elevations during the same time ($\sim 180r_g$), effectively twisting field lines less due to the smaller degree of differential rotation between the inner edge of the accretion disc and the BH horizon.

2. A stronger radial decay of the initialization current (cf. Yuan et al., 2019; Mahlmann et al., 2020), i.e., a stronger prominence of the innermost loop, seems to favor a rapid opening of the loop structures. However, it also seems to expose the flux tubes to kink instabilities.

3. Smaller BH dimensionless rapidity can prevent loops to open up due to less exposure of the field lines to differential rotation.

These results, as visualized in Figures 4.3 to 4.5 and supplementary to the analysis proposed in Mahlmann et al. (2020), may be used as a starting point for the design of future analysis of small magnetic structure accretion from co-rotating BH/AD systems. Though they do not include the accretion dynamics, which play a key role in Parfrey et al. (2015) and Mahlmann et al. (2020), they still provide very clean laboratories that enable us to understand elements of field line dynamics and dissipation. The shown ancillary simulations emphasize the existence of several time scales which can prevent the opening up of field lines to significant vertical distances: Short loop length with shorter accretion cycles (figure 4.2) develop a significant kink. Also, moderately spinning BHs (e.g., corresponding to $a^* = 0.7$ in figure 4.5) do not induce sufficient differential rotation of field lines to reach significant opening angles in short times. We will continue to explore the interplay of time scales and magnetospheric dissipation in our future investigation.

4.3.1 The Accretion Disc as a Non-Force-Free Boundary

Several challenges arise in the transport of magnetic flux structures in GRFFE. The most important one is the modeling of the accretion disc. Physical accretion discs need non-ideal effects to allow the transport of mass and magnetic flux to the central object. However, by construction, force-free electromagnetic fields do not permit non-ideal processes, among which, Ohmic resistivity is explicitly excluded. This fact forced us to make an (admittedly) complicated model in Mahlmann et al. (2020) to mimic the structure of the accretion disc and the plunging region endowing a spinning BH. Furthermore, as we expand in Mahlmann et al. (2020), force-free closed magnetic loops are not allowed (see also Gralla and Jacobson, 2014). This means that closed magnetic loops must surround regions where the force-free conditions are not satisfied. Magnetic loops emerging from the accretion disc can be closed only because they pierce the accretion disc, where resistive effects restrict the validity of the force-free treatment. A basic restriction that one faces trying to set up an accretion disc in GRFFE is the lack of a fluid-frame. This is required in order to define an accretion plasma velocity. These challenges urge us to motivate the assumptions we impose in parts of the physical domain by comparison to observations (i.e., the basic theory of transport in ADs) and GRMHD models.

In simple and essentially one-dimensional thin AD models, Lubow et al. (1994) and Heyvaerts et al. (1996) found that magnetic diffusion is much faster than magnetic advection if the field lines threading the disc and connecting it to the external medium bend significantly. The bending of the (large-scale) magnetic field lines has been considered as a natural outcome from the accumulation of magnetic flux in the central part of the disc (e.g., Bisnovatyi-Kogan and Ruzmaikin, 1976; Narayan et al., 2003; Spruit and Uzdensky, 2005). The contrary has been presented by Jafari and Vishniac (2018). If the results of Lubow et al. (1994) and Heyvaerts et al. (1996) hold in actual (astrophysical) ADs, they would imply that the magnetic flux accretion could not produce a significant magnetic field amplification (because of fast magnetic diffusion), and also would suggest that the production of large-scale magnetic fields is hampered in thin ADs. Both of these effects would severely limit the ability of thin ADs to launch magneto-centrifugal (MC) winds. Several ways out of these paradoxical results have been suggested.

Spruit and Uzdensky (2005) proposed that the magnetic field is not uniform and non-axisymmetrically distributed in the disc (the simulations of Igumenshchev, 2008, provide some support to this idea). Instead, most of the magnetic flux accumulates in small patches, where the magnetic diffusion is diminished because strong magnetic fields prevent turbulence. These patches can quickly lose angular momentum through MC winds and drift towards the central accretor. Another possibility is that the disc develops a vertical structure with surface layers being diffuse and magnetically dominated. In these layers, turbulence is suppressed and the conductivity is very high, facilitating the inward transport of magnetic flux (Rothstein and Lovelace, 2008a,b; Guilet and Ogilvie, 2012). On a similar line of thinking, Jafari and Vishniac (2018) show that vertical diffusion and magnetic buoyancy will lead to the vertical straightening of the magnetic field in thin discs, thus alleviating the challenge of fast magnetic diffusion in the radial direction.

The difficulties in accreting magnetic flux signaled by Lubow et al. (1994) are associated with the existence of large-scale magnetic fields connecting the AD to infinity (i.e., to regions far away from the AD). However, other possibilities to drive inwards sufficient magnetic flux to power outflows from the central compact object involve small-scale magnetic fields, likely produced by internal dynamos in situ (e.g., Tout and Pringle, 1992; Pariev et al., 2007; Guan and Gammie, 2009; Tomei et al., 2020). In Mahlmann et al. (2020) we base our justification of the existence of small scale magnetic loop structures in thin accretion discs on these arguments. However, GRMHD models and fully kinetic simulation of ADs and their coronae will be indispensable in order to grasp realistic dynamics of small scale structures on all the involved scales: The feeding of a thin AD from accreting material (GRMHD), the energy flows at the BH horizon (GRFFE) and the accurate treatment of dissipation in extended regions of the magnetosphere (GRPIC).

4.3.2 (Transient) Equilibrium Kerr Magnetospheres

In Mahlmann et al. (2018), we present a highly accurate extension to the numerical iterative solution techniques of the Grad-Shafranov equation as presented in similar approaches by Macdonald (1984), Contopoulos et al. (2013), Nathanail and Contopoulos (2014), and Yuan et al. (2019). We treat the singular surfaces of the GSE (Alfvén surfaces) as internal boundaries of the domain, discretizing the integrals of motion (magnetic flux, field line angular velocity, and magnetospheric current) at either side of them (using biased discretization stencils of the derivatives), only partially interchanging information across in every step of the solution. The smoothness of the final result is ensured by occasional smoothing of the function over various cells of the numerical grid. By these biased stencils, we have achieved accuracy at the level of numerical rounding errors.

We have elaborated on higher-order estimates of the power of the Blandford/Znajek process for very high BH spin factors $a/M > 0.95$. These were obtained by searching for equilibrium in time-dependent GRMHD simulations in the force-free limit by Tchekhovskoy et al. (2010) and are amply employed to interpret very recent observations (e.g., Event Horizon Telescope Collaboration et al., 2019b). By using the results of our numerical experiments (Mahlmann et al., 2018), we were able to quantify the angular dependence of these higher-order corrections to the total energy flow across the BH horizon. For close to extremely spinning BHs, the maximum isotropic power output was found to happen at a latitude of $\theta \approx 10^\circ$. In other words, distant observers are likely to see the most luminous events at a slight offset from the head-on axis (i.e., the axis through the midpoint of the central object and perpendicular to the equator).

The work done in Mahlmann et al. (2018) - constructing equilibrium force-free magnetospheres - is a task that seems to serve primarily the purpose of building initial models for their subsequent time evolution in GRFFE. However, we have also found it very useful to understand and interpret important topologies of the magnetic field occurring during time-dependent simulations. Two particular configurations appear to be of paramount importance for the analysis of astrophysically realistic BH magnetospheres: (a) Field line structures which extend in a paraboloid from the BH to infinity (see e.g., Blandford and Znajek, 1977; Tchekhovskoy et al., 2010; Nathanail and Contopoulos, 2014; Mahlmann et al., 2018), and (b) BH/AD systems in which all (or part of the) field lines which thread the BH are anchored to a prograde AD (as found in Uzdensky, 2005; Mahlmann et al., 2018; Yuan et al., 2019). In Mahlmann et al. (2020), both of these equilibrium states have been identified in the course of our 3D dynamical simulations as the transient phase of maximum energy extraction from the central object (a) and the contrasting phase of inefficient operation of the BZ process (b).

Chapter 5

Conclusions and Outlook

5.1 Conclusions and Milestones of the Thesis

Since this thesis is presented as a compendium of refereed publications, the conclusions of each paper are already incorporated in each of them. Here, we provide a global view of the most salient milestones and conclusions reached during this doctoral thesis. In order to best serve the goals enumerated in section 1.4, we have pursued our research along with the following milestones (in chronological order):

1. **Energy flows in axisymmetric equilibrium magnetospheres.** All through the literature (e.g., Contopoulos et al., 2013; Nathanail and Contopoulos, 2014), the split-monopole and the paraboloidal field solutions to the GSE emerged as standard magnetospheric topologies to model astrophysical scenarios of energy extraction associated to rotating BHs. In these solutions all the magnetic field lines crossing the ergosphere reach infinity. Alternative, non-trivial stationary configurations displaying a magnetic link between the BH and the accretion disc have also proven to exist (e.g., Uzdensky, 2005). These solutions suggest an indirect way to transfer energy-momentum from the BH to the disc, which needs to be connected to infinity by open magnetic field lines to further transfer energy to a distant observer. To a large extent, this is a consequence of the focus on radially pointing energy flows, which only require radial and toroidal magnetic fields. In order to confirm these standard configurations and to quantify their efficiency in spinning down rapidly rotating BHs, we have implemented a numerical Grad-Shafranov solver. We improved the

numerical techniques used to solve the GSE across its singular surfaces and provide a first detailed review of convergence properties (Mahlmann et al., 2018, included in appendix A). In our comparison with different implementations, we achieved an improvement of numerical accuracy of more than ten orders of magnitude by employing biased discretization stencils across the BH light cylinders. We have confirmed the corrections to the approximation of Blandford/Znajek power for extremal spin BHs, as given by Tchekhovskoy et al. (2010). We have confirmed the existence of equilibrium models (advanced by Uzdensky, 2005) where the magnetic topology is hybrid, namely, including open magnetic field lines connecting part of an (idealized) accretion disc to infinity as well as closed field lines joining the BH to the accretion disc. Numerical solutions to the GSE are possible sets of initial data for 3D GRFFE simulations and have been used in the course of this project.

2. **A 3D General Relativistic force-free electrodynamics code.** Due to the huge computational needs demanded by 3D simulations, and the fact that the most advanced computational facilities are composed of thousands of computing cores, we need to resort to numerical codes which are parallel and highly scalable. The EINSTEIN TOOLKIT (ET; Löffler et al., 2012; Etienne et al., 2017) provides an excellent framework for the development of specific routines (known as THORNS) which take advantage of the computational infrastructure of the ET to run on the largest available computational facilities. Furthermore, the ET includes the General Relativistic evolution of spacetime. We have implemented an evolution thorn for force-free electrodynamics (building upon Baumgarte and Shapiro, 2003; Komissarov, 2004; McKinney, 2006; Paschalidis and Shapiro, 2013) (see chapter 2) and applied it to a variety of astrophysical problems. A suite of numerical tests is presented in chapter 3 of this thesis and will be further elaborated in the near future. Especially the quantification of the numerical resistivity of our GRFFE method (currently approximated by $\eta_* \sim 10^{-5} - 10^{-4}$) will provide a firm benchmark for the reliability of the physical results obtained by our scientific code. Recent developments in the field (Baumgarte et al., 2013; Montero et al., 2014) emphasize the need for using coordinates which are adapted to the geometry of the problem at hand. Such geometric considerations are especially relevant when it is necessary to identify the origin of stability associated with the loss of certain equilibrium magnetospheric models (see item 3, below) and the influence of 3D effects. We have recently extended the current (Cartesian)

version of our GRFFE code to an orthonormal finite volume scheme in spherical coordinates on dynamically evolving spacetimes.

3. **Instabilities of high energy twisted magnetar magnetospheres.** We evolved initial data from degenerate solutions of the GSE (with the same boundary conditions, but of different magnetospheric energy) for magnetar magnetospheres on flat background geometry (Akgün et al., 2018) in time with the newly developed GRFFE code (item 2). Some of the degenerate models prove to be unstable and release large amounts of energy near the magnetar surface. Such instabilities may act as the triggering mechanism of the most powerful SGRs, especially of its initial (largest) luminosity outbursts. In a recently published paper (Mahlmann et al., 2019, included in appendix A), we examine the mechanism of energy release and the expected bolometric fingerprint in detail.

4. **BZ jets by accretion of small scale structures.** A typical caveat attributed to the BZ mechanism is the necessity of having a large-scale (ordered) poloidal magnetic field, the flux of which should be non-zero across any of the two hemispheres of the BH horizon. Parfrey et al. (2015) suggested that the energy extraction could be undertaken if magnetic loops of alternating polarity (even of zero net magnetic flux) are accreted by the central BH. For that, it is necessary that the magnetic loops which are plunging onto the BH are wound up by the action of frame dragging and, as a result, become very elongated in the poloidal plane (so much that they become effectively open field lines). We have generalized the proposal of Parfrey et al. (2015), who showed the viability of their model in axial symmetry, to 3D by considering the electromagnetic output via the accretion of 3D magnetic loop structures onto a rapidly rotating BH (spin $a^* = 0.9$). It is necessary to emphasize the fact that the mechanism could work in axisymmetry did not guarantee, a priory, its efficiency in 3D. The foremost reason for this is the potentially very disruptive nature of genuine 3D instabilities (e.g., non-axisymmetric kink modes) acting on the process of winding up and lifting magnetic field lines. In a parameter study focusing on the influence of loop height and width on the energy flow, we confirm the possibility of energy extraction by the Blandford/Znajek mechanism in such 3D dynamical magnetospheres with an average efficiency of $\langle \epsilon \rangle \approx 40\%$ (Mahlmann et al., 2020, included in appendix A).

5.2 Outlook

The amazing images of black hole shadows from the Galactic center and the M87 galaxy (Event Horizon Telescope Collaboration et al., 2019a) provide a first direct glimpse into the physics of accretion flows in the most extreme environments of the universe. This exciting perspective calls for further exploration of the interplay between strong gravity, plasma physics, radiation, fluid, and particle dynamics. Scientific codes used to model these processes and their possible observational signatures face a dilemma. The numerical methods for mildly magnetized fluids (magnetohydrodynamics, or MHD) currently cannot accurately address the highly magnetized (so-called force-free) plasma regime, and vice-versa. The lack of microscopic physics in our global models creates a gap between theoretical predictions and observations of high-energy phenomena driven by particle-scale processes. Our current virtual laboratories are not yet apt for experiments which embrace all magnetization regimes and length scales.

The magnetization can be defined as the (local) ratio between the electromagnetic Poynting flux and the matter-energy flux,

$$\sigma = \frac{B^2}{4\pi\gamma^2 w}, \tag{5.1}$$

where $\gamma^2 = 1 + u^2$ is defined by the fluid four-velocity u, and w is the proper enthalpy density. Already Kennel and Coroniti (1984) realized the role of magnetization downstream the relativistic shocks in pulsar winds. There, the conversion of wind luminosity into synchrotron luminosity critically depends on σ. In studies of relativistic jets, the magnetization is identified as one main parameter governing the flow properties (e.g., Drenkhahn and Spruit, 2002; Vlahakis and Königl, 2003; Giannios and Spruit, 2006), attributing stronger and faster jets to larger σ. At the same time, Tzeferacos et al. (2009) attribute superfast outflows to accretion disc magnetizations of around unity. Still, the conducted MHD simulations (e.g., Stepanovs and Fendt, 2016) are only able to consider $\sigma \lesssim 1$. The analysis of recent breakthrough observations of the M87 galaxy rely on numerical simulations unable to resolve even $\sigma \gtrsim 1$, following the widely used practice to artificially load the jet launching region with an in situ particle density (cf. Event Horizon Telescope Collaboration et al., 2019b). In simulations of accretion discs around BHs, the force-free limit is not suited best to consistently model the plasma which in turn is essential to support the in-spiraling magnetic flux. A disc is necessary to hold the magnetosphere in place and the inertia of the plasma is important to describe it, as has been argued by Parfrey et al. (2015) and our subsequent 3D parameter analysis (Mahlmann et al., 2020). Due to these persisting discrepancies between theoretical expectations and modeling in (numerical) laboratories, hardly any reliable constraint on the magnetic field strength involved in these astrophysical processes can be made (see also Eatough et al., 2013). In consequence, closure of key questions remains sought-after:

How do compact astrophysical objects transport huge energy reservoirs in magnetized plasma and convert it into observable radiation? *Which observational effects and limits on the magnetic field strength in astrophysical flows are to be expected from extending the modeling of plasma dynamics and radiation to the high-magnetization ($\sigma \gg 1$) regime? How do magnetically dominated BH accretion flows influence the mass loading along the accretion funnel as well as in the jet launching region? To what extent are dissipation processes encountered in force-free magnetospheres (ensuring the conditions $\mathbf{B} \cdot \mathbf{D} = 0$ and $\mathbf{B}^2 > \mathbf{D}^2$ between the electromagnetic fields $\mathbf{D}$ and $\mathbf{B}$) physically motivated?*

In general force-free models, one may only rely on crudely estimated lower limits on charge densities when studying radiative processes. Usually, they are given by $n \sim |j|/ec$, effectively counting the number density of electrons moving with the speed of light in a current density j (Beloborodov, 2013). We have recently used this reasoning in Mahlmann et al. (2019) in order to estimate the optical thickness of magnetar magnetospheres. This prescription, however, seems insufficient for radiation modeling in the view of rapidly improving modern telescopes, as it provides merely a crude estimate of the number density of charge carriers. Deducing plasma inertial properties (like the density, and particle velocities) for all magnetization regimes, will be a paramount goal of future research. The consistent coupling between simulations in different approximations, i.e., GRMHD and GRFFE, will be supported by dynamical models rather than mere numerical recipes. More so, it enables the direct comparison of theoretical models of radiation to observational data. The gap between simulations of highly-magnetized astrophysical plasma and their observational counterpart will become bridgeable. It empowers us to explore theoretically the full potential of current and future generation telescopes.

Gravitational waves are one important channel in the era of multi-messenger astrophysics. Predicting source dynamics and the corresponding gravitational waveforms is important to understand hoped-for observations in the current generation of astronomical instruments. Beyond this, it is an essential ingredient to achieve design sensitivity in future observational campaigns envisioned in space-based gravitational wave detectors (see, e.g., Vitale, 2014), as well as third-generation gravitational wave interferometers (see, e.g., Adhikari et al., 2019; Maggiore et al., 2020; Reitze et al., 2019). One future application of our GRFFE method immersed into the powerful infrastructure of the Einstein Toolkit will be the exploration of a full coupling between a dynamical evolution of General Relativistic spacetimes and force-free electromagnetic fields.

The project mardigras.pri (**ma**gnetosphe**r**ic **d**issipation **i**n **G**eneral **R**elativistic **as**trophysics) aims to redefine the current understanding of the phenomena behind the observation of the most luminous energy outbreaks in the surroundings of BHs and strongly magnetized neutron stars (magnetars) by innovative numerical simulations of plasma (electro-)dynamics. Well designed models for the transport of charges as carriers of electromagnetic fields have to be developed and tested in order to bridge the microscopic physics gap, hence, to connect theory with observation. Within mardigras.pri, we will quantify magnetospheric dissipation in General Relativistic (GR) astrophysics by inferring (analytic) closure relations of subgrid dynamics from local simulations and by employing powerful particle-in-cell (PIC) tools on global scales. In the long term, **I intend to employ a new resistive/kinetic framework** (to be developed and optimized during the upcoming research) which can **resolve all magnetization regimes** up to highly magnetized ($\sigma \gg \mathbf{1}$) plasma on dynamical spacetimes.

Part II

Appendices

Appendix A

Publications

The format of the presented doctoral thesis as a compendium of publications requires the permission from the corresponding publishers. Permission to re-use published material was obtained from all journals.

- Copyright credit to Monthly Notices of the Royal Astronomical Society, whose publisher is Oxford University Press.

Monthly Notices of the ROYAL ASTRONOMICAL SOCIETY

MNRAS **477,** 3927–3944 (2018) doi:10.1093/mnras/sty858
Advance Access publication 2018 April 06

Numerically solving the relativistic Grad–Shafranov equation in Kerr spacetimes: numerical techniques

J. F. Mahlmann,★ P. Cerdá-Durán and M. A. Aloy★
Departament d'Astronomia i Astrofísica, Universitat de València, E-46100 Burjassot, Spain

Accepted 2018 April 3. Received 2018 March 26; in original form 2018 February 2

ABSTRACT

The study of the electrodynamics of static, axisymmetric, and force-free Kerr magnetospheres relies vastly on solutions of the so-called relativistic Grad–Shafranov equation (GSE). Different numerical approaches to the solution of the GSE have been introduced in the literature, but none of them has been fully assessed from the numerical point of view in terms of efficiency and quality of the solutions found. We present a generalization of these algorithms and give a detailed background on the algorithmic implementation. We assess the numerical stability of the implemented algorithms and quantify the convergence of the presented methodology for the most established set-ups (split-monopole, paraboloidal, BH disc, uniform).

Key words: black hole physics – magnetic fields – methods: numerical.

1 INTRODUCTION

The so-called Grad–Shafranov equation (GSE) (Lüst & Schlüter 1954; Grad & Rubin 1958; Shafranov 1966) appears as the master equation to determine axisymmetric magnetostatic equilibrium configurations. In particular, it has been applied to obtain force-free magnetospheres around Kerr black holes in the context of the energy extraction mechanisms for relativistic jets by Blandford & Znajek (1977). In their seminal work, analytic solutions for the case in which the black hole (BH) spin is small were obtained. More general solutions including arbitrarily large values of the BH-specific angular momentum require a numerical evaluation of the solution of the GSE (e.g. MacDonald 1984; Fendt 1997; Uzdensky 2004; Contopoulos, Kazanas & Papadopoulos 2013; Nathanail & Contopoulos 2014). As an alternative to the solution of the GSE, the topology of the electromagnetic field around a rotating BH has been determined as an asymptotic steady state of force-free degenerate electrodynamics (FFDE) evolution (Komissarov 2001; Komissarov 2002, 2004; Tchekhovskoy, Narayan & McKinney 2010). Tchekhovskoy et al. (2010) also construct steady state models for BH magnetospheres for a range of spin factors employing general relativistic magnetohydrodynamic (GRMHD) simulations in the force-free limit. These time-evolving approaches to reach a steady state usually impose boundary conditions at the outer BH event horizon as well as at the position of an assumed thin accretion disc.

Drawing from previous findings on neutron star magnetospheres, Contopoulos, Kazanas & Fendt (1999), Contopoulos et al. (2013) presented a numerical scheme for the solution of the GSE in a split-monopole set-up. Contopoulos et al., aimed to find a field line configuration passing smoothly through the singular surfaces of the problem [i.e. the light surfaces (LSs), as previously suggested by Lee, Wijers & Brown 2000]. For that, they implemented a numerical methodology relying vastly on subtle, empirically determined relaxation procedures of all involved functions. In other words, the relaxation to the numerical solution requires recipes which seem to work, but there is no explicit mathematical justification about why they do. The original algorithm of Contopoulos et al. (2013) has later been improved in two ways (Nathanail & Contopoulos 2014). First, it has been supplemented by further smoothing steps in the numerical algorithm. Secondly, Nathanail & Contopoulos (2014) also included paraboloidal configurations of the magnetic field. In their study of systems of non-rotating BHs and thin accretion discs, Uzdensky (2004) found a solution to the GSE for a fixed field line angular velocity. He employs the minimization of a suitably chosen error function at the LSs in order to mathematically drive the numerical relaxation procedure. A similar approach was followed by Uzdensky (2005) in the case of rotating BHs connected to thin accretion discs.

This paper begins by giving a recapitulation of the GSE and its singular surfaces (Section 2). With regard to realistic field configurations in BH magnetospheres, we formulate the underlying equations of force-free electrodynamics in both the potential and field representation. Subsequently (Section 3), we present a comprehensive approach to the numerical solution of the GSE. The strategy of minimizing a suitable error function at the LS (Uzdensky 2004) is extended to the relaxation procedures of both, the field line angular velocity as well as the current profile. We are able to quantify the numerical errors and, hence, substantiate the quality and stability of the found solutions. In Section 4, the GSE solution scheme is tested on split-monopole and paraboloidal configurations, as well as the test case of vertical magnetic fields (cf. Contopoulos et al. 2013; Nathanail & Contopoulos 2014). Furthermore, a current-free solution (as found in Uzdensky 2005) is reproduced. The BZ process

---

★ E-mail: jens.mahlmann@uv.es (JFM); miguel.a.aloy@uv.es (MAA)

Published by Oxford University Press on behalf of the Royal Astronomical Society

power is studied for the split-monopole configurations in Section 5, emphasizing the need for reliable initial data of BH magnetospheres with a large spin parameter a.

2 GRAD–SHAFRANOV EQUATION FOR RELATIVISTIC FORCE-FREE KERR MAGNETOSPHERES

The Kerr solution is a suitable approximation of the spacetime in astrophysical scenarios of jet formation. It embodies the geometry of a spinning BH of mass M and specific angular momentum $a = J/M$ (with its dimensionless equivalent $a_* = a/M$), where J is the angular momentum. Throughout this work, the speed of light and gravitational constant will be set as $c = G = 1$. In Boyer–Lindquist coordinates, the line element of the Kerr metric is

$$\mathrm{d}s^2 = \left(1 - \frac{2Mr}{\Sigma}\right)\mathrm{d}t^2 + \frac{4Mar\sin^2\theta}{\Sigma}\,\mathrm{d}t\,\mathrm{d}\phi - \frac{\Sigma}{\Delta}\,\mathrm{d}r^2 - \Sigma\,\mathrm{d}\theta^2 - \frac{A\sin^2\theta}{\Sigma}\,\mathrm{d}\phi^2,$$

$$\begin{aligned}\Sigma &:= r^2 + a^2\cos^2\theta\,,\\ A &:= \left(r^2+a^2\right)^2 - \Delta\,a^2\sin^2\theta\,,\\ \Delta &:= r^2 - 2Mr + a^2 := (r-r_+)(r-r_-)\,,\end{aligned}$$

where $r_\pm$ represents the locations of the outer and inner horizons of the BH, respectively. $r_\pm^*$ defines the locations of the outer and inner ergosurfaces:

$$r_\pm = M \pm \sqrt{M^2 - a^2} \quad ; \quad r_\pm^*(\theta) = M \pm \sqrt{M^2 - a^2\cos^2\theta}. \tag{1}$$

The frame-dragging frequency induced by the rotation of the BH is

$$\Omega := 2aMr/A, \tag{2}$$

which is also the angular velocity of the (local) *zero angular momentum observer* or ZAMO (cf. Thorne, Price & MacDonald 1986), i.e. $\Omega = (\mathrm{d}\phi/\mathrm{d}t)_{\mathrm{ZAMO}}$. At the outer event horizon, the frame-dragging frequency reads

$$\Omega_{\mathrm{BH}} := \Omega(r = r_+) = \frac{a}{2Mr_+} = \frac{a}{r_+^2 + a^2}. \tag{3}$$

The redshift or lapse function is

$$\alpha := \sqrt{\frac{\Sigma\Delta}{A}}, \tag{4}$$

which accounts for the lapse of proper time τ in the ZAMO frame with respect to the global (Boyer–Lindquist) time t, thus, $\alpha = (\mathrm{d}\tau/dt)_{\mathrm{ZAMO}}$. While the global Boyer–Lindquist observer uses a spatial coordinate basis made by the set of orthogonal vectors $\{\partial_i\} = \{\boldsymbol{e}_i\}$, the local ZAMO observers have an attached tetrad $\{\hat{\boldsymbol{e}}_i\} = \{\boldsymbol{e}_i/\sqrt{g_{ii}}\}$, where the Latin index i runs over the three spatial coordinates (r, θ, ϕ). g_{ii} are the diagonal components of the metric tensor, namely

$$g_{rr} = \frac{\Sigma}{\Delta}, \qquad g_{\theta\theta} = \Sigma, \qquad g_{\phi\phi} = \frac{A\sin^2\theta}{\Sigma}. \tag{4}$$

The covariant Maxwell equations governing the dynamics and topology of the electromagnetic field around a BH read

$$F^{\mu\nu}_{\ \ ;\nu} = \epsilon_0^{-1}J^\mu \qquad\qquad {}^*F^{\mu\nu}_{\ \ ;\nu} = 0, \tag{5}$$

where $F^{\mu\nu}$ and $*F^{\mu\nu}$ are the Maxwell tensor and its dual, respectively, J^μ is the electric current four vector and ϵ_0 is the vacuum permittivity. The semicolon denotes the covariant derivative. Since we seek time independent, force-balance configurations of the magnetosphere of a BH, we ignore the time derivatives involved in equation (5). Under this assumption, the former set of equations can be cast in terms of three vectors measured by a ZAMO observer. Employing Boyer–Lindquist coordinates, the former equations read (cf. Thorne et al. 1986; Zhang 1989; Camenzind 2007; Beskin 2010):

$$\nabla \cdot \boldsymbol{E} = 4\pi\rho, \tag{6}$$

$$\nabla \cdot \boldsymbol{B} = 0, \tag{7}$$

$$\nabla \times (\alpha\boldsymbol{E}) = -(\boldsymbol{B}\cdot\nabla\Omega)\cdot\hat{\boldsymbol{e}}_\phi, \tag{8}$$

$$\nabla \times (\alpha\boldsymbol{B}) = -4\pi\alpha\boldsymbol{j} + (\boldsymbol{E}\cdot\nabla\Omega)\,\hat{\boldsymbol{e}}_\phi, \tag{9}$$

where ρ, the three vectors $\boldsymbol{E}$, $\boldsymbol{B}$, and $\boldsymbol{j}$ are the electric charge density, the electric field, the magnetic field, and the current density measured by the ZAMO observer, respectively. $\hat{\boldsymbol{e}}_\phi$ is the unit normal vector of the tetrad associated to the ZAMO in the ϕ-coordinate direction. In axisymmetric spacetimes, it is possible to distinguish between poloidal (along the potential lines symmetric around the ϕ-axis) and toroidal ($\boldsymbol{e}_\phi$ direction) components (see e.g. Punsly 2001; Camenzind 2007).

To build up a stationary magnetosphere, it is necessary to guarantee that there are either no forces acting on the system or, more generally, that the forces of the system are in equilibrium. Except along current sheets the latter condition implies that the electric 4-current J^μ satisfies the force-free condition (Blandford & Znajek 1977):

$$F_{\mu\nu}J^\nu = 0. \tag{10}$$

Equation (10) is equivalent to a vanishing Lorentz force on the charges in the local ZAMO frame (see e.g. Camenzind 2007):

$$\begin{aligned}\boldsymbol{E}\cdot\boldsymbol{j} &= 0\,,\\ \rho\boldsymbol{E} + \boldsymbol{j}\times\boldsymbol{B} &= 0\,.\end{aligned} \tag{10}$$

These equations also imply the degeneracy condition $\boldsymbol{E}\cdot\boldsymbol{B} = 0$. Combining equations (5) and (10) yields the force–balance equation (or GSE) as introduced by Blandford & Znajek (1977). It relates the magnetic flux $\Psi(r, \theta)$ enclosed in the circular loop $r =$ constant, $\theta =$ constant (divided by 2π) to the field line angular velocity $\omega(\Psi)$ and the poloidal electric current $I(\Psi)$ (this version of the GSE is also used in e.g. Nathanail & Contopoulos 2014):

$$\begin{aligned}4\frac{\Sigma}{\Delta}II' = {}&\left(\Psi_{,rr} + \frac{1}{\Delta}\Psi_{,\theta\theta} + \left(\frac{A_{,r}}{A} - \frac{\Sigma_{,r}}{\Sigma}\right)\Psi_{,r} - \frac{1}{\Delta}\frac{\cos\theta}{\sin\theta}\Psi_{,\theta}\right)\\ &\times\left[\frac{\omega^2A\sin^2\theta}{\Sigma} - \frac{4Mar\omega\sin^2\theta}{\Sigma} - 1 + \frac{2Mr}{\Sigma}\right]\\ &+\left(\frac{A_{,r}}{A} - \frac{\Sigma_{,r}}{\Sigma}\right)\Psi_{,r} + \frac{4Mar\omega\sin^2\theta}{\Delta\Sigma}\frac{A_{,\theta}}{A}\Psi_{,\theta}\\ &-\frac{2Mr}{\Delta\Sigma}\frac{\Sigma_{,\theta}}{\Sigma}\Psi_{,\theta}\\ &+\left(2\frac{\cos\theta}{\sin\theta}+\frac{A_{,\theta}}{A}-\frac{\Sigma_{,\theta}}{\Sigma}\right)A\omega\left(\omega-\frac{4Mar}{A}\right)\frac{\sin^2\theta}{\Delta\Sigma}\Psi_{,\theta}\\ &-\left(\frac{2Mr}{\Sigma} - \frac{4Mar\omega\sin^2\theta}{\Sigma}\right)\left(\frac{A_{,r}}{A} - \frac{1}{r}\right)\Psi_{,r}\\ &+\frac{\sin^2\theta}{\Sigma\Delta}(A\omega - 2Mar)\left(\Delta\,\omega_{,r}\,\Psi_{,r} + \omega_{,\theta}\,\Psi_{,\theta}\right).\end{aligned} \tag{11}$$

The subscript comma indicates respective partial derivatives. From the mathematical viewpoint, this equation is, in most of the space, an elliptic, second-order partial differential equation (PDE) for the magnetic flux (e.g. Beskin 1997). This means that we shall provide suitable boundary conditions to determine the solution of the system. Since we are interested in employing the magnetospheric configurations obtained with our new methodology as initial data for evolutionary calculations, we shall compute the solution from the outer event horizon of the BH to infinity. There is an added complexity in the solution of the equation, since there are singular surfaces of the spacetime, where the equation becomes a first-order PDE (see Section 2.1). Taking together these facts, we shall devise a numerical method which adapts to the mathematical (and physical) challenges in the type of PDE we have at hand.

A numerical solution to the GSE (equation 11) will consist of a relaxed configuration of the three functions $\Psi(r, \theta)$, $\omega(\Psi)$, and $I(\Psi)$. These functions fully determine the vector fields $\{\boldsymbol{E}, \boldsymbol{B}\}$ employed in equation (9) (see e.g. Camenzind 2007):

$$\boldsymbol{E} = -\frac{\omega - \Omega}{2\pi\alpha}\nabla\Psi \qquad \boldsymbol{B}_P = \frac{\nabla\Psi \times \boldsymbol{e}_\phi}{2\pi\varpi^2} \qquad B^T = -\frac{2I}{\alpha\varpi^2}. \tag{12}$$

Here, $\varpi = \sqrt{-g_{\phi\phi}}$ is the cylindrical radius, $\boldsymbol{B}_{\mathrm{P}}$ represents the poloidal magnetic field, and B^{T} the toroidal magnetic field component. In their field representation, solutions to the GSE will eventually be employed in conservative time evolution schemes of force-free electrodynamics (as suggested e.g. by Komissarov 2004; Komissarov 2007).

2.1 Light surfaces

The numerical solution of the GSE relies on the use of additional regularity conditions at the singular surfaces of equation (11). Throughout the domain, the so-called light surfaces are situated where the coefficient multiplying the second-order derivatives vanishes, i.e. where the condition

$$\mathcal{D} := \frac{\omega^2 A \sin^2\theta}{\Sigma} - \frac{4Mar\omega\sin^2\theta}{\Sigma} - 1 + \frac{2Mr}{\Sigma} = 0 \tag{13}$$

is satisfied. In an analogy to the pulsar magnetosphere (Ruderman & Sutherland 1975), the LS can be understood as singular surfaces where magnetic field lines rotate superluminally with respect to the ZAMO observer (e.g. Komissarov 2004). In that context they are known as light cylinders. Outside of the outer light surface (OLS), magnetic field lines rotate faster than the speed of light with respect to ZAMOs. Inside the inner light surface (ILS), magnetic field lines counterrotate superluminally with respect to the ZAMO. The ILS falls inside the ergosphere and touches its boundary (and, hence, also the outer horizon) at the rotational axis of the system (located at $\theta = 0$). As explicitly shown in Komissarov (2004), while the radial coordinate r of the ILS increases monotonically with θ between the rotational axis and the equator, the opposite holds for the OLS.

Across these singular surfaces, we demand regularity of the three scalar functions $\Psi(r, \theta)$, $\omega(\Psi)$, and $I(\Psi)$. More specifically, we require that the magnetic flux function Ψ crosses smoothly through the ILS and through the OLS. The remaining two functions $\omega(\Psi)$ and $I(\Psi)$ will be reconstructed from the smooth Ψ function. If condition (13) holds, then equation (11) becomes the *reduced* GSE, which allows us to relate the aforementioned three functions through

$$\begin{aligned}
4\frac{\Sigma}{\Delta}II' = {} & \left(\frac{A_{,r}}{A} - \frac{\Sigma_{,r}}{\Sigma}\right)\Psi_{,r} - \frac{2Mr}{\Delta\Sigma}\frac{\Sigma_{,\theta}}{\Sigma}\Psi_{,\theta} + \frac{4Mar\omega\sin^2\theta}{\Delta\Sigma}\frac{A_{,\theta}}{A}\Psi_{,\theta} \\
& + \left(2\frac{\cos\theta}{\sin\theta} + \frac{A_{,\theta}}{A} - \frac{\Sigma_{,\theta}}{\Sigma}\right)A\omega\left(\omega - \frac{4Mar}{A}\right)\frac{\sin^2\theta}{\Delta\Sigma}\Psi_{,\theta} \\
& - \left(\frac{2Mr}{\Sigma} - \frac{4Mar\omega\sin^2\theta}{\Sigma}\right)\left(\frac{A_{,r}}{A} - \frac{1}{r}\right)\Psi_{,r} \\
& + \frac{\sin^2\theta}{\Sigma\Delta}(A\omega - 2Mar)\left(\Delta\,\omega_{,r}\,\Psi_{,r} + \omega_{,\theta}\,\Psi_{,\theta}\right).
\end{aligned} \tag{14}$$

As noted by Uzdensky (2005), the reduced GSE must be fulfilled, both, at the ILS and at the OLS. Thus, we have two relations among the freely specifiable functions $\omega(\Psi)$ and $I(\Psi)$.

3 A GENERALIZED NUMERICAL GRAD–SHAFRANOV SOLVER

Our method is based on a finite-difference solution of equation (11). For that, we discretize all the physical and geometrical quantities in a two-dimensional grid. The radial coordinate is compactified according to the transformation $R(r) = r/(r + M)$ as introduced by Contopoulos et al. (2013). Radial derivatives are mapped to the $R(r)$ coordinate by the following transformations:

$$\begin{aligned}
\frac{\partial}{\partial r} &= \left[\frac{M}{(r+M)^2}\right]\frac{\partial}{\partial R} \\
\frac{\partial^2}{\partial r^2} &= -\left[\frac{2}{(r+M)^3}\right]\frac{\partial}{\partial R} + \left[\frac{M}{(r+M)^2}\right]^2\frac{\partial^2}{\partial R^2}.
\end{aligned} \tag{15}$$

The computational domain covers the region $[R_{\min}, R_{\max}] \times [0, \theta_{\max}]$, where $R_{\min} = r_+/(r_+ + M)$ (i.e. the computational domain extends radially down to the outer event horizon) and $R_{\max}$ is specified differently according to the application we seek. The region mapped by the grid may easily be extended to reach all the way to infinity at $R_{\max} = 1$. In most cases, we set $\theta_{\max} = \pi/2$ and symmetry with respect to the equatorial plane. Given that the Kerr metric fulfils this property, it is reasonable to search for solutions of the GSE with this symmetry as well. The (R, θ) domain is covered by a uniform mesh, where the number of mesh points in the r and θ directions is n_r and n_θ, respectively. The discrete values of the magnetic flux $\Psi_{ij} := \Psi(R(r_i), \theta_j)$ are stored on a two-dimensional array of the same size as the numerical grid, whereas the two remaining functions $\omega(\Psi)$ and $II'(\Psi)$ are tabulated as a one-to-one map of Ψ. For practical purposes, instead of working directly with the function $I(\Psi)$, we use $II'(\Psi)$ (cf. Nathanail & Contopoulos 2014). The latter is related to the former by

$$|I(\Psi)| = \left[2\int_0^\Psi II'(\Psi)\right]^{1/2}. \tag{15}$$

One should note that the additional arbitrariness of sign induced by the prescribed recovery of the current $I(\Psi)$ from the function $II'(\Psi)$ should be handled carefully in equation (12). The numerical solution determining Ψ, $\omega(\Psi)$, and $II'(\Psi)$ is obtained using an iterative procedure. In this iteration, the initial values of these functions can be specified freely.

Physically the magnetosphere is divided into three disconnected regions by the two LSs of the problem. Mathematically, we shall map this property by solving *independently* for the scalar function Ψ in each subdomain. The only connection between domains are the regularity conditions at the separatrices among subdomains.

Accounting for these facts, the numerical method we propose splits each iteration into three basic blocks of (1) the finite difference solution of the GSE in each of the subdomains, (2) the matching of the solutions across the LSs to obtain regular functions, and (3) the build-up or update of the functional tables for $\omega(\Psi)$ and $I\!I'(\Psi)$. In the following sections, the details of each of these blocks are provided.

3.1 Finite difference solution of the GSE in each subdomain

For the finite difference solution of the GSE in each subdomain, we take advantage of the existing computational infrastructure for linear elliptic PDEs used in Adsuara et al. (2016). In order to apply these methods to the non-linear equation at hand, we split the GSE into a term linear in the derivatives of Ψ (right-hand side of equation 11) and into a part comprising the non-linear source terms (left-hand side of equation 11). The coefficients of the derivatives as well as the source terms are discretized on the mesh. The GSE (11) can be written in a canonical form as

$$\mathcal{C}_{rr}\Psi_{,rr} + \mathcal{C}_{\theta\theta}\Psi_{,\theta\theta} + \mathcal{C}_{r}\Psi_{,r} + \mathcal{C}_{\theta}\Psi_{,\theta} = \mathcal{S}, \tag{16}$$

where $(\mathcal{C}_r, \mathcal{C}_{rr}, \mathcal{C}_\theta, \mathcal{C}_{\theta\theta})$ are the PDE coefficients and $\mathcal{S}$ the sources (left-hand side of equation 11). We note that the GSE is linear in the higher order derivatives, and that it contains no terms proportional to $\Psi_{,r\theta}$, i.e. $\mathcal{C}_{r\theta} = 0$. Following, e.g. Beskin (1997), it is then easy to see from the canonical form of the GSE (equation 16) that the character of the equation depends on the sign of the discriminant $\mathcal{C}_{r\theta}^2 - 4\mathcal{C}_{rr}\mathcal{C}_{\theta\theta} = -4\mathcal{D}^2/\Delta$. Since $\Delta > 0$ for $r > r_+$ and $\mathcal{D}^2 > 0$ everywhere except at the LSs, the GSE is elliptic. At the LSs ($\mathcal{D} = 0$), the character of the equation does not change because of the regularity condition given in equation (14).

Employing a second-order centred finite difference scheme on an equally spaced grid, the discretized form of the GSE reads

$$\begin{aligned}\mathcal{S}_{i,j} = {} & \Psi_{i-1,j}\left[\frac{\mathcal{C}_{rr}}{\delta r^2} - \frac{\mathcal{C}_r}{2\delta r}\right] - \Psi_{i,j}\left[\frac{\mathcal{C}_{rr}}{\delta r^2} + \frac{\mathcal{C}_{\theta\theta}}{\delta\theta^2}\right] \\ & + \Psi_{i+1,j}\left[\frac{\mathcal{C}_{rr}}{\delta r^2} + \frac{\mathcal{C}_r}{2\delta r}\right] + \Psi_{i,j-1}\left[\frac{\mathcal{C}_{\theta\theta}}{\delta\theta^2} - \frac{\mathcal{C}_\theta}{2\delta\theta}\right] \\ & + \Psi_{i,j+1}\left[\frac{\mathcal{C}_{\theta\theta}}{\delta\theta^2} + \frac{\mathcal{C}_\theta}{2\delta\theta}\right],\end{aligned} \tag{17}$$

where we have dropped subscripts (i, j) of the coefficients $(\mathcal{C}_r, \mathcal{C}_{rr}, \mathcal{C}_\theta, \mathcal{C}_{\theta\theta})$ to avoid cluttering the formulae with subindices. From this discretization, a coefficient matrix is built and used for the iterative relaxation procedure:

$$\mathcal{G}_S := \begin{pmatrix} \mathcal{I}^c & \mathcal{I}^u & 0_{n_r\times n_\theta} & \cdots & \cdots & \cdots & 0_{n_r\times n_\theta} \\ \mathcal{I}^d & \mathcal{I}^c & \mathcal{I}^u & 0_{n_r\times n_\theta} & \cdots & \cdots & 0_{n_r\times n_\theta} \\ 0_{n_r\times n_\theta} & \mathcal{I}^d & \mathcal{I}^c & \mathcal{I}^u & 0_{n_r\times n_\theta} & \cdots & 0_{n_r\times n_\theta} \\ \vdots & 0_{n_r\times n_\theta} & \ddots & \ddots & \ddots & \vdots & 0_{n_r\times n_\theta} \\ \vdots & \vdots & \ddots & \ddots & \ddots & \ddots & 0_{n_r\times n_\theta} \\ \vdots & \vdots & \vdots & \vdots & \mathcal{I}^d & \mathcal{I}^c & \mathcal{I}^u \\ 0_{n_r\times n_\theta} & \cdots & \cdots & \cdots & 0_{n_r\times n_\theta} & \mathcal{I}^d & \mathcal{I}^c \end{pmatrix}, \tag{18}$$

Here, $\mathcal{I}^c$, $\mathcal{I}^u$, and $\mathcal{I}^d$ are matrices with dimensions $n_r \times n_\theta$, which contain the combinations of coefficients of equation (17) and $0_{n_r\times n_\theta}$ is the null matrix with dimensions $n_r \times n_\theta$.

The numerical elliptic PDE solver is used with an iterative SOR (successive overrelaxation) scheme to find the magnetic flux function Ψ. For the complex non-linear system at hand, there is no known optimal relaxation coefficient of the SOR scheme, $\omega_{\mathrm{SOR,\,opt}}$. Thus, we need to choose a value ω_{SOR} empirically. Numerical experience tells that we shall take a value as close as possible to 2, but not too large such that the iterative scheme diverges. The choice of ω_{SOR} strongly depends upon the grid properties (e.g. number of grid points, physical domain size) as well as the numerical treatment of the LS.

Both, the grid extension and the discretization stencil have an impact on the diagonal dominance of the resulting coefficient matrices (equation 18) of the solver. In case of the relativistic GSE (equation 11), diagonal dominance may be greatly breached at the location of the singular surfaces (cf. condition 13), where the coefficients $\mathcal{C}_{rr}$ and $\mathcal{C}_{\theta\theta}$ vanish. This is mostly due to the fact that points across a separatrix of the computational domain should not be bridged by the finite difference discretization. Stated differently, a derivative on a given computational subdomain must not include values on a different subdomain in its stencil. We point out that this fact was brought about by Camenzind (1987), but in the context of the finite element solution of the GSE. Camenzind (1987) points out, that, as the finite element grid must follow the shape of the LSs, the nodal points had to be redistributed iteratively in his numerical method. Turning to our finite difference discretization, we shall see that, e.g. a standard second-order centred finite difference approximation of the first derivatives Ψ' couples points across LS, rendering a poor convergence (if at all) to the solution. This fact forces us to employ ω_{SOR} closer to 1, instead of 2. Changing the discretization for the cells around the LS to a left/right biased second-order scheme or reducing the approximation to first order of accuracy greatly improves diagonal dominance of the coefficient matrix and, hence, convergence behaviour of the numerical solver (see Fig. 1).

If not stated otherwise, Dirichlet boundary conditions are imposed along the symmetry axis as well as on the equator in the simulations, where we fix the minimum and maximum values of the potential Ψ, respectively. Newman boundary conditions are set up along the radial edges of the computational domain. The latter implies that we set up the derivatives of Ψ normal to the outer horizon at $r = r_+$. Note that the value of Ψ, or of any other free function of Ψ, is not imposed at the outer event horizon. In particular, the so-called Znajek condition (Blandford & Znajek 1977; Znajek 1977) is not explicitly enforced there.

The iterative solution is stopped when we attain a prescribed reduction of the residual, defined as

$$\mathcal{R}_\Psi = \left|\Psi^{(n)} - \Psi^{(n-1)}\right|_\infty, \tag{19}$$

where $|.|_\infty$ stands for the L^∞ norm computed over all the discrete points of our numerical grid (for more details, see Appendix A1).

3.2 Matching across subdomains

To ensure regularity of the potential Ψ across the LSs, we have employed two strategies. First, we perform a cycle consisting of iterative overrelaxations of the GSE interleaved with numerical resets of the values of Ψ developed at the LSs. The mentioned cycle starts computing a series of iterations of the solution on each of the three subdomains independently. This brings a mismatch between solutions across subdomains. The most severe mismatch happens at the ILS, where numerical artefacts develop. In order to smooth out the solution, we build high-order Lagrange interpolation polynomials in the radial direction for Ψ. These polynomials have a stencil centred around the LSs on each different discrete value of θ_j ($j = 1, \ldots, n_\theta$). Thus, they encompass points in two different computational domains. At the radial location of the LSs we obtain

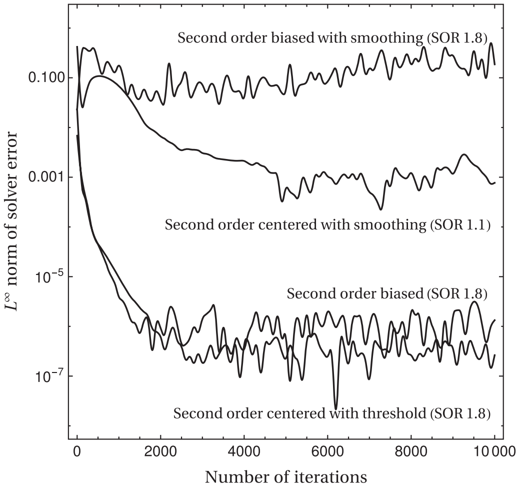

Figure 1. Evolution of the L^∞ norm of the solver residual (cf. equation 19). Comparison of different discretization schemes and their convergence behaviour inside the OLS ($[r_+, 3.0] \times [0, 90^\circ]$, $[n_r \times n_\theta] = [200 \times 100]$) for a BH with $a_* = 0.9999$, during relaxation of $II'(\Psi)$ for $\omega(\Psi) = 0.5\Omega_{\rm BH}$ fixed to the initial value. The initial magnetic flux distribution corresponds to that of a split-monopole (see Section 4.1). Relaxation coefficients of the successive overrelaxation (SOR) scheme are chosen according to maximal convergence without numerical breakdown of the iterative scheme. Their values are written in parenthesis for each different case. The presented tests consist of (i) a second-order finite difference discretization with smoothing at the LS in every iteration, (ii) a second-order finite difference discretization with a threshold on the coefficients $\mathcal{C}_{rr}$ and $\mathcal{C}_{\theta\theta}$ ensuring diagonal dominance of equation (18), (iii) the second-order discretization with biased stencil at the LS and additional smoothing in every step, and (iv) the second-order discretization with biased stencil at the LS with no additional smoothing.

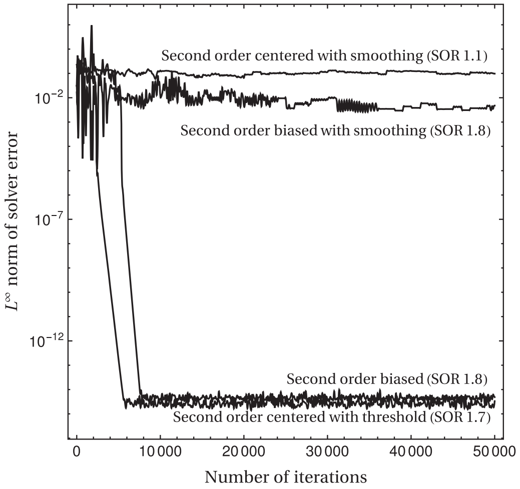

Figure 2. Evolution of the L^∞ norm of the solver error. Comparison of different discretization schemes and their convergence behaviour including the ILS and the OLS ($[r_+, \infty] \times [0, 90^\circ]$, $[n_r \times n_\theta] = [200 \times 100]$) for a BH with $a_* = 0.9999$, during relaxation of both $II'(\Psi)$ and $\omega(\Psi)$. The iterative procedure on ω and II' proceeds as long as $\mathcal{R}_\Psi > 10^{-5}$. SOR factors are chosen according to maximal convergence without numerical breakdown of the iterative scheme. Their values are written in parenthesis for each different case. The initially guessed magnetic flux distribution corresponds to that of a split-monopole (see Section 4.1).

an smooth interpolant of Ψ, which replaces the numerical values (artefacts) developed there in the course of the iterative solution. We repeat the whole cycle until convergence is reached. This first strategy follows from Nathanail & Contopoulos (2014), but we employ higher order polynomial interpolants for Ψ (fifth-order Lagrangian interpolation, instead of just taking for Ψ the average between its values on both sides of an LS – cf. equation 15 of Nathanail & Contopoulos 2014).

The second strategy consists in producing a central, second-order finite difference discretization in all points of the computational domain except close to the LSs. There we switch to a (left/right) biased, second-order, finite difference discretization of the first derivatives of the GSE. This procedure notably reduces the coupling between different physical domains. However, since the LSs are not spherical, some unwanted couplings may develop due to the discretization of angular derivatives. As a result of the biased discretization the coefficient matrix of the linear system to be solved (equation 18) improves its diagonal dominance. The improved diagonal dominance results in a faster convergence of the method than when no biased discretizations are employed (as we shall see in Section 4). In Fig. 1 we clearly see that a second-order biased discretization around the LSs works better if no smoothing is applied to Ψ. Indeed, with the use of a biased discretization the need of any smoothing of the solution at the LSs disappears and we do not apply it. This matching strategy follows the general guidelines devised by Leveque & Li (1994) for the treatment of immersed boundaries in second-order elliptic equations.

A third strategy has also been tested, namely, we employ a second-order centred discretization everywhere, but at the LSs we use a threshold for the coefficients $\mathcal{C}_{rr}$ and $\mathcal{C}_{\theta\theta}$ ensuring diagonal dominance of the matrix of the system (equation 18). Note that $\mathcal{C}_{rr} = \mathcal{C}_{\theta\theta} = 0$ on the LSs. Thus, the proposed recipe consists of replacing the aforementioned coefficients by

$$\begin{aligned} \mathcal{C}_{rr} &= \mathrm{sign}(\mathcal{C}_{rr}) \times \max\left(|\mathcal{C}_{rr}|, \epsilon\right), \\ \mathcal{C}_{\theta\theta} &= \mathrm{sign}(\mathcal{C}_{\theta\theta}) \times \max\left(|\mathcal{C}_{\theta\theta}|, \epsilon\right), \end{aligned} \tag{19}$$

with $\epsilon \sim 10^{-5}$. As in the case of the second strategy, the thresholding of the coefficients of the second-order derivatives renders unnecessary any smoothing procedure at the LSs. Fig. 1 shows that the second and third strategies yield a quite similar reduction of the residual with the number of iterations.

In Fig. 2, we show the evolution of the residual with the number of iterations in the solver, again, for different matching strategies. Differently from Fig. 1, in this case we include the whole space–time ($r_{\rm max} = \infty$). Regardless of whether we set the outer boundary conditions at finite or infinite distance, the qualitative conclusion is the same. Namely, either thresholding the coefficients of the second-order derivatives, or employing a biased discretization close to the LSs brings a much larger reduction (by roughly nine orders of magnitude) than smoothing the solution across the LSs. Furthermore, smoothing procedures are unable to reduce substantially the residual for coarse discretizations. The results shown in Figs 1 and 2 also hold for higher resolutions.

Since the second strategy presented in this section (left/right biased stencils) does not depend on any additional tunable parameter and since it yields a reduction of the residual comparable to the case of using thresholding, we will use it as our default method to match the solution across different subdomains.

3.3 Update of the potential functions

The potential functions $\omega(\Psi)$ and/or $II'(\Psi)$ could be updated every time the magnetic flux Ψ changes in the course of the iterative relaxation sketched in Section 3.1. In practice, it is unnecessary to update $\omega(\Psi)$ and $II'(\Psi)$ with this frequency. Instead, the mentioned update is performed after $n_{\mathrm{u}} \geq 1$ iterations. The choice of n_{u} comes as a tradeoff between accuracy and computational time.

The update of both functions simultaneously (see Contopoulos et al. 2013), as well as with one of them fixed (cf. Uzdensky 2004) to an initially specified value are equally possible in our scheme. For convergence testing we have considered both cases, i.e. the relaxation of either $\omega(\Psi)$ (not shown here) or $II'(\Psi)$ (Fig. 1) and of both functions simultaneously (Fig. 2). A cautionary note must be added here. The number of LSs in the computational domain determines whether one or none of the potential functions can be arbitrarily set up. More precisely, the number of freely specifiable potential functions equals two minus the number of LSs in the domain. For instance, if the OLS radius is sufficiently large (e.g. when $a \rightarrow 0$), the outermost radial computational domain may be set inside of the OLS for numerical convenience. In this case, we are allowed to freely specify either $\omega(\Psi)$ or $I(\Psi)$. This is the simplification we employ to obtain the results shown in Fig. 1. Note, however, that if the numerical domain contains both LS, there is no freedom to set the potential functions. They must be recovered from equation (20) applied both at the ILS and the OLS. The convergence properties of the latter case can be seen in Fig. 2. In view of the results, the global convergence properties of the algorithm are not sensitively dependent on the choice of updating only one or both potential functions.

The updates of the potential functions are conducted by minimizing the error of equation (14) after determining the exact radial position of the LS and the corresponding interpolated quantities. More specifically, we define the residual at the LS as

$$\begin{aligned}\mathcal{R}_{\mathrm{LC}} = \Bigg| & 4\frac{\Sigma}{\Delta} I I' - \left(\frac{A_{,r}}{A} + \frac{\Sigma_{,r}}{\Sigma}\right)\Psi_{,r} - \frac{2Mr}{\Delta\Sigma}\frac{\Sigma_{,\theta}}{\Sigma}\Psi_{,\theta} \\ & - \frac{4Mar\omega\sin^2\theta}{\Delta\Sigma}\frac{A_{,\theta}}{A}\Psi_{,\theta} \\ & - \left(2\frac{\cos\theta}{\sin\theta} + \frac{A_{,\theta}}{A} - \frac{\Sigma_{,\theta}}{\Sigma}\right) A\omega\left(\omega - \frac{4Mar}{A}\right)\frac{\sin^2\theta}{\Delta\Sigma}\Psi_{,\theta} \\ & + \left(\frac{2Mr}{\Sigma} - \frac{4Mar\omega\sin^2\theta}{\Sigma}\right)\left(\frac{A_{,r}}{A} - \frac{1}{r}\right)\Psi_{,r} \\ & - \frac{\sin^2\theta}{\Sigma\Delta}\left(A\omega - 2Mar\right)\left(\Delta\,\omega_{,r}\,\Psi_{,r} + \omega_{,\theta}\,\Psi_{,\theta}\right)\Bigg| \end{aligned} \tag{20}$$

and attempt to minimize it (see also the convergence criterion in Appendix A1). The process of minimizing R_{LC} depends on whether we fix one of the two free potential functions (and which one of them) or if we leave both to be numerically obtained from the reduced GSE (equation 14) applied at both LSs. Independent of the fixing or relaxing of the function $\omega(\Psi)$ (see below), the functional update of II' is achieved in a straightforward manner by substitution of ω and ω' into the right-hand side of expression (equation 14) at the LS. If we do not initially specify the rotational profile and keep it throughout the iterative solution, then we need to provide initial guesses ω_0 and ω_0' for ω and its derivative, respectively. We note that every time ω is changed, the location of the LS (equation 13) changes. The practical procedure consists on taking a set of a few thousands of values ω_0 and ω_0' uniformly selected in the intervals $[\omega(\Psi) - \xi, \omega(\Psi) + \xi]$ (throughout the shown tests we use $\xi = 0.15$) and for each of these values we compute R_{LC} (equation 20). Among all these pairs of values ω_0 and ω_0' we pick the one which minimizes R_{LC}.

Optimal and stable results require an exact localization of the LS positions. Since we employ a finite difference method, the spatial discretization determines the numerical accuracy with which the singular surfaces are resolved. However, for practical grid resolutions, it is necessary to exceed the accuracy of the numerical grid in order to achieve high accuracy in resolving equation (20). Once it is detected that a given numerical cell between grid points, namely, bounding the region $[r_i, r_{i+1}] \times [\theta_j, \theta_{j+1}]$, is traversed by an LS, our algorithm improves the accuracy of its localization using either Lagrangian interpolation polynomials or bicubic spline interpolation if a higher resolution is desired. In the presented solutions, especially for lower values of the BH spin parameter a, the numerical grid is refined before every update of the potential functions and bicubic spline interpolation is used to determine the quantities at the respective LSs. For small values of θ (i.e. the first few zones at the $\theta_{\min}$ boundary), we approximate the potential Ψ by the initially guessed function in order to avoid numerical artefacts due to the small distance between the ILS and the event horizon (as suggested by Contopoulos et al. 2013).

The functions $\omega_{\mathrm{ns}}(\Psi)$ and $I I_{\mathrm{ns}}'(\Psi)$ obtained with the previous procedures tend to be non-smooth. This lack of smoothness degrades the convergence properties of the finite difference solution. Thus, we replace ω_{ns} and $I I_{\mathrm{ns}}'$ by smooth cubic spline interpolants of the latter functions (cf. Contopoulos et al. 2013; Nathanail & Contopoulos 2014). For that, we pick a sample of n_{int} values of both ω_{ns} and $I I_{\mathrm{ns}}'$ as nodal points for the cubic spline interpolation. The number of nodal points may be chosen in the algorithm set-up and may influence the accuracy of the solution (the presented runs employed $n_{\mathrm{int},\,\omega} = 5$ and $n_{\mathrm{int,II'}} = 10$). Especially for the first relaxation steps, a lower order of $n_{\mathrm{int},\,\omega}$ and $n_{\mathrm{int,II'}}$ may be beneficial in order to prevent undesired oscillations. The presented procedure has been tested as well with $n_{\mathrm{int},\,\omega} = 10$ and $n_{\mathrm{int,II'}} = 20$ differing in the rate of initial convergence without noticeable changes to the relaxed solution.

Uzdensky (2004) has applied the update of the current function employing equation (14) in order to find the field configuration of a central engine with the field line angular velocity fixed by the disc's rotation. With the suggested methodology for the updating of the potential functions, we generalize his approach by allowing the fixing of either potential function.

3.4 The Znajek condition at r_+

A key ingredient of the derivation of an outflowing energy and a process efficiency measure at the horizon in Blandford & Znajek (1977) is the so-called Znajek boundary condition. Historically by Weber & Davis (1967) and context-specific by Znajek (1977), the question for asymptotic fields in magnetohydrodynamics was posed. Requiring finite field and potential quantities at the horizon, the so-called Znajek 'boundary condition' sets a link among the angular derivative of Ψ and the potential functions $I(\Psi)$ and $\omega(\Psi)$ at the outer BH horizon:

$$I_Z\left(\Psi\right) = -\frac{Mr_+\sin\theta}{r_+^2 + a^2\cos^2\theta}\left[\Omega - \omega\left(\Psi\right)\right]\Psi_{,\theta} \tag{21}$$

Despite its original purpose as a boundary condition, recent studies suggest that equation (21) is a regularity condition which is auto-

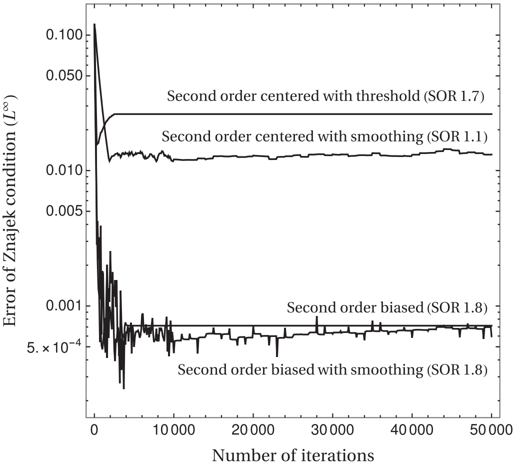

Figure 3. Same problem set-up and numerical methodologies as in Fig. (2) but here showing the evolution of the L^∞ norm of the deviation from the Znajek condition at the horizon. The second-order biased stencil provides both fast convergence and evolution towards a configuration fulfilling the Znajek condition.

matically satisfied in numerical procedures demanding smoothness at the LS (Komissarov 2004; Nathanail & Contopoulos 2014). Observing the behaviour of the L^∞ norm of the difference between the function $I(\Psi)$ and $I_Z(\Psi)$ for different stencils at $r = r_+$, we are able to confirm the status of equation (21) as a regularity condition, which is automatically fulfiled throughout the numerically iterative procedure with the imposed regularity at the LS (see Fig. 3). As we can see from that figure, the reduction of the error in the preservation of the Znajek condition happens for all the matching strategies presented in Section 3.2. However, the error level in the preservation of such condition is some orders of magnitude smaller when employing a biased discretization of the second-order radial derivatives, regardless of the application of any smoothing procedure for Ψ at the LSs.

The initial error depends on the chosen spin factor a and becomes greater for BHs which are close to maximally rotating. The deviations between the numerical solution and the Znajek condition are dominated by the matching point between the BH horizon and the equator as well as close to the axis of rotation, where an approximation of Ψ becomes necessary (cf. Contopoulos et al. 2013).

4 NUMERICAL RESULTS

4.1 Split-monopole configurations

The first test for the numerical solution of the GSE is the split-monopole (cf. Ghosh 2000), which has also been discussed by many authors (e.g. Komissarov 2004; Contopoulos et al. 2013; Nathanail & Contopoulos 2014). In the limit of a slowly rotating BH, the split-monopole matches the flat spacetime solution of Michel (1973) at large radii, while at the same time it satisfies the so-called Znajek condition (equation 21) at the event horizon. Admittedly, this solution is unphysical since in astrophysical conditions the magnetic field threading the horizon of a BH is supported by the electric currents in an accretion disc (cf. Blandford & Znajek 1977; Komissarov 2004). Nevertheless, it is likely the simplest configuration that allows one to demonstrate the extraction of energy through the BZ mechanism.[1] The initial guess for the potential Ψ corresponds to a homogeneous solution of equation (11) in the case of $a = 0$ (also called the Schwarzschild monopole, e.g. Ghosh 2000):

$$\Psi_0\,(r, \theta) = 1 - \cos\theta, \tag{22}$$

where the maximum value of Ψ has been normalized to 1. In order to set the initial functional dependence of $\omega(\Psi)$ and $I(\Psi)$, we adopt the field line angular velocity as being half the BH angular velocity $\omega = \Omega_{\rm BH}/2$ (Blandford & Znajek 1977). For the currents we employ the analytical solution of the pulsar magnetosphere. More specifically, we set:

$$\omega_0\,(\Psi) = \qquad \tfrac{1}{2}\,\tfrac{a}{r_+^2+a^2} \tag{22}$$

$$I_0\,(\Psi) = -\frac{1}{2}\omega\,(\Psi)\,\Psi\,(2-\Psi)$$

for $\Psi_{\rm min} \le \Psi \le \Psi_{\rm max}$, where $\Psi_{\rm min} := 0$ and $\Psi_{\rm max} := 1$ are given by the potential on the (Dirichlet) boundaries at the axis of rotation ($\theta = 0$) and the equator ($\theta = \pi/2$), respectively (equation 22). As stated before, Newman boundary conditions are set up along the radial edges of the computational domain (i.e. at $r = r_+$ and at $r = r_{\rm max}$). Using equation (12), the corresponding initial magnetic fields are

$$B^r(r, \theta) = \tfrac{\sin\theta}{2\pi\sqrt{\gamma}}, \tag{23}$$

$$B^\theta(r, \theta) = 0, \tag{24}$$

$$B^\phi(r, \theta) = \tfrac{a}{4(r_+^2+a^2)}\sqrt{\tfrac{\Sigma}{A\Delta}}. \tag{25}$$

Fig. 4 shows the topology of the magnetic flux Ψ computed solving numerically the GSE until our convergence criterion (equation A1) is reached. We display the case of a nearly maximally rotating BH ($a_* = 0.9999$) in Fig. 4. The isocontours of Ψ pass smoothly through both LSs (displayed with thick blue lines). A comparison of solutions to the GSE for different spin parameters is shown in Fig. 5.

In all tests where ω and I are let to relax from their initial values, the error measures $\mathcal{R}_\Psi$ and $\mathcal{R}_{\rm LC}$ can be reduced substantially after a sufficiently large number of iterative steps. This demonstrates that our method is robust and converges to a smooth, numerically stable solution. For this to happen, a number of technical comments are crucial at this point. First, we find convergence to a smooth solution if we set a double convergence criterion both on $\mathcal{R}_\Psi$ and $\mathcal{R}_{\rm LC}$ (see Appendix A1). In contrast to Nathanail & Contopoulos (2014), if we restrict our solution procedure to relax the initial set-up for 3000–4000 iterations, one does not find a steady state solution. As shown in the bottom panels of fig. 1 of Nathanail & Contopoulos (2014), the solution displays kinks close to the ILS. Many more iterations are necessary to qualify the numerical solution as a ‘steady state’ (for details, see the Appendix).

4.2 Paraboloidal configurations

Collimated magnetospheres are an important ingredient of jet outflows from compact objects and may be found, e.g. in the parabolically shaped solutions to the GSE which have been studied by, e.g.

---

[1] Komissarov (2001) showed the action of the BZ mechanism for the first time in time-dependent, force-free numerical simulations on a static space–time.

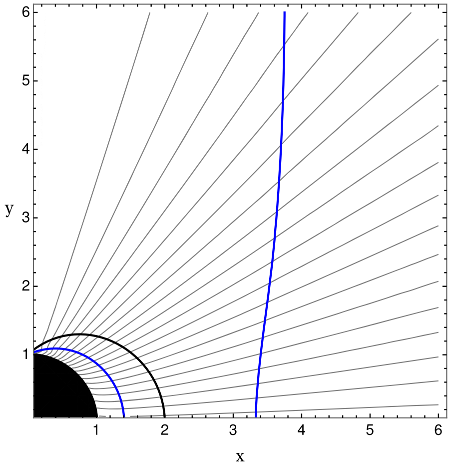

Figure 4. Distribution of the magnetic flux Ψ in the vicinity of a fast rotating ($a_* = 0.9999$) BH. In order to reach the configuration displayed, the GSE has been solved numerically until the convergence criterion (A1) has been reached in a physical domain $[r_+, \infty] \times [0, 90°]$, covered with a numerical grid $[n_r \times n_\theta] = [200 \times 64]$. The location of the ergosphere is represented by the black line, the two LS are drawn as blue lines. Magnetic flux configurations have been studied for various spin parameters, some of which are visualized in Appendix A1.

Fendt (1997) and Nathanail & Contopoulos (2014). Fendt (1997) considers an asymptotically cylindrical shape of the magnetic field and suggests to set up the outer radial boundary at $r_{\rm max}$ according to

$$\Psi_{\rm out}(x) = \frac{1}{b}\ln\left(1+\frac{x^2}{d^2}\right), \qquad (26)$$

where the constants d and b determine the degree of collimation and $x = r \times \sin\theta$. Fendt (1997) adapts his finite element computational domain to provide a parabolically shaped outer jet boundary. Indeed, we have considered setting up Fendt's boundaries at radial infinity, resulting into a final solution which resembles that of a split-monopole (i.e. effectively unconfined). Bringing condition (26) to a finite distance, solutions with a degree of confinement larger than the split-monopole case are possible. For instance, in Fig. 6 (upper panel), we show the solution for Ψ when setting the Dirichlet boundary condition (26) at $r_{\rm max} = 100$ for values of the confinement parameters $b = 9.2$, $d = 1.0$.

The numerical relaxation proceeds without obstacles and ultimately yields solutions, which show higher confinement at the OLS (comparing to the split-monopole solutions in Section 4.1). It should be noted, that an appropriate choice of boundary conditions at $r_{\rm max}$ is crucial for the relaxation towards a paraboloidal set-up. Using a parabolic topology as initial guess but with Newman boundary conditions (zero derivative) at $r_{\rm max}$ and no further induced confinement will result in a split-monopole solution.

However, setting Fendt's condition at finite distance is artificial and difficult to justify in astrophysical BH magnetospheres. As an alternative, Nathanail & Contopoulos (2014)[2] suggest to solve the GSE for a confined parabolic set-up limiting the computational

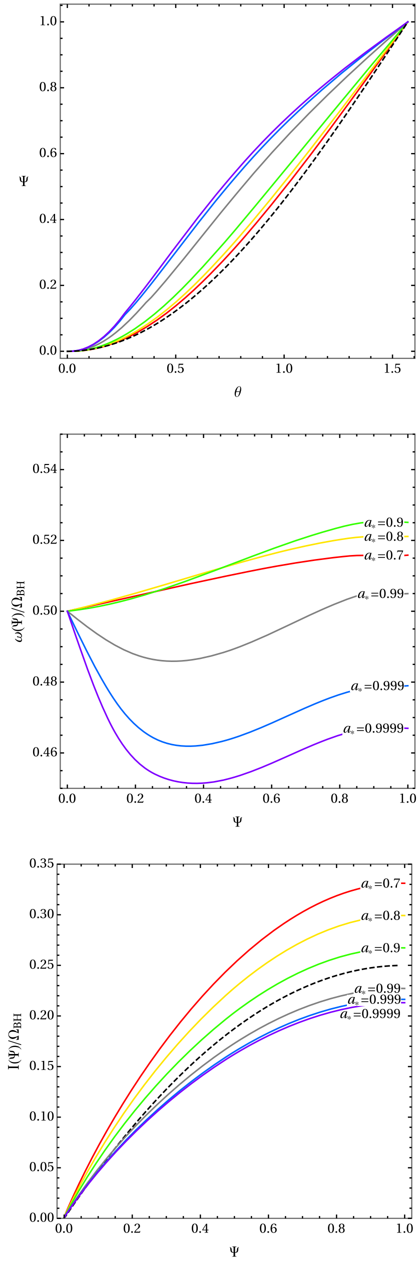

Figure 5. Comparison of split-monopole solutions to the GSE for different spin parameters $a_* = \{0.7, 0.8, 0.9, 0.99, 0.999, 0.9999\}$ in a physical domain $[r_+, \infty] \times [0, 90°]$, covered with a numerical grid $[n_r \times n_\theta] = [200 \times 64]$. *Top:* Angular distribution of the magnetic flux at the location of the inner light surface. The dashed line represents the initial values of the potential Ψ_0. *Middle:* Distribution of $\omega(\Psi)$ after convergence. *Bottom:* Distribution of $I(\Psi)$ after convergence.

---

[2] See also Tchekhovskoy et al. (2010) for an equivalent set-up in FFDE and GRMHD.

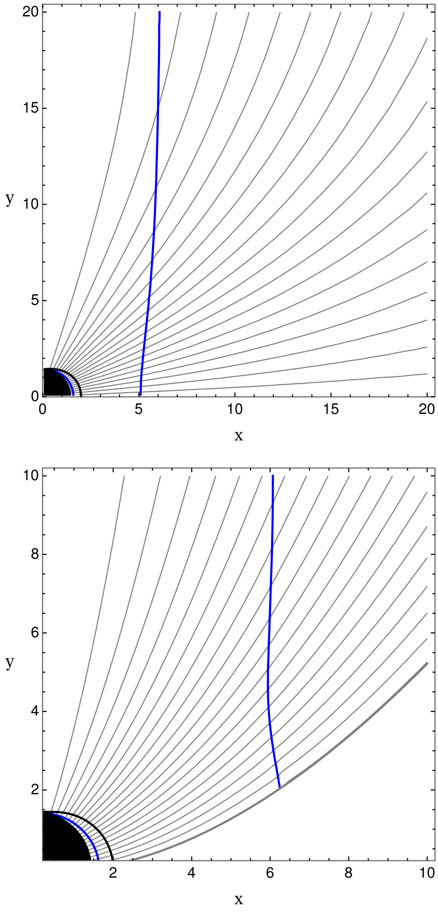

Figure 6. Distribution of the magnetic flux Ψ in the vicinity of a fast rotating $a_* = 0.9$ BH employing appropriate boundary conditions for paraboloidal confinement (cf. Section 4.2) in a physical domain $[r_+, 100] \times [0, 90°]$, covered with a numerical grid $[n_r \times n_\theta] = [200 \times 64]$. *Top:* Far boundary according to Fendt (1997). *Bottom:* Paraboloidal confinement following the Nathanail & Contopoulos (2014) set-up ($r_0 = 10$).

domain to a region $0 \leq \Theta \leq 1$, where

$$\Theta\,(r, \theta) = \frac{\theta}{\theta_{\rm wall}\,(r)} \tag{26}$$

and $\theta_{\rm wall}(r)$ describes a paraboloidal wall according to the function

$$1 - \cos\theta_{\rm wall} = \left(\frac{r + r_0}{r_+ + r_0}\right)^{-\nu}. \tag{27}$$

Here, r_0 and ν are parameters determining the degree of confinement of the parabolic boundary wall, e.g. a choice of $r_0 = \infty$ or $\nu = 0$ reduces to the split-monopole initial guess in equation (22). Employing $\Theta(r, \theta)$ to define the angular coordinate (cf. Nathanail & Contopoulos 2014) allows us to use the numerical solver as in previous examples without the need for *excising* regions of the computational domain in the vicinity of the equatorial plane in order to ensure the paraboloidal character of the solution. Employing the function

$$\theta\,(r, \Theta) = \Theta \times \theta_{\rm wall}\,(r)\,, \tag{27}$$

where $\Theta \in [0, 1]$, as well as the following coordinate changes in the angular derivatives [cf. equation (15) for the radial derivatives]

$$\begin{aligned} \frac{\partial}{\partial\theta} &= \frac{1}{\theta_{\rm wall}\,(r)}\frac{\partial}{\partial\Theta} \\ \frac{\partial^2}{\partial\theta^2} &= \left(\frac{1}{\theta_{\rm wall}\,(r)}\right)^2 \frac{\partial^2}{\partial\Theta^2}, \end{aligned} \tag{27}$$

no further changes to the update and LS routines are necessary. After setting up an initial guess for the potential according to (following Nathanail & Contopoulos 2014)

$$\Psi\,(r, \theta) = \Psi_{\rm max}\left(\frac{r + r_0}{r_+ + r_0}\right)^{\nu}(1 - \cos\theta)\,, \tag{28}$$

with $\Psi_{\rm max} = 1$ for simplicity, as well as $\omega(\Psi)$ and $II'(\Psi)$ like in Section 4.1, the numerical solution converges without obstacles. We observe, however, that with larger confinement (i.e. lower values of r_0), the kinks at the OLS become stronger, especially close to the equatorial plane. The growing artefacts may be reduced with lower relaxation factors in the SOR routines. The presented example (Fig. 6 bottom panel) shows the converged solution (demanding condition A1) for $\omega_{\rm SOR} = 1.0$ after 42.740 iterations. The solid lines in Fig. 7 display the distributions of $\omega(\Psi)$ and $I(\Psi)$ after convergence is reached employing the set-up of Nathanail & Contopoulos (2014). For comparison, we also display (with dashed lines) the final distributions of $\omega(\Psi)$ and $I(\Psi)$ employing the paraboloidal problem set-up of Fendt (1997). From the top panel of Fig. 7, it is evident that the latter set-up tends to produce solutions with faster rotating field lines, not only in the equatorial plane (corresponding to a value $\Psi = 1$), but at almost every other latitude in the domain ($\Psi = 0$ corresponds to the axis of symmetry).

4.3 Vertical field configurations

Another well-studied exemplary fieldline configuration is the embedding of a BH into a vertical magnetic field. Originally considered by Wald (1974) for the electrovacuum limit, it has since been studied in dynamical evolutions (see e.g. Komissarov 2004; Komissarov & McKinney 2007; Palenzuela et al. 2010) as well as with a focus on the BH 'Meissner effect' (Komissarov & McKinney 2007; Nathanail & Contopoulos 2014), or on the uniqueness of the numerical solutions (Pan, Yu & Huang 2017). The case of vertical fieldlines opens up the possibility of fieldlines crossing only the ILS (for a detailed discussion, see also Nathanail & Contopoulos 2014) and, hence, the freedom of fixing either $\omega(\Psi)$ or $I(\Psi)$ throughout the relaxation procedure (cf. Section 3.3).

We employ a Dirichlet boundary at $\theta = 0$, as we have done in Section 4.1. In order to fill up the initial magnetic field configuration, we divide the computational domain into three regions. The first region is the spherical shell surrounding the BH and extending slightly beyond the ergosphere defined by

$$r > 1.25 \times r_+^*(\pi/2) \equiv r_0\,, \tag{28}$$

where we employ the split-monopole potential Ψ_0 (equation 22). The second region extends beyond the previous spherical shell up to infinity in the vertical direction, i.e. enclosing the region

$$r_0 \leq r < r \times \sin\theta\,, \tag{28}$$

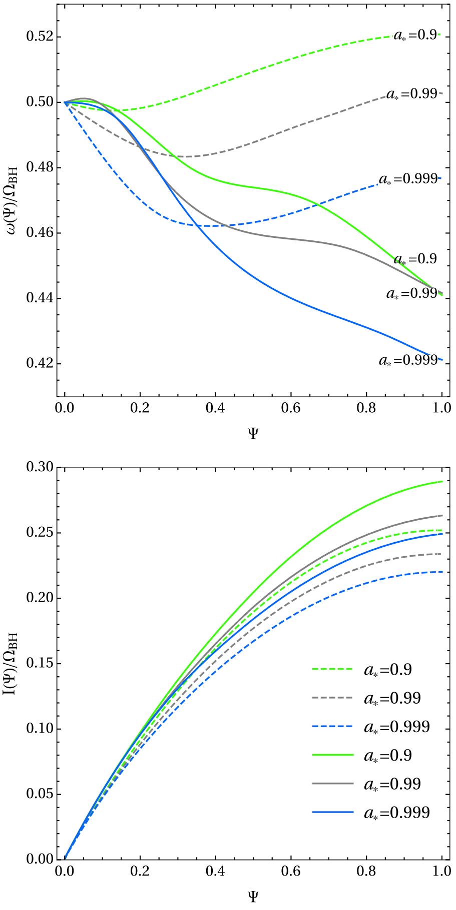

Figure 7. Final distributions (after convergence is reached) of the scalar functions $\omega(\Psi)$ (top panel) and $I(\Psi)$ (bottom panel) in the vicinity of fast rotating BHs of different spin parameters $a_* = \{0.9, 0.99, 0.999\}$ embedded in paraboloidal magnetic field magnetosphere (cf. Section 4.2). The physical domain $[r_+, 100] \times [0, 90^\circ]$ is covered with a numerical grid $[n_r \times n_\theta] = [200 \times 64]$. The relaxed solution of the Fendt (1997) approach is represented with dashed lines, the Nathanail & Contopoulos (2014) strategy by solid lines.

where the isolines of Ψ are vertical and their values correspond to

$$\Psi(r,\theta) = \Psi_0\left(r, \arcsin\left(\frac{r \times \sin\theta}{r_0}\right)\right) . \tag{28}$$

Finally, in the third region, defined by $r \times \sin\theta > r_0$, we use

$$\Psi\,(r,\theta) = \left(\frac{r \times \sin\theta}{r_0}\right)^2 . \tag{28}$$

We apply the following Dirichlet boundary condition at the equator:

$$\Psi\left(r, \theta = \frac{\pi}{2}\right) = \begin{cases} 1.0 & \text{if } r > r_0 \\ \left(\dfrac{r}{r_0}\right)^2 & \text{otherwise} \end{cases} \tag{28}$$

Newman boundary conditions are set up along the radial edges of the computational domain (i.e. at $r = r_+$ and at $r = r_{\max}$). Following Nathanail & Contopoulos (2014), we initiate the fieldline angular velocity to one of the two functions

$$\omega\,(\Psi) = \frac{\Omega_{\rm BH}}{2} \times (1-\Psi)^2 \tag{29}$$

$$\omega\,(\Psi) = \frac{\Omega_{\rm BH}}{2} \times \left(1 - \frac{\Psi}{2}\right), \tag{30}$$

for $\Psi_{\min} \leq \Psi \leq \Psi_{\max}$, where $\Psi_{\min} := 0$ and $\Psi_{\max} := 1$, and zero otherwise. This choice of $\omega(\Psi)$ pushes the OLS to infinity and allows us to update only the current function $I(\Psi)$ throughout the numerical relaxation. By the construction of the boundary conditions, equation (29) ensures that the ILS touches the outer ergosphere r_+^* at the equator, while equation (30) provides an ILS well inside the outer ergosphere r_+^*.

The initial values employed for the numerical algorithm and the equatorial boundary conditions slightly differ from those employed in Nathanail & Contopoulos (2014), but they provide smooth profiles of the ILS and no glitches in the field lines in the region enclosed in between of the ILS and the outer ergosphere (see the left and middle panels of Fig. 8). These results can be compared with the ones presented by Nathanail & Contopoulos (2014; fig. 3) or by Pan et al. (2017; fig. 1). The fact that the configurations we find are slightly different to those of the previous works is simply a consequence of the different boundary conditions employed, and not necessarily related to a lack of uniqueness of the GSE solution (see Pan et al. 2017 and Section 6 for a discussion of the uniqueness of the GSE solution for the vertical magnetic field configuration).

We have further explored the influence of the equatorial boundary conditions by setting up an approximately vertical magnetic field employing a paraboloidal set-up as discussed in Section 4.2, e.g. by using the parameters $r_0 = 0$ and $\nu = 2$ in equations (27) and (28). The relaxed solutions are as smooth as those obtained with the previous initialization for Ψ and the corresponding equatorial boundary conditions. In none of the two cases the Meissner effect is observed, in full agreement with the findings of e.g. Nathanail & Contopoulos (2014) or Pan & Yu (2016).

4.4 BH-disc models

Uzdensky (2005) suggests the set-up of a BH-disc system via a suitable choice of boundary conditions in the numerical solution of the GSE. In these configurations, field lines threading the BH horizon connect to the equatorial plane and rotate with Keplerian velocity. Following Uzdensky (2005), the boundary along the axis of rotation and the equatorial plane are set up as follows:

$$\begin{aligned} \Psi\,(\theta = 0) &= \Psi_{\rm s} \\ \Psi\left(r > r_{\rm in}, \theta = \frac{\pi}{2}\right) &= \Psi_{\rm d}\,(x) \\ \Psi\left(r \leq r_{\rm in}, \theta = \frac{\pi}{2}\right) &= \Psi_{\max}. \end{aligned} \tag{30}$$

Here, $r_{\rm in} = r_{\rm ISCO}(a)$ is the radial location of the innermost circular orbit as a function of a. $\Psi_{\rm s}$ fixes the value of the separatrix between open field lines and field lines linking the BH to the disc. Their potential is connected to the disc radius by

$$\Psi_{\rm d}\,(r) = \Psi_{\max}\left(\frac{r_{\rm in}}{r}\right). \tag{30}$$

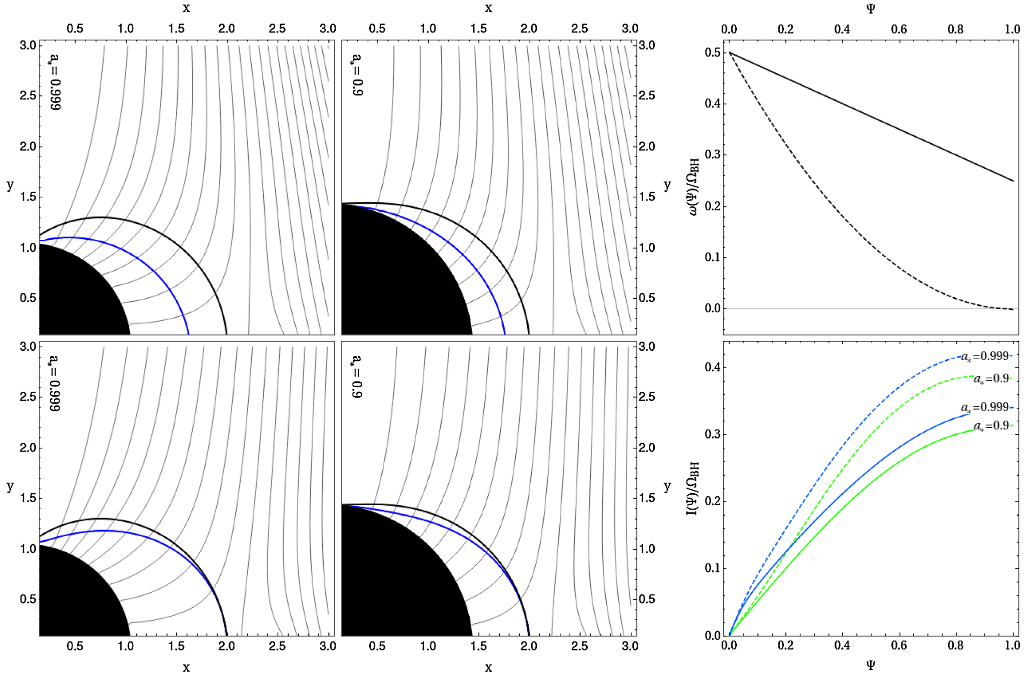

Figure 8. Distribution of Ψ (left and central columns), of $\omega(\Psi)$ (top right panel) and of $I(\Psi)$ (bottom right panel) in the vicinity of fast rotating BHs of different spin parameters $a_* = \{0.9, 0.999\}$ embedded in a vertical magnetic field (cf. Section 4.3). The physical domain $[r_+, 100] \times [0, 90^\circ]$ is covered with a numerical grid $[n_r \times n_\theta] = [200 \times 200]$. In the top right panel, we depict the (fixed) fieldline profiles of $\omega(\Psi)$ given by equation (30) (*solid line*) and equation (29) (*dashed line*). The upper left and middle panels show the spatial distribution of Ψ corresponding to the imposed profile of $\omega(\Psi)$ given by equation (30). The bottom left and middle panels show the spatial distribution of Ψ corresponding to $\omega(\Psi)$ given by equation (29). The relaxed values of $I(\Psi)$ corresponding to the two (fixed) distributions of $\omega(\Psi)$ are shown on the bottom right panel (using the same line styles as in the upper right panel).

Homogeneous Neumann boundary conditions are set at the outer event horizon,

$$\Psi_{,r}\,(r = r_+) = 0. \qquad (30)$$

We find that it is necessary to fix the boundary at $r_{\max}$ to a predefined shape function similar to the paraboloidal case presented in Section 4.2:

$$\Psi\,(r = r_{\max}) = \Psi_s + [\Psi_d\,(r) - \Psi_s]\,(1 - \cos\theta)\,. \qquad (30)$$

As for the field line angular velocity ω, it is assumed that the field lines connected to the BH rotate with the Keplerian angular velocity Ω_K of the disc,

$$\Omega_K\,(r) = \frac{\sqrt{M}}{r^{3/2} + a\sqrt{M}}, \qquad (30)$$

and do not rotate for $\Psi < \Psi_s$, namely,

$$\omega\,(\Psi) = \begin{cases} 0 & \text{if } \Psi > \Psi_s \\ \Omega_K\,[r_0\,(\Psi)]\tanh^2\left(5\dfrac{\Psi - \Psi_s}{\Psi_{tot} - \Psi_s}\right) & \text{otherwise} \end{cases} \qquad (30)$$

where r_0 represents the footpoint of a given field line with potential Ψ on the disc.

Following Uzdensky (2005), we use a grid of $[n_r \times n_\theta] = [200 \times 200]$ numerical nodes. However, relatively small values of a let the ILS approach the outer BH event horizon r_+, rendering insufficient the previous radial grid resolution (see the LS position in the mid-panel of Fig. 9). Therefore, we choose to adapt the radial coordinate for the discretization to the function $R_{\min} = r_+/(r_+ + 10M)$, and refine the grid increasing by a factor of 20 the number of nodes in the radial direction whenever we update the potential functions $I(\Psi)$ and $\omega(\Psi)$, e.g. we employ $[n_r \times n_\theta] = [4000 \times 200]$ for $a_* = 0.5$ in order to ensure sufficient data points around the ILS. As $I(\Psi) = 0$ and $\omega(\Psi) = 0$ for $\Psi < \Psi_s$, the OLS is pushed to infinity and the magnetosphere is current-free along the open field lines. The numerical relaxation proceeds smoothly towards a converged equilibrium solution (see Fig. 9), which closely matches that found by Uzdensky (2005).

5 POWER OF THE BZ PROCESS

The question of whether relativistic jets can be formed extracting the reducible energy of a rotating BH has been recurrently investigated in the last decades, both in the context of AGN jets (e.g. McKinney 2005; Hawley & Krolik 2006; Reynolds, Garofalo & Begelman 2006; Komissarov & McKinney 2007; Garofalo 2009; Palenzuela et al. 2011), and in the context of gamma-ray bursts (e.g. Komissarov & Barkov 2009; Nagataki 2009; Tchekhovskoy & Giannios 2015; Nathanail, Strantzalis & Contopoulos 2016). In this section, we employ the obtained solutions of the GSE in the split-monopole

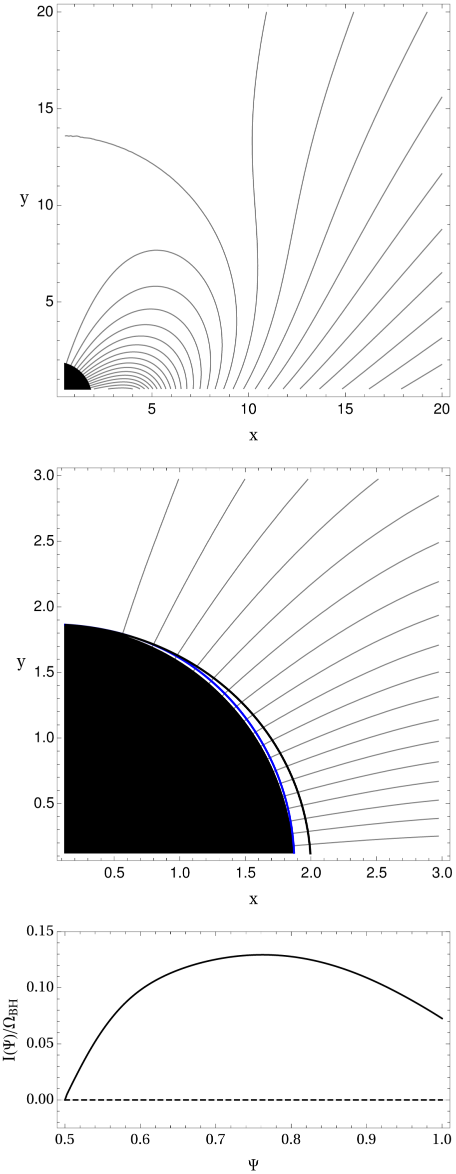

Figure 9. BH-disc model following the set-up by Uzdensky (2005) after the relaxation procedure ($a_* = 0.5$, $[r_+, 100] \times [0, 90°]$, $[n_r \times n_\theta] = [200 \times 200]$). The fieldlines connecting the BH to the disc rotate with Keplerian velocity. The open fieldlines are free of rotation and current. *Top/Middle:* Global structure and zoom of the inner region showing in detail the location of the ILS (blue line) in between the ergosphere (thick black line) and the outer event horizon. *Bottom:* Distribution of $I(\Psi)$ after convergence. The dashed line represents the initial configuration $I_0(\Psi) = 0$.

magnetic field configuration to provide some analytic estimates of the total BZ power, as well as its distribution with latitude.

We compute the total BZ power (cf. also, Thorne et al. 1986; Lee, Wijers & Brown 2000; McKinney & Gammie 2004; Uzdensky 2004; Tanabe & Nagataki 2008; Tchekhovskoy, Narayan & McKinney 2010; Penna, Narayan & Sądowski 2013) using equation (4.5) in Blandford & Znajek (1977)

$$S^r(\theta) = \epsilon_0 \omega \left(\Omega_{\rm BH} - \omega\right) \left(\frac{\Psi_{,\theta}}{r_+^2 + a^2 \cos^2\theta}\right)^2 \left(r_+^2 + a^2\right), \qquad (31)$$

where S^r is the radial energy flow. Then, employing equation (4.11) of Blandford & Znajek (1977), we obtain the total power outflow across the event horizon by integration of equation (31):

$$\begin{aligned} P_{\rm tot} &= \int_0^{2\pi} {\rm d}\phi \int_0^{\pi} {\rm d}\theta\, S^r(\theta)\, \Sigma \sin\theta \\ &= \frac{4\pi\epsilon_0 a}{\Omega_{\rm BH}} \int_0^{\pi/2} {\rm d}\theta\, \omega\left(\Omega_{\rm BH} - \omega\right) \frac{\sin\theta}{r_+^2 + a^2\cos^2\theta} \left[\Psi_{,\theta}\right]^2, \qquad (32) \end{aligned}$$

where we have used the relations defined in equation (3). The radial magnetic field component, $B^{\hat{r}} \equiv B_H$, in the local tetrad base of the ZAMO (see e.g. Lee et al. 2000; Komissarov 2009) may be defined as

$$\Psi_{,\theta} = \sqrt{g_{\theta\theta}}\sqrt{g_{\phi\phi}}\, B^{\hat{r}} = \sqrt{A} \sin\theta\, B^{\hat{r}}. \qquad (32)$$

At the event horizon ($\Delta = 0$), this expression reduces to

$$\Psi_{,\theta} = \left(r_+^2 + a^2\right) \sin\theta\, B^{\hat{r}}. \qquad (33)$$

Following the ideas sketched in Lee et al. (2000) to obtain an approximate expression for the BZ power, we assume that the ideal fieldline angular velocity (Blandford & Znajek 1977) is constant, $\omega \simeq \Omega_{\rm BH}/2$,[3] which in combination with equation (33) and $\epsilon_0 = 1/(4\pi)$ yields

$$P_{\rm tot} \simeq \frac{1}{4} a_*^2 M^2 \left[1 + \left(\frac{r_+}{a}\right)^2\right] \int_0^{\pi/2} {\rm d}\theta\, \frac{\sin^3\theta}{\frac{r_+^2}{a^2} + \cos^2\theta} B_H^2, \qquad (34)$$

or, if we want to express the results in CGS units, we have

$$\begin{aligned} P_{\rm tot}^{\rm cgs} \simeq 1.34 \times 10^{51} {\rm erg\,s^{-1}} \times a_*^2 \left(\frac{M}{{\rm M}_\odot}\right)^2 \left(\frac{B_{\rm cgs}}{10^{15}{\rm G}}\right)^2 \times \\ \left[1 + \left(\frac{r_+}{a}\right)^2\right] \int_0^{\pi/2} {\rm d}\theta\, \frac{\sin^3\theta}{\frac{r_+^2}{a^2} + \cos^2\theta} \left(\frac{B_H}{B_{\rm cgs}}\right)^2, \end{aligned}$$

where the magnetic field at the horizon is normalized to some reference value $B_{\rm cgs}$. In the following, we will compare different methods in order to evaluate the integral

$$\tilde{P}\,(a) \equiv \int_0^{\pi/2} {\rm d}\theta\, \frac{\sin^3\theta}{\frac{r_+^2}{a^2} + \cos^2\theta} B_H^2 \qquad (36)$$

in expression (34). In order to approximate B_H, we proceed as follows. The obtained numerical results of the split-monopole magnetosphere for different spin parameters, $a_* \geq 0.7$ (see Section 4.1, especially Fig. 5) suggest that there exists a smooth dependence of $\Psi(r_+, \theta)$ on the polar angle and a. For small values of a, this is certainly the case (Blandford & Znajek 1977; MacDonald 1984; McKinney & Gammie 2004). We have found the following fit function approximating the angular dependence of the final and relaxed

---

[3] This result was confirmed also numerically by Komissarov (2001); but see Pan & Yu (2015).

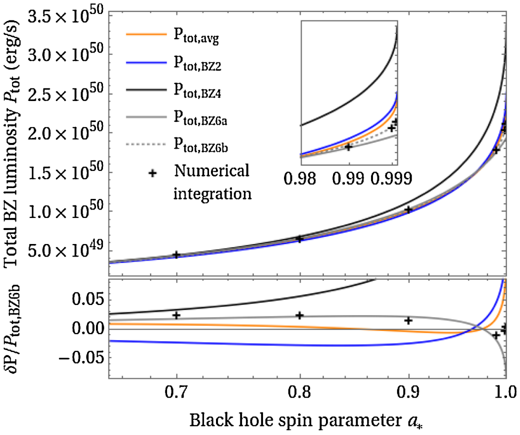

Figure 10. Comparison of the power of split-monopole solutions to the GSE in a physical domain $[r_+, \infty] \times [0, 90^\circ]$, covered with a numerical grid $[n_r \times n_\theta] = [200 \times 64]$. The figure shows the total process power derived for different BH spin parameters of a $1\mathrm{M}_\odot$ BH computed using the direct numerical evaluation of equation (32) (black crosses), the approximated value of Lee et al. (equation 34; orange line), as well as the second-order (blue line) and sixth-order (grey line) approximations of the BZ power as suggested by Tchekhovskoy et al. (2010). The sixth-order approximation (equation 46) fitted to the numerical data (following equation 35) is denoted by the dotted line. The extremal spin segment is magnified within the plot.

potential, as obtained from the solution of the GSE along the inner radial boundary (outer event horizon) for moderate to maximal values of a_*:

$$\begin{aligned}\Psi_f(r_+,\theta) &\approx \Psi_0(r_+,\theta) + c_1 \times f(a_*)^{c_2} \times \sin(c_3\theta) \times \theta^{c_4}\\ c_1 &= 0.29,\ \ c_2 = 2.46,\ \ c_3 = 2.03,\ \ c_4 = 0.38,\\ f(a_*) &= \frac{a_*}{1+\sqrt{1-a_*}^2} = 2M\Omega_{\mathrm{BH}}. \end{aligned} \tag{37}$$

The fit function reproduces the final values of Ψ computed with the GSE with an accuracy of $|\Psi_f(r_+, \theta) - \Psi(r_+, \theta)| < 0.02$. B_H may be approximated by using the relation defined in equation (33):

$$B_H(r_+,\theta) = \frac{1}{r_+^2+a^2}\frac{1}{\sin\theta}\frac{\partial\Psi_f(r_+,\theta)}{\partial\theta} \tag{38}$$

For several values of a, we have integrated numerically equation (34) using the numerical solution of the GSE for $B_H(r_+, \theta)$. The results are plotted in Fig. 10 (black crosses).

Building upon Lee et al. (2000), we employ equation (37) to estimate $\langle\Psi_{,\theta}^2\rangle$ at the outer event horizon, finding

$$\begin{aligned}\langle\left[\Psi_{,\theta}\right]^2\rangle &= \int_0^{\frac{\pi}{2}} \mathrm{d}\theta \sin\theta \left[\Psi_{,\theta}\right]^2\\ &= \frac{2}{3} - 0.43 f(a_*)^{2.46} + 0.18 f(a_*)^{4.92}. \end{aligned} \tag{39}$$

The integrand in equation (36) may then be approximated as follows:

$$\begin{aligned}\tilde{P}(a) &\approx \frac{\langle\left[\Psi_{,\theta}\right]^2\rangle}{\left[r_+^2+a^2\right]^2}\int_0^{\pi/2}\mathrm{d}\theta \frac{\sin\theta}{\frac{r_+^2}{a^2}+\cos^2\theta}\\ &= \frac{\langle\left[\Psi_{,\theta}\right]^2\rangle}{\left[r_+^2+a^2\right]^2}\frac{a}{r_+}\arctan\frac{a}{r_+}. \end{aligned} \tag{40}$$

Inserting the latter expression into equation (34), we obtain a total power for the BZ process

$$P_{\mathrm{tot}} \simeq \frac{1}{4}\frac{\langle\left[\Psi_{,\theta}\right]^2\rangle}{\left[r_+^2+a^2\right]}\frac{a}{r_+}\arctan\frac{a}{r_+}\ , , \tag{41}$$

or, equivalently,

$$P_{\mathrm{tot}} \simeq \frac{\epsilon_0\pi}{2}\langle\left[\Psi_{,\theta}\right]^2\rangle\Omega_{\mathrm{BH}}M(1+4M^2\Omega_{\mathrm{BH}}^2)\arctan(2\Omega_{\mathrm{BH}}M)\ , , \tag{42}$$

which, expanding in series of Ω_{BH} and retaining terms up to second order, yields

$$P_{\mathrm{tot},2} \simeq \epsilon_0\frac{2\pi}{3}M^2\Omega_{\mathrm{BH}}^2. \tag{43}$$

In their study of the spin dependence of the power of the BZ process, Tchekhovskoy et al. (2010) introduce expansions of the cumulative power (i.e. the angular power density integrated up to a certain angle θ_j instead of up to $\pi/2$ as in equation 32) in terms of Ω_{BH}. The resulting second-, fourth-, and sixth-order accurate expressions of the total power (i.e. the cumulative power up to $\theta_j = \pi/2$) are in our notation and units[4]

$$P_{\mathrm{tot,BZ2}} = \epsilon_0\frac{2\pi}{3}M^2\Omega_{\mathrm{BH}}^2\Psi_{\mathrm{tot}}^2\ , , \tag{44}$$

$$P_{\mathrm{tot,BZ4}} = \epsilon_0\frac{2\pi}{3}\left[M^2\Omega_{\mathrm{BH}}^2 + b_1M^4\Omega_{\mathrm{BH}}^4\right]\Psi_{\mathrm{tot}}^2\ , , \tag{45}$$

$$P_{\mathrm{tot,BZ6}} = \epsilon_0\frac{2\pi}{3}\left[M^2\Omega_{\mathrm{BH}}^2 + b_1M^4\Omega_{\mathrm{BH}}^4 + b_2M^6\Omega_{\mathrm{BH}}^6\right]\Psi_{\mathrm{tot}}^2\ , , \tag{46}$$

where Ψ_{tot} corresponds to the total flux between $\theta = 0$ and $\theta = \pi/2$, i.e. $\Psi_{\mathrm{tot}} = 1.0$. We note that the second-order accurate expression of this work (equation 43) and of Tchekhovskoy et al. (2010), equation (44), are identical. The coefficient of the term proportional to Ω_{BH}^4, $b_1 = 8(67 - 6\pi^2)/45 \simeq 1.38$, is computed analytically. For the sixth-order accurate expression in equation (46), Tchekhovskoy et al. (2010) obtain $b_2 = -9.2$ from a least-squares fit to their full analytic formulae.[5] As an alternative to the coefficients employed in Tchekhovskoy et al. (2010), we may compute the coefficients employed in equation (46) according to our specific numerical solution derived with the chosen fit function (equation 37). The resulting coefficients are then $b_1 = 0.81$ and $b_2 = -5.62$. For brevity, we refer to this parameter set as BZ6b hereafter. We shall point out that the expression (equation 46) is, indeed, not formally sixth-order accurate. It neglects the (typically small) corrections introduced by approximating the fieldline angular velocity as $\omega \simeq \Omega_{\mathrm{BH}}/2$. An expansion of ω accurate up to $O(\Omega_{\mathrm{BH}}^6)$ can be found in Pan & Yu (2015).

We compare the approximations obtained by Tchekhovskoy et al. (2010) to ours in Fig. 10. We find that the approximation as suggested by Lee et al. (2000) is equally good or comparable to the suggested sixth-order approximation (equation 46) up to spin parameters of $a_* \leq 0.98$, and more accurate than the second- and fourth-order formulae (equations 44 and 45, respectively) for the entire range of a_*. For extremal spins above this threshold, equation (46) yields very accurate estimates. However, using our fit parameters in the sixth-order approximation of equation (46), we obtain even more accurate results as compared to the remaining numerical models.

The global accuracy of the results is assessed in Table 1. The

---

[4] Tchekhovskoy et al. (2010) employ units in which $\epsilon_0 = 1$.

[5] We note that Pan & Yu (2015) obtain the same value of b_1 as Tchekhovskoy et al. (2010), but $b_2 = -11.09$.

Table 1. RMS error of the different approximations computed for the total BZ power presented in Fig. 10. The results are normalized to the RMS of the sixth-order approximation computed using equation (46) and the fit parameters $b_1 = 0.81$ and $b_2 = -5.61$ (BZ6b).

Approximation	$P_{\mathrm{tot,\,avg}}$	$P_{\mathrm{tot,\,BZ2}}$	$P_{\mathrm{tot,\,BZ4}}$	$P_{\mathrm{tot,\,BZ6a}}$
RMS error	9.23	13.21	50.49	7.19

table shows the root mean square (RMS) deviations of the different approximations employed to compute the total BZ power, i.e.

$$E = \left(\sum_i (P_{\mathrm{GSE},i} - P_i)^2\right)^{1/2}, \tag{47}$$

where $P_{\mathrm{GSE},\,i}$ and P_i represent, respectively, the power computed numerically from the solution of the GSE and the estimation of the total BZ power obtained with equations (34), (44), (45), or (46) using the original parameters of Tchekhovskoy et al. (2010) or our own parameters (BZ6b). In order to facilitate the comparison, all the RMS errors are normalized to the RMS deviations of the model BZ6b. The relatively simple approximation of equation (34) displays a RMS error which is $\lesssim 30$ per cent larger than the original sixth-order approximation to estimate the BZ total power (equation 46). We observe that the sixth-order approximation (equation 45) deviates more from the data than even the second-order estimate (equation 44) or the BZ total power estimation using our equation (34). This is not surprising, since it was also anticipated in Tchekhovskoy et al. (2010).

If the power of the BZ process drives a collimated relativistic outflow from the neighbourhood of the BH, a distant observer may only see a small angular patch of the whole outflow due to relativistic beaming. Thus, following a common practice for the approximate estimation of the angular energy distribution in GRB ejecta (e.g. Janka et al. 2006; Mizuta & Aloy 2009; Lazzati, Morsony & Begelman 2009) that avoids performing a complete (and much more involved) radiation transport problem (Broderick & Blandford 2003; Miller et al. 2003; Birkl et al. 2007; Cuesta-Martínez, Aloy & Mimica 2015), it is useful to define an equivalent isotropic power $P_{\mathrm{iso}}(\theta)$ in each (narrow) angular region $\Delta\theta = \theta^+ – \theta^-$ centred around θ [i.e. $\theta = (\theta^+ – \theta^-)/2$] as

$$P_{\mathrm{iso}}(\theta) = \frac{4\pi\epsilon_0}{\cos\theta^- - \cos\theta^+}\frac{a}{\Omega_{\mathrm{BH}}} \times \int_{\theta^-}^{\theta^+} \mathrm{d}\theta\, \omega\,(\Omega_{\mathrm{BH}} - \omega)\,\frac{\sin\theta}{r_+^2 + a^2\cos^2\theta}\,\left[\Psi_{,\theta}\right]^2. \tag{48}$$

This integral may be further simplified by using equation (39) to replace $[\Psi_{,\theta}]^2$ by its angular average. The remaining integral is the same as in equation (40) and can be solved analytically yielding

$$P^{(1)}_{\mathrm{iso}}(\theta) = \frac{2\pi\epsilon_0}{\cos\theta^- - \cos\theta^+}\frac{\Omega_{\mathrm{BH}}}{r_+^2 + a^2}\left[\Psi_{,\theta}\right]^2 \times \left\{\arctan\left(\frac{a}{r_+}\cos\theta^-\right) - \arctan\left(\frac{a}{r_+}\cos\theta^+\right)\right\}. \tag{49}$$

Alternatively, equation (48) can be computed using the midpoint approximation and plugging in for $\Psi_{,\theta}$ the angular derivative of $\Psi_{\mathrm{f}}(r_+, \theta)$ as given in equation (37). The angular dependence of the isotropic power then reduces to

$$P^{(2)}_{\mathrm{iso}}(\theta) = \frac{\pi\epsilon_0\Delta\theta}{\cos\theta^+ - \cos\theta^-}a\Omega_{\mathrm{BH}}\frac{\sin\theta}{r_+^2 + a^2\cos^2\theta}\left[\Psi_{,\theta}\right]^2. \tag{50}$$

Fig. 11 shows the isotropic power employing equation (49) plotted for intervals of $\Delta\theta = \left|\theta^+ - \theta^-\right| = \pi/200$, as well as the angular approximation given in equation (50). For comparison, we also plot the isotropic equivalent power distribution following the fourth- and sixth-order approximations of Tchekhovskoy et al. (2010). Precisely, we show

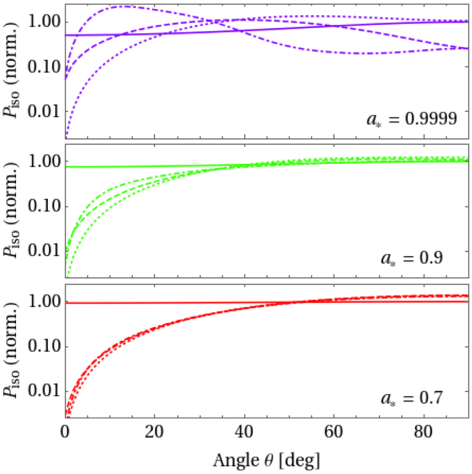

Figure 11. Isotropic power (equation 48) for different spin parameters $a_* = \{0.7, 0.9, 0.9999\}$. The solid lines refer to the approximated analytic integration of equation (49) plotted for intervals of $\left|\theta^+ - \theta^-\right| = \pi/200$. The dashed lines show the direct integration of equation (48) using the mid-point rule (i.e. using equation 50). The dotted and dot–dashed lines represent the angular power derivation following the fourth- and sixth-order approximations given by equations (51) and (52), respectively. All lines are normalized to the maximum value of the isotropic power provided by equation (49) in the interval $[0, \pi/2]$.

$$P_{\mathrm{iso,BZ4}}(\theta) = \tfrac{2}{\cos\theta^+ - \cos\theta^-}\left(P^{\mathrm{cum}}_{\mathrm{BZ4}}(\theta^+) - P^{\mathrm{cum}}_{\mathrm{BZ4}}(\theta^-)\right),, \tag{51}$$

and

$$P_{\mathrm{iso,BZ6}}(\theta) = \tfrac{2\Delta\theta}{\cos\theta^+ - \cos\theta^-}\tfrac{dP_{\mathrm{BZ6}}}{d\theta}(\theta),, \tag{52}$$

where the fourth-order accurate expression of the cumulative power as a function of the angle is (cf. Tchekhovskoy et al. 2010, equation B6)

$$\begin{aligned} P^{\mathrm{cum}}_{\mathrm{BZ4}}(\theta) = \frac{1}{270}\pi\Omega^4_{\mathrm{BH}}\Big(& 90\left(3\pi^2 - 32\right)\cos(\theta) + \\ & 5\left(194 - 21\pi^2\right)\cos(3\theta) + \\ & 9\left(3\pi^2 - 26\right)\cos(5\theta) + \\ & 32\left(67 - 6\pi^2\right)\Big) + \\ \frac{1}{3}\pi\Omega^2_{\mathrm{BH}}\Big(& 4\sin^4\left(\frac{\theta}{2}\right)(\cos(\theta) + 2)\Big) \end{aligned} \tag{53}$$

and the differential power per unit angle is given by

$$\frac{\mathrm{d}P_{\mathrm{BZ6}}}{\mathrm{d}\theta}(\theta) = \pi a\Omega_{\mathrm{BH}}\tfrac{\sin\theta}{r_+^2 + a^2\cos^2\theta}\quad \Psi^{(6)}_{,\theta}\quad{}^2, \tag{53}$$

with $\Psi^{(6)}_{,\theta}$ the angular derivative of the sixth-order accurate approximation for the magnetic flux (cf. Tchekhovskoy et al. 2010, equations C1 and C2)

$$\Psi^{(6)} = \Psi_0(r_+,\theta) + 16\Omega_{\rm BH}^2 \tfrac{8(67-6\pi^2)}{45}\sin^2\theta\cos\theta + \Omega_{\rm BH}^4\sin^2\theta\,\left(26.12\cos^{25}\theta + 22.72\cos^7\theta + 13.54\cos^3\theta + 2.08\cos\theta\right). \tag{53}$$

Looking at the central and bottom panels of Fig. 11, it is evident that estimating the isotropic equivalent power with the approximation leading to equation (49) is not optimal, especially for $\theta \lesssim 40^\circ$ and moderate to large values of a_*. This is not surprising, since the average performed to compute (equation 39) extends over the whole interval $\theta \in [0, \pi/2]$, while the isotropic power is evaluated for a relatively small angular patch, with angular extension $\Delta\theta$. Our isotropic power estimate employing the mid-point rule (equation 50) yields much better results. It is closer to the sixth-order accurate estimation of equation (52) than the fourth-order accurate estimation of equation (51). However, it falls short to predict the isotropic power for $\theta \lesssim 25^\circ$ and almost maximal values of the BH spin ($a_* = 0.9999$). At small or moderate values of $a_* \lesssim 0.7$, the isotropic power estimations yield quantitatively similar results, regardless of the approximation employed to compute the angular distribution of the BZ power (with the notable exception of $P^{(1)}_{\rm iso}(\theta)$). The differences show up more clearly as the value of a_* grows. There is, however, a consistent trend in all cases: larger values of the BH spin parameter a_* show larger powers closer to the axis of rotation. Indeed, we observe a transition in the curves of $P_{\rm iso}$. For $a_* > 0.9$ the maximum value of $P_{\rm iso}$ shifts from $\theta = 90^\circ$ to lower latitudes. For nearly maximally rotating BHs, the maximum isotropic equivalent power happens for $\theta \simeq 10^\circ$. Regardless of the exact location of the maximum, Fig. 11 clearly shows that a distant observer would not see a maximum power for events seen ‘head-on’. Since the value of $P_{\rm iso}$ grows very steeply from zero, for events generated out of BHs with $a_* \gtrsim 0.9$, it is much more likely to observe luminous events when observing them at angles $\theta \gtrsim 10^\circ$.

6 DISCUSSION

Motivated by the study of relativistic outflows from spinning BHs (Blandford & Znajek 1977), magnetospheric force-free electrodynamics for static and axisymmetric spacetimes have become a matter of active research (e.g. Camenzind 2007; Beskin 2010). Appl & Camenzind (1993) found the first non-linear analytical solution for a cylindrically collimated, asymptotic flux distribution, in special relativity. Until now, most of these studies have been done in the context of *open field* configurations, primarily because of its relevance to the jet problem. However, complex magnetic field topologies encompassing closed fieldlines may also develop in the course of the dynamical evolution arising from the accreting BHs (Goodman & Uzdensky 2008; Parfrey, Spitkovsky & Beloborodov 2016). Indeed, it has been encountered in simulations of neutron star mergers (e.g. Rezzolla et al. 2011; Kiuchi et al. 2014), that the post merger BH magnetic fields are not necessarily of split-monopole or paraboloidal type. The exact topology of the magnetic field in the BH magnetosphere is of paramount importance to set the efficiency of energy extraction from the central compact object. This extraction of energy is supposed to be channeled out along the low-density funnel developed in the course of the merger around the rotational axis of the system. Especially in the low density funnel, field reversals have been encountered, possibly limiting the efficiency of outflow production.

Studying these phenomena requires accurate initial data for magnetospheric configurations and motivates us to build both transparent and versatile initial data solvers. In particular, it requires a proper characterization of the numerical methodology to solve the GSE.

The numerical method we propose splits into three basic blocks: (1) The finite difference solution of the GSE in each of the subdomains set by the LSs in the magnetosphere, (2) the matching of the solutions across the LSs to obtain regular functions, and (3) the build-up or update of the functional tables for $\omega(\Psi)$ and $II'(\Psi)$.

We have shown that the convergence of the presented numerical technique greatly depends on a suitable selection of finite difference discretization around the LS and, hence, the diagonal dominance of the coefficient matrix of the SOR solver. Numerical artefacts develop around the LS if the ‘smoothing-across-subdomains’ techniques are used (as in e.g. Nathanail & Contopoulos 2014; Pan et al. 2017). These artefacts slow down the convergence of the GSE solution significantly, and the quality of the results is limited (see Fig. 1). However, we find the choice of an inward/outward biased second-order discretization around and with respect to the LS to be the most efficient set-up to achieve fast convergence with convenient overrelaxation and no need for additional smoothing of the potential Ψ across the LS.

We have extended the strategy of employing equation (14) to relax the current $II'(\Psi)$ (Uzdensky 2004) also to the potential function ω. This allows us to use the error of the GSE at the LS (equation 11) as an additional measure of convergence for the presented numerical method. Despite the fact that we can also incorporate a local mesh refinement around the ILS, the method is, however, limited by the ability to fit sufficient grid cells between the BH horizon and the ILS. In the presented tests, we were able to ensure sufficient cells around the ILS for values as low as $a_* = 0.5$. Nevertheless, the numerical solution of the GSE for spin factors lower than $a_* = 0.7$ is perhaps unnecessary. As shown in Fig. 5, even for a BH spin as large as $a_* = 0.7$, the overall solution approached the initially guessed potential functions, which are the (exact) solutions of the case $a_* = 0$. Thus, we find that with our method it is possible to explore the region very close to the horizon for rotating BHs with $a_* \gtrsim 0.7$. Resolving this region, which is near the location of the zero space-charge, and which is expected to be the source of the pairs that will populate the BH magnetosphere (Globus & Levinson 2014), is very important for models of jet formation (as it is in pulsar magnetospheres; e.g. Belyaev & Parfrey 2016).

In the literature, the solutions found by the numerical relaxation of the GSE seem to evolve towards a unique solution as long as the boundary conditions, especially the thin-disc assumption, hold (Contopoulos et al. 2013; Nathanail & Contopoulos 2014). We have observed and discussed (see Section 3.3) the relaxation of both potential functions ω and I as a necessity for convergence under the criterion given in Appendix (A1). The relaxation of only one of these two functions may converge under the residual function $\mathcal{R}_\Psi$, but shows non-convergence under the (mathematical) measure $\mathcal{R}_{LC}$, employing the GSE at the location of its singular surfaces (equation 20). Hence, we cannot disprove the uniqueness of the solutions reproduced in Section 4.

Proving the uniqueness of the solution of the GSE, given a set of boundary conditions, is not an easy task. The customary way of demonstrating uniqueness is to find a maximum principle. If no maximum principle can be found multiple solutions may arise for a given set of boundary conditions. Such an example can be found in Akgün et al. (2018), where the authors solved the Newtonian GSE equations without rotation for the case of a neutron star with a twisted magnetosphere, in some cases finding numerically multiple solutions with identical boundary conditions. In some particular cases, uniqueness can be proven as in the case of current-free configurations (see e.g. Akgün et al. 2018) or for small twists (Bineau 1972). Regarding BH magnetospheres, Pan et al. (2017) have investigated the uniqueness of the solution of the GSE. These authors found that if the field lines cross smoothly the LSs (which is a 'constraint condition' the solutions must satisfy), the boundary conditions at the horizon and at infinity are not independent. Therefore, for a given pair of functions $\omega(\Psi)$ and $I(\Psi)$, the boundary conditions are uniquely defined. Although this does not completely prove the uniqueness of the solution for given boundary conditions, it is a significant step in this direction. However, for the asymptotically uniform field, there is a variety of possibilities regarding uniqueness. Time-dependent simulations (e.g. Komissarov 2005; Komissarov & McKinney 2007; Yang, Zhang & Lehner 2015) apparently converge to a unique solution. Several analytic studies find a unique perturbative solution that agrees with GRMHD simulations (Beskin & Zheltoukhov 2013; Pan & Yu 2015; Gralla, Lupsasca & Rodriguez 2016).

As a byproduct of the study of split-monopole magnetospheres, we have provided an approximation for the potential Ψ at the outer event horizon for different values of a (equation 37). In Section 5, we examined the angular resolution as well as the total value of the power outflow (cf. Lee et al. 2000; Uzdensky 2004) employing equation (37). For higher values of the BH spin parameter a, one especially finds a higher total power of the BZ process with more isotropic power provided closer to the axis of rotation and, hence, in the regions which are presumably critical for the production of BZ jets. Our estimations of the power of the BZ process using the fit formula (equation 34) deviate less than 1 per cent from the *exact* power computed numerically from the solutions of the GSE equations for the potential Ψ. Remarkably, this compares fairly well with the fourth order accurate expression of Tchekhovskoy et al. (2010) (their equation B6), since their formula requires more than a factor of 3 correction to reproduce their numerical results for high BH spin (namely, $a_* \gtrsim 0.95$), as the authors point out. Thus, our relatively simple estimate of the BZ power provides estimates quantitatively comparable to the sixth order accurate expression of Tchekhovskoy et al. (2010; their equation 9).

We also find that using our fit formula (equation 37) to compute the angular derivative of the flux (which is proportional to the radial component of the magnetic field evaluated at the BH horizon; equation 38) is an excellent approach to estimate the isotropic equivalent power as a function of the latitude. Our simple estimate is competitive with the sixth order accurate estimation of Tchekhovskoy et al. (2010) for BH spins $a_* \lesssim 0.98$. However, for nearly maximally rotating BH ($a_* \gtrsim 0.9999$), our isotropic equivalent power estimate falls short by factors $2-3$ with respect to the estimation employing a sixth order accurate formula. Remarkably, even for such large values of a_*, our mid-point approximation for the isotropic BZ luminosity (equation 50) is better than the fourth order accurate estimation of equation (51).

The stability of most of the stationary solutions found in this paper (and in the preceding literature in the field) has been assessed by means of time-dependent FFDE or GRMHD simulations (e.g. Komissarov 2002, 2004; Tchekhovskoy et al. 2010) with a fixed background metric (the one provided by the BH). However, the stability of the solutions in cases where the space–time may evolve due to the feedback between the BH and its magnetosphere has not been assessed so far. One application of the presented solving scheme will be the use of these configurations as initial data for time evolution simulations of *dynamical* space–times on the *Carpet* grid of the *Einstein Toolkit*. The discussed test cases are thought to be especially applicable in combination with recent methods to support rapidly rotating Kerr BHs in numerical simulations (Liu, Etienne & Shapiro 2009) and their numerically stable magnetohydrodynamic evolution (Faber et al. 2007). The current practice of evolving space-times without excising the BHs (for GRMHD simulations, cf. Faber et al. 2007) requires highly accurate initial data, especially at the BH apparent event horizons. The behaviour under time evolution of *dynamical* space–times (without excising BHs) with the respective time-dependent feedback on the electromagnetic force-free fields will be an indicator of the stability of the found solutions of the GSE and may foster further optimization of the proposed numerical procedure. The results of the application of this methodology will be the subject of our subsequent work.

ACKNOWLEDGEMENTS

We thank the referee, Prof. I. Contopoulos, for his constructive comments and criticism. We kindly acknowledge Amir Levinson for his careful reading and feedback on the draft of this paper. We acknowledge the support from the *European Research Council* (grant CAMAP-259276) and the partial support of grants AYA2015-66899-C2-1-P and PROMETEO-II-2014-069. JM acknowledges the *Grisolia* Grant GRISOLIAP/2016/097 and a PhD grant of the *Studienstiftung des Deutschen Volkes*. PC acknowledges the Ramon y Cajal program (RYC-2015-19074) supporting his research.

REFERENCES

Adsuara J. E., Cordero-Carrión I., Cerdá-Durán P., Aloy M. A., 2016, J. Comput. Phys., 321, 369
Akgün T., Cerdá-Durán P., Miralles J. A., Pons J. A., 2018, MNRAS, 474, 625
Appl S., Camenzind M., 1993, A&A, 274, 699
Belyaev M. A., Parfrey K., 2016, ApJ, 830, 119
Beskin V. S., 1997, Phys.–Usp., 40, 659
Beskin V. S., 2010, MHD Flows in Compact Astrophysical Objects. Springer, Berlin
Beskin V. S., Zheltoukhov A. A., 2013, Astron. Lett., 39, 215
Bineau M., 1972, Commun. Pure Appl. Math., 25, 77
Birkl R., Aloy M. A., Janka H.-T., Müller E., 2007, A&A, 463, 51
Blandford R. D., Znajek R. L., 1977, MNRAS, 179, 433
Broderick A., Blandford R., 2003, MNRAS, 342, 1280
Camenzind M., 1987, A&A, 184, 341
Camenzind M., 2007, Compact Objects in Astrophysics: White Dwarfs, Neutron Stars, and Black Holes, Springer, Berlin
Contopoulos I., Kazanas D., Fendt C., 1999, ApJ, 511, 351
Contopoulos I., Kazanas D., Papadopoulos D. B., 2013, ApJ, 765, 113
Cuesta-Martínez C., Aloy M. A., Mimica P., 2015, MNRAS, 446, 1716
Faber J. A., Baumgarte T. W., Etienne Z. B., Shapiro S. L., Taniguchi K., 2007, Phys. Rev. D, 76
Fendt C., 1997, A&A, 319, 1025
Garofalo D., 2009, ApJ, 699, 400
Ghosh P., 2000, MNRAS, 315, 89
Globus N., Levinson A., 2014, ApJ, 796, 26
Goodman J., Uzdensky D., 2008, ApJ, 688, 555
Grad H., Rubin H., 1958, Proceedings of the Second United Nations Conference on the Peaceful Uses of Atomic Energy, Geneva, 31, 190.
Gralla S. E., Lupsasca A., Rodriguez M. J., 2016, Phys. Rev. D, 93, 044038
Hawley J. F., Krolik J. H., 2006, ApJ, 641, 103
Janka H.-T., Aloy M.-A., Mazzali P. A., Pian E., 2006, ApJ, 645, 1305
Kiuchi K., Kyutoku K., Sekiguchi Y., Shibata M., Wada T., 2014, Phys. Rev. D, 90
Komissarov S. S., 2001, MNRAS, 326, L41
Komissarov S. S., 2002, MNRAS, 336, 759
Komissarov S. S., 2004, MNRAS, 350, 427
Komissarov S. S., 2005, MNRAS, 359, 801

Komissarov S. S., 2007, MNRAS, 382, 995
Komissarov S. S., 2009, J. Korean Phys. Soc., 54, 2503
Komissarov S. S., Barkov M. V., 2009, MNRAS, 397, 1153
Komissarov S. S., McKinney J. C., 2007, MNRAS, 377, L49
Lazzati D., Morsony B. J., Begelman M. C., 2009, ApJ, 700, L47
Lee H. K., Wijers R., Brown G., 2000, Phys. Rep., 325, 83
Leveque R. J., Li Z., 1994, SIAM J. Numer. Anal., 31, 1019
Liu Y. T., Etienne Z. B., Shapiro S. L., 2009, Phys. Rev. D, 80
Lüst R., Schlüter A., 1954, ZAp, 34, 263
MacDonald D. A., 1984, MNRAS, 211, 313
McKinney J. C., 2005, ApJ, 630, L5
McKinney J. C., Gammie C. F., 2004, ApJ, 611, 977
Michel F. C., 1973, ApJ, 180, L133
Miller W. A., George N. D., Kheyfets A., McGhee J. M., 2003, ApJ, 583, 833
Mizuta A., Aloy M. A., 2009, ApJ, 699, 1261
Nagataki S., 2009, ApJ, 704, 937
Nathanail A., Contopoulos I., 2014, ApJ, 788, 186
Nathanail A., Strantzalis A., Contopoulos I., 2016, MNRAS, 455, 4479
Palenzuela C., Garrett T., Lehner L., Liebling S. L., 2010, Phys. Rev. D, 82, 044045
Palenzuela C., Bona C., Lehner L., Reula O., 2011, Class. Quantum Gravity, 28, 134007
Pan Z., Yu C., 2015, ApJ, 812, 57
Pan Z., Yu C., 2016, ApJ, 816, 77
Pan Z., Yu C., Huang L., 2017, ApJ, 836, 193
Parfrey K., Spitkovsky A., Beloborodov A. M., 2016, ApJ, 822, 33
Penna R. F., Narayan R., Sądowski A., 2013, MNRAS, 436, 3741
Punsly B., 2001, Black Hole Gravitohydromagnetics. Springer, Berlin
Reynolds C. S., Garofalo D., Begelman M. C., 2006, ApJ, 651, 1023
Rezzolla L., Giacomazzo B., Baiotti L., Granot J., Kouveliotou C., Aloy M. A., 2011, ApJ, 732, L6
Ruderman M. A., Sutherland P. G., 1975, ApJ, 196, 51
Shafranov V., 1966, Rev. Plasma Phys., 2, 103
Tanabe K., Nagataki S., 2008, Phys. Rev. D, 78, 024004
Tchekhovskoy A., Giannios D., 2015, MNRAS, 447, 327
Tchekhovskoy A., Narayan R., McKinney J. C., 2010, ApJ, 711, 50
Thorne K. S., Price R. H., MacDonald D. A. 1986, Black Holes: The Membrane Paradigm. Yale University Press, New Haven, Connecticut
Uzdensky D. A., 2004, ApJ, 603, 652
Uzdensky D. A., 2005, ApJ, 620, 889
Wald R. M., 1974, Phys. Rev. D, 10, 1680
Weber E. J., Davis Leverett J., 1967, ApJ, 148, 217
Yang H., Zhang F., Lehner L., 2015, Phys. Rev. D, 91, 124055
Zhang X.-H., 1989, Phys. Rev. D, 39, 2933
Znajek R. L., 1977, MNRAS, 179, 457

APPENDIX: TECHNICAL NOTES

A1 Numerical convergence criteria

As shown in Figs 1 and 2, the L^∞ norm of the residual of the SOR scheme decreases rapidly for the applied biased stencil at the LSs. However, we find that a smooth solution for Ψ in the entire domain (cf. Section 2.1) requires an additional constraint imposed by the error $\mathcal{R}_{LC}$ at the LS. Kinks across an LS may remain present even though the solution converged under $\mathcal{R}_\Psi$. Furthermore, especially for non-extremal spin parameters a, we observe that both $\mathcal{R}_{LC}$ and $\mathcal{R}_\Psi$ are very small already in the first iterations of the solving routine. An exclusive focus on the residual $\mathcal{R}_\Psi$ may, hence, rapidly trigger a convergence decision without a full relaxation of ω and II'. In these cases, kinks remain across the LS. For the shown tests, we demand the simultaneous fulfilment of the following conditions as a convergence criterion:

$$\mathcal{R}_\Psi > 10^{-6} \qquad \wedge \qquad \mathcal{R}_{LC} > 5\times 10^{-4/\sqrt{a}} \tag{54}$$

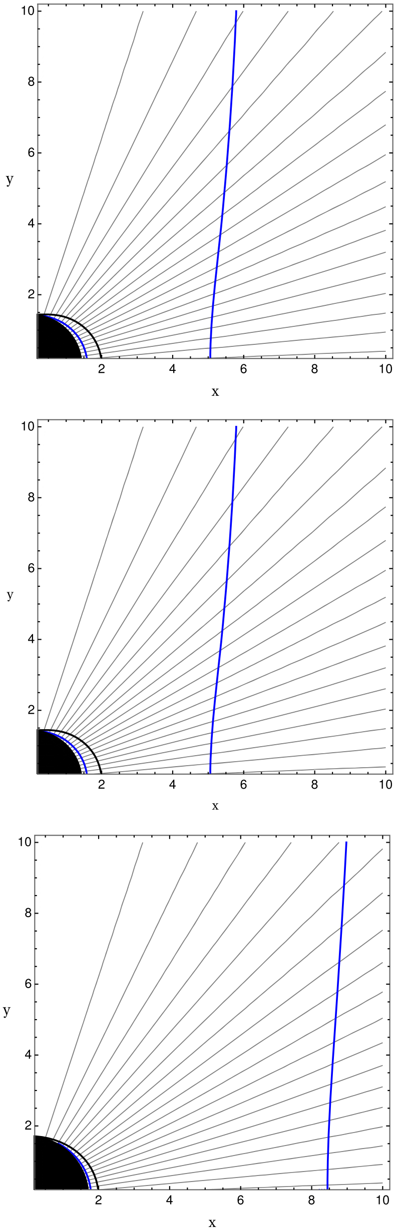

Figure A1. Distribution of the magnetic flux Ψ in the vicinity of a black hole rotating at $a_* = 0.999$ (top), $a_* = 0.9$ (middle), and $a_* = 0.7$ (bottom) after converging under the criteria in equation (A1) on the physical domain $[r_+, \infty] \times [0, 90^\circ]$, covered with a numerical grid $[n_r \times n_\theta] = [200 \times 64]$. Both functions $\omega(\Psi)$ and $II'(\Psi)$ are relaxed throughout the iterative procedure. The location of the ergosphere is represented by the black line, the two LS are drawn as blue lines.

Table A1. Number of iterations until the convergence criterion (A1) is reached for the *split-monopole* set-up described in Section 4.1.

Spin (a_*)	Iterations until convergence
0.9999	50.161
0.999	29.100
0.99	64.117
0.9	43.153
0.8	12.100
0.7	19.129

Fig. (A1) shows selected split-monopole configurations after condition A1 has been reached. For different values of the BH spin a, the required iterations to reach convergence are shown in Table A1.

This paper has been typeset from a TEX/LATEX file prepared by the author.

Monthly Notices
of the
ROYAL ASTRONOMICAL SOCIETY

MNRAS **490,** 4858–4876 (2019)
Advance Access publication 2019 October 03

doi:10.1093/mnras/stz2729

Instability of twisted magnetar magnetospheres

J. F. Mahlmann,[1]★ T. Akgün,[2] J. A. Pons,[2] M.A. Aloy[1] and P. Cerdá-Durán[1]

[1]*Departament d'Astronomia i Astrofísica, Universitat de València, E-46100 Burjassot, Spain*
[2]*Departament de Fisica Aplicada, Universitat d'Alacant, E-03690 Alicante, Spain*

Accepted 2019 September 25. Received 2019 September 22; in original form 2019 July 31

ABSTRACT

We present 3D force-free electrodynamics simulations of magnetar magnetospheres that demonstrate the instability of certain degenerate, high energy equilibrium solutions of the Grad–Shafranov equation. This result indicates the existence of an unstable branch of twisted magnetospheric solutions and allows us to formulate an instability criterion. The rearrangement of magnetic field lines as a consequence of this instability triggers the dissipation of up to 30 per cent of the magnetospheric energy on a thin layer above the magnetar surface. During this process, we predict an increase of the mechanical stresses on to the stellar crust, which can potentially result in a global mechanical failure of a significant fraction of it. We find that the estimated energy release and the emission properties are compatible with the observed giant flare events. The newly identified instability is a candidate for recurrent energy dissipation, which could explain part of the phenomenology observed in magnetars.

Key words: magnetic fields – methods: numerical – stars: magnetars – stars: neutron – X-rays: bursts.

1 INTRODUCTION

Soft gamma-ray repeaters (SGRs) are neutron stars with recurrent X-ray activity in the form of short bursts with duration ∼0.1 s and luminosities in the range 10^{36}–10^{43} erg s^{-1}. Over the last 40 yr, three bursts have been uniquely energetic, the so-called *giant flares* (GFs) with luminosities of the order of 10^{44}–10^{47} erg s^{-1} (SGR 0525-66, SGR 1900 + 14, and SGR 1806-20; see Cline et al. 1980; Hurley et al. 1999, 2005). In the three referenced cases, a short initial peak was followed by a softer X-ray tail lasting for 50–400 s. The engine behind these extraordinary events are *magnetars*, neutron stars with the strongest known magnetic fields (10^{14}–10^{16} G; see comprehensive reviews of magnetar observations and physics, e.g. in Woods & Thompson 2006; Rea & Esposito 2011; Mereghetti, Pons & Melatos 2015; Turolla, Zane & Watts 2015; Kaspi & Beloborodov 2017).

The precise mechanism producing such energetic events is still unclear. Strong magnetic fields are a gigantic energy reservoir in magnetars, generally of the order

$$\mathcal{E}_{\mathrm{magnetar}} \sim 1.6 \times 10^{47}\,\mathrm{erg} \left(\frac{B}{10^{15}\,\mathrm{G}}\right)^2 \left(\frac{R_*}{10\,\mathrm{km}}\right)^3, \qquad (1)$$

where we consider a neutron star with radius R_*.

The time-scale on which the magnetar is evolving, mainly due to Hall drift and Ohmic dissipation in the crust, is of the order of 10^3–10^6 yr (Jones 1988; Goldreich & Reisenegger 1992; Pons & Geppert 2007; Pons, Miralles & Geppert 2009; Gourgouliatos, Wood & Hollerbach 2016), by itself too slow to explain this phenomenology. Two complementary models have tried to explain these observations. In the *crustquake* model (Thompson & Duncan 1996; Perna & Pons 2011) the dynamical trigger is the mechanical failure of patches of the magnetar crust due to large stresses built during its magnetothermal evolution. Numerical simulations of the Hall evolution of the crust (Viganò et al. 2013) show that it is possible to recurrently reach the maximum stress supported by the very same (Horowitz & Kadau 2009; Baiko & Chugunov 2018). At this point, the crust likely becomes plastic (Levin & Lyutikov 2012), i.e. the crust generates thermoplastic waves emerging from such a localized trigger, or in other words *yields* (Beloborodov & Levin 2014; Li, Levin & Beloborodov 2016). The waves propagate into the magnetosphere, probably resulting in rapid dissipation through a turbulent cascade triggered by reconnection on slightly displaced flux surfaces (Thompson & Duncan 1996, 2001; Li, Zrake & Beloborodov 2018). The energy released in those events suffices to explain the observed luminosities, even for GFs (Thompson & Duncan 1996; Lander et al. 2015). The burst duration (∼0.1 s) is related to the crossing time of shear waves through the whole crust (1–100 ms). A limitation is that, if stressed for long periods of time (∼ 1 yr) as it is the case due to the slow magnetothermal evolution, the crust may yield at significantly lower breaking stresses (Chugunov & Horowitz 2010). In that case, it would effectively deform as a plastic flow, and, depending on its (unknown) properties, cease to yield altogether (Lyutikov 2015; Lander & Gourgouliatos 2019). Thompson, Yang & Ortiz (2017) has argued that even in this case the crust could yield.

★ E-mail: jens.mahlmann@uv.es

Published by Oxford University Press on behalf of the Royal Astronomical Society

The *magnetospheric instability* model requires a strongly twisted magnetosphere that becomes unstable and leads to a rapid reconnection event (Lyutikov 2003). The existence of long-lived magnetospheric twists is supported by the observation of hard X-ray emission in persistent magnetars (Beloborodov 2013a; Hascoët, Beloborodov & den Hartog 2014). During the magnetothermal evolution of the crust, the displacement of the magnetic field footprints can generate large twists in the magnetosphere (Akgün et al. 2017, 2018b). Above a critical twist, the magnetosphere becomes unstable and undergoes a rapid rearrangement where energy is dissipated by reconnection (Lyutikov 2003; Gill & Heyl 2010; Elenbaas et al. 2016) in a similar fashion as in the crustquake model. The main challenge of this scenario is the ability of the crust to produce significant twists in the magnetosphere. Beloborodov (2009) estimated that currents supporting magnetospheric twist are bound to dissipate on time-scales of years, effectively leading to a progressive untwisting. Therefore, Hall evolution is required to proceed relatively fast in order to allow for significant twists. Plastic viscosity may also be a problem for similar reasons (Lander & Gourgouliatos 2019). The latter authors have also suggested that the dynamical crust fractures of the crustquake model could be substituted by sustained episodes of accelerated plastic flows which are able to generate large magnetospheric twists on times shorter than the untwisting time-scale.

Numerical simulations by Parfrey, Beloborodov & Hui (2012), Parfrey, Beloborodov & Hui (2013), and Carrasco et al. (2019) confirm the instability of the magnetosphere beyond a critical twist, accompanied by the formation of plasmoids. These results are an analogy to the context of eruption processes in the solar corona as found in numerical experiments by Roumeliotis, Sturrock & Antiochos (1994), Mikic & Linker (1994). The energy dissipated in the reconnection events is sufficient to explain the GF processes (Parfrey et al. 2012). A caveat to these simulations is that the applied twisting rate is larger than the one expected from the respective magnetothermal evolution, although it would be fine if the trigger was a rapid plastic deformation.

An alternative approach to the above is the study of stability properties of magnetospheres. A number of authors have constructed equilibrium solutions to the Grad–Shafranov equation (GSE) for neutron star magnetospheres (Fujisawa & Kisaka 2014; Glampedakis, Lander & Andersson 2014; Pili, Bucciantini & Del Zanna 2015; Akgün et al. 2016; Kojima 2017, 2018; Kojima & Okamoto 2018; Akgün et al. 2018a). Akgün et al. (2017) performed magnetothermal evolutions coupling the crustal magnetic field at the stellar surface with an exterior equilibrium solution. The results showed that large twists grow in the magnetosphere up to a critical point beyond which no stable equilibrium solutions where found. A more detailed analysis by Akgün et al. (2018a) showed that, for sufficiently large twists, the solutions of the GSE are degenerate with several possible configurations of different energies but matching boundary conditions at the surface. This suggests the possibility of an unstable branch of the solutions and, thus, a possible explanation for the occurrence of bursts and GFs. In this work we explore this possibility by performing 3D numerical simulations of the equilibrium models in Akgün et al. (2018a). We assess their stability properties and their potential as candidates for transient magnetar phenomenology.

This work is organized as follows. In Section 2 we review and discuss the physics involved in magnetars relevant to the processes that we want to study. In Section 3 we briefly review the equations of force-free electrodynamics (FFE) implemented for simulations conducted on the infrastructure of the `Einstein Toolkit` (supplemented by Appendix A1). A detailed description of the derivation of initial models according to Akgün et al. (2018a) is given in Section 4. In Section 5 we present the numerical setup of our simulations as well as the outcome of the conducted 3D force-free simulations of twisted magnetospheres (reviewing details on maintaining the force-free regime in Appendix A2). The observed rapid dissipation of electromagnetic energy through the magnetar crust is interpreted and related to observable quantities, such as luminosity estimates, shear stresses on the stellar crust, and opacity models, in Section 6. Along this paper we use Gaussian units in CGS, except for Section 3 in which we use Heaviside-Lorentz with geometrized units ($G = c = \mathrm{M}_{\odot} = 1$). For convenience we express current densities in A m^{-2} and voltages in V, instead of the corresponding CGS units.

2 PHYSICS OF MAGNETARS

The basic structure of the magnetar interior is a (likely) fluid core of $\sim$10 km radius, amounting for most of the mass of the object, surrounded by a solid crust of about 1 km size. Outside, there is a tenuous, corotating magnetosphere connected to the NS by magnetic field lines (threading the central object) that extend up to the light cylinder at distances larger than 10^5 km. We start by discussing some basic properties of the different parts of the magnetosphere relevant for the interpretations and models presented later in this work.

2.1 Currents supporting the magnetosphere

For the typical rotation periods of magnetars ($P \sim$ 1–10 s) the Goldreich–Julian particle density (Goldreich & Julian 1969) for a magnetar magnetosphere has the typical value

$$n_{\mathrm{GJ}} = 7 \times 10^{12}\,\mathrm{cm}^{-3} \left(\frac{B_{\mathrm{pole}}}{10^{15}\,\mathrm{G}}\right) \left(\frac{R_*}{r}\right)^3 \left(\frac{10\,\mathrm{s}}{P}\right), \tag{2}$$

where B_{pole} is the magnetic field strength at the magnetar pole, R_* the magnetar radius, and r the distance to the centre of the star. This limits the magnetospheric current density close to the surface to $J < e\,c\,n_{\mathrm{GJ}} \approx 3 \times 10^8\,\mathrm{A\,m}^{-2}$, much below the typical values needed to support currents in strongly twisted magnetospheres of magnetars, of the order of

$$J \sim \frac{Bc}{4\pi r} \sim 8.2 \times 10^{12}\,\mathrm{A\,m}^{-2} \left(\frac{B_{\mathrm{pole}}}{10^{15}\,\mathrm{G}}\right) \left(\frac{R_*}{10\,\mathrm{km}}\right)^{-1}. \tag{3}$$

In general, magnetospheric currents in magnetars cannot be supported neither by Goldreich–Julian charges nor by charges lifted from the surface. Beloborodov & Thompson (2007) proposed that the currents are supported by e^+–e^- pairs generated in the magnetosphere in an intermittent discharge process that can be sustained for voltages along magnetic field lines of about 10^8–10^9 V. This voltage can be maintained by self-induction in untwisting magnetospheres (Beloborodov 2009). This untwisting is driven by the effective resistivity of the magnetosphere; the thermal photons from the magnetar's surface scatter resonantly off the charges supporting the magnetospheric currents, taking energy away, at the same time that pairs are produced. The untwisting time-scale is $\sim$1 yr, and it may explain the spectral evolution of some magnetars (Beloborodov 2009).

2.2 Time-scales

Changes in magnetars take place during two different time-scales. On the one hand, there is a *secular time-scale* of thousands of years during which the magnetar is essentially in equilibrium. On the other hand, there is a *dynamical time-scale* associated to energetic events (burst, flares) that can produce observable variations on time-scales as fast as 0.1s. The latter are likely associated to out-of-equilibrium states.

2.2.1 Secular time-scales

The *secular time-scale* is set by the slow magnetothermal evolution of the cooling object. The interior magnetic field evolution is dominated by Hall drift and Ohmic diffusion at the crust (see e.g. Viganò, Pons & Miralles 2012; Fujisawa & Kisaka 2014, and references therein), which proceeds on typical time-scales of 10^3–10^6 yr. The long-term evolution of the magnetosphere is driven by the changes in the crustal magnetic field, which displaces the footprints of the magnetospheric magnetic field lines. Since this evolution is much slower than the dynamical time-scale of the magnetosphere (see below), it can be considered that the magnetosphere evolves through a series of equilibrium states. This evolution creates a twist in the magnetosphere supported by currents – until a critical maximum twist is reached ($\varphi_{\rm crit} \sim 1$ rad) beyond which no magnetospheric equilibrium solutions exist (Akgün et al. 2017). The stability of the magnetosphere close to this critical point is the subject of this paper.

At the same time as the crustal magnetic field evolves, other processes in the magnetosphere can also contribute to the evolution. The untwisting of the magnetosphere on time-scales of ∼1 yr (Beloborodov 2009, and discussion in Section 2.2.1), may be a competing action to the twisting process described above.

Although the velocity of the footprints is typically very slow, numerical simulations of the magnetothermal evolution of magnetars including the magnetosphere show that, close to the critical point, it can be as fast as $v_\varphi \sim 1\,{\rm km\,yr^{-1}}$ (see Akgün et al. 2017) in the most optimistic scenario. Therefore, close to the critical twist, the magnetosphere twists slowly ($\dot{\varphi}_{\rm max,crit} \lesssim 0.1\,{\rm rad\,yr^{-1}}$), evolving on time-scales $\gtrsim 10$ yr. In the best case scenario, this time-scale is comparable to the untwisting time-scale (∼1 yr) and, hence, parts of the magnetosphere could sustain a significant twist. This time-scale is still much longer than the dynamical time-scale of the system (see below). Therefore, in our study of the dynamical behaviour we can neglect the secular evolution of the field.

2.2.2 Dynamical time-scales

The *dynamical time-scale* is set by the traveltime of waves propagating in the different regions of the magnetar. In the magnetosphere, the mass density can be neglected in view of the dominating magnetic field energy density. Also, the velocity of Alfvén and fast magnetosonic waves is degenerated to the speed of light. Hence, within ∼100 km the whole magnetosphere is coupled through time-scales smaller than 1 ms, which sets the scale for the dynamical evolution of the magnetosphere. In this region it is possible to neglect the inertia of the fluid in the evolution equations of the so-called FFE, which is used in the numerical simulations of this work.

In the outermost parts of the crust, the force-free condition still holds because of low densities. At sufficiently high densities, elastic forces of the solid crust and pressure gradients break this condition.

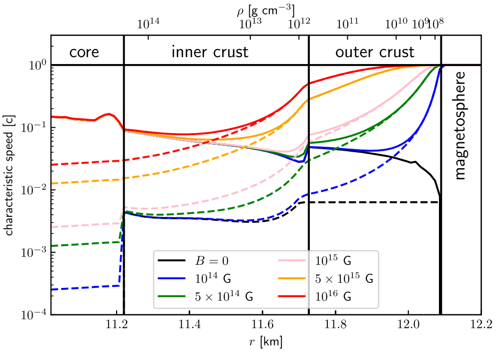

Figure 1. Fast magnetosonic (solid lines) and magnetoelastic (dashed lines) speed in the outer layers of a magnetar, for different magnetic field strengths ranging from 0 to 10^{16} G. The neutron star model corresponds to the $1.4 M_\odot$ mass APR + DH model of Gabler et al. (2012). The magnetic field is considered to be constant for simplicity.

To estimate the transition density one may consider the depth at which waves propagate at a velocity significantly different to the speed of light. Two possible waves can travel in the interior of the magnetized crust, the so-called magnetosonic (ms) waves, related to sound waves, and magneto-elastic (me) waves, a combination of Alfvén and shear waves. The complete eigenvalue structure of relativistic ideal MHD equations in the presence of an elastic solid is not known. To make a simple order of magnitude estimate of the different wave speeds, we use the expression of magnetoelastic torsional waves parallel to the magnetic field derived in Gabler et al. (2012) as well as the expression for fast magnetosonic waves perpendicular to the field:[1]

$$v_{\rm me}/c = \sqrt{\frac{\mu_s + B^2}{e + B^2}} \qquad\qquad v_{\rm ms}/c = \sqrt{\frac{e c_s^2 + B^2}{e + B^2}}, \tag{4}$$

where e is the energy density and μ_s the shear modulus. Note that in the limit of low magnetic field ($B^2 \ll \mu_s$, $B^2 \ll e$) we recover the shear and sound speed, respectively. In the high magnetic field limit ($B^2 \gg \mu_s$, $B^2 \gg e$) both, $v_{\rm me}$ and $v_{\rm ms}$, coincide with the speed of light. Inside the fluid core ($\mu_s = 0$) the magnetoelastic speed becomes the Alfvén speed.

Fig. 1 shows the value of the characteristic speeds in the outer layers of a typical NS model for different magnetic fields in the magnetar range. Indeed, both fast magnetosonic waves and Alfvén waves have a degenerate speed equal to the speed of light in the magnetosphere. Inside the outer crust ($\rho < 4 \times 10^{11}\,{\rm g\,cm^{-3}}$), all characteristic speeds transition from the speed of light to a significantly lower value, in a region that can still be considered force-free. This transition depends on the magnetic field strength, happening deeper inside the star for larger values of $B_{\rm pole}$. Given these characteristic speeds, any global rearrangement of the magnetosphere can modify the entire structure of the crust (of size $\sim 2\pi R_*$) on a time-scale of ∼1 ms for magnetosonic waves and ∼10 ms for magnetoelastic waves.

---

[1] Slow magnetosonic waves are also possible but their velocity is much smaller and not relevant for this work, in fact, for the case of waves perpendicular to the magnetic field their speed is zero.

One last aspect to consider is the ability of magnetospheric waves to transmit energy into the crust. The discussion should be limited to Alfvén waves, which become magnetoelastic waves once they penetrate the crust; the energy carried by fast magnetosonic waves in the magnetosphere can be neglected due to the small density, which renders the compressibility effects of fast-magnetosonic waves unimportant.

Since the characteristic time in the magnetosphere is ∼1 ms, the typical frequency of the waves generated during its dynamics is in the kHz range. At this frequency, the crust can be considered as a thin layer because its thickness (∼1 km) is much smaller than the typical wavelength in the magnetosphere ($\lambda \sim 100$ km). In this case the energy transmission coefficient for waves perpendicular to the surface is approximately (cf. Link 2014; Li & Beloborodov 2015)

$$\mathcal{T} = \frac{4v_{\rm me}/c}{(1+v_{\rm me}/c)^2} \approx 0.04\left(\frac{v_{\rm me}/c}{0.01}\right), \tag{5}$$

for typical physical conditions in the magnetar crust. Given the low transmission coefficients of magnetospheric Alfvén waves hitting the crust as well as the differences on time-scales between the crust and the magnetosphere (typically ∼10 times shorter in the later) it is reasonable to consider that most of the crust remains rigid during any dynamical rearrangement of the magnetosphere.

In our magnetar model we will consider two regions: A force-free region (*exterior*, hereafter) consisting of the magnetosphere and the force-free part of the outer crust as well as the magnetar *interior* for the remainder of the NS, which we will consider to be fixed during our simulations. The limit between both regions is a spherical surface below the NS surface, where magnetic field lines are anchored, and is located below the transition density between inner and outer crust at a density $\rho < 4\times10^{11}\,\mathrm{g\,cm^{-3}}$. For the purpose of describing the simulations we will refer to this transition point simply as *surface*.

3 FORCE-FREE ELECTRODYNAMICS

In analogy to Komissarov (2004) and Parfrey, Spitkovsky & Beloborodov (2017) we solve Maxwell's equations in the force-free limit:

$$\frac{\partial\tilde{\boldsymbol{B}}}{\partial t} = -\nabla\times\tilde{\boldsymbol{E}} \qquad \text{and} \qquad \frac{\partial\tilde{\boldsymbol{E}}}{\partial t} = \nabla\times\tilde{\boldsymbol{B}} - \tilde{\boldsymbol{J}}_{\rm FF}, \tag{6}$$

where $\tilde{\boldsymbol{E}}$, $\tilde{\boldsymbol{B}}$, and $\tilde{\boldsymbol{J}}_{\rm FF}$ are the electric field, the magnetic field, and the so-called force-free current, respectively. We place a tilde to distinguish quantities expressed in our Heaviside-Lorentz *geometrized* (HLG) system of units, while the same symbols without tilde express quantities in the Gaussian *non-geometrized* (GNG) system of units (see Table 1). We explicitly include the charge conservation equation

$$\frac{\partial\tilde{\rho}_{\rm e}}{\partial t} + \nabla\cdot\tilde{\boldsymbol{J}}_{\rm FF} = 0, \tag{7}$$

where $\tilde{\rho}_{\rm e}$ represents the charge density. Furthermore, we use a mixed hyperbolic/parabolic correction by the introduction of additional potentials (further discussed in Appendix A1) in order to numerically ensure the constraints $\nabla\cdot\tilde{\boldsymbol{B}} = 0$ and $\nabla\cdot\tilde{\boldsymbol{E}} = \tilde{\rho}_{\rm e}$ (Dedner et al. 2002; Palenzuela et al. 2009; Mignone & Tzeferacos 2010).

In the force-free limit it is necessary to guarantee that there are either no forces acting on the system or, more generally, that the forces of the system balance each other. This is equivalent to a vanishing net Lorentz force on the charges $\tilde{\rho}_{\rm e}$ (see e.g. Camenzind 2007):

$$\tilde{\boldsymbol{E}}\cdot\tilde{\boldsymbol{J}}_{\rm FF} = 0 \tag{8}$$

$$\tilde{\rho}_{\rm e}\tilde{\boldsymbol{E}} + \tilde{\boldsymbol{J}}_{\rm FF}\times\tilde{\boldsymbol{B}} = 0. \tag{9}$$

Table 1. Conversion table between code output in Heaviside-Lorentz *geometrized* units ($M_\odot = G = c = 1$) and *non-geometrized* Gaussian units. In order to transform the respective quantities from code quantities to the *non-geometrized* system, one has to multiply the *geometrized* quantity by its conversion factor expressed in CGS.

Quantity	Non-geometrized unit	Conversion factor
Mass	M	$\mathrm{M}_\odot$
Length	L	$\mathrm{M}_\odot Gc^{-2}$
Time	T	$\mathrm{M}_\odot Gc^{-3}$
Electric charge	$\mathrm{L}^{3/2}\mathrm{M}^{1/2}\mathrm{T}^{-1}$	$(4\pi)^{-1/2}\mathrm{M}_\odot G^{1/2}$
Electric field	$\mathrm{L}^{-1/2}\mathrm{M}^{1/2}\mathrm{T}^{-1}$	$(4\pi)^{1/2}\mathrm{M}_\odot^{-1}G^{-3/2}c^4$
Magnetic field	$\mathrm{L}^{-1/2}\mathrm{M}^{1/2}\mathrm{T}^{-1}$	$(4\pi)^{1/2}\mathrm{M}_\odot^{-1}G^{-3/2}c^4$
Current density	$\mathrm{L}^{-1/2}\mathrm{M}^{1/2}\mathrm{T}^{-2}$	$(4\pi)^{-1/2}\mathrm{M}_\odot^{-2}G^{-5/2}c^7$
(EM) Energy	$\mathrm{L}^2\mathrm{M}\,\mathrm{T}^{-2}$	$\mathrm{M}_\odot\, c^2$
(EM) Stress	$\mathrm{L}^{-1}\mathrm{M}\,\mathrm{T}^{-2}$	$\mathrm{M}_\odot^{-2}G^{-3}c^8$

From equation (9) one readily obtains the degeneracy condition

$$\tilde{\boldsymbol{E}}\cdot\tilde{\boldsymbol{B}} = 0. \tag{10}$$

Additionally, force-free fields are required to be magnetically dominant, the magnetic field being always stronger than the electric one, such that the following condition must hold:

$$\tilde{\boldsymbol{B}}^2 - \tilde{\boldsymbol{E}}^2 \geq 0. \tag{11}$$

Conditions (10) and (11), as well as the conservation condition $\partial_t\left(\tilde{\boldsymbol{E}}\cdot\tilde{\boldsymbol{B}}\right) = 0$ can be combined in order to obtain an explicit expression for $\tilde{\boldsymbol{J}}_{\rm FF}$ (cf. Komissarov 2011; Parfrey et al. 2017):

$$\tilde{\boldsymbol{J}}_{\rm FF} = \left[\tilde{\boldsymbol{B}}\cdot\nabla\times\tilde{\boldsymbol{B}} - \tilde{\boldsymbol{E}}\cdot\nabla\times\tilde{\boldsymbol{E}}\right]\frac{\tilde{\boldsymbol{B}}}{\tilde{B}^2} + \tilde{\rho}_{\rm e}\frac{\tilde{\boldsymbol{E}}\times\tilde{\boldsymbol{B}}}{\tilde{B}^2}. \tag{12}$$

Across the literature (e.g. Komissarov 2004; Alic et al. 2012; Parfrey et al. 2017) we find various modifications in the definition of $\tilde{\boldsymbol{J}}_{\rm FF}$ in order to drive the numerical solution of the system of partial differential equations (6) towards a state which fulfils equation (10) by introducing a suitable cross-field conductivity. In the numerical setup, we choose to combine the prescription of Komissarov (2004) with the force-free current given above. This strategy effectively minimizes the violations of equations (10) and (11) by exponentially damping the (numerically induced) components of the electric field parallel to $\tilde{\boldsymbol{B}}$ and suitably adjusting the electric field in magnetospheric current sheets in order to obtain $\tilde{\boldsymbol{B}}^2 - \tilde{\boldsymbol{E}}^2 \to 0$ at these locations.

Throughout the literature, the magnetic dominance condition (11) condensates to a necessary condition of FFE (e.g. Uchida 1997; McKinney 2006). For some authors (e.g. McKinney 2006) the breakdown of the magnetic dominance implies the invalidity of the numerical model. Others (e.g. Uchida 1997) claim that some physical processes (e.g. radiation losses) taking place in the regions where condition (11) is breached may restore the magnetic dominance condition. Indeed, Uchida (1997) explicitly allows for transient phases violating condition (11) – these regions are then interpreted as abandoning the freezing of magnetic flux on to the flux of matter, being necessarily accompanied by dissipation. Following Uchida (1997), the force-free regime continues to be a valid approximation as long as the dissipative effects are only a small fraction of the total energy. The violation of the perpendicularity condition (10) is an additional source of (Ohmic) dissipation (studied for example in the context of Alfvén waves in force-free electrodynamics by Li et al. 2019). In practice, this channel of dissipation occurs when $\tilde{\boldsymbol{E}} \cdot \tilde{\boldsymbol{B}} \neq 0$ such that $\tilde{\boldsymbol{J}} \cdot \tilde{\boldsymbol{E}} \neq 0$. Currently used force-free codes aim to avoid the transient into this regime by numerically cutting back all violations of condition (11) (e.g. Palenzuela et al. 2010; Paschalidis & Shapiro 2013; Carrasco & Reula 2016) or include a suitable Ohm's law (e.g. Komissarov 2004; Spitkovsky 2006; Alic et al. 2012; Parfrey et al. 2017) in order to minimize these violations during a transient phase. Fig. 5 shows the breakdown of condition (11) during the simulation and hints towards the aforementioned dissipative processes. We refer to Appendix A2 as well as, for example, Lyutikov (2003) for further details on the necessary constraint preservation and limitations of the highly magnetized regime (such as the lack of physical reconnection). We will give a thorough review of the procedures employed in our code in a subsequent technical paper.

4 TWISTED MAGNETAR MAGNETOSPHERE MODELS

4.1 Magnetospheres

Due to the long rotational period of observed magnetars pushing the location of the light cylinder to great distances, it is possible to neglect the rotation of the neutron star when building numerical models of magnetospheres in the near zone. The equilibrium structure of a non-rotating axisymmetric force-free magnetosphere is given through the well-known GSE (Lüst & Schlüter 1954; Grad & Rubin 1958; Shafranov 1966). This approach has been followed in several recent papers (e.g. Spitkovsky 2006; Beskin 2010; Viganò, Pons & Miralles 2011; Fujisawa & Kisaka 2014; Glampedakis et al. 2014; Pili et al. 2015; Akgün et al. 2016, 2018a; Kojima 2017, 2018; Kojima & Okamoto 2018). In most of these works, the toroidal field is confined within a magnetic surface near the equator, smoothly transitioning to vacuum at large distances. In stationary, non-rotating, axisymmetric magnetosphere models, the toroidal field cannot extend to the poles. Otherwise, the toroidal field would extend all the way to infinity, thus, violating the requirements of finite magnetic energy. Following the notation of Akgün et al. (2016, 2018a), we write the axisymmetric magnetic field in terms of its poloidal and toroidal components:

$$\boldsymbol{B} = \nabla P \times \nabla\varphi + T\nabla\varphi, \tag{13}$$

where φ is the azimuthal angle in spherical coordinates. Here, P and T are the poloidal and toroidal stream functions. Expressed in the orthonormal spherical basis corresponding to the coordinates (r, θ, φ), the magnetic field can be explicitly computed from the potentials P and T as

$$B^r = \frac{1}{r^2\sin\theta}\partial_\theta P, \tag{14}$$

$$B^\theta = -\frac{1}{r\sin\theta}\partial_r P, \tag{15}$$

$$B^\varphi = \frac{T}{r\sin\theta}. \tag{16}$$

For an axially symmetric force-free field, the functions T and P may be expressed in terms of each other and appear as solutions of the force-free GSE:

$$\left[\partial_r^2 + \frac{1-\mu^2}{r^2}\partial_\mu^2\right] P + T\frac{\mathrm{d}T}{\mathrm{d}P} = 0, \tag{17}$$

where $\mu = \cos\theta$. P and T are constant on magnetic surfaces or, equivalently, along magnetic field lines. P is related to the magnetic flux passing through the area centred on the axis and delineated by the magnetic surface. Therefore, its value at the poles is zero and increases towards the equator. The function T is related to the current passing through the same area. Its functional dependence on P can be chosen freely (consistently with any continuity and convergence requirements, particularly for the currents), which is equivalent to setting boundary conditions for T at the surface of the star. Here, we invoke the same functional form for $T(P)$ as in Akgün et al. (2016, 2018a). Thus, the toroidal field is confined within some *critical* magnetic surface ($P = P_\mathrm{c}$),

$$T\,(P) = \begin{cases} s\times(P-P_\mathrm{c})^\sigma & : \; P \geqslant P_\mathrm{c} \\ 0 & : \; \text{else} \end{cases}, \tag{18}$$

s being a parameter determining the relative strength of the toroidal field with respect to the poloidal field. In order to avoid divergences in the currents we must demand that the power index satisfies $\sigma \geq 1$. For a pure dipolar field, the poloidal stream function in the magnetosphere is

$$P = \frac{1}{2}B_\mathrm{pole}\frac{R_*^3}{r}\sin^2\theta, \tag{19}$$

while the toroidal stream function is $T = 0$ everywhere. We will consider the simplest cases where the boundary value of P at the surface of the magnetar coincides with that of a dipolar field, and, therefore, the initial data are symmetric with respect to the equator. For different choices of the functional relation $T(P)$ given by equation (18) we solve the GSE and obtain a twisted magnetospheric initial model. We would like to note that all equations can be rescaled with B_pole, hence, the results of our numerical simulations can be normalized to the field strength of interest.

The energy stored in the magnetosphere can be computed as a volume integral

$$\mathcal{E} = \frac{1}{8\pi}\int(\boldsymbol{B}^2 + \boldsymbol{E}^2)\,\mathrm{d}V. \tag{20}$$

For later reference and in order to normalize the energetic content of our models, we provide the energy stored in the magnetosphere of a pure dipolar magnetic field ($\vec{E} = 0$, $B^r = B_\mathrm{pole}(R_*/r)^3\cos\theta$, $B^\theta = (B_\mathrm{pole}/2)(R_*/r)^3\sin\theta$, $B^\varphi = 0$):

$$\mathcal{E}_\mathrm{d} = \frac{1}{12}B_\mathrm{pole}^2R_*^3 = 8.3\times10^{46}\,\mathrm{erg}\left(\frac{B_\mathrm{pole}}{10^{15}\,\mathrm{G}}\right)^2\left(\frac{R_*}{10\,\mathrm{km}}\right)^3. \tag{21}$$

Once the surface value of P and the functional relation $T(P)$ are defined, one can solve the GSE iteratively (as it is a non-linear equation), while imposing vacuum boundary conditions at large distances. We use the numerical code described in Akgün et al. (2018a) to build our initial data. Using this parametrization, the boundary condition at the surface of the neutron star for the GSE (values of P and T) is fully determined by four parameters B_pole, s, P_c, and σ. However, the solution of the GSE with this fixed boundary condition is not necessarily unique. Akgün et al. (2018a) showed that for sufficiently large magnetospheric twists, there exist degeneracies, i.e. different solutions of the GSE for the same boundary conditions (the same set of four parameters). These solutions differ in their energy, twist, and the radial extent of the toroidal currents.

Table 2 shows the parameters used to construct the initial data for our numerical simulations. Each of the series A, B, and C of initial models were chosen to have identical parameters but *different* magnetospheric energies and, hence, represent degenerate

Table 2. Overview of initial data models used in our simulations. s, σ, and P_c are the parameters determining the boundary condition at the surface of the neutron star (see Section 4.1). $\mathcal{E}$ denotes the total electromagnetic energy in the magnetospheres, which is normalized to the vacuum dipole energy $\mathcal{E}_\mathrm{d}$ (equation 21), hence without dimension. $\tilde{J}_\mathrm{max}$ denotes the maximum current density at $t = 0$ (see Section 2.1 as well as Table 1 for unit conversion). The maximum initial electromagnetic stresses on the magnetar surface (equation 24) at $t = 0$ are shown in the last two columns (i.e. $\tilde{T}^{ra}_\mathrm{max} := \max_{\{|\boldsymbol{x}|=R_*\}}\{\tilde{T}^{ra}(t = 0, \boldsymbol{x})\}$, with $a = \theta, \varphi$). Values of $\tilde{J}_\mathrm{max}$ and $\tilde{T}^{ra}_\mathrm{max}$ are given in HLG units for an NS with $B_\mathrm{pole} = 10^{15}$ G and $R_* = 13.7$ km .

	s	σ	P_c	$\mathcal{E}/\mathcal{E}_\mathrm{d}$	$\tilde{J}_\mathrm{max}$	$\tilde{T}^{r\varphi}_\mathrm{max}$	$\tilde{T}^{r\theta}_\mathrm{max}$
A1	2	2	0.3294	1.1553	1.71e-6	8.97e-10	1.44e-9
A2	2	2	0.3303	1.3356	1.58e-6	8.95e-10	1.24e-9
B1	1	1	0.3717	1.1547	1.08e-6	7.68e-10	1.39e-9
B2	1	1	0.3720	1.2276	1.07e-6	7.68e-10	1.31e-9
C1	1	1	0.4400	1.0653	1.95e-6	6.68e-10	1.56e-9
C2	1	1	0.4412	1.1943	1.03e-6	6.68e-10	1.44e-9
C3	1	1	0.4396	1.2738	1.03e-6	6.71e-10	1.35e-9

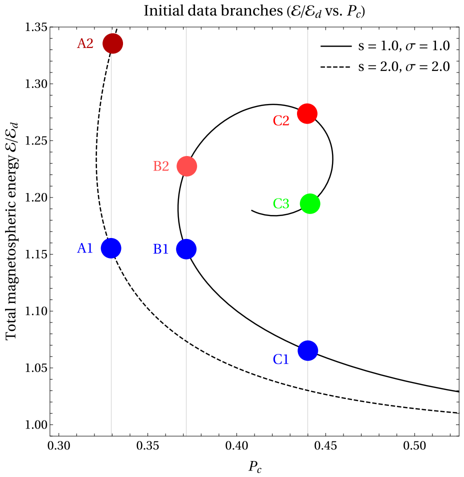

Figure 2. Magnetospheric energy normalized to the vacuum dipole energy (equation 21) of the initial equilibrium models, for different values of the parameter P_c (in units of P at the equator). The solid and dashed lines correspond to a series of models with constant s and σ. The coloured dots correspond to the initial data models used in our simulations.

magnetospheric models. We would like to point out that the value of P_c is only equal, within each series, up to the second significant digit, due to numerical reasons. Fig. 2 shows the energy of the initial models as a function of the parameter P_c. Models within each spiral curve (constant s and σ) and with the same value of P_c have identical boundary conditions but different energies. In the interpretation made by Akgün et al. (2018a), the lower energy state for each series of degenerate models (i.e. A1, B1, and C1) corresponds to stable configurations, while high energy states (i.e. A2, B2, C2, and C3) may be unstable and would evolve towards the stable configuration releasing the respective energy difference. This instability is a possible scenario for the flare activity observed in magnetars.

The lowest energy solutions are the ones that are most similar to the vacuum solutions, with all field lines connected to the surface, while the higher energy solutions are more radially extended, and can contain disconnected field lines.

4.2 Magnetar interior

The initial models described above provide solutions only for the magnetosphere. For each possible magnetospheric model one can build infinite solutions to describe the neutron star interior. The magnetospheric (exterior) values of P and T determine the magnetic field $\boldsymbol{B}$ at the exterior side of the surface (equations 14 to 16). To match this solution to the interior, one has to ensure the continuity of B^r at the surface. This is valid if P is continuous and, hence, T and B^φ are continuous as well. However, B^θ does not necessarily match continuously to the neutron star interior because current sheets (thin current-carrying layers across which the magnetic field changes either direction or magnitude) in the φ direction may occur. Even if all components of $\boldsymbol{B}$ are continuous at the surface, the magnetic field structure in the interior depends completely on how currents are internally distributed.

In the astrophysical scenario we are considering, the magnetar reaches the initial state in which we start our numerical simulation after a slow magnetothermal evolution that proceeds in a long time-scale compared to the dynamical time-scales (cf. Section 2.2) of the magnetosphere (∼1 ms) or the crust (∼10 ms). On such long time-scales, any current close to the surface of the NS is expected to be dissipated by Ohmic diffusion. Therefore, we consider that initially all fields are continuous across the surface. We build our interior solution by extrapolating the exterior magnetic field towards the stellar interior across a number of grid cells as needed by the reconstruction algorithm used for the magnetospheric evolution in our simulations. Since the neutron star is basically a perfect conductor, the initial charge density and electric field in the interior (and the magnetosphere) are set to zero.

The surface values of B^r and B^φ are coincident for degenerate models (e.g. within the series C1, C2, and C3 in Fig. 2) because P and T at the surface are identical. However, since P and T may have a different radial dependence outside of the magnetar, and B^θ depends on the radial derivative of P (equation 15), it is different for every model of the same series.

5 SIMULATIONS

We have performed numerical simulations of the neutron star magnetosphere using the initial models in Table 2. For all the simulations we employ our own implementation of a General Relativistic FFE code in the framework of the `Einstein Toolkit`[2] (Löffler et al. 2012). The EINSTEIN TOOLKIT is an open-source software package utilizing the modularity of the `Cactus`[3] code (Goodale et al. 2003) which enables the user to specify the so-called thorns in order to set up customary simulations. There exist other code packages such as `GiRaFFE` (Etienne et al. 2017), which integrate the equations of force-free electrodynamics employing an evolution scheme based on the Poynting flux as a conserved quantity (cf. McKinney 2006; Paschalidis & Shapiro 2013) rather than the electric field and its current sources (as formulated in e.g. Komissarov 2004; Parfrey et al. 2017). The `Einstein Toolkit` employs units where $\mathrm{M}_\odot = G = c = 1$, which sets the respective time and length scales to be $1\,\mathrm{M}_\odot \equiv 4.93 \times 10^{-6}$ s $\equiv 1477.98$ m. This unit system is a

[2] http://www.einsteintoolkit.org
[3] http://www.cactuscode.org

variation of the so-called system of *geometrized units* (as introduced in appendix F of Wald 2010), with the additional normalization of the mass to 1 $\mathrm{M}_\odot$ (i.e. our HLG units, as introduced in Section 3). For easy reference, we provide a set of conversion factors for relevant physical quantities in Table 1.

5.1 Numerical setup

All shown simulations are conducted on a 3D box with dimensions $[4741.12\,\mathrm{M}_\odot \times 4741.12\,\mathrm{M}_\odot \times 4741.12\,\mathrm{M}_\odot]$ with a grid spacing of $\Delta_{x,y,z} = 74.08\,\mathrm{M}_\odot$ on the coarsest grid level. For the chosen magnetar model of radius $R_* = 9.26\,\mathrm{M}_\odot$ ($\simeq 13.7$ km) this corresponds to a $[512R_* \times 512R_* \times 512R_*]$ box with a grid spacing of $\Delta_{x,\,y,\,z} = 8R_*$. For the low and high resolution tests we employ seven and eight additional levels of mesh refinement, each increasing the resolution by a factor of two and encompassing the central object, respectively. This means that the finest resolution of our models (close to the magnetar surface) are $\Delta^{\mathrm{min}}_{x,y,z} = 0.0625 \times R_* = 0.5787\,\mathrm{M}_\odot$ and $\Delta^{\mathrm{min}}_{x,y,z} = 0.03125 \times R_* = 0.2894\,\mathrm{M}_\odot$ for the low and high resolution models, or in other words 16 and 32 points per R_*, respectively. The initial data are evolved for a period of $t = 1185.28\,\mathrm{M}_\odot \simeq 5.84$ ms, which is chosen to be well below the dynamical time-scale of the magnetar crust, which can be considered as a fixed boundary (see Section 2.2).

In order to ensure the conservation properties of the algorithm, it is critical to employ *refluxing* techniques correcting numerical fluxes across different levels of mesh refinement (see e.g. Collins et al. 2010). Specifically, we make use of the thorn `Refluxing`[4] in combination with a cell-centred refinement structure (cf. Shibata 2015). We highlight the fact that employing the refluxing algorithm makes the numerical code 2−4 times slower for the benefit of enforcing the conservation properties of the numerical method (especially of the charge). Refluxing also reduces the numerical instabilities, which tend to develop at mesh refinement boundaries.

In conservative schemes, numerical reconstruction algorithms (we employ an MP7 scheme; cf. Suresh & Huynh 1997) derive intercell approximations of the conservative variables by making use of their values at several adjacent grid-points (for MP7, one requires seven points). As a result of the numerical coupling between the magnetosphere and the magnetar crust introduced by the intercell reconstruction at the stellar surface, the field dynamics induce a mismatch in the current flowing through the surface and effectively trigger a (numerical) flow of charges leaving or entering the domain. In order to avoid this artefact, we replace the reconstructed values of the radial current $\tilde{J}^r_{\mathrm{FFE}}$ at interfaces between the stellar interior and exterior by the cell-centred value in the stellar interior. This procedure ensures a conservation of magnetospheric charge.

The (3D) initial data are imported from the (2D) initial models (see section 4.1) by bicubic spline interpolation. Throughout the numerical evolution, all quantities on grid-points inside of the magnetar radius are fixed to their initial values.

5.2 Instability onset and magnetospheric energy balance

We have performed simulations with initial models in the low energy branch (A1, B1, and C1) and in the high energy branch (A2, B2, C2, C3). We observe a differentiated behaviour in the evolution of the system depending on the class of initial model. For models in the low energy branch we find that the magnetosphere is stable and that the system remains essentially unchanged. The energy of the system remains constant throughout the simulation (see blue lines in Fig. 3), confirming the stability of these configurations, at least on dynamical time-scales. This is especially true in the high resolution models, which exhibit a smaller numerical dissipation. The slightly larger numerical dissipation of the low resolution models explains the small drift in time with respect to the initial energy displayed by the blue dashed lines in Fig. 3. On the other hand, models in the high energy branch become unstable on a time-scale of a few milliseconds and the magnetosphere changes its shape roughly at the same time as the energy of the magnetosphere decreases (see red and green lines in Fig. 3). This numerical experiment confirms the hypothesis of Akgün et al. (2018a) that, for degenerate initial models, only the lowest energy state is stable, and that all corresponding degenerate cases of high energy are unstable. In addition, we note that the lower energy states are closer to a purely dipolar magnetosphere, hence, the minimized circumference of the magnetic surfaces minimize the magnetospheric energy content (cf. Thompson & Duncan 1996).

For configurations in the unstable branch, the onset of the instability proceeds earlier for lower numerical resolution. This is expected because a coarser grid contains larger numerical discretization errors acting as a seed for the instability onset. However, the rapid drop in energy during the instability proceeds in a similar fashion for both numerical resolutions, indicating that the instability has a physical origin and is not a numerical artefact. In the case of the high energy initial model C2 we observe a rearrangement of the lobes of magnetic twist towards a dipolar structure (see Fig. 4) prior to a significant drop of magnetospheric energy (by approximately 30 per cent of its initial value). During the phase of full validity of the force-free condition (see equation 11) the loss of magnetospheric energy is dominated by an outgoing Poynting flux at the innermost boundary (see Fig. 5). For our boundary condition it can be interpreted as the formation of a strong current on a thin layer below the surface, where energy can be efficiently dissipated.

Following Parfrey et al. (2013) in the context of twisted magnetar fields and Li et al. (2019) in a study of energy dissipation in collisions of force-free Alfvén waves, the onset of the (topological) relaxation is likely to be linked to Ohmic heating $\boldsymbol{J} \cdot \boldsymbol{E} \neq 0$, which occurs as a result of (minor) violations of the force-free condition (10), as can be seen in the bottom panel of Fig. 5 (note the much smaller scale of that panel compared to the middle one). We give a more detailed review of the treatment of these violations in our code and throughout the literature in Appendix A2.

5.3 Surface currents and long-time evolution

Following the initial instability and subsequent rapid rearrangement of the magnetar magnetosphere (Section 5.2), thin currents form at the magnetar surface (see Figs 6 and 7). These currents are expected to appear as the initial model in the high energy state tries to relax to the lowest energy magnetospheric configuration, while keeping the interior field fixed (see the discussion in Section 4.2). There are two possible fates for these currents: (i) they could propagate inwards, inside the magnetar crust, deforming the magnetic field inside, and creating a mechanical stress in the crust, on a time-scale of several 10 ms, or (ii) they could form a thin surface current dissipating on a time-scale shorter that the time it takes to deform the crust. These two possibilities are not mutually exclusive and a combination of both is possible. In none of the cases our simulations can give a conclusive answer because (i) we are not evolving the

---

[4] Refluxing at mesh refinement interfaces by Erik Schnetter: https://svn.cct.lsu.edu/repos/numrel/LSUThorns/Refluxing/trunk

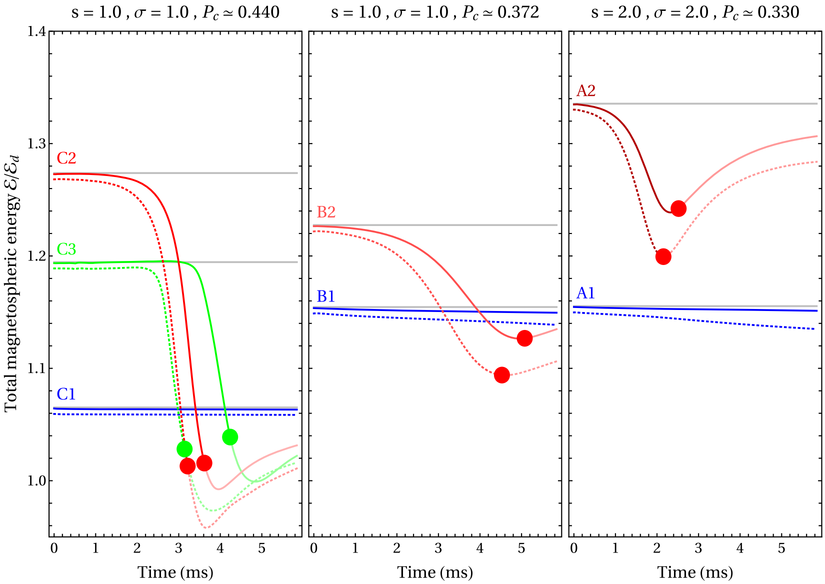

Figure 3. Time evolution of total magnetospheric energy content for the models in Table 2. The instability of the field configuration for degenerate solutions of higher energy triggers the rearrangement of magnetic field lines as well as a release of energy into the magnetosphere and on to the magnetar surface. The simulated time-scale on which the instabilities are observed falls within the dynamical time-scale of the magnetar crust. Low resolution simulations (16 points per R_*) are shown in dotted lines, high resolution simulations (32 points per R_*) in solid lines. The initial (analytical) value of total magnetospheric energy for each configuration is indicated by grey lines. The approximate time of the breakdown of the force-free condition $\tilde{\boldsymbol{E}}^2 - \tilde{\boldsymbol{B}}^2 < 0$ (see Appendix A2) is depicted by coloured dots.

magnetar interior as we are considering only time-scales smaller than the dynamical time-scale of the crust, (ii) the formation of thin surface currents is numerically challenging (would require a computationally prohibitively high resolution near the magnetar surface), and (iii) it would eventually violate the FF conditions (10) and (11), hence invalidating our current numerical approach.

The aforementioned current layers are expected to be regions of strong energy dissipation and the breakdown of the force-free conditions (see e.g. Uchida 1997; McKinney 2006; Palenzuela et al. 2010; Parfrey et al. 2013). Figs 5 and 7 link the breakdown of the force-free condition (11) and the occurrence of surface currents with the opening of dissipation channels different to the energy flow through the magnetar surface (see Appendix A2 for a short review of the force-free breakdown). We find the violation of condition (10) to be continuously occurring with peaks at the instance of rapid energy dissipation. Condition (11) starts to fail on longer time-scales at the moment of fastest transfer of magnetic energy through the surface. At this time, further dissipation mechanisms (see Fig. 5) come into play, as is expected throughout the literature (Uchida 1997; McKinney 2006; Li et al. 2019).

It should be noted that the total magnetospheric energy for the models B2, C2, and C3 drops below the energy of their respective low energy equilibrium solutions, and even below the magnetospheric energy of the vacuum dipole (equation 21). However, this energy drop is (slightly) smaller for the high resolution simulations, and shows some dependence on the chosen setup of the hyperbolic/parabolic cleaning procedures (see Appendix A1) at the magnetar surface. The sensitivity of this behaviour to the numerical details at the location of the (3D Cartesian) crust may be attributed to the numerical dissipation of the employed code.

6 DISCUSSION

6.1 Energy release during the instability

During the rearrangement of magnetic field lines in the high energy models A2, B2, C2, and C3, an amount $\Delta\mathcal{E}$ of electromagnetic energy is released into the magnetosphere and on to the magnetar crust (Poynting flux through the stellar surface, see Fig. 5). The amount of released energy in CGS units, $\mathcal{E}_r$, can be quantified directly from Table 3 by employing the conversion formula

$$\mathcal{E}_\mathrm{r} = 2.14 \times 10^{47}\,\mathrm{erg} \left(\frac{\Delta\mathcal{E}}{\mathcal{E}_\mathrm{d}}\right) \left(\frac{B_\mathrm{pole}}{10^{15}\,\mathrm{G}}\right)^2 \left(\frac{R_*}{13.7\,\mathrm{km}}\right)^3 . \qquad (22)$$

For the changes in energy ($\Delta\mathcal{E}/\mathcal{E}_\mathrm{d} \approx 0.1 - 0.3$) observed in our simulations with the highest energy within each series (C2, C3, B2, and A2) the released energy is in the range $\mathcal{E}_\mathrm{r} \approx 2.1 \times 10^{46} - 6.4 \times 10^{46}$ erg. This energy range is compatible with that of observed GFs (10^{45}–10^{48} erg). For instance, the energy liberated during the peak of the GF of SGR 1806-20 is $\sim 3.7 \times 10^{46}$ erg (Hurley et al. 2005), which is compatible with values $\Delta\mathcal{E}/\mathcal{E}_\mathrm{d} \simeq 0.17$. However, the other two known GF events (SGR 0525-66 and SGR 1900 + 14; see Cline et al. 1980; Hurley et al. 1999) display significantly smaller amounts of energy during their initial peaks.

The range of $\Delta\mathcal{E}/\mathcal{E}_\mathrm{d}$ in our simulations depends on the choice of initial models. The detailed analysis in Akgün et al. (2018a) shows that $\Delta\mathcal{E}/\mathcal{E}_\mathrm{d}$ could, in principle, be as large as 0.8 for models with the appropriate values of s and σ and the value of P_c to be at the maximum of the corresponding sequence (see fig. 3 in Akgün et al. 2018a). However, the astrophysical path that could lead to an unstable configuration this far away from the equilibrium branch is

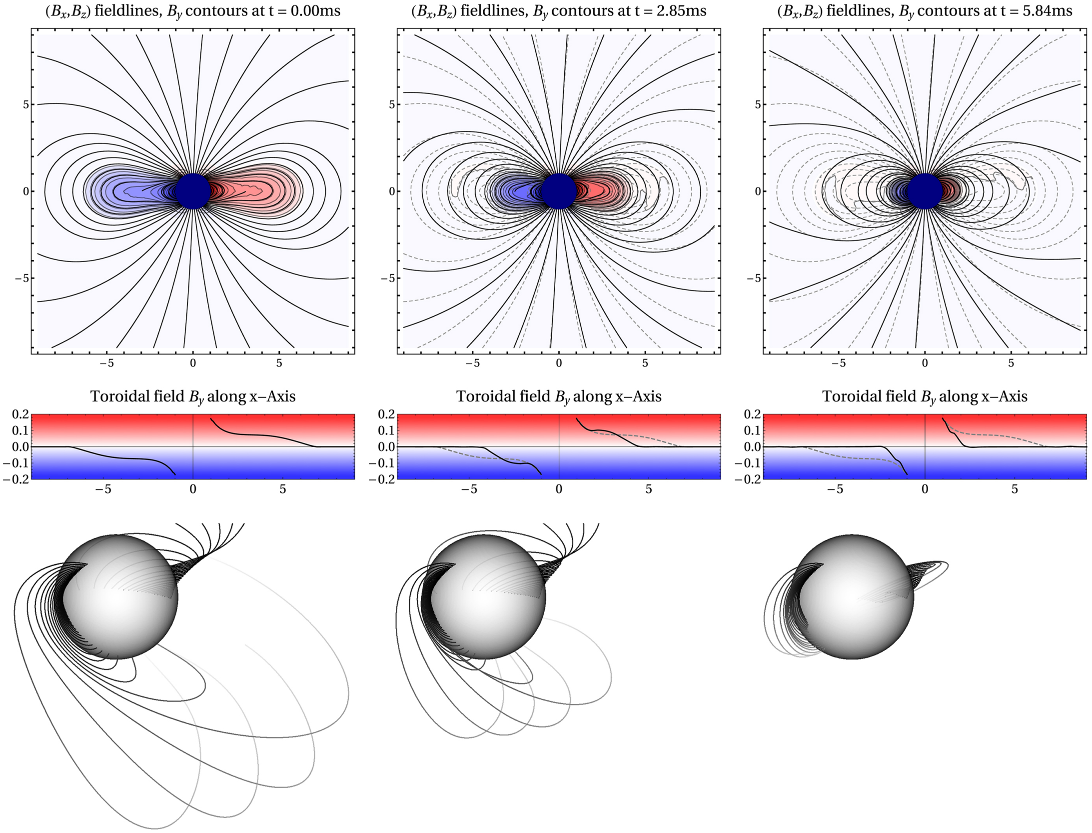

Figure 4. Field line evolution (high resolution, 32 points per R_*) of the C2 initial model (Table 2). The initially extended lobes of magnetic twist relax towards a dipolar structure and fall towards the central object. Strong energy dissipation (see Fig. 3) occurs when the magnetic twist collapses on to the magnetar crust. The final configuration is dipole-like, though it fully relaxes on a much longer dynamical time-scale. *Top:* Poloidal field lines (cross-section through the 3D data) and colour-filled contours of the toroidal magnetic field (same colour coding as below). The initial field line configuration is indicated by grey dashed lines. *Middle:* Toroidal field distribution along the *x*-axis. The initial toroidal magnetic field is denoted by grey dashed lines. *Bottom:* Evolution of selected field lines in 3D, displaying the twist relaxation. *Click for animation:* Evolution of total magnetospheric energy and selected field lines in 3D of the (high resolution) C2 initial model (Acrobat Reader only).

unclear. Speaking in terms of evolution, models close to the stability threshold for which $\Delta\mathcal{E}/\mathcal{E}_{\mathrm{d}}$ could be a small fraction of the energy encountered in our simulations are much more likely than models with values of e.g. $\Delta\mathcal{E}/\mathcal{E}_{\mathrm{d}} > 0.2$.

The time-scale on which $\mathcal{E}_{\mathrm{r}}$ is released ($\Delta t_{\mathrm{r}} \sim 1{-}5$ ms; see Table 3) is consistent with the dynamical time-scales in the magnetosphere (Section 2.2.2). If we estimate the luminosity of the energy released as

$$L_0 := \frac{\mathcal{E}_{\mathrm{r}}}{\Delta t_{\mathrm{r}}}\,, \tag{23}$$

we find that $L_0 \sim (0.7-4)\times 10^{49}\,\mathrm{erg\,s^{-1}}$ for the unstable models listed in Table 4. This dynamical luminosity is significantly larger than the peak luminosity of GFs (e.g. the peak luminosity of SGR 1806-20 is $\sim 2\times 10^{47}\,\mathrm{erg\,s^{-1}}$; Hurley et al. 2005), and suggests that only a fraction of the released energy contributes to explain the thermal properties of GFs in SGRs. As an alternative, not necessarily exclusive, we consider different mechanisms to broaden the time-scale over which the energy leaks out of the system, hence reducing L_0, in the following sections.

6.2 Stresses induced in the crust

Fig. 5 suggests that a significant part of the released energy is transferred into the magnetar crust during the (fully force-free) evolution. We would like to point out that an exact modelling of magnetar crust physics will be necessary in order to simulate respective feedback mechanisms between the stellar surface and the magnetosphere. However, in this section we make some crude estimates regarding the stresses induced in the crust as a result of the magnetospheric evolution of our models.

The stresses induced in the crust by the evolving magnetosphere can be computed studying the momentum-transfer from the magnetosphere to the crust. The stress tensor in the (force-free)

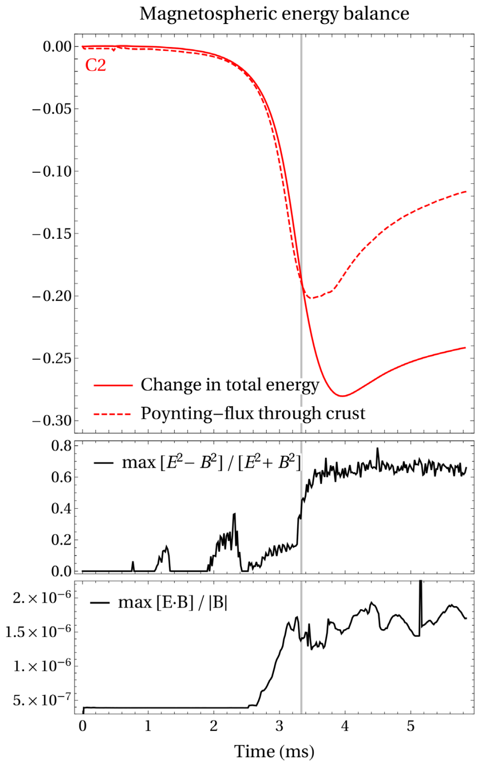

Figure 5. Energy balance during the evolution of the high resolution model C2 (Table 2). *Top:* Comparison of the change in total magnetospheric energy, normalized to the energy of a magnetosphere equipped with a pure dipolar magnetic field, $\Delta\mathcal{E}/\mathcal{E}_\mathrm{d}$, as well as the Poynting flux through the magnetar surface. Up to a simulation time of $t \sim 3.33$ ms the energy change is dominated by Poynting flux on to the magnetar crust. *Middle:* Maximum violation of the $\tilde{\boldsymbol{B}}^2 - \tilde{\boldsymbol{E}}^2 \geq 0$ condition throughout the numerical grid. *Bottom:* Maximum violation of the $\tilde{\boldsymbol{B}} \cdot \tilde{\boldsymbol{E}} = 0$ constraint throughout the numerical grid. At the time of the breakdown of conditions (10) and (11), the energy change is dominated by secondary (possibly numerical) effects.

magnetosphere is

$$T^{ij}_{\mathrm{ms}} = \frac{1}{4\pi}\left(\frac{1}{2}\delta^{ij}\left(E^2_{\mathrm{ms}} + B^2_{\mathrm{ms}}\right) - E^i_{\mathrm{ms}}E^j_{\mathrm{ms}} - B^i_{\mathrm{ms}}B^j_{\mathrm{ms}}\right), \qquad (24)$$

where B^i_{ms}, and E^i_{ms} are the magnetic and electric fields in the magnetosphere. The stress tensor in the crust consists of the contribution of the magnetic field, the fluid, and the stress of the solid

$$T^{ij}_{\mathrm{c}} = \mathcal{P}\delta^{ij} + \frac{1}{4\pi}\left(\frac{1}{2}\delta^{ij}B^2_{\mathrm{c}} - B^i_{\mathrm{c}}B^j_{\mathrm{c}}\right) + \sigma^{ij}, \qquad (25)$$

where $\mathcal{P}$ is the pressure of the fluid, B^i_{c} the magnetic field inside the crust, and σ^{ij} is the stress tensor of the deformed solid. Especially, $\sigma^{ij} = 0$ for a non-deformed solid – which holds at the beginning of the presented simulations in which the crust is relaxed after the long-term magneto-thermal evolution during which plastic deformations can keep this relaxed state. Throughout the instability phase captured in our simulations, the magnetosphere induces a stress in the crust that effectively deforms it. The Lagrangian displacement of any point in the crust with respect to the relaxed state is given by the deformation vector ξ^i. For linear displacements, the stress tensor can be expressed in terms of the deformation vector (Landau & Lifshitz 2012) as follows:

$$\sigma^{ij} = K\xi^k_{;k}f^{ij} + 2\mu\left(\frac{1}{2}(\xi^{j;i} + \xi^{i;j}) - \frac{1}{3}f^{ij}\xi^k_{;k}\right), \qquad (26)$$

where semicolon indicates the covariant derivative, f_{ij} the flat 3-metric, K is the bulk modulus, and μ the shear modulus. Crust and magnetosphere can only interchange momentum through $T^{r\theta}$ and $T^{r\varphi}$. Hence, these are the only relevant components. Imposing continuity of these two components at the surface of the star ($\mathcal{P} = 0$) one finds

$$-\frac{1}{4\pi}\left(E^r_{\mathrm{ms}}E^a_{\mathrm{ms}} + B^r_{\mathrm{ms}}B^a_{\mathrm{ms}}\right) = -\frac{1}{4\pi}B^r_cB^a_c + \sigma^{ra} \qquad a = \{\theta, \varphi\}, \qquad (27)$$

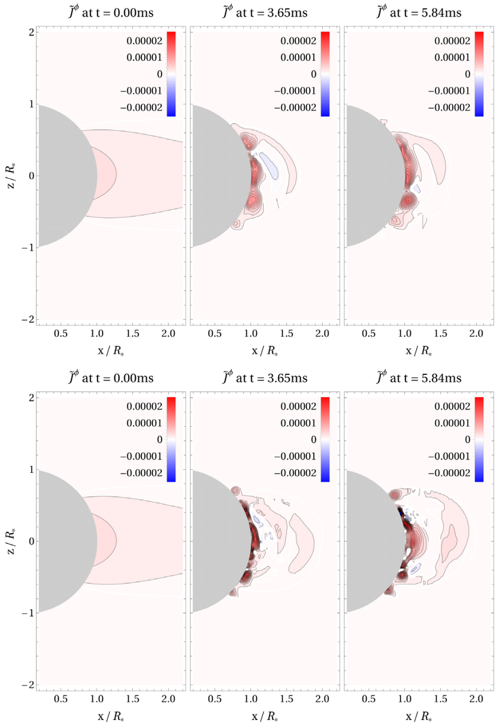

Figure 6. *xz*-cross-sections of the toroidal current in geometrized units showing the development of strong surface currents during the evolution, in addition to other currents extended on larger magnetospheric volumes. *Top:* Low resolution model C2 (16 points per R_*). *Bottom:* High resolution model C2 (32 points per R_*). The high resolution evolution shows currents located around the magnetar surface with more detailed structures, emphasizing their interpretation as surface currents. The spatial coincidence of the currents in both resolutions reinforce the argument that the observed currents are of physical origin (in spite of the – relatively small – differences among different resolutions).

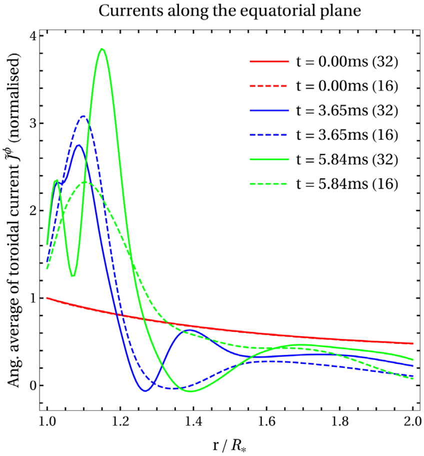

Figure 7. Azimuthal angular averages of the toroidal current (normalized to its initial value at the stellar surface) in the equatorial plane showing the development of surface currents during the evolution of the C2 initial model. We display the current evolution for both low resolution (16 points per R_*, denoted by dashed lines), and high resolution (32 points per R_*, denoted by solid lines) models. The increase of the toroidal current during the transient of energy dissipation (see Fig. 3) at the lower resolution (compare the two blue lines) may be attributed to a faster onset of the twist instability for this model.

Table 3. Selection of electromagnetic quantities monitored throughout the (high resolution, 32 points per R_*) simulation of the models of Table 2. The total change in energy $\Delta\mathcal{E}$ (displayed as a fraction of the vacuum dipole energy; equation 21) corresponds to the maximum drop of electromagnetic energy during the total runtime (see Section 6.1). The operator $\Delta_{\rm mx}$ acting on any quantity $A(t,\boldsymbol{x})$ is defined as $\Delta_{\rm mx}A := \max_{\{t,|\boldsymbol{x}|=R_*\}}\{A(t,\boldsymbol{x})-A(0,\boldsymbol{x})\}/\max_{\{|\boldsymbol{x}|=R_*\}}A(0,\boldsymbol{x})$. Hence, $\Delta_{\rm mx}J$ is the maximum increase in current density in the magnetosphere during the relaxation relative to the initial values (see Section 2.1). In the right-hand columns, $\Delta_{\rm mx}T^{r\varphi}$ and $\Delta_{\rm mx}T^{r\theta}$ denote the maximum increase of electromagnetic stresses relative to their corresponding initial values (see Section 6.2) on the stellar surface compared to its initial value. We highlight with bold face the maximum values of each of the last four columns.

Model	$\Delta t_{\rm r}$(ms)	$\Delta\mathcal{E}/\mathcal{E}_{\rm d}$	$\Delta_{\rm mx}J$	$\Delta_{\rm mx}T^{r\varphi}$	$\Delta_{\rm mx}T^{r\theta}$
A1	5.8400	0.0033	0.0159	0.0012	0.0010
A2	1.4162	0.0963	1.6350	0.0295	0.0150
B1	5.8400	0.0042	0.0363	0.0012	0.0014
B2	3.0427	0.1002	0.9805	0.0358	0.0232
C1	5.8400	0.0009	0.0640	0.0008	0.0013
C2	2.1604	**0.2808**	**3.5400**	0.0851	0.0414
C3	1.0490	0.1962	3.1720	**0.1008**	**0.0811**

and therefore

$$\sigma^{ra} = \frac{1}{4\pi}\left(B^r_{\rm c}B^a_{\rm c} - E^r_{\rm ms}E^a_{\rm ms} - B^r_{\rm ms}B^a_{\rm ms}\right) \qquad a = \{\theta, \varphi\}. \tag{28}$$

For the equilibrium configuration at the beginning of the simulation, in which $\boldsymbol{E} = 0$ and $\boldsymbol{B}$ is continuous (no initial current sheets), the mechanical stress is zero ($\sigma^{ra} = 0$) and, hence, the stress at the surface is just $T^{ra}_{\rm c} = -B^r_{\rm ms}(t=0)B^a_{\rm ms}(t=0)/(4\pi)$. Therefore, we can compute the mechanical stress at any time as

$$\sigma^{ra} = T^{ra}_{\rm ms} - T^{ra}_{\rm ms}(t=0). \tag{29}$$

As discussed in Section 2.2.2, the magnetic fields are dominant in the outermost low-density part of the crust and can be considered to be force-free (Beloborodov 2009). The point at which the magnetic field lines are anchored is not the surface of the star, but some radius, $r_{\rm c}$, below it (see also the discussion referencing Fig. 1). However, equation (28) still holds at this radius, because P is continuous, and the relevant terms cancel out. In other words, from the point of view of the numerical simulation, the inner boundary condition therein used corresponds to $r_{\rm c}$, and not the radius of the star. The force-free region of the crust corresponds to the region where shear stresses do not play a role in the dynamics, i.e. $\mu \ll B^2$. For typical magnetar magnetic fields of $B \sim 10^{15}$ G this is fulfilled for $\mu_{\rm c} \ll 10^{30}\,{\rm erg\,cm^{-3}}$, which typically and for a large variety of equations of state (Steiner & Watts 2009) corresponds to densities of $\rho \ll 10^{14}\,{\rm g\,cm^{-3}}$.

For the discussion at hand, we will consider that the anchoring is produced at some point between the inner crust outer boundary ($\rho \approx 4\times10^{11}\,{\rm g\,cm^{-3}}$), with $\mu_{\rm IC} \approx 1.4\times10^{28}\,{\rm erg\,cm^{-3}}$, and $\mu_{14} \sim 10^{30}\,{\rm erg\,cm^{-3}}$, its value close to the core-crust transition, at about $10^{14}\,{\rm g\,cm^{-3}}$. The relevant components of the stress tensor in spherical coordinates are

$$\sigma^{r\theta} = 2\mu\, s^{r\theta} = \mu\left[r\partial_r\left(\frac{\xi^\theta}{r}\right) + \frac{1}{r}\partial_\theta\xi^r\right], \tag{30}$$

$$\sigma^{r\varphi} = 2\mu\, s^{r\varphi} = \mu\left[r\partial_r\left(\frac{\xi^\varphi}{r}\right) + \frac{1}{r\sin\theta}\partial_\varphi\xi^r\right], \tag{31}$$

where s^{ij} is the strain tensor. For sufficiently large strains the crust will fail and a rapid plastic deformation will deform the crust persistently. The breaking strain of the crust has been estimated to be about 0.1 (Horowitz & Kadau 2009). Therefore, any stress larger than $\sim 0.2\mu_{\rm c}$ will likely produce a failure in the crust. The maximum mechanical stress exerted on the magnetar crust, $\sigma^{ra}_{\rm max}$, can be quantified directly from the results shown in Tables 2 and 3 by employing the conversion formula

$$\sigma^{ra}_{\rm max} = 5.55\times10^{28}\,{\rm erg\,cm^{-3}}\left(\frac{\Delta_{\rm mx}T^{ra}}{0.1}\right)\left(\frac{\tilde{T}^{ra}_{\rm max}}{10^{-9}}\right)\left(\frac{B_{\rm pole}}{10^{15}\,{\rm G}}\right)^2. \tag{32}$$

The maximum mechanical stress (see Fig. 8) on the magnetar crust measured throughout the shown simulations (see Tables 2 and 3) correspond to $\sigma^{ra} \approx 10^{28}\,{\rm erg\,cm^{-3}}$ for $B_{\rm pole} \approx 10^{15}$ G. Considering the quadratic leverage of the magnetic field strength, mechanical stresses of $\sigma^{ra} \approx 10^{30}\,{\rm erg\,cm^{-3}}$ are likely to be reached for $B_{\rm pole} \approx 10^{16}$ G and beyond. The largest mechanical stresses are exerted in case of the high energy models A2, B2, C2, and C3.

Our numerical simulations indicate that the instability occurs in a quasi-axisymmetric way (cf. Fig. 4), with deviations from axisymmetry of less than 1 per cent.[5] In axisymmetry, axial displacements (ξ^φ) and polar displacements (ξ^r, ξ^θ) decouple and it is possible to estimate the axial displacement from the $\sigma^{r\varphi}$ component of the stress tensor. Although the magnetospheric dynamics can, in principle, induce radial deformations, ξ^r, in reality those deformations are strongly suppressed because they involve the motion of matter parallel to the gravitational field (not included in our calculation). Therefore, in practice one can consider $\xi^r = 0$, such that

$$\sigma^{r\varphi} = \mu\, r\partial_r\left(\frac{\xi^\varphi}{r}\right), \tag{33}$$

---

[5] We quantify these deviations performing a multipolar expansion of the eletromagnetic energy and evaluating the energy stored in modes with azimuthal numbers $m > 0$.

Table 4. Energetics of our models scaled to a magnetic field strength $B_{\rm pole} = 10^{15}$ G. (i) Energy released. (ii) Estimates of dynamic luminosity L_0 (equation 23). (iii) Estimates of photospheric luminosity $L_{\rm ph}$ (equation 53). (iv) Estimates of photospheric temperature $k_{\rm B}T_{\rm ph}$ (equation 52). Rows (v) and (vi) display the estimated photospheric luminosity $\mathcal{L}_{\rm ph}$ and temperature $k_{\rm B}\mathcal{T}_{\rm ph}$ computed for the case in which $\eta < \eta_*$, assuming that the energy is released over a time-scale $\Delta t_{\rm spike} = 0.1$ s (equation 56). Finally, rows (vii) and (viii) show the initial luminosity $\mathcal{L}_0$ (equation 56) and temperature $k_{\rm B}\mathcal{T}_0$ also assuming that the energy is released over a time-scale $\Delta t_{\rm spike} = 0.1$ s. Note that the last two rows coincide with the photospheric values if $\eta > \eta_*$.

		C2	C3	B2	A2
(i)	$\mathcal{E}_{\rm r}$ (erg)	6.03×10^{46}	4.21×10^{46}	2.15×10^{46}	2.07×10^{46}
(ii)	L_0 (erg s^{-1})	2.78×10^{49}	4.00×10^{49}	7.05×10^{48}	1.46×10^{48}
(iii)	$L_{\rm ph}$ (erg s^{-1})	9.32×10^{47}	2.31×10^{47}	5.9×10^{47}	3.49×10^{47}
(iv)	$k_{\rm B}T_{\rm ph}$ (keV)	25	21	43	84
(v)	$\mathcal{L}_{\rm ph}$ (erg s^{-1})	2.60×10^{47}	2.31×10^{47}	1.84×10^{47}	1.82×10^{47}
(vi)	$k_{\rm B}\mathcal{T}_{\rm ph}$ (keV)	121	140	186	189
(vii)	$\mathcal{L}_0$ (erg s^{-1})	6.03×10^{47}	4.21×10^{47}	2.15×10^{47}	2.07×10^{47}
(viii)	$k_{\rm B}\mathcal{T}_0$ (keV)	281	257	217	215

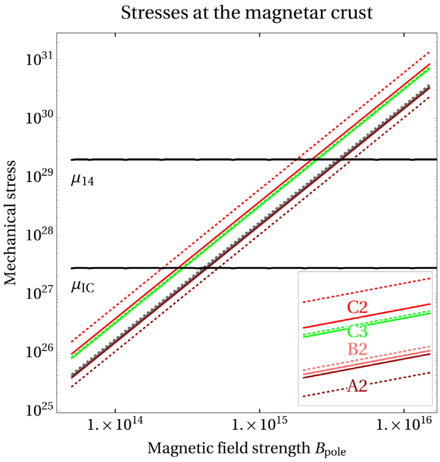

Figure 8. Mechanical stresses exerted on the magnetar crust (according to equation 32) for the maximum stresses (Tables 2 and 3) observed during the high resolution simulations of models A2, B2, C2, and C3. The stress component $\sigma^{r\varphi}$ is denoted by solid lines, the component $\sigma^{r\theta}$ by dotted lines. The colour coding corresponds to the initial models as introduced in Fig. 3. The black lines denote the approximate breaking stresses $\sim 0.2\mu_{\rm IC}$, and $\sim 0.2\mu_{14}$, at the inner crust boundary and near the core-crust transition, respectively. The high energy models reach the limit of a possible breaking of field lines for field strengths of $B_{\rm pole} \approx 10^{15}$–$10^{16}$ G.

$$\sigma^{r\theta} = \mu\, r\, \partial_r \left(\frac{\xi^\theta}{r}\right). \tag{34}$$

The transition at the anchoring point happens across a small distance, $h \equiv R_* - r_{\rm c}$, over which we can consider that $\mu = \mu_{\rm c}$ and σ^{ra} are constant. Integrating the stress tensor along this distance we obtain:

$$\xi^a_{\rm c} = r_{\rm c}\frac{\sigma^{ra}}{\mu_{\rm c}} \ln\left(\frac{r_{\rm c}}{r_{\rm c} + h}\right) \approx R_* \frac{\sigma^{ra}}{\mu_{\rm c}}, \tag{35}$$

for $h \ll r_{\rm c}$, R_*, and independent of the size of the transition layer, h. The radial force per unit volume induced by the applied stress is (Landau & Lifshitz 2012)

$$f^r = \sigma^{rk}{}_{;k} = \frac{1}{r}\left(\partial_\theta \sigma^{r\theta} + \cot\theta\, \sigma^{r\theta}\right) + \frac{1}{r\sin\theta}\partial_\varphi \sigma^{r\varphi}, \tag{36}$$

where we have considered that the only non-vanishing components are $\sigma^{r\theta}$ and $\sigma^{r\varphi}$. We can estimate the radial displacement ξ^r balancing this force with the gravitational force on the displaced mass, taken out of hydrostatic equilibrium. We can make an order of magnitude estimate using linear perturbation theory if one neglects terms including gradients of background quantities and perturbations of the gravitational potential. In that case, the force balance reads:

$$c_s^2\, \rho\, \partial_{rr} \xi^r \approx -f_r. \tag{37}$$

Integrating over the transition length h we get

$$\xi^r \approx -\frac{f_r\, h^2}{2\, c_s^2\, \rho} \approx -\frac{c^2_{\rm shear}}{c_s^2} h^2 s^{rk}{}_{;k}, \tag{38}$$

where $c^2_{\rm shear} \equiv \mu/\rho$ is the shear speed. For typical values in the crust one assumes $c^2_{\rm shear}/c^2_s \sim 10^{-2}$. If we consider the maximum possible strain, i.e. the breaking strain, $s^{ij} \sim h s^{ij}{}_{;j} \sim 0.1$ (Horowitz & Kadau 2009), and the maximum possible value for $h \sim \Delta R \sim 1$ km, the size of the crust, one finds an upper limit for the radial displacement of $\xi^r_{\rm max} \sim 100$ cm. At the same time, the displacement components may be estimated directly from the results displayed in Fig. 8 by employing equation (35) and $\mu_{\rm c} = 0.5 \times (\mu_{14} + \mu_{\rm IC})$:

$$\xi^a_{\rm c} \approx 2.7 \times 10^4\ {\rm cm} \left(\frac{\sigma^{ra}}{10^{28}\ {\rm erg\ cm^{-3}}}\right)\left(\frac{B_{\rm pole}}{10^{15}\ {\rm G}}\right)^2\left(\frac{R_*}{13.7\ {\rm km}}\right). \tag{39}$$

Our results show that for typical magnetar field strengths ($B \gtrsim 10^{15}$ G) the instability is likely to break a large fraction of the crust down to the inner crust. For the largest magnetic fields ($B \gtrsim 10^{16}$ G) the stresses induced in the crust are sufficient to shatter the entire crust. We should mention that the three magnetars that have showed GFs are among the more magnetized known ones and all three exceed 5×10^{14} G.

6.3 Emission processes

6.3.1 Estimation of observational properties of the energy release

We have advanced that our models may release $\mathcal{E}_{\rm r} \approx 2.1 \times 10^{46} - 6.4 \times 10^{46}$ erg on time-scales of milliseconds, producing, therefore, dynamic luminosities $L_0 \sim (0.7 - 4) \times 10^{49}$ erg s^{-1} for the unstable models listed in Table 4. Following the reasoning of Thompson & Duncan (1995), confining this energy in the form of a photon-pair plasma by a closed magnetic flux loop of outer radius r requires that the field pressure at the outer boundary of the loop exceed the deposited energy density

$$\frac{B(r)^2}{8\pi} \gtrsim \frac{\mathcal{E}_\mathrm{r}}{4\pi/3(r^3 - R^3)}. \tag{40}$$

In a dominantly dipolar magnetosphere, $B(r) \sim B_\mathrm{pole}(R_*/r)^3$, the plasma can be confined if $\mathcal{E}_\mathrm{r} < \mathcal{E}_\mathrm{d}/2$ within a radius r in the range

$$\frac{\mathcal{E}_\mathrm{d}}{\mathcal{E}_\mathrm{r}}\left[1-\sqrt{1-2\frac{\mathcal{E}_\mathrm{r}}{\mathcal{E}_\mathrm{d}}}\right] \lesssim \left(\frac{r}{R_*}\right)^3 \lesssim \frac{\mathcal{E}_\mathrm{d}}{\mathcal{E}_\mathrm{r}}\left[1+\sqrt{1-2\frac{\mathcal{E}_\mathrm{r}}{\mathcal{E}_\mathrm{d}}}\right]. \tag{41}$$

For the range of values of $\mathcal{E}_\mathrm{r}/\mathcal{E}_\mathrm{d} \sim \Delta\mathcal{E}/\mathcal{E}_\mathrm{d}$ from our models (Table 3) we obtain that the size of the confinement region, $\Delta R \equiv r - R_*$, is limited by

$$(1.8 - 6) \times 10^{-2}\, R_* \lesssim \Delta R \lesssim (0.8 - 1.7)\, R_*. \tag{42}$$

Note that this result is independent of the magnetic field strength B_pole.

Our numerical simulations show that most of the energy is released in a thin and numerically unresolved surface current of the star, that we measure as a Poynting flux (see Fig. 5) and in a region close to the surface ($r \lesssim 1.25R_*$) with large currents (see Figs 6 and 7). Energy deposited there, essentially at the footprints of magnetic field lines, is expected to distribute efficiently along those lines aided by the flowing pair plasma. As a result, we expect that the energy will fill an extended region of the magnetosphere comparable in size to the region filled with currents (see Fig. 4). This region can be as large as $\sim 4R_*$ at the time of maximum energy dissipation. For magnetic field lines extending within the limits given by equation (42), the energy is expected to be confined. However, for lines extending beyond $(0.8{-}1.7)R_*$, the energy will not be confined and it may yield an ultrarelativistic fireball composed of pairs, photons, and a small amount of baryons lifted up from the outer crust by the large energy released there. Depending on the structure of the magnetosphere, the energy released in this form can be a significant fraction of $\mathcal{E}_\mathrm{r}$. Obviously, our methodology does not allow us to track the evolution of the released energy, but we may obtain a rough estimation of its bolometric properties. For the estimate we will consider that most of the energy is released in the fireball, which gives us upper limits.

The physics of such expanding fireball has been considered in many papers (e.g. Goodman 1986; Paczynski 1986; Shemi & Piran 1990; Meszaros, Laguna & Rees 1993; Piran, Shemi & Narayan 1993), especially addressing the generation of gamma-ray burst (GRBs), but also applied to SGRs (e.g. Nakar, Piran & Sari 2005). The sudden energy release results into a thermal burst carrying *most* of the initial energy, and according to the canonical interpretation (e.g. Hurley et al. 2005), with roughly the original temperature and a fraction of the energy in the form of relativistic pairs. The observed thermal spectrum of the flare and its temperature support this idea.

Here we follow the model of Mészáros & Rees (2000), which suffices for the basic estimates we aim at. Assuming that in a region of size $R_0 \simeq R_*$ (initially at rest), energy is released at a rate L_0, the initial temperature of the fireball in units of the electron rest mass is (Mészáros & Rees 2000, equation 2)

$$\Theta_0 = \left(\frac{k_\mathrm{B}}{m_e c^2}\right)\left(\frac{L_0}{4\pi R_0^2 c a_r}\right)^{1/4}$$
$$= 1.43\left(\frac{L_0}{2.8\times 10^{49}\,\mathrm{erg\,s^{-1}}}\right)^{1/4}\left(\frac{R_0}{1.37\times 10^{6}\,\mathrm{cm}}\right)^{-1/2}, \tag{43}$$

where $m_e = 9.1095 \times 10^{-28}$ g is the electron mass, $a_r = 7.57 \times 10^{-15}$ g cm^{-1} s^{-2} K^{-4} is the radiation constant, and $k_\mathrm{B} \simeq 1.38 \times 10^{-16}$ erg K^{-1} is the Boltzmann constant. In the previous equation (and hereafter) we have scaled the luminosity to the dynamical luminosity estimated for model C2, but a similar exercise has been undertaken for models C3, B2, and A2, being the results listed in Table 4. The value of Θ_0 in equation (43) corresponds to a comoving temperature $k_\mathrm{B}T_0 \simeq 732$ keV. Starting from its initial radius, R_0, the fireball expands and accelerates until it converts most of its internal energy into kinetic energy at a distance R_s, commonly called the saturation radius (see equations 50 and 51 below). The Lorentz factor, Γ, of the expanding fireball is approximately given by

$$\Gamma = \begin{cases} \dfrac{r}{R_0} & \text{if } r < R_\mathrm{s}, \\[2mm] \dfrac{R_\mathrm{s}}{R_0} & \text{if } r \geq R_\mathrm{s}. \end{cases} \tag{44}$$

The amount of mass that may be unbound due to an energy release as large as suggested by our models ($\mathcal{E}_\mathrm{r}$) is uncertain, but we may estimate it to be as small as $M_\mathrm{ex} \simeq 3 \times 10^{-10}\,\mathrm{M}_\odot$. The period over which this mass is extracted we assume to be the same as that over which the energy is released, Δt_r. This implies a mass-loss rate from the magnetar surface $\dot{M} \simeq M_\mathrm{ex}/\Delta t_\mathrm{r} \simeq 2.8 \times 10^{26}$ g s^{-1}. The dimensionless entropy of the fireball for this baryon load is

$$\eta = \frac{L_0}{\dot{M}c^2}$$
$$\simeq 110\left(\frac{L_0}{2.8\times 10^{49}\,\mathrm{erg\,s^{-1}}}\right)\left(\frac{\dot{M}}{2.8\times 10^{26}\,\mathrm{g\,s^{-1}}}\right)^{-1}. \tag{45}$$

As usual, we define the photospheric radius as the distance at which the fireball becomes optically thin, which may happen before the Lorentz factor saturates or after that, i.e. in the regime where the fireball coasts

$$R_\mathrm{ph} \simeq \frac{L_0 \sigma_\mathrm{T} Y}{4\pi m_\mathrm{p} c^3 \eta^3}, \qquad (R_\mathrm{ph} > R_\mathrm{s}) \tag{46}$$

$$R_\mathrm{ph} \simeq \left(\frac{L_0 \sigma_\mathrm{T} Y}{4\pi m_\mathrm{p} c^3 \eta}\right)^{1/3}. \qquad (R_\mathrm{ph} \leq R_\mathrm{s}) \tag{47}$$

Here, $\sigma_\mathrm{T} = 6.6525 \times 10^{-25}$ cm^2 and $m_\mathrm{p} = 1.6726 \times 10^{-24}$ g are the Thompson cross-section and the proton mass, respectively. Y represents the number of electrons per baryon. In the following, we will take $Y \simeq 1$, which is appropriate once pairs are not present in the system. Indeed, this shall be the case for radii larger than R_p (Mészáros & Rees 2000, equation 3)

$$R_\mathrm{p} = R_0 \frac{\Theta_0}{\Theta_p} \simeq 5.8 \times 10^7\,\mathrm{cm}$$
$$\times \left(\frac{L_0}{2.8\times 10^{49}\,\mathrm{erg\,s^{-1}}}\right)^{1/4}\left(\frac{R_0}{1.37\times 10^{6}\,\mathrm{cm}}\right)^{1/2}\left(\frac{\Theta_p}{0.03}\right)^{-1}, \tag{48}$$

where the comoving dimensionless temperature below which $e^\pm$ pairs drop out of equilibrium is $\Theta_p \simeq 0.03$ (equivalently, $k_\mathrm{B}T_p \simeq 17.4$ keV). Note that $R_p \ll R_\mathrm{ph}$ (see equations 46 and 47).

The critical baryon load, η_* for which the photospheric radius equals the saturation radius, i.e. $R_\mathrm{ph} = R_\mathrm{s}$, is given by (Mészáros & Rees 2000, equation 5)

$$\eta_* = \left(\frac{L_0 \sigma_\mathrm{T}}{4\pi m_p c^3 R_0}\right)^{1/4}$$
$$\simeq 393\left(\frac{L_0}{2.8\times 10^{49}\,\mathrm{erg\,s^{-1}}}\right)^{1/4}\left(\frac{R_0}{1.37\times 10^{6}\,\mathrm{cm}}\right)^{-1/4}. \tag{49}$$

Depending on the value of the parameter η, there are two regimes. Either the photospheric radius happens beyond the saturation radius ($\eta < \eta_*$) or, otherwise, the saturation radius happens when the fireball is still expanding ($\eta > \eta_*$). In the former case, the saturation radius is

$$R_\mathrm{s} = \eta R_0 \simeq 1.5\times 10^8\,\mathrm{cm}\left(\frac{R_0}{1.37\times 10^6\,\mathrm{cm}}\right)\left(\frac{\eta}{110}\right), \qquad (50)$$

where we have used for η the value computed in equation (45) for the assumed value of $\dot{M}$. If the photosphere appears when the fireball is still accelerating, the saturation radius is attained at a distance (Mészáros & Rees 2000, equation 11)

$$R_\mathrm{s} = \eta_* R_0 \simeq 5.4\times 10^8\,\mathrm{cm} \times\left(\frac{L_0}{2.8\times 10^{49}\,\mathrm{erg\,s^{-1}}}\right)^{1/4}\left(\frac{R_0}{1.37\times 10^6\,\mathrm{cm}}\right)^{3/4}, \qquad (51)$$

Interestingly, Hurley et al. (2005) model the peak of SGR 1806-20 assuming that the dimensionless entropy of the fireball is $\eta > \eta_*$ because for the observed peak luminosity (much smaller than that implied in our models, namely, $\sim 2\times 10^{47}$ erg s^{-1}), the critical baryon load would be 3–4 times smaller than estimated in equation (49) and, hence, Hurley et al. (2005) naturally obtain $\eta \gtrsim \eta_*^{(1806-20)}$. The observational difference between the two described regimes is notable for our models as we see next in the estimation of the photospheric temperature and luminosity of the events. In the case $\eta < \eta_*$, the photospheric temperature and luminosity are, respectively,

$$k_\mathrm{B}T_\mathrm{ph} = k_\mathrm{B}T_0\left(\frac{R_\mathrm{ph}}{R_\mathrm{s}}\right)^{-2/3} \simeq 25\,\mathrm{keV}\left(\frac{L_0}{2.8\times 10^{49}\,\mathrm{erg\,s^{-1}}}\right)^{-5/12} \times\left(\frac{\eta}{110}\right)^{8/3}\left(\frac{R_0}{1.37\times 10^6\,\mathrm{cm}}\right)^{-5/6}, \qquad (52)$$

and (Mészáros & Rees 2000, equation 9),

$$L_\mathrm{ph} = L_0\left(\frac{R_\mathrm{ph}}{R_\mathrm{s}}\right)^{-2/3} \simeq 9.3\times 10^{47}\,\mathrm{erg\,s^{-1}}\left(\frac{L_0}{2.8\times 10^{49}\,\mathrm{erg\,s^{-1}}}\right)^{7/12} \times\left(\frac{\eta}{110}\right)^{8/3}\left(\frac{R_0}{1.37\times 10^6\,\mathrm{cm}}\right)^{-5/6}. \qquad (53)$$

The value obtained in equation (52) must be compared with the ones obtained from observations, namely $k_\mathrm{B}T_\mathrm{peak}^\mathrm{obs} \simeq 175 - 250$ keV. Our result underestimates the observed temperature significantly. However, we are neglecting Comptonization effects, which may slightly raise the estimated photospheric temperature (still below the observational data). Note that smaller values of L_0, in line with the observed luminosities at peak for SGRs, would bring the observed photospheric temperature to the observed values, but, at the same time, they would significantly raise the photospheric luminosity, hence yielding events much more luminous than observed. The dependence on $\eta^{8/3}$ is the same in both equations (52) and (53), therefore, changes in the assumed baryon loading may not improve the consistency of our estimated photospheric values with the observed ones. However, if the baryon load is sufficiently small such that $\eta > \eta_*$ (as assumed in Hurley et al. 2005), the declining temperature and luminosity in the outflow are compensated by the relativistic blueshift. In this case, we would estimate the following photospheric temperature

$$k_\mathrm{B}T_\mathrm{ph} = k_\mathrm{B}T_0 \simeq 723\,\mathrm{keV}\left(\frac{L_0}{2.8\times 10^{49}\,\mathrm{erg\,s^{-1}}}\right)^{1/4}\left(\frac{R_0}{1.37\times 10^6\,\mathrm{cm}}\right)^{-1/2}, \qquad (54)$$

and luminosity

$$L_\mathrm{ph} = L_0 \simeq 2.8\times 10^{49}\,\mathrm{erg\,s^{-1}}\,\mathrm{erg\,s^{-1}}. \qquad (55)$$

In this case, both estimations for T_ph and L_ph significantly overestimate the observed values for SGRs.

We have found in this section that independently of whether the photosphere of the expanding fireball happens in the acceleration phase or in the coasting phase, the estimated values of T_ph and L_ph are not compatible with observations. The root for the discrepancies found are the very large dynamic luminosities (L_0) of most of our models. These large values result from considering magnetospheric initial data where the twist is so large that they release a large amount of energy on time-scales of milliseconds. We note that models with larger relative toroidal fields (as induced by a power-index $\sigma = 2$, and $s = 2$) spanning a larger fraction of the magnetar surface (due to their smaller values of P_c), e.g. model A2 (Table 4), show values of T_ph and L_ph broadly compatible with the most energetic GFs observed so far (see e.g. Hurley et al. 2005; Coti Zelati et al. 2018). This is in contrast to models where we have built up the magnetosphere with $s = \sigma = 1$ (namely, C2, C3, and B2), which systematically yield overluminous and too cold photospheric conditions. Thus, our results suggest that twisting magnetospheres to the largest (theoretical) levels we have considered here may not be realized in nature. Well before reaching the largest twists of models C3, C2, or B2 the dynamical instability may set in releasing smaller amounts of energy (and hence, producing smaller dynamical luminosities).

A potential handicap in our models is the duration of the observational signal that yield the fireballs modelled so far. In the canonical fireball model, the energy release leads to a *frozen pulse* whose duration approximately equals the time-scale over which the energy is deposited, Δt_r (e.g. Piran et al. 1993, but see Janka et al. 2006). Since $\Delta t_\mathrm{r} \ll \Delta t_\mathrm{spike}$, the quasi-thermal radiation bursts that we have estimated are too short to account for the typical time-scale of the initial spike of GFs in SGRs ($\Delta t_\mathrm{spike} \sim 0.1$ s). In our simulations, the energy change in the magnetosphere is driven by the Poynting flux through the star surface. However, the ability of the crust to absorb all this energy on the dynamical time-scale of the magnetosphere is limited because of the low transmission coefficient (see equation 5). So far we have considered that all this energy is temporarily stored in a thin layer above the magnetospheric surface, where intense currents may convert the stored magnetic energy into thermal energy. This is consistent with the boundary conditions imposed in our numerical simulations. Alternatively, we could have chosen boundary conditions that avoid the formation of strong thin surface currents (as e.g. in Carrasco & Reula 2016). In that case, Alfvén waves propagating towards the surface of the star get reflected and collide at some distance from the surface. This forces the formation of reconnection points at some distance from the neutron star surface. Li et al. (2019) have estimated that this process is relatively inefficient in dissipating the energy of the magnetosphere and that it may take multiple bounces in the magnetosphere to dissipate all the energy. This may allow for a slower energy deposition on time-scales $\sim\Delta t_\mathrm{spike}$.

Unfortunately, our numerical models do not include the relevant microphysics to fully address the conversion of magnetic into thermal energy. Thus, we can only warn the reader that the milliseconds time-scales over which we have made our (simple) estimations of the dynamical luminosity of the models at hand are only lower bounds of the true time-scales on which the released energy may leave the magnetosphere. Taking into account this caveat, the values of L_0 listed in Table 4 are upper bounds to the effective initial luminosity, $\mathcal{L}_0$,

$$\mathcal{L}_0 := \frac{\mathcal{E}_\mathrm{r}}{\Delta t_\mathrm{spike}} \simeq 10^{47}\,\mathrm{erg\,s^{-1}} \left(\frac{\mathcal{E}_\mathrm{r}}{10^{46}\,\mathrm{erg}}\right)\left(\frac{\Delta t_\mathrm{spike}}{0.1\,\mathrm{s}}\right)^{-1}. \tag{56}$$

Redoing the previous estimations for the photospheric conditions, we find the values $\mathcal{L}_\mathrm{ph}$ and $k_\mathrm{B}\mathcal{T}_\mathrm{ph}$ listed in Table 4. In addition to these estimates of the photospheric luminosity and temperature corresponding to the values of the initial luminosity given by equation (56) when the photosphere happens beyond the saturation radius (i.e. for $\eta < \eta_*$), we also provide the estimation of the photospheric luminosity ($\mathcal{L}_0$) and temperature ($k_\mathrm{B}\mathcal{T}_0$) in the complementary case when the photospheric conditions are reached during the acceleration phase of the fireball (i.e. $\eta > \eta_*$). All these new values of the photospheric luminosity and temperature are perfectly compatible with observational data. Not surprisingly, we find that depending on whether we assume that photospheric conditions are met in the accelerating phase or in the coasting phase of the fireball, the values obtained for the photospheric temperature *bracket* the typical values found for the spike of SGRs.

6.3.2 Optical depth of the magnetosphere

The observed maximum current density throughout the magnetosphere, J_max, can be quantified directly from the results shown in Tables 2 and 3 by employing the conversion formula

$$J_\mathrm{max} = 4.4926 \times 10^{12}\,\mathrm{A\,m^{-2}} \left(\frac{\tilde{J}_\mathrm{max}}{10^{-6}}\right)\left(\frac{B_\mathrm{pole}}{10^{15}\,\mathrm{G}}\right). \tag{57}$$

The presented results compare well to the expected current density stated in equation (3). Close to the surface of the star, where the highest currents appear, the particle density is

$$n_e = \frac{J}{ce}\mathcal{M} \sim 10^{19}\,\mathrm{cm^{-3}}, \tag{58}$$

where $\mathcal{M}$ is the multiplicity. Beloborodov (2013b) has estimated that in extended regions close to the poles the multiplicity can be as large as $\mathcal{M} \sim 100$, while close to the equator $\mathcal{M} \sim 1$.

The dominant contribution to the opacity in the magnetosphere is the resonant cyclotron scattering of thermal photons off charge particles in the vicinity of the neutron star.[6] Thompson, Lyutikov & Kulkarni (2002) have estimated that for twists of $\Delta\varphi \sim 1$ the typical optical depth in the magnetosphere is $\sim$1. In general, computing the optical depth for magnetar magnetospheres is a complicated problem, because one needs a self-consistent solution of the photon field and the momentum distribution of charged particles travelling along the magnetic field lines (see Beloborodov 2013b). In this work we make an estimation for radially streaming photons and a simplified momentum distribution of charged particles. We only consider 1 keV photons, which are typical for the observed surface temperature in magnetars. Inspired by Beloborodov (2013b) we use a simple waterbag momentum distribution (see Appendix B) which is characterized by two parameters, the mean specific momentum ($\bar{p}$, where $p = vW$) and $\mathcal{M}$. We integrate the optical depth (τ) radially inwards (see appendix B, equation B1 for details on the computation) and identify the photosphere as the place where $\tau = 1$.

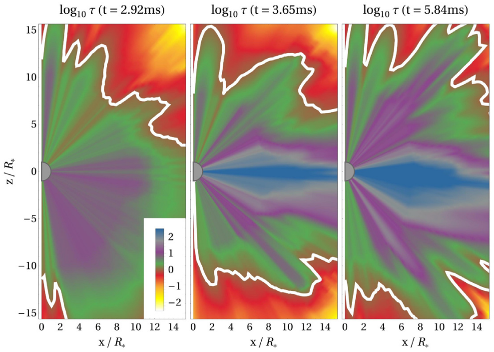

Figure 9. Snapshots of the logarithm of the optical thickness during the evolution of the high resolution version of model C2. The logarithm of the optical thickness for the $\{\mathcal{M} = 100, \gamma = 30\}$ model is displayed by the colour scale, the photosphere ($\tau = 1$) is displayed as a white solid line. See appendix B for further details.

Fig. 9 shows estimates for the optical thickness of the magnetosphere at three different times (during and after the rapid drop of magnetospheric energy) computed with parameters $\{\mathcal{M} = 100, \gamma = 30\}$. During the rearrangement of the magnetosphere, the coronal region along the equator becomes optically thick. The initial configuration is optically thin and, hence, not shown here. An important conclusion is that close to the critical point, most of the magnetosphere, if not all, is optically thin, which gives rise to a blackbody spectrum with the typical temperature of the NS surface ($\sim$ 1 keV) plus a possible non-thermal contribution of up-scattered photons. However, during the instability, the increase of the magnetospheric currents, makes a large fraction of the magnetosphere of a few stellar radii optically thick. This region is filled up with pair plasma and will emit thermal radiation through its photosphere. Its lifetime is related to the presence of strong currents in the magnetosphere and may be an explanation for the X-ray tail ($k_\mathrm{B}T \sim 30\,\mathrm{keV}$) observed after GFs and lasting for a few 100 s. We note that only a relatively small fraction of the total energy released in the magnetosphere by the instability may contribute to the tail, while most of it may contribute to the initial peak characteristic of GFs (see discussion in Section 6.3.1).

Our model to compute the magnetospheric optical thickness for resonant cyclotron scattering assumes uniform values of the multiplicity and of the electron Lorentz factor. Neither for the multiplicity (as we have argued above) nor for γ this is completely correct. Modelling locally the values of the parameters $\{\mathcal{M}, \gamma\}$ is beyond the scope of this paper. However, we may test the robustness of our results by exploring the parameter space determined by $\mathcal{M}$ and γ. In Fig. 10, we display the time evolution of the optical thickness at the equator of the magnetar for various parameter sets. As expected, the larger the value of $\mathcal{M}$, the larger the number density of leptons and, consistently, the larger the opacity (note the

---

[6] If there is a dynamical mass ejection a result of the large energy release close to the magnetar surface (Section 6.3.1), the Thompson scattering (in the expanding fireball) may be the dominant source of opacity at sufficiently large distances.

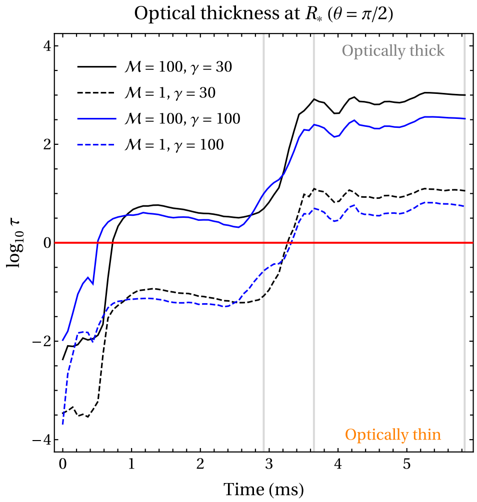

Figure 10. Evolution of the optical thickness at the equator of the magnetar ($\theta = \pi/2$, $r = R_*$) of the high resolution initial model C2 ($B_{\rm pole} = 10^{15}$ G) and various parameter sets (see legends). The modelled optical thickness depends sensitively on the chosen multiplicity $\mathcal{M}$ and Lorentz factor γ (cf. Section 6.3.2 and Appendix B). Initially, the magnetosphere is optically thin. During the onset of the instability ($\sim$1 ms) charges are produced in the magnetosphere. Depending on the chosen model ($\mathcal{M}$, γ), the magnetosphere becomes optically thick at different times. The times used for the visualization of optical thickness in Fig. 9 are denoted in grey lines.

nearly two orders of magnitude difference between the solid lines with $\mathcal{M} = 100$ and the dashed lines with $\mathcal{M} = 1$). The effect of the variation of the Lorentz factor (electrons or positrons) is small compared to the strong impact of $\mathcal{M}$ on the opacity. Although the magnetosphere becomes eventually optically thick for all the parameter sets under investigation, models with $\mathcal{M} = 100$ develop regions with $\tau > 1$ very early ($t \lesssim 0.8$ ms), while models computed with $\mathcal{M} = 1$ become optically thick only when the instability in the magnetosphere fully develops.

Emission by resonant scattering in magnetar magnetospheres may be subject to ($\perp$ or $\shortparallel$) polarization (see e.g. Fernández & Davis 2011; Beloborodov 2013b). In the presented (approximate) modelling of optical thickness, however, we have found differences in these polarization states of < 1 per cent. We will further explore the emission properties of force-free twisted magnetospheres on suitable high-resolution numerical data in our future work.

7 CONCLUSIONS

In this work, we explore the stability properties of force-free equilibrium configurations of magnetar magnetospheres by performing numerical simulations of a selection of the models computed in Akgün et al. (2018a). For the case of degenerate magnetospheres (i.e. the same boundary conditions but different energies) we validate the hypothesis of Akgün et al. (2018a) that configurations in the high-energy branches are unstable while those in the lowest energy branch are stable. This confirms the existence of an unstable branch of twisted magnetospheres. It also allows us to formulate an instability criterion for the sequences of models computed in Akgün et al. (2018a). Our results are consistent with an interesting scenario where bursts and GFs in magnetars are triggered without involving crustal failures. The twist that is naturally produced in the magnetosphere by the Hall evolution of the crust (Akgün et al. 2017) can lead to unstable configurations that will release up to a 10 per cent of the energy stored in the magnetosphere, sufficient to explain the observations.

Akgün et al. (2017) have shown that the magnetothermal evolution of the crust leads naturally to configurations close to the instability threshold. However, the amount of energy released depends on how far away from the stable branch can the evolution drive the configuration. This is essentially a problem of comparing the evolution time-scale and the instability time-scale. For the models studied in this work the instability time-scale is of the order of milliseconds, much shorter than the magnetothermal evolution time-scales of the object (see Section 2.2.1). However, close to the critical point, the growth rate of the instability could be significantly smaller (actually, it should be zero at the critical point) which would allow us to overshoot the instability threshold. Note that, since the energy reservoir is large ($\sim$$10^{46}$ erg), even a very small fraction of energy release could explain many of the phenomenology of magnetars. Alternatively, there could be phenomena leading to fast dynamics in the crust such as sustained episodes of accelerated plastic flows triggered by the magnetic stresses in the crust (Lander & Gourgouliatos 2019).

For the unstable models, we observe the development of almost axisymmetric instabilities on a time-scale of a few ms rearranging the magnetic field to a configuration similar to those in the (stable) lower energy branch. The energy of the magnetosphere also decreases towards the value of the stable configuration. Differences with respect to the corresponding stable configuration can be attributed to the influence of the non-preservation of the force-free constraints (10) and (11). Using (much) larger numerical resolution (beyond the scope of our computational resources) we envision that the violation of the force-free constraints would be significantly reduced and the expected (low-energy) states would be the endpoint of the evolution after a full relaxation of the magnetosphere takes place. The energy decrease is explained, mainly, by a flow of energy towards the surface of the star, where it is dissipated efficiently. A large fraction of this energy is also dissipated in the magnetosphere at locations where the force-free conditions break. This contrasts with the work of Beloborodov (2011), Parfrey et al. (2013), and Carrasco et al. (2019) in which most of the energy is dissipated by the formation and ejection of plasmoids. The different setup used in these works (dynamically twisting versus unstable equilibrium configurations) makes a direct comparison difficult. A possible source for the qualitative discrepancy may be differences in the boundary condition at the surface of the star. While we use a boundary condition that dissipates very efficiently any strong currents formed at the surface, in their work, their use of essentially non-dissipative boundary conditions make the surface perfectly reflective. For the future it would be interesting to compare more closely the differences in the boundary condition and to develop a better physical model for dissipation at the NS surface.

The magnetic field remains nearly axisymmetric throughout the simulation indicating that the instability is mostly an $m = 0$ instability. A complete theoretical analysis of the origin of the instability and its properties is beyond the scope of this paper. However, we anticipate that such analysis has to be carried out on a global scale either by calculating the eigenmodes or by using the so-called energy principle of Bernstein et al. (1958) and is not trivial due to the presence of both poloidal and toroidal components (Akgün et al. 2013, and references therein). However, we note that, since the poloidal field structure changes somewhat less than the toroidal field, this instability could be compared to the interchange instability discussed by Tayler (1973), where displacing the toroidal field radially decreases the energy (even in the absence of a fluid).

We have made a crude estimation of the observational properties of the energy liberated in the magnetosphere as a result of the instability. The fact that large amounts of energy (in excess of 10^{46} erg) are released on milliseconds time-scales results in dynamical luminosities significantly larger than 10^{48} erg s^{-1} (reaching in some models 4×10^{49} erg s^{-1}). This should trigger the expansion of a pair-photon fireball polluted with baryons unbound from the magnetar crust. The bolometric signature of these fireballs seems incompatible with the observations of the initial spikes observed in GFs. With our simple analytic model, most of the unstable magnetospheres produce overluminous, too cool, and excessively short flashes. However, this problem can be solved if the energy can be liberated on longer time-scales, of the order of the observed GF spikes ($\Delta t_{\mathrm{spike}} \sim 0.1$ s). This could be possible in a scenario of slow energy dissipation as the one proposed by Li et al. (2019), which we plan to explore in the future.

The currents produced during the instability increase significantly the amount of pairs in the magnetosphere, a large fraction of which, of size $\sim 10 R_*$, becomes optically thick. The hot plasma magnetically confined in this region could be responsible for the extended thermal X-ray emission lasting for 50−300 s after GFs.

Our force-free numerical method cannot properly deal with the evolution of extremely thin surface currents. Therefore, the dynamical millisecond time-scales computed in our models should be taken as a lower bound for the physical time-scales. The magnetic dissipation taking place at these locations can be due to, e.g. Ohmic processes or to non-linear Alfvén wave interactions. Assuming that energy is released on $\sim \Delta t_{\mathrm{spike}}$, our estimate of the electromagnetic signature yields photospheric luminosities and temperatures compatible with observational data. Since this is a sound physical assumption, we conclude that observed GFs in SGRs are broadly compatible with the development of instabilities in twisted magnetospheres.

ACKNOWLEDGEMENTS

We thank Amir Levinson for his support in challenging our numerical code prior to the production of the presented results. We also thank Oscar Reula, Federico Carrasco, and Carlos Palenzuela for their valuable discussions on the boundary conditions. We acknowledge the support from the grants AYA2015-66899-C2-1-P and PROMETEO-II-2014-069. JM acknowledges a Ph.D. grant of the *Studienstiftung des Deutschen Volkes*. PC acknowledges the Ramon y Cajal funding (RYC-2015-19074) supporting his research. We acknowledge the partial support of the PHAROS COST Action CA16214 and GWverse COST Action CA16104. The shown numerical simulations have been conducted on *MareNostrum 4* of the *Red Española de Supercomputación* (AECT-2019-1-0004) as well as on the computational infrastructure of the University of Valencia. We thank the *EWASS 2019* and *GR22* conferences for the possibility to disseminate the results of this work.

REFERENCES

Akgün T., Reisenegger A., Mastrano A., Marchant P., 2013, MNRAS, 433, 2445
Akgün T., Miralles J. A., Pons J. A., Cerdá-Durán P., 2016, MNRAS, 462, 1894
Akgün T., Cerdá-Durán P., Miralles J. A., Pons J. A., 2017, MNRAS, 472, 3914
Akgün T., Cerdá-Durán P., Miralles J. A., Pons J. A., 2018a, MNRAS, 474, 625
Akgün T., Cerdá-Durán P., Miralles J. A., Pons J. A., 2018b, MNRAS, 481, 5331
Alic D., Moesta P., Rezzolla L., Zanotti O., Jaramillo J. L., 2012, ApJ, 754, 36
Baiko D. A., Chugunov A. I., 2018, MNRAS, 480, 5511
Baumgarte T. W., Montero P. J., Cordero-Carrión I., Müller E., 2013, Phys. Rev. D, 87, 044026
Beloborodov A. M., 2009, ApJ, 703, 1044
Beloborodov A. M., 2011, Astrophys. Space Sci. Proc., 21, 299
Beloborodov A. M., 2013a, ApJ, 762, 13.
Beloborodov A. M., 2013b, ApJ, 777, 114
Beloborodov A. M., Levin Y., 2014, ApJ, 794, L24
Beloborodov A. M., Thompson C., 2007, ApJ, 657, 967
Bernstein I. B., Frieman E. A., Kruskal M. D., Kulsrud R. M., 1958, Proc. R. Soc. A, 244, 17
Beskin V. S., 2010, MHD Flows in Compact Astrophysical Objects. Springer-Verlag, Heidelberg
Camenzind M., 2007, Compact Objects in Astrophysics: White Dwarfs, Neutron Stars, and Black Holes. Springer, Heidelberg
Carrasco F., Viganò D., Palenzuela C., Pons J. A., 2019, MNRAS, 484, L124
Carrasco F. L., Reula O. A., 2016, Phys. Rev. D, 93, 085013
Chugunov A. I., Horowitz C. J., 2010, MNRAS, 407, L54
Cline T. L. et al., 1980, ApJ, 237, L1
Collins D. C., Xu H., Norman M. L., Li H., Li S., 2010, ApJS, 186, 308
Coti Zelati F., Rea N., Pons J. A., Campana S., Esposito P., 2018, MNRAS, 474, 961
Dedner A., Kemm F., Kröner D., Munz C.-D., Schnitzer T., Wesenberg M., 2002, J. Comput. Phys., 175, 645
Elenbaas C., Watts A. L., Turolla R., Heyl J. S., 2016, MNRAS, 456, 3282
Etienne Z. B., Wan M.-B., Babiuc M. C., McWilliams S. T., Choudhary A., 2017, Class. Quantum Gravity, 34, 215001
Fernández R., Davis S. W., 2011, ApJ, 730, 131
Fujisawa K., Kisaka S., 2014, MNRAS, 445, 2777
Gabler M., Cerdá-Durán P., Stergioulas N., Font J. A., Müller E., 2012, MNRAS, 421, 2054
Gill R., Heyl J. S., 2010, MNRAS, 407, 1926
Glampedakis K., Lander S. K., Andersson N., 2014, MNRAS, 437, 2
Goldreich P., Julian W. H., 1969, ApJ, 157, 869
Goldreich P., Reisenegger A., 1992, ApJ, 395, 250
Goodale T., Allen G., Lanfermann G., Massó J., Radke T., Seidel E., Shalf J., 2003, in Vector and Parallel Processing – VECPAR'2002, 5th International Conference, Lecture Notes in Computer Science. Springer, Berlin, Available at: http://edoc.mpg.de/3341
Goodman J., 1986, ApJ, 308, L47
Gourgouliatos K. N., Wood T. S., Hollerbach R., 2016, Proc. Natl. Acad. Sci., 113, 3944
Grad H., Rubin H., 1958, in Proceedings of the Second United Nations Conference on the Peaceful Uses of Atomic Energy, Vol. 31. UN, Geneva, p. 190
Hascoët R., Beloborodov A. M., den Hartog P. R., 2014, ApJ, 786, L1
Horowitz C. J., Kadau K., 2009, Phys. Rev. Lett., 102, 191102
Hurley K. et al., 1999, Nature, 397, 41
Hurley K. et al., 2005, Nature, 434, 1098
Janka H. T., Aloy M. A., Mazzali P. A., Pian E., 2006, ApJ, 645, 1305
Jones P. B., 1988, MNRAS, 233, 875
Kaspi V. M., Beloborodov A. M., 2017, ARA&A, 55, 261
Kojima Y., 2017, MNRAS, 468, 2011
Kojima Y., 2018, MNRAS, 477, 3530
Kojima Y., Okamoto S., 2018, MNRAS, 475, 5290
Komissarov S. S., 2004, MNRAS, 350, 427
Komissarov S. S., 2011, MNRAS, 418, L94
Landau L. D., Lifshitz E. M., 2012, Theory of Elasticity. Elsevier
Lander S. K., Gourgouliatos K. N., 2019, MNRAS, 486, 4130

Lander S. K., Andersson N., Antonopoulou D., Watts A. L., 2015, MNRAS, 449, 2047

Levin Y., Lyutikov M., 2012, MNRAS, 427, 1574

Li X., Beloborodov A. M., 2015, ApJ, 815, 25

Li X., Levin Y., Beloborodov A. M., 2016, ApJ, 833, 189

Li X., Zrake J., Beloborodov A. M., 2019, ApJ, 881, 13

Link B., 2014, MNRAS, 441, 2676

Löffler F. et al., 2012, Class. Quantum Gravity, 29, 115001

Lüst R., Schlüter A., 1954, Z. Astrophys., 34, 263

Lyutikov M., 2003, MNRAS, 346, 540

Lyutikov M., 2015, MNRAS, 447, 1407

McKinney J. C., 2006, MNRAS, 367, 1797

Mereghetti S., Pons J. A., Melatos A., 2015, Space Sci. Rev., 191, 315

Mészáros P., Rees M. J., 2000, ApJ, 530, 292

Meszaros P., Laguna P., Rees M. J., 1993, ApJ, 415, 181

Mignone A., Tzeferacos P., 2010, J. Comput. Phys., 229, 2117

Mikic Z., Linker J. A., 1994, ApJ, 430, 898

Miranda-Aranguren S., Aloy M. A., Rembiasz T., 2018, MNRAS, 476, 3837

Montero P. J., Baumgarte T. W., Müller E., 2014, Phys. Rev. D, 89, 084043

Nakar E., Piran T., Sari R., 2005, ApJ, 635, 516

Paczynski B., 1986, ApJ, 308, L43

Palenzuela C., Lehner L., Reula O., Rezzolla L., 2009, MNRAS, 394, 1727

Palenzuela C., Garrett T., Lehner L., Liebling S. L., 2010, Phys. Rev. D, 82, 044045

Parfrey K., Beloborodov A. M., Hui L., 2012, ApJ, 754, L12

Parfrey K., Beloborodov A. M., Hui L., 2013, ApJ, 774, 92

Parfrey K., Spitkovsky A., Beloborodov A. M., 2017, MNRAS, 469, 3656

Paschalidis V., Shapiro S. L., 2013, Phys. Rev. D, 88, 104031

Perna R., Pons J. A., 2011, ApJ, 727, L51

Pili A. G., Bucciantini N., Del Zanna L., 2015, MNRAS, 447, 2821

Piran T., Shemi A., Narayan R., 1993, MNRAS, 263, 861

Pons J. A., Geppert U., 2007, A&A, 470, 303

Pons J. A., Miralles J. A., Geppert U., 2009, A&A, 496, 207

Rea N., Esposito P., 2011, Astrophys. Space Sci. Proc., 21, 247

Roumeliotis G., Sturrock P. A., Antiochos S. K., 1994, ApJ, 423, 847

Shafranov V., 1966, Rev. Plasma Phys., 2, 103

Shemi A., Piran T., 1990, ApJ, 365, L55

Shibata M., 2015, Numerical Relativity. 100 Years of General Relativity. World Scientific Publishing Company, Singapore

Spitkovsky A., 2006, ApJ, 648, L51

Steiner A. W., Watts A. L., 2009, Phys. Rev. Lett., 103, 181101

Suresh A., Huynh H. T., 1997, J. Comput. Phys., 136, 83

Tayler R. J., 1973, MNRAS, 161, 365

Thompson C., Duncan R. C., 1995, MNRAS, 275, 255

Thompson C., Duncan R. C., 1996, ApJ, 473, 322

Thompson C., Duncan R. C., 2001, ApJ, 561, 980

Thompson C., Lyutikov M., Kulkarni S. R., 2002, ApJ, 574, 332

Thompson C., Yang H., Ortiz N., 2017, ApJ, 841, 54

Turolla R., Zane S., Watts A. L., 2015, Rep. Prog. Phys., 78, 116901

Uchida T., 1997, Phys. Rev. E, 56, 2181–2197

Viganò D., Pons J. A., Miralles J. A., 2011, A&A, 533, A125

Viganò D., Pons J. A., Miralles J. A., 2012, Comput. Phys. Commun., 183, 2042

Viganò D., Rea N., Pons J. A., Perna R., Aguilera D. N., Miralles J. A., 2013, MNRAS, 434, 123

Wald R., 2010, General Relativity. University of Chicago Press, Chicago

Woods P. M., Thompson C., 2006, Soft Gamma Repeaters and Anomalous X-Ray Pulsars: Magnetar Candidates. Cambridge University Press, Cambridge, UK, p. 547

APPENDIX A: NUMERICAL DETAILS

A1 The augmented system

In order to preserve the physical conditions $\mathrm{div}\tilde{\boldsymbol{B}} = 0$ and $\mathrm{div}\tilde{\boldsymbol{E}} = \tilde{\rho}_\mathrm{e}$ we make use of hyperbolic/parabolic cleaning potentials (Dedner et al. 2002; Palenzuela et al. 2009; Mignone & Tzeferacos 2010).

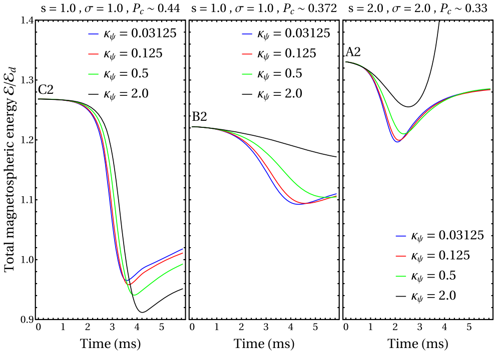

Figure A1. Energy evolution of the high energy initial data models A2, B2, and C2 using different damping constants κ_ψ (divergence cleaning) in a low resolution study (16 points per R_*). While one observes a converging evolution for the lower cleaning potentials $\kappa_\psi = 0.03125$ and $\kappa_\psi = 0.125$, the energy evolution shows a strong (non-physical) dependence on κ_ψ for larger damping constants. This effect is amplified in the high resolution (32 points per R_*).

Specifically, we implement an augmented system of Maxwell's equations as follows (Palenzuela et al. 2009; Miranda-Aranguren, Aloy & Rembiasz 2018):

$$\partial_t \phi - \partial_i \tilde{E}^i = -\tilde{\rho}_\mathrm{e} - \kappa_\phi \phi \tag{A1}$$

$$\partial_t \tilde{E}^i - \partial_j \left(\epsilon^{ijk} \tilde{B}_k + \delta^{ij} \phi \right) = -\tilde{J}^i_\mathrm{FF} \tag{A2}$$

$$\partial_t \psi + \partial_i \tilde{B}^i = -\kappa_\psi \psi \tag{A3}$$

$$\partial_t \tilde{B}^i + \partial_j \left(\epsilon^{ijk} \tilde{E}_k + \delta^{ij} \psi \right) = 0. \tag{A4}$$

Here, ψ (divergence cleaning) and ϕ (charge conservation) are the scalar potentials, κ_ϕ and κ_ψ the respective damping constants and δ^{ij} denotes the Kronecker delta. As for the practical implementation, we follow a Strang splitting approach (as employed e.g. in Komissarov 2004), effectively solving part of the scalar equations (A1) and (A3) analytically. Prior (before `MoL_Step`) and after (before `MoL_PostStep`) the time integration of the EINSTEIN TOOLKIT thorn `MoL` we evolve in time the equations

$$\phi(t) = \phi_0 \exp\left[-\kappa_\phi t\right], \tag{A5}$$

$$\psi(t) = \psi_0 \exp\left[-\kappa_\psi t\right], \tag{A6}$$

for a time $t = \Delta t/2$. The coefficients κ_ϕ and κ_ψ have to be chosen by optimization in accordance with the grid properties.

We find it beneficial to choose a large value for κ_ϕ, effectively dissipating charge conservation errors on very short time-scales. As for the divergence cleaning, we conducted a series of tests, optimizing κ_ψ to yield stable and converging evolution for all shown resolutions, ultimately resorting to $\kappa_\psi = 0.125$ (see Fig. A1 for a review of the optimization process).

It should be noted at this point that Mignone & Tzeferacos (2010) present a promising scheme of choosing κ_ψ according to the grid resolution that has also been used in Miranda-Aranguren et al. (2018). In the framework of mesh refinement of the Einstein Toolkit, this would result in a different damping of the cleaning potentials across the refinement levels. We have found that the optimization of the hyperbolic/parabolic cleaning becomes a very subtle issue and may experience strong numerical effects when increasing the overall resolution. This observation may, however, be an artefact of the fixed boundary of the magnetar surface – which on a Cartesian grid, resembles an accumulation of boxes rather than a perfectly aligned spherical boundary. The exploration of these effects and the transition to a fully spherical version of this force-free thorn (as introduced in Baumgarte et al. 2013; Montero, Baumgarte & Müller 2014) will be a subject of future efforts.

A2 Conservation of force-free constraints

FFE codes are valid in the limit of high electromagnetic energy compared to the rest mass and thermal energy of the respective plasma. The dynamics of force-free fields is described entirely without the plasma four velocity. However, demanding the existence of a physical, time-like velocity field $\boldsymbol{u}$ with $F_{\mu\nu}u^{\nu} = 0$, as well as the degeneracy condition $F_{\mu\nu}J^{\nu} = 0$ (see Uchida 1997, for a detailed algebraic review) one is left with the aforementioned constraints:

$$\tilde{\boldsymbol{E}} \cdot \tilde{\boldsymbol{B}} = 0 \tag{A7}$$

$$\tilde{\boldsymbol{B}}^2 - \tilde{\boldsymbol{E}}^2 \geq 0. \tag{A8}$$

Within the shown simulations we find it beneficial to employ an approach presented in Komissarov (2011) and Parfrey et al. (2017) in order to archive $\partial_t \left(\tilde{\boldsymbol{E}} \cdot \tilde{\boldsymbol{B}}\right) = 0$ throughout the evolution (by making use of the force-free current as in equation 12) without the employment of target currents (as discussed in Parfrey et al. 2017). Additionally, we include a suitable Ohm's law (Komissarov 2004, section C3) into our Strang splitting approach aiming towards an evolution minimizing the violation of conditions (A7), and (A8).

In order to build up a force-free current, Komissarov (2004) introduces a generalized Ohm's law in the context of FFE:

$$\tilde{\boldsymbol{J}} = \sigma_{\parallel}\tilde{\boldsymbol{E}}_{\parallel} + \sigma_{\perp}\tilde{\boldsymbol{E}}_{\perp} + \tilde{\boldsymbol{j}}_d, \tag{A9}$$

where the subscripts $_{\parallel}$ and $\perp$ denote the components parallel and perpendicular to the magnetic field, $\tilde{\boldsymbol{B}}$. A to be specified model for σ introduces a suitable resistivity into the force-free system (see also Lyutikov 2003, for further comments on resistive FFE), while $\tilde{\boldsymbol{j}}_d$ is the drift current perpendicular to the electric and magnetic fields. In its general form, (A9) plays the central role in ensuring the force-free conditions (A7) and (A8). Komissarov (2004) suggests a resistivity model that depends on the time-step of the evolution Δt (throughout the presented simulations we employ CFL =0.2), where

$$\sigma_{\parallel} = \frac{d}{\Delta t}. \tag{A10}$$

The cross-field resistivity $\sigma_{\perp}$ is strongly linked to the violation of condition (A8),

$$\sigma_{\perp} = \begin{cases} 0 & : \boldsymbol{B}^2 \geq \boldsymbol{E}^2 \\ b\dfrac{\left(\tilde{E}_{\perp} - \tilde{E}^*_{\perp}\right)}{\tilde{E}^*_{\perp}} & : \tilde{\boldsymbol{B}}^2 < \tilde{\boldsymbol{E}}^2 \end{cases}, \tag{A11}$$

where $\tilde{E}_{\perp} = \left|\tilde{\boldsymbol{E}}_{\perp}\right|$ and $\left(\tilde{E}^*_{\perp}\right)^2 = \left(\tilde{\boldsymbol{B}} - \tilde{\boldsymbol{E}}_{\parallel}\right)^2$ and b is an scalar parameter controlling the magnitude of $\sigma_{\perp}$. Equations (A10) and (A11) have a pair of analytic solutions:

$$\tilde{\boldsymbol{E}}_{\parallel}(t) = \tilde{\boldsymbol{E}}_{\parallel}(0) \times e^{-\sigma_{\parallel} t} \tag{A12}$$

$$\tilde{\boldsymbol{E}}_{\perp}(t) = \left[\tilde{E}^*_{\perp}(0) + \frac{\tilde{E}^*_{\perp}(0)\left[\tilde{E}_{\perp}(0) - \tilde{E}^*_{\perp}(0)\right] \times e^{-b\sigma_{\parallel} t}}{\tilde{E}_{\perp}(0) - \left[\tilde{E}_{\perp}(0) - \tilde{E}^*_{\perp}(0)\right] \times e^{-b\sigma_{\parallel} t}}\right] \times \frac{\tilde{\boldsymbol{E}}_{\perp}(0)}{\tilde{E}_{\perp}(0)}. \tag{A13}$$

During our numerical simulations, we usually choose $d = 5.0$, and $b = 0.1$, and solve equation (A12) prior to equation (A13) in a Strang splitting scheme in direct analogy to the implementation described in Section A1. This resistivity model ensures the validity of the force-free regime throughout time, in other words, the evolution is driven towards a force-free state

$$\begin{aligned} &\tilde{\boldsymbol{E}} \cdot \tilde{\boldsymbol{B}} \to 0 \\ &\tilde{\boldsymbol{B}}^2 - \tilde{\boldsymbol{E}}^2 \to 0 \qquad : \tilde{\boldsymbol{B}}^2 < \tilde{\boldsymbol{E}}^2. \end{aligned} \tag{A14}$$

APPENDIX B: OPTICAL DEPTH TO RESONANT CYCLOTRON SCATTERING

For the presented modelling of the optical thickness of highly magnetized force-free plasmas around magnetars (see Section 6.3), we adapt the techniques describing resonant scattering as presented by Beloborodov (2013b) (from now on Be13). In the following, we will give a short review of the underlying equations. In order to derive the optical thickness τ, we integrate equation (Be13/A15),

$$\frac{\mathrm{d}\tau}{\mathrm{d}s} = 2\pi^2 r_e \frac{c}{\omega} \frac{\xi}{|\tilde{\mu}|} n_e \left[f_e\left(p_1\right) + f_e\left(p_2\right)\right]. \tag{B1}$$

Here, $r_e = e^2/m_e c^2$ denotes the photon wavelength, ω the frequency of the seed photon (we consider 1 keV photons), and $\xi = 1$ or $\xi = \tilde{\mu}^2$ depending on the photon polarization ($\perp$ or $_{\parallel}$, respectively). The relativistic particles require the specification of the quantities $\mu = \cos\vartheta$ and $\tilde{\mu} = \cos\tilde{\vartheta}$, where ϑ is the angle between the photon path and the magnetic field $\boldsymbol{B}$ in the lab frame and $\tilde{\vartheta}$ in the rest frame of the electron. The dimensionless momenta $p_{1,2}$ correspond to the electron (or positron) velocities favoured by the resonant scattering model. As both polarizations yield similar results, we only consider the slightly dominant $\perp$ orientation for our model. Beloborodov (2013b) estimated that the contribution of non-resonant scattering to the optical depth is negligible and will not be considered in our calculations (see, however, footnote 6).

Following Be13, we employ the so-called waterbag model as a distribution function for electron (or positron) momenta. In analogy to a two-fluid model, the distribution function is characterized by the two parameters (dimensionless momenta) p_+ and p_-, with the overall shape

$$f_e(p) = \begin{cases} \left(p_+ - p_-\right)^{-1} & : p_- < p < p_+ \\ 0 & : \text{else} \end{cases}. \tag{B2}$$

Applying the waterbag model (B2) in equation (B1) selects the relevant electron (or positron) momenta for the scattering process. The distribution of this normalization factor throughout the magnetosphere especially depends on the flow direction of charges along $\boldsymbol{B}$. As described in Section 5.2 of Be13, we adjust their model according to a flow of electrons (or positrons) which turns back to the central object when field lines cross the equator. We apply this to all field lines crossing regions with $B < 10^{13}$ G (this holds everywhere except in the inner coronal region of strong closed magnetic field lines).

This paper has been typeset from a TEX/LATEX file prepared by the author.

Monthly Notices
of the
ROYAL ASTRONOMICAL SOCIETY

MNRAS **494,** 4203–4225 (2020)
Advance Access publication 2020 April 15

doi:10.1093/mnras/staa943

Striped Blandford/Znajek jets from advection of small-scale magnetic field

J. F. Mahlmann ,[1]★ A. Levinson[2] and M. A. Aloy [1]

[1]*Departament d'Astronomia i Astrofísica, Universitat de València, E-46100 Burjassot, Spain*
[2]*The Raymond and Beverly Sackler School of Physics and Astronomy, Tel Aviv University, Tel Aviv 69978, Israel*

Accepted 2020 March 31. Received 2020 March 2; in original form 2020 January 9

ABSTRACT

Black hole – accretion disc systems are the central engines of relativistic jets from stellar to galactic scales. We numerically quantify the unsteady outgoing Poynting flux through the horizon of a rapidly spinning black hole endowed with a rotating accretion disc. The disc supports small-scale, concentric, flux tubes with zero net magnetic flux. Our general relativistic force-free electrodynamics simulations follow the accretion on to the black hole over several hundred dynamical time-scales in 3D. For the case of counter-rotating accretion discs, the average process efficiency reaches up to $\langle \epsilon \rangle \approx 0.43$, compared to a stationary energy extraction by the Blandford/Znajek process. The process efficiency depends on the cross-sectional area of the loops, i.e. on the product $l \times h$, where l is the radial loop thickness and h its vertical scale height. We identify a strong correlation between efficient electromagnetic energy extraction and the quasi-stationary setting of ideal conditions for the operation of the Blandford/Znajek process (e.g. optimal field line angular velocity and fulfillment of the so-called Znajek condition). Remarkably, the energy extraction operates intermittently (alternating episodes of high and low efficiency) without imposing any large-scale magnetic field embedding the central object. Scaling our results to supermassive black holes, we estimate that the typical variability time-scale of the system is of the order of days to months. Such time-scales may account for the longest variability scales of TeV emission observed, e.g. in M87.

Key words: accretion, accretion discs – black hole physics – magnetic fields – methods: numerical.

1 INTRODUCTION

The recent observations of the *shadow* around the event horizon of the black hole (BH) in the nucleus of the elliptical galaxy M87 (Event Horizon Telescope Collaboration 2019a) have sparked further interest for numerical models of BHs surrounded by magnetized accretion discs (ADs). Strong magnetic fields in these astrophysical systems (BH/AD) have been established as efficient mediators to tap a fraction of the gravito-rotational energy of the system and power relativistic jets (e.g. Blandford, Meier & Readhead 2019; Martí 2019, and references therein) from stellar (e.g. jets associated with microquasars and γ-ray bursts; GRBs) to galactic scales [e.g. kiloparsec-scale jets associated with active galactic nuclei (AGNs)]. Two basic mechanisms of energy extraction out of BH/AD systems have been extensively studied, namely the Blandford/Znajek (BZ) mechanism (Blandford & Znajek 1977) and the magneto-centrifugal (MC) jet launching (Bisnovatyi-Kogan & Ruzmaikin 1976; Blandford & Payne 1982). The BZ process posits the existence of large-scale poloidal magnetic fields threading the horizon of a spinning BH, which carry away the reducible energy of the central object to infinity. In contrast, the MC mechanism needs a large-scale magnetic field anchored to the AD (with an adequate inclination away from the vertical) in order to provide sufficient magneto-centrifugal thrust to generate a plasma outflow.

Mounting evidence for the important role of magnetic fields in the jet launching process has been provided by general relativistic magnetohydrodynamics (GRMHD) simulations (e.g. Koide et al. 2000; McKinney & Gammie 2004; Hawley & Krolik 2006; Komissarov & Barkov 2009; Tchekhovskoy, Narayan & McKinney 2011; McKinney, Tchekhovskoy & Blandford 2012; Tchekhovskoy & McKinney 2012; Tchekhovskoy, McKinney & Narayan 2012; McKinney et al. 2014; Sądowski & Narayan 2016; Chatterjee et al. 2019; Liska et al. 2019; Vourellis et al. 2019). In many of these numerical models (e.g. Koide et al. 2000; McKinney & Gammie 2004; Hawley & Krolik 2006; Komissarov & Barkov 2009; Tchekhovskoy et al. 2011; McKinney et al. 2012; Tchekhovskoy & McKinney 2012; Tchekhovskoy et al. 2012), the initial magnetic structure is not self-consistently generated, but assumed to have some large-scale poloidal topology as a starting point. Because of the numerical challenge that simulating a thin disc represents, most GRMHD simulations begin with a geometrically thick torus, even

---

★ E-mail: jens.mahlmann@uv.es

Published by Oxford University Press on behalf of the Royal Astronomical Society

though thin discs may be more physically suited, e.g. for BH/AD systems in AGNs. Furthermore, the microphysics associated with electron and ion heating and cooling, energy transfer between electrons and ions, and plasma production in the force-free section of the magnetosphere is poorly understood. They are either ignored or prescribed using ad hoc assumptions.

While advection of large-scale magnetic fields by the hot accretion flow can lead to the efficient production of a powerful jet (particularly in the magnetically arrested disc – MAD – regime Narayan, Igumenshchev & Abramowicz 2003), as demonstrated by GRMHD simulations (e.g. Igumenshchev 2008), some key issues remain unresolved. The most burning one is the dissipation of the jet magnetic field. The current-driven kink instability has been considered as a potential mechanism to generate strong distortions that can ultimately lead to the formation of current sheets and turbulence, however, under which conditions this instability develops, and at what scales, is yet unclear. Recent numerical experiments of the relativistic kink instability of Poynting dominated jets (Bromberg et al. 2019; Davelaar et al. 2019) invoke special (and artificial) setups for numerical convenience (e.g. non-rotating, stationary cylindrical flux tubes, but see Mizuno et al. 2012, for inclusion of rotation). These experiments indicate that cylindrical jets with dominant toroidal fields should become kink unstable, and may be disrupted over a time-scale of $\sim 10^2 R/c$ or longer, where R is the cross-sectional radius of the jet. Favourable conditions for such dissipation are anticipated in strong collimation sites (Bromberg & Tchekhovskoy 2016). Such strong collimation is expected in GRBs during the propagation of the jet inside the star (Aloy et al. 2000b; Bromberg & Tchekhovskoy 2016; Obergaulinger & Aloy 2017; Aloy, Cuesta-Martínez & Obergaulinger 2018), and is occasionally seen in AGN reconfinement zones, e.g. the *HST*-1 knot in M87. However, these zones are usually located far from the BH, typically at radii 10^5–$10^7 r_g$. Yet, in many objects dissipation is seen or inferred on much smaller scales. Velocity maps of the inner M87 jet (Mertens et al. 2016) and its apparent limb brightening (Kim et al. 2018) are indicative of a dissipative boundary layer (or sheath) down to horizon scales, as also suggested by the recent ETH analysis (Event Horizon Telescope Collaboration 2019b). The nature of the dissipation mechanism in the sheath is unclear, but it is, most likely, unrelated to the kink instability (the sheath may result from the turbulence induced by the non-linear development of Kelvin–Helmholtz instabilities, see e.g. De Young 1993; Aloy et al. 2000a; Aloy & Mimica 2008).

The rapid variability observed in many blazars and other radio-loud AGNs, and in particular the extreme gamma-ray flares, also require rapid dissipation of the inner jet, on scales at which the jet is not expected to be prone to instabilities. Notable examples are M87 (Acciari et al. (Aharonian et al. 2003; Acciari et al. 2009) and IC310 (Aleksić et al. 2014) that exhibit occasional strong flares with durations as short as one day (roughly r_g/c) in M87, and a few minutes in IC310 (Aleksić et al. 2014). These flares are likely produced in the innermost regions, close to the BH (but see Barkov, Bosch-Ramon & Aharonian 2012 for a different interpretation). It has been proposed that the variable TeV emission in M87 (and conceivably IC310) may originate from a magnetospheric spark gap located at the base of a jet (Levinson 2000; Neronov & Aharonian 2007; Levinson & Rieger 2011; Hirotani & Pu 2016; Hirotani et al. 2016, 2017; Levinson & Segev 2017; Lin et al. 2017). Recent attempts to study this process using 1D GRPIC simulations (Levinson & Cerutti 2018; Chen & Yuan 2019) confirm that such gaps are self-sustained when the pair production opacity contributed by the disc emission is large enough, and that they are potential sources of intermittent TeV emission. However, these simulations are local and, thus, missing information about the feedback of the global magnetosphere. Global 2D GRPIC simulations, as those described in Parfrey, Philippov & Cerutti (2019), may be able to shed more light on the gap emission.

Alternatively, dissipation and rapid variability can more naturally arise from advection of small-scale magnetic fields by the accretion flow, as demonstrated by recent 2D general relativistic (Parfrey, Giannios & Beloborodov 2015) and 3D special relativistic (Yuan, Blandford & Wilkins 2019a; Yuan et al. 2019b) force-free simulations. Along this idea, Giannios & Uzdensky (2019) have argued that the variability time-scales are related to the growth of the magnetorotational dynamo in the AD. But can accretion of small-scale magnetic field leads to formation of a striped relativistic jet with a substantial mean power? This is the prime question addressed in this paper.

The picture envisaged here is inspired by the model described in Uzdensky & Goodman (2008). They describe the AD corona as a statistical ensemble of magnetic loops (Coroniti 1985; Tout & Pringle 1992; Hughes et al. 2003), continuously emerging from and submerging into the disc due to magnetic buoyancy (or a *boiling magnetic foam*). Reconnection between these loops is able to rapidly dissipate magnetic energy (Di Matteo, Celotti & Fabian 1999) and to produce spatially extended (loop) structures in the AD and its corona (Romanova et al. 1998; Uzdensky & Goodman 2008). The existence of such loop structures of zero net flux in the AD was acknowledged by McKinney (2005) as possibly relevant to power BZ-like energy flows in thin BH/AD systems. In the *coronal mechanism* (Beckwith, Hawley & Krolik 2009), the magnetic flux is advected as a consequence of the reconnection of loops across the equator, which induce the formation of magnetic loops in the corona. The poloidal magnetic fields added to the accretion funnel in this way are a requirement for the formation of a BZ-type jet. The premise of accreting (zero net flux) loops was recently used in 2D axisymmetric, general relativistic force-free electrodynamics (GRFFE) simulations by Parfrey et al. (2015) to confirm an efficient working of the BZ process. However, whether a similar behaviour is expected in 3D is yet an open issue. For instance, Beckwith, Hawley & Krolik (2008) find a significant sensitivity of the jet power on the topology of the accreted (small net flux) magnetic field. In this paper, we present results of 3D GRFFE simulations of loop accretion, using a similar setup to that invoked in Parfrey et al. (2015). We find that substantial power can be extracted in the form of a striped BZ jet for a range of conditions, and that dissipation in current sheets at the jet boundary is anticipated due to interaction of loops.

This work is organized as follows. In Section 2, we introduce the notation to deal with the general relativistic problem at hand, which includes a Kerr BH (Section 2.1) surrounded by an *idealized* AD, where loops of alternate polarity and zero net magnetic flux are set up (2.3). We provide the equations of GRFFE (Section 2.2) implemented for simulations conducted on the infrastructure of the `Einstein Toolkit` (supplemented by Appendix A1). Section 3 summarizes numerical simulations of accreting tubes of magnetic flux in magnetospheres of rapidly spinning BHs (with a dimensionless rotation rapidity $a^* = 0.9$) for both counter-rotating and co-rotating disc systems. Our work improves on the 2D axisymmetric model of Parfrey et al. (2015) by considering full-fledged 3D BH/AD systems. Inclusion of 3D is insurmountable to properly understand the dynamics of the electromagnetic fields developed in the BH magnetosphere, where finite resistivity (in our models of numerical origin) may yield episodes of fast dissipation and, thus, rapid variability of the plasma in the vicinity of the BH. Besides, our models aim to explore systematically the dependence of the variability time-scales on the (simple) parametrization of the magnetic loops in the AD. We discuss general trends through the chosen parameters in Section 4 and provide relevant scaling to supermassive BHs. Section 4 concludes the astrophysical implications of the presented simulations.

2 MAGNETOSPHERE SETUP AND EVOLUTION

The following sections and the `Einstein Toolkit` employ units where $M_\odot = G = c = 1$, which sets the respective time and length-scales to be $1\,\mathrm{M}_\odot \equiv 4.93 \times 10^{-6}\,\mathrm{s} \equiv 1477.98\,\mathrm{m}$. This unit system is a variation of the so-called system of *geometrized units* (as introduced in appendix F of Wald 2010), with the additional normalization of the mass to $1\,\mathrm{M}_\odot$ (see also Mahlmann et al. 2019, on unit conversion in the `Einstein Toolkit`).

2.1 The Kerr solution

The Kerr solution embodies the geometry of a spinning BH of mass M and specific angular momentum $a = J/M$, where J is the angular momentum and $a^* = J/M^2$ is the dimensionless rotation rapidity (cf. Frolov & Zelnikov 2011). In Boyer–Lindquist coordinates, the line element of the Kerr metric is

$$\mathrm{d}s^2 = -\left(1 - \frac{2Mr}{\Sigma}\right)\mathrm{d}t^2 - \frac{4Mar\sin^2\theta}{\Sigma}\,\mathrm{d}t\mathrm{d}\phi + \frac{\Sigma}{\Delta}\,\mathrm{d}r^2 + \Sigma\,\mathrm{d}\theta^2 + \frac{A\sin^2\theta}{\Sigma}\,\mathrm{d}\phi^2, \tag{1}$$

$$\Sigma := r^2 + a^2\cos^2\theta,$$

$$A := \left(r^2 + a^2\right)^2 - \Delta\, a^2\sin^2\theta,$$

$$\Delta := r^2 - 2Mr + a^2 := (r - r_+)(r - r_-), \tag{2}$$

where $r_\pm$ represent the locations of the inner and outer horizons of the BH, respectively

$$r_\pm = M \pm \sqrt{M^2 - a^2}. \tag{3}$$

The BH mass is a scale parameter of the presented line element (1), i.e. one can write $\mathrm{d}s^2 = M^2\mathrm{d}\tilde{s}^2$ where $\mathrm{d}\tilde{s}^2$ is a (dimensionless) function of a^* only (cf. Frolov & Zelnikov 2011). The frame-dragging frequency induced by the rotation of the BH is

$$\Omega := 2aMr/A, \tag{4}$$

which is also the angular velocity of the (local) *zero angular momentum observer* or ZAMO (cf. Thorne, Price & MacDonald 1986), i.e. $\Omega = (\mathrm{d}\phi/\mathrm{d}t)_{\mathrm{ZAMO}}$. At the outer event horizon, the frame dragging frequency reads

$$\Omega_{\mathrm{BH}} := \Omega(r = r_+) = \frac{a}{2Mr_+}. \tag{5}$$

The redshift which accounts for the lapse of proper time τ in the ZAMO frame with respect to the global (Boyer–Linquist) time t, thus, $\alpha = (\mathrm{d}\tau/\mathrm{d}t)_{\mathrm{ZAMO}}$ is

$$\alpha := \sqrt{\frac{\Sigma\Delta}{A}}. \tag{6}$$

While quantities in Boyer–Lindquist coordinates are represented in a spatial basis made by the set of orthogonal vectors $\{\partial_i\} = \{\boldsymbol{e}_i\}$, the local ZAMO observers have an attached triad $\{\hat{\boldsymbol{e}}_i\} = \{\boldsymbol{e}_i/\sqrt{g_{ii}}\}$, where the index i runs over the three spatial coordinates (r, θ, ϕ). g_{ii} are the diagonal components of the metric tensor, namely

$$g_{rr} = \frac{\Sigma}{\Delta}, \qquad g_{\theta\theta} = \Sigma, \qquad g_{\phi\phi} = \frac{A\sin^2\theta}{\Sigma}. \tag{7}$$

The ZAMO's four velocity is $n_\mu = (-\alpha, 0, 0, 0)$ and may be used to introduce a projection tensor on the spatial components of a suitable $3 + 1$ decomposition of space-time

$$\gamma_{\mu\nu} = g_{\mu\nu} + n_\mu n_\nu \tag{8}$$

The determinants of the metric tensors will be denoted by g or γ, respectively.

2.2 Force-free electrodynamics

In analogy to Komissarov (2004) and Parfrey, Spitkovsky & Beloborodov (2017), we solve Maxwell's equations in the force-free limit

$$\nabla_\nu F^{\mu\nu} = I^\mu \tag{9}$$

$$\nabla_\nu^* F^{\mu\nu} = 0 \tag{10}$$

Here, $F^{\mu\nu}$ and ${}^*F^{\mu\nu}$ are the Maxwell tensor and its dual, respectively. I^μ is the electric current four vector associated with the charge density $\rho = \alpha I^t$, and the current three vector $J^i = \alpha I^i$. ∇ denotes the covariant derivative, Greek indices reflect arbitrary space-time quantities, Latin indices will refer to the coordinate directions of a $3 + 1$ space-time decomposition (see equation 8). We separately evolve the continuity equation of total electric charge

$$\nabla_\nu I^\nu = 0, \tag{11}$$

in order to ensure conservation of (total) electric charge in the computational domain. Komissarov (2004) introduces the equivalent of the classical field quantities $\boldsymbol{E}$, $\boldsymbol{B}$, $\boldsymbol{D}$, and $\boldsymbol{H}$ in a $3 + 1$ decomposition of space-time

$$E_i = F_{it}, \tag{12}$$

$$B^i = \frac{1}{2}e^{ijk}F_{jk}, \tag{13}$$

$$D^i = \frac{1}{2}e^{ijk*}F_{jk}, \tag{14}$$

$$H_i = {}^*F_{ti}, \tag{15}$$

where $e^{ijk} = \alpha\eta^{0ijk}$, with the volume element $\eta^{\mu\nu\lambda\zeta} = [\mu\nu\lambda\zeta]/\sqrt{-g}$, and the completely antisymmetric Levi–Civita symbol $[\mu\nu\lambda\zeta]$. These equivalents to the classical electric field and magnetic induction as well as the electric displacement and the magnetic field encode the geometry of space-time (i.e. the lapse in time and frame dragging of space) as non-vacuum effects in the full set of macroscopic Maxwell equations. In order to solve equations (9) and (10), one specifies the following constitutive relations (cf. Jackson 1999)

$$\boldsymbol{E} = \alpha\boldsymbol{D} + \boldsymbol{\beta} \times \boldsymbol{B}, \tag{16}$$

$$\boldsymbol{H} = \alpha\boldsymbol{B} - \boldsymbol{\beta} \times \boldsymbol{D}. \tag{17}$$

We may now write the Maxwell tensor as measured by the normal observer (ZAMO) in terms of the macroscopic field quantities (cf. Antón et al. 2006)

$$F^{\mu\nu} = n^\mu D^\nu - D^\mu n^\nu - e^{\mu\nu\lambda\zeta}B_\lambda n_\zeta, \tag{18}$$

$$ {}^{*}F^{\mu\nu} = -n^{\mu}B^{\nu} + B^{\mu}n^{\nu} - e^{\mu\nu\lambda\zeta}D_{\lambda}n_{\zeta}. \tag{19}$$

To build-up a stationary magnetosphere around the central BH, it is necessary to guarantee that there are either no forces acting on the system or, more generally, that the forces of the system are in equilibrium. The latter condition implies that the electric 4-current I^{μ} satisfies the force-free condition (Blandford & Znajek 1977)

$$F_{\mu\nu}I^{\nu} = 0, \tag{20}$$

With the above definition (18), this condition (20) reduces to

$$D^{\mu}B_{\mu} = 0 \qquad \Leftrightarrow \qquad {}^{*}F_{\mu\nu}F^{\mu\nu} = 0. \tag{21}$$

The component of the electric field parallel to the magnetic field vanishes. A second condition of magnetic dominance is given by

$$F_{\mu\nu}F^{\mu\nu} > 0. \tag{22}$$

In the language of the full system of Maxwell's equations in 3 + 1 decomposition, expressions (21), and (22) respectively read

$$\boldsymbol{D}\cdot\boldsymbol{B} = 0 \tag{23}$$

$$\boldsymbol{B}^2 - \boldsymbol{D}^2 \geq 0. \tag{24}$$

Conditions (23) and (24), as well as the conservation condition $\partial_t\left(\boldsymbol{D}\cdot\boldsymbol{B}\right) = 0$ can be combined in order to obtain an explicit expression for the so-called force-free current $I^{\mu}_{\rm FF}$ (cf. Komissarov 2011; Parfrey et al. 2017)

$$\begin{aligned} I^{\mu}_{\rm FF} = \rho n^{\mu} &+ \frac{\rho}{\boldsymbol{B}^2}e^{\nu\mu\alpha\beta}n_{\nu}D_{\alpha}B_{\beta} \\ &+ \frac{B^{\mu}}{\boldsymbol{B}^2}\,e^{\alpha\beta\mu\sigma}n_{\sigma}\left(B_{\mu;\beta}B_{\alpha} - D_{\mu;\beta}D_{\alpha}\right). \end{aligned} \tag{25}$$

In practice, the combination of the force-free current (25) as a source-term to equation (9) with numerically enforcing conditions (23) and (24) restricts the evolution to the force-free regime. The discussion of techniques in order to ensure a *physical* (cf. McKinney 2006) evolution of numerical force-free codes can be found throughout the literature (e.g. Lyutikov 2003; Komissarov 2004; Palenzuela et al. 2010; Alic et al. 2012; Paschalidis & Shapiro 2013; Carrasco & Reula 2016; Parfrey et al. 2017). A review of the employed conservative system of equations, and techniques to minimize numerical errors are given in Appendix A1, as well as Mahlmann et al. (2019).

2.3 Magnetic loop accretion systems

Since the force-free approximation corresponds to the limit of vanishing plasma inertia, it is not possible to construct an AD self-consistently around a central BH. Thus, we resort to introducing a suitable AD setup that is a crucial ingredient in our models and resembles, to some extent, the procedure sketched in Parfrey et al. (2015). We consider the force-free evolution of a system composed by a BH surrounded by an (idealized) equatorial AD of finite vertical extension. There, the magnetic field can be anchored. In practical terms, the ad hoc equatorial structure that we construct serves for the purpose of providing conditions that may mimic the accretion process found in self-consistently built ADs.

In our model, the equatorial region around the BH is set up using different types of electric currents (Fig. 1) that serve two purposes. First, they mimic the accretion flow in the AD, and secondly, they drive the plasma from the innermost stable circular orbit (ISCO) to the BH. The AD is split into two regions located at different vertical distances from the equator. In the innermost region, $|z| \leq h_{\rm LAL}$, referred to in the following as the *lower accretion layer* (LAL; violet-to-yellow shades in Fig. 1), we impose a toroidal current (equation 32), whose effect is the generation of a set of concentric magnetic flux tubes that move radially inward at a prescribed *accretion speed*. In the limit of GRFFE, there is no actual fluid and, hence, the fluid velocity is not even a variable of the governing equations. Thus, the accretion speed is not the self-consistent result of the physical transport of angular momentum towards the exterior. Additionally, we impose the rotational speed of the AD in our models. Finding a poloidal current that effectively induces the sought for rotational profile is not an easy task. Instead, we specify the rotational profile resorting to a different procedure, namely, adding a further (resistive MHD) layer surrounding the LAL. Extending vertically for $h_{\rm LAL} \leq |z| \leq h$, ($h$ is, thus, the disc half-thickness) we define the *upper accretion layer* (UAL). There, we prescribe a resistive MHD current (red-shaded region in Fig. 1, equation 29) that replaces the force-free current in the GRFFE equations. In this resistive MHD current, besides the radial motion, the rotational profile of the AD can be easily specified (see equation 31 below). We drive the *free-fall* of plasma from the ISCO to the BH by prescribing a free-falling geodesic motion in the equatorial region (Fig. 1, blue shaded). We refer to the paraboloidally shaped region $r_+ < r_{\rm c} < r_{\rm ISCO}$ and $|z| \leq h\sqrt{(r_{\rm c} - r_+)/(r_{\rm ISCO} - r_+)}$ as *plunging region*. Here, $r_{\rm c} = \sqrt{g_{\phi\phi}}$ is the cylindrical radius from the central object. As in the UAL, the kinematics of the plunging region are prescribed by employing a resistive MHD current whose velocity field follows a free-falling geodesic motion in the equatorial plane,

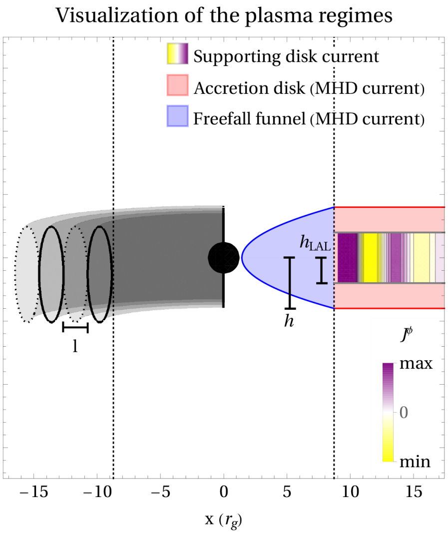

Figure 1. Schematic visualization of the employed accretion disc model. Left half: Sketch of the flux tubes (length l and scale height h) supported by the AD model. Flux tubes with opposite polarity are denoted by enclosing their cross-section with dashed and solid-line ellipses. Right half: Structure of the different currents in the simulation domain. The supporting current maintains the loop structure over long periods of time by imposing an alternating (toroidal) current density in the LAL (violet-to-yellow shades). The MHD currents in the UAL (red shade) introduce the accretion dynamics in the system for the assumed equatorial velocity field. In the white region, we employ full force-free electrodynamics (see Section 2.2).

matching the angular velocity to the BH rotation smoothly (see equation 5). Since the plunging region is relatively thin, we employ an exclusively radially dependent velocity prescription all over its volume, regardless of the vertical distance to the equator.

In the following paragraphs, we describe the specific form of the currents employed in every region in detail. We begin by specifying the form of the resistive MHD current used in the UAL. For that, we need to provide a closure relation, the Ohm's law (see e.g. Baumgarte & Shapiro 2003; Palenzuela et al. 2010; Parfrey et al. 2017), for which we take

$$I_\mu - \tilde{\rho} u_\mu = \sigma F_{\mu\nu} u^\nu . \tag{26}$$

Here, σ is the plasma conductivity, $\tilde{\rho} = -I^\nu u_\nu$ denotes the charge density as seen by an observer co-moving with the fluid (Baumgarte & Shapiro 2003), while $\rho = -I^\nu n_\nu$ (with the definitions given in Sections 2.2 and 2.1) is the charge density observed by a normal observer (Komissarov 2004). For the four velocity u^μ we define the Lorentz factor

$$W = -n_\mu u^\mu = \alpha u^t , \tag{27}$$

and the normal observer 3-velocity (cf. Baumgarte & Shapiro 2003)

$$v^i = \frac{u^i}{u^t}. \tag{28}$$

Inserting the definition of fields from equations (12)–(15) into equation (26), and using the notation introduced in equations (27) and (28), one obtains the resistive MHD current used in the presented simulations

$$I^i = W\sigma \left[E^i + e^{ijk} v_j B_k - \frac{1}{\alpha} D^a v_a v^i \right] + \rho v^i . \tag{29}$$

In practice, we set $\sigma = 1$ as (approximately) the highest possible value without reaching stiffness in the evolution equations. In cgs units this corresponds to $\sigma \sim 1.6 \times 10^4\,\mathrm{s}^{-1}$.

In the UAL (beyond the ISCO), we impose a uniform radial accretion speed, v_0 and nearly Keplerian angular velocity

$$v^r = v_0, \qquad \text{and} \qquad v^\phi(r_\mathrm{c}) = \pm \frac{\sqrt{M}}{r_\mathrm{c}^{3/2} \pm a\sqrt{M}}. \tag{30}$$

The + and − signs represent co-rotating and counter-rotating disc systems, respectively. Physically, this simple prescription for the accretion speed can be motivated by the fact that in a standard Shakura & Sunyaev (1973) disc, the accretion speed is related to the α_SS parameter, the disc half-thickness, h, and the Keplerian speed, $v_\mathrm{K} \simeq (r_g/r)^{1/2} c$, through $v_0 \simeq \alpha_\mathrm{SS}(h/r)^2 v_\mathrm{K}$. In our case, we approximate $\chi_\mathrm{h} := h/r \lesssim 0.5$ (a thin disc would require $\chi_\mathrm{h} \ll 1$, but simulating very thin discs is numerically challenging), and evaluate the Keplerian speed at $r = r_\mathrm{ISCO}$. Employing the typical value $\alpha_\mathrm{SS} \simeq 0.1$, we obtain for counter-rotating discs

$$v_0 \lesssim 0.02(\alpha_\mathrm{SS}/0.1)(\chi_\mathrm{h}/0.5)^2. \tag{31}$$

We prescribe a toroidal current J^ϕ_disc in order to create an electric current in the LAL that supports the ad hoc magnetic structure (i.e. a series of concentric magnetic flux tubes with alternate polarity). This current is driven during the initialization and also during the whole evolution of the system. Otherwise, the loop structure in the AD and elsewhere is distorted, rapidly dissipated, and eventually destroyed. It is located underneath the UAL, precisely in the region $r_\mathrm{c} > r_\mathrm{ISCO}$ and $|z| \leq h_\mathrm{LAL}$

$$J^\phi_\mathrm{disc}(r_\mathrm{c}, t) = J_0 \times \cos\left(\pi \frac{r_\mathrm{c} - r_\mathrm{ISCO} + t v_0}{l}\right) \times \frac{\alpha}{\sqrt{g}\sqrt{g_{rr} g_{\phi\phi}}}. \tag{32}$$

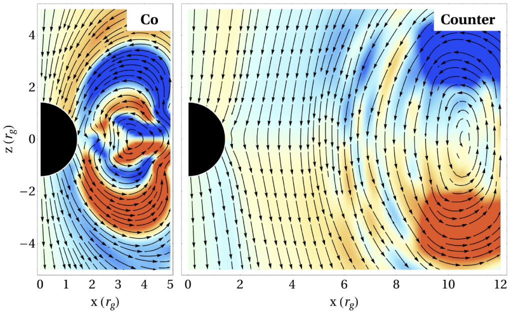

Figure 2. Zoom of the innermost region of the computational domain showing poloidal streamlines. The colours show the values of the toroidal field B^T (blue negative, red positive) for an (exemplary) initialization of the co-rotating AD (left) and the counter-rotating AD (right) for $v^r = 0$.

Here, l denotes the length of the loop along r_c. In our setup, each model is characterized by three parameters defining the magnetic structure and accretion of the loops in the AD: The loop length l, the loop height within the disc, h, which reaches the maximal vertical extension of the UAL, and the (uniform) accretion speed v_0. The latter is applied to shift J^ϕ_disc inwards in time and to prescribe a plasma velocity for the current in the UAL (29). We employ $J_0 = 0.1$ for all the presented setups. By construction, the total magnetic flux accumulated by one tube can differ for different loop dimensions. Also, we use smooth transitions functions blending the different regions composing our BH/AD system into one-another at their interfaces. Outside of the disc and plunging region, the time evolution is fully force-free (uncolored regions in Fig. 1). Fig. 2 shows the (exemplary) initialization of a loop system by the prescribed current (32) for the simplified case without accretion ($v^r = 0$) and a force-free plunging region.

2.4 Toy-model accretion disc setup

The transport of magnetic flux in the plunging region (cf. Fig. 1, Section 2.3) is a central ingredient in our models. Without imposing a *fluid velocity* corresponding to a geodesic in-fall motion in the ad hoc resistive MHD current (29), the magnetic loops of zero net flux are rapidly destroyed. The governing equations of force-free electrodynamics can be written in terms of the evolution of the Poynting flux S^j and the field energy density e, rather than the electromagnetic fields (the latter as introduced in Section 2.2). The time evolution of e reads

$$\left(\sqrt{\gamma} e\right)_{,t} = \left(\sqrt{\gamma} S^j\right)_{,j} - \alpha\sqrt{\gamma} D_i J^i + \mathcal{S}_t . \tag{33}$$

Here, $\mathcal{S}_t$ corresponds to source terms induced by the geometry or the cleaning of numerical errors. The term $\alpha\sqrt{\gamma} D_i J^i$ vanishes if there is no dissipation, otherwise, it accounts for the losses due to ohmic heating. The electromagnetic fields surrounding a resistance wire (cf. fig. 27-5, Feynman, Leighton & Sands 2011) are comparable to those imprinted by the innermost current in the plunging region of our model. In the UAL and LAL, the electric field **D** is (in part) aligned with the current J^ϕ_disc, such that

$$D_i J^i = D_\phi J^\phi_\mathrm{disc} \neq 0. \tag{34}$$

In a stationary magnetic loop structure, the left-hand side of (equation 33) vanishes, and the Poynting flux S^j points towards the centre of the flux tubes. This is counter-balanced by the ohmic heating term. If $J^{\phi}_{\rm disc}$ is replaced by the force-free current $\alpha I^{\mu}_{\rm FF}$ (25), such heating is prevented by conditions (23) and (24)

$$D_i J^i = \alpha D_i I^i_{\rm FF} = 0. \qquad (35)$$

The Poynting flux is no longer balanced and the loop becomes a sink for the energy of the force-free field. As the rate of dissipation is given by $\nabla \cdot \mathbf{S}$, a quenching of the loop (i.e. steeper gradients) by the subsequently accreting structure will enhance energy dissipation.

More generally, Gralla & Jacobson (2014) revisit and extend arguments by MacDonald & Thorne (1982) proving that *a contractible force-free region of closed poloidal field lines cannot exist in a stationary, axisymmetric, force-free Kerr BH magnetosphere*. Also, *a stationary, axisymmetric, force-free, magnetically dominated field configuration cannot possess a closed loop of poloidal field lines* (Gralla & Jacobson 2014). Though the presented simulations are fully dynamic across all spatial dimensions, closed magnetic loops – wrapped to toroidal flux tubes – or 'closed zones' of field lines connecting the BH to itself seem to be merely transient phenomena in the force-free domain. We conclude that a current for the transport of magnetic field lines through the plunging region, especially the addition of a suitable non-force-free domain along the equator, is essential to sustain closed magnetic loops in their advection towards the BH.

3 SIMULATIONS

For all the simulations we employ our own implementation of a GRFFE code (see Appendix A1 for an overview of the employed conservative scheme) in the framework of the `Einstein Toolkit`[1] (Löffler et al. 2012). The `Einstein Toolkit` is an open-source software package utilizing the modularity of the `Cactus`[2] code (Goodale et al. 2003), which enables the user to specify so-called `thorns` in order to set up tailored simulations. The space–time is integrated in time using the `ML_BSSN`[3] implementation of the BSSN formalism (Brown et al. 2009). We make use of a variety of open-source software, such as the event horizon finder `AHFinderDirect` (Thornburg 2004), the extraction of quasilocal quantities `QuasiLocalMeasures` (Dreyer et al. 2003), and the efficient `SummationByParts` (Diener et al. 2007).

We have performed numerical simulations of the accretion of magnetic loops on to rapidly spinning black BHs using the rescaled Liu, Etienne & Shapiro (2009) space−time initial data (as employed also by Mewes et al. 2016) for a mass $M = 1$ and a reference rotation rapidity $a^{*} = 0.9$. In this paper, we evolve the space–time metric quantities decoupled (i.e. without feedback) from the electromagnetic fields. This decoupling facilitates the comparison to the previous results with a similar (though axisymmetric) setup (Parfrey et al. 2015). The metric quantities only experience a *numerical relaxation* from the initially set up values to the chosen mesh and gauge during the first $\Delta t = 50\, r_g$. Throughout the entire simulation ($\Delta t = 1024 r_g$), a^{*} decreases by ~ 1.4 per cent of its initial value for numerical reasons. Values of a^{*} very close to 1 are numerically challenging for our code, which, by design, evolves the space–time metric quantities. Liu et al. (2009) are able to obtain a numerically stable evolution, where the metric quantities do not evolve by more than $\sim$ 1 per cent with respect to their initial values, for a BH $a^{*} = 0.99$ during a relatively short period of time employing larger numerical resolution than used here. However, we have performed a comprehensive parameter space coverage running our models for significantly longer times ($\Delta t \simeq 1000\, M$), making it impractical to employ larger numerical resolution than we have used. Hence, we consider cases with $a^{*} = 0.9$. This value is not as close to 1 as would be desirable to address nearly maximally spinning BHs in AGNs, and it is slightly smaller than the value employed by Parfrey et al. (2015). However, the outward-going Poynting flux is comparable to the nominal radiative efficiency for $a^{*} \backsimeq 0.9$ (Hawley & Krolik 2006), and the value we employ suffices to demonstrate the efficiency of the (intermittent) BZ mechanism when there is no net magnetic flux supplied to the BH. Initially, the electromagnetic field is set to zero everywhere. For an initialization period $\Delta t_{\rm init} = 250 r_g$, we let the numerical code to build-up the electromagnetic fields according to the set of currents described in Section 2.3. At this point of the evolution, the space–time has fully relaxed to its numerical state of equilibrium, and we start our analysis of physical quantities for an interval $\Delta t_{\rm tot} = [0 r_g, 774 r_g]$.

Table 1. Overview of the parameters of our models clustered by series (first column). From the second to the last column, we list the orientation of the disc rotation (counter- or co-rotation; annotated with a prefix C or R, respectively), the loop length, l and the height h of the disc, the height h_i of the supporting current, and the accretion speed v_0 outside of the ISCO.

Series	Model	Orientation	h	h_i	l	v_0
A	C-H2-L1	Counter	2.0	0.75	1.0	0.01
	C-H2-L2	Counter	2.0	0.75	2.0	0.01
	C-H2-L25	Counter	2.0	0.75	2.5	0.01
	C-H2-L3	Counter	2.0	0.75	3.0	0.01
	C-H2-L4	Counter	2.0	0.75	4.0	0.01
	C-H4-L1	Counter	4.0	2.0	1.0	0.01
	C-H4-L2	Counter	4.0	2.0	2.0	0.01
	C-H4-L25	Counter	4.0	2.0	2.5	0.01
	C-H4-L3	Counter	4.0	2.0	3.0	0.01
	C-H4-L4	Counter	4.0	2.0	4.0	0.01
B	C-H4-L2-005	Counter	4.0	2.0	2.0	0.005
	C-H4-L2-02	Counter	4.0	2.0	2.0	0.02
	C-H4-L2-04	Counter	4.0	2.0	2.0	0.04
C	R-H1-L2	Co	1.0	0.5	2.0	0.01
	R-H1-L3	Co	1.0	0.5	3.0	0.01
	R-H1-L4	Co	1.0	0.5	4.0	0.01

3.1 Numerical setup

All shown simulations are conducted in a 3D box of dimensions $[2056 r_g \times 2056 r_g \times 2056 r_g]$ with a grid spacing of $\Delta_{x,\,y,\,z} = 64 r_g$ on the coarsest grid level. We employ 11 additional levels of mesh refinement, each increasing the resolution by a factor of 2 and encompassing the central object. In order to increase resolution in the funnel and disc regions, several levels are stretched in the equatorial direction. Each model (see Table 1) is evolved for a period of $t = 1024 r_g$, or approximately $\sim$50 revolutions of the central object (corresponding to $a^{*} = 0.9$). On the finest refinement level, we employ a CFL of 0.25, while on coarser levels the time-step needs to be limited to $\delta t \leq 1.0$ due to instabilities introduced by the BSSN gamma driver (Schnetter 2010).

Since all characteristics at the BH horizon point inwards (Faber et al. 2007), information does not propagate from the interior of the horizon outwards. Thus, for numerical convenience, we may reset

---

[1] http://www.einsteintoolkit.org

[2] http://www.cactuscode.org

[3] http://www.cct.lsu.edu/~eschnett/McLachlan/

all variables inside the outer horizon for numerical convenience. Otherwise, close to the BH singularity, the FF equations develop large numerical errors that may result in the failure of the method. A similar strategy has been employed, e.g. in Mewes et al. (2016).

In order to ensure the conservation properties of the algorithm, it is critical to employ *refluxing* techniques, correcting numerical fluxes across different levels of mesh refinement (see e.g. Collins et al. 2010). Specifically, we make use of the thorn `Refluxing`[4] in combination with a cell-centred refinement structure (cf. Shibata 2015). We highlight the fact that employing the refluxing algorithm makes the numerical code 2–4 times slower for the benefit of enforcing the conservation properties of the numerical method (specially of the charge). Refluxing also reduces the numerical instabilities that tend to develop at mesh refinement boundaries.

3.2 Energy outflow

Efficient energy extraction of the reducible energy from rapidly spinning BHs via the BZ process happens if the field line angular velocity, $\Omega_{\rm F}$, equals half the BH angular frequency, i.e. $\Omega_{\rm F} = \Omega_{\rm BH}/2$ (Blandford & Znajek 1977). Under this optimal condition, a second-order accurate estimation[5] of the luminosity of the BZ process reads (Tchekhovskoy & Giannios 2015)

$$\mathcal{L}_{\rm BZ} \approx \frac{1}{24\pi^2}\Omega_{\rm BH}^2\Phi^2 = \frac{1}{96\pi^2}\left(\frac{\Phi a^*}{r_+}\right)^2. \tag{36}$$

The factor $1/96\pi^2 \approx 10^{-3}$ corresponds to the split-monopole BH magnetosphere,[6] and depends weakly on the field geometry (cf. Tchekhovskoy, Narayan & McKinney 2010). Φ denotes half of the absolute magnetic flux through the BH horizon. Our models do not set any initial magnetic field close to the BH horizon, only attached to the AD. Hence, in order to compute an estimate for the BZ luminosity that can be used as a normalization of our results, we make the following assumption: the entire poloidal magnetic flux of a tube detaching from the AD would ideally thread the BH horizon. Thus, we integrate the vertical flux through the equatorial plane $(r, \phi \in [r_{\rm ISCO} + l/2,\ r_{\rm ISCO} + l] \times [0, 2\pi])$ for the last loop outside of the ISCO, in order to derive an upper limit to Φ:

$$\Phi = \iint_{r\phi} \left|B^\theta\right| \, {\rm d}A_\theta. \tag{37}$$

Here, ${\rm d}A_i$ denotes a suitable area element. In actuality, part of this flux may be lost due to magnetic reconnection and may never end up touching the BH horizon. Following Parfrey et al. (2015), we define the process luminosity $\mathcal{L}_{\rm LA}$ during the accretion of magnetic loops as the surface integral of the outgoing Poynting flux S^r_+ over the BH horizon, hence, only including the sum of positive contributions to the total energy flow

$$\mathcal{L}_{\rm LA} = \iint_{\theta\phi} S^r_+ \, {\rm d}A_r \tag{38}$$

The Poynting flux S^r_+ is derived from the corresponding components of the energy–momentum tensor (Komissarov 2004),

$$S^i = T^i{}_t = -\frac{1}{\alpha} e^{ijk} E_j H_k. \tag{39}$$

The process efficiency relating the energy extracted by the in-fall of magnetic loops on to the central object compared to an optimal BZ powered energy extraction then reads

$$\epsilon = \frac{\mathcal{L}_{\rm LA}}{\mathcal{L}_{\rm BZ}}. \tag{40}$$

Besides the instantaneous variation of the efficiency shown in Figs 3 and 5, it is important to asses whether the accretion of loops with zero net magnetic flux drives, on average, a significantly luminous outflow. For that we may compute the time-averaged efficiency, $\bar{\epsilon}$, over the whole computed time $\Delta t_{\rm tot}$. However, we realize that in many models one needs to wait for two or three cycles before some quasi-periodic behaviour takes place. Since evolving our 3D models much longer is prohibitive, we consider an alternative measurement of the average efficiency. Namely, we quantify the average efficiency $\langle\epsilon\rangle$ during the accretion period $\Delta t_{\rm acc} = l/v_0$ of the final accretion cycle in the computed time.

3.2.1 *Counter-rotating accretion disc*

The simulation time for all models of series A (see Table 1) is sufficient to detach several loops from the AD and model their plunge on to the central BH. Fig. 3 visualizes the evolution of the process efficiency ϵ. Peaks of efficient outgoing Poynting fluxes can be seen throughout all models of the series. While the calculated peak efficiency of $\epsilon_P \approx 85$ per cent is similar for all the shown models, consecutive peaks often differ in shape and fine structure. The efficiency peaks are related to the structure of magnetic loops in the AD in a complex and non-linear way. They do not follow the simplistic expectation according to which, after the accretion of half of a complete magnetic loop, an efficiency peak develops while low efficiency occurs only for times in between of two consecutive loops of alternated polarity (when the magnetic flux threading the BH horizon is closest to zero). Furthermore, the temporal width of the peaks is not a one-to-one map of the time need to accrete half of a complete magnetic flux tube from the accretion disc, namely, $\Delta t_{\rm acc}$. Indeed, the consecutive episodes of efficient energy extraction show, in many cases, a lot of substructure and both the peak shape and ϵ_P notably differ from peak to peak (e.g. see models C-H2-L2, C-H2-L3, and C-H4-L4). This contrasts with the results of Parfrey et al. (2015), where the high-efficiency pulses of the single model (shown in their Fig. 2) are very regular and reach nearly the same value of $\epsilon_P \simeq 0.75$ in all cases. Only during the first peak, some transitory relaxation of the initial conditions is observed in their 2D models. We attribute the differences to the complex 3D dynamics and to the fact that the loop cross-sectional size is a factor of foremost importance shaping the efficiency of energy extraction.

Models with small length of the loops, $l = 1r_g$ (C-H2-L1 and C-H4-L1), convert magnetic flux into a Poynting dominated energy outflow less efficiently. The difference in the vertical extension of the AD between models C-H2-L1 and C-H4-L1 induces significant differences in the regularity of the high-efficiency episodes. Three relatively regular episodes of high efficiency (at the peak, $\epsilon_P > 0.8$) with duration $\Delta t \sim 100\,r_g$ follow each other in model C-H4-L1, while only two peaks with $\epsilon_P > 0.8$ and duration $\Delta t \sim 100\,r_g$ are irregularly distributed in $\Delta t_{\rm tot}$ for model C-H2-L1. In both cases, efficient episodes are followed by less powerful cycles. During

---

[4] Refluxing at mesh refinement interfaces by Erik Schnetter: https://svn.cct.lsu.edu/repos/numrel/LSUThorns/Refluxing/trunk.

[5] We note that in the preceding work Mahlmann, Cerdá-Durán & Aloy (2018), the BZ power has a misplaced factor of M^2 in equation (42) of Mahlmann et al. (2018).

[6] In Heaviside–Lorentz geometrized units (cf. Mahlmann et al. 2019), which differ by a factor $1/\sqrt{4\pi}$ when compared to Gaussian cgs units (as displayed, e.g. by Event Horizon Telescope Collaboration 2019b).

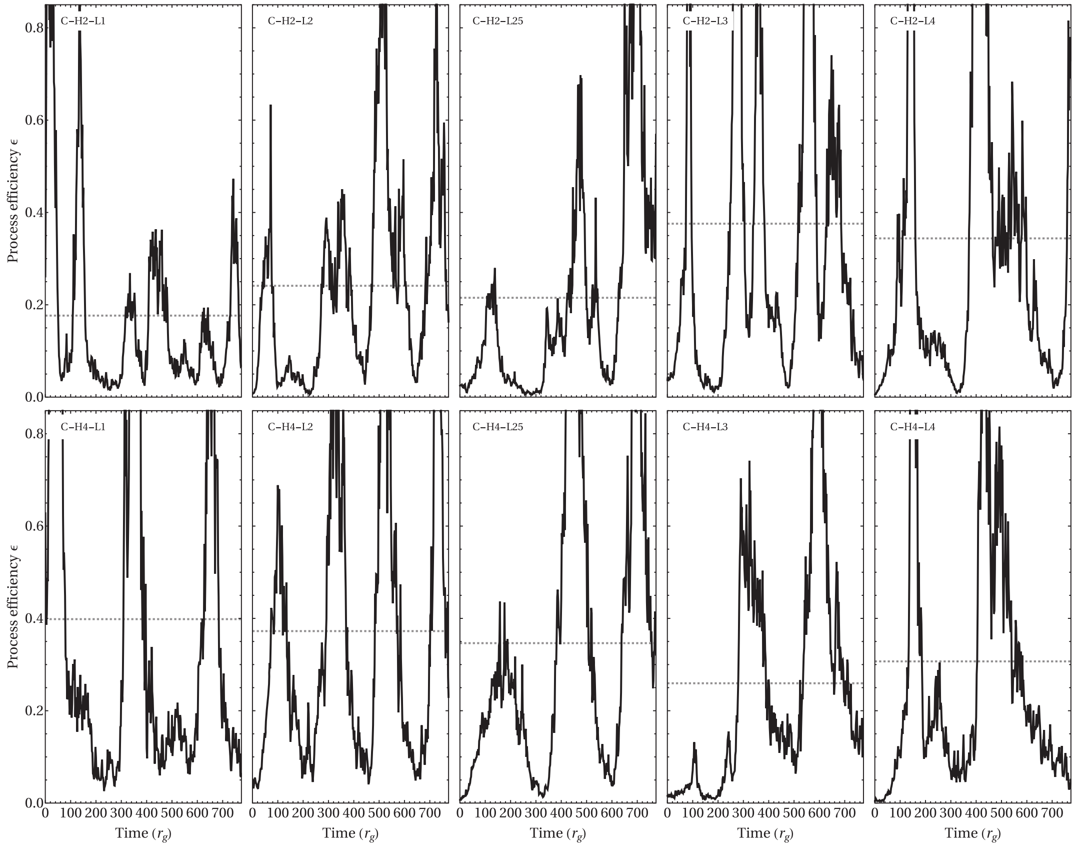

Figure 3. Efficiency of the BZ process ϵ (equation 40) during the evolution of selected models of counter-rotating discs (cf. Table 1). The process efficiency depends on the structure of the magnetic loops in the AD, specifically on the chosen loop scale height and length, in a complex and non-linear way. The average efficiency $\bar{\epsilon}$ of each model over the entire simulation period Δt_{tot} is indicated by a grey dashed line.

the absence of powerful outflows, we observe that the structure of wound up field lines threading the BH horizon fails to open up to high vertical extensions (see discussion in Section 4.2). The rapid release of flux tubes of shorter length is also imprinted on to the shown efficiency curves by an increased small-scale variability due to more incoherent flux structures arriving at the BH horizon.

For series A, average efficiencies during the accretion of one (or two, in case of the models of loop length $l = 1r_g$) magnetic loops are shown in Fig. 4 (black symbols) as a function of the logarithm of $l \times h$, which is proportional to the cross-sectional area (in the poloidal plane) of the magnetic flux tubes setup in the AD. In this representation, one can identify a range of optimal loop cross-section areas for which the average efficiency is nearly maximal, $\langle\epsilon\rangle \approx 0.36$–$0.43$. This range is rather broad and corresponds to models with very similar loop cross-sectional area, namely, C-H2-L2 and C-H4-L1 as well as C-H2-L4 and C-H4-L2. For very small and very large loop areas, $\langle\epsilon\rangle$ drops to lower values. We stress that $\langle\epsilon\rangle$ cannot be interpreted using independently l or h as parameters. Only the combination of both (in the form $h \times l$) permits finding some empirical correlation between the geometrical properties of the loops and the process efficiency. After testing many different possibilities, we find that the average process efficiency can be fit by (see black line in Fig. 4)

$$\langle\epsilon\rangle \simeq -0.21\,[\ln(h \times l)]^2 + 0.82\ln(h \times l) - 0.29. \tag{41}$$

We also display the average efficiency over the whole computed time, $\bar{\epsilon}$, in Fig. 4 (magenta symbols). The dependence on the surface area of the loops found for $\langle\epsilon\rangle$ is much less evident for $\bar{\epsilon}$. This is due to the fact that during the accretion of the first loop the dynamics in the BH magnetosphere is still rather violent and an approximately steady state has not been formed. We note that a qualitatively similar difference between the first loop of the series and the subsequent ones was also found by Parfrey et al. (2015). This behaviour justifies our choice of measuring the average efficiency over the last loop accreted during Δt_{tot}, $\langle\epsilon\rangle$. It provides a cleaner interpretation of the dependence of results on the model parameters.

3.2.2 *Co-rotating accretion disc*

Fig. 5 visualizes the evolution of the instantaneous efficiency ϵ of the models in series C (see Table 1). All of these models

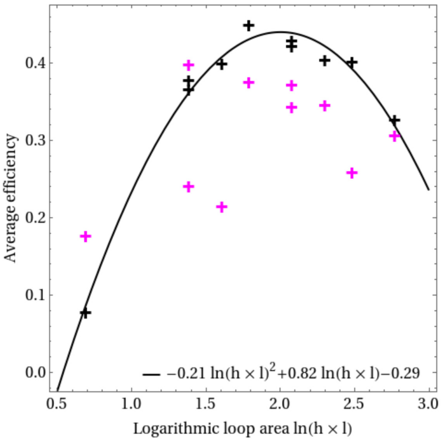

Figure 4. Average efficiency of the BZ energy extraction in selected models of counter-rotating discs (series A, cf. Fig. 3 and Table 1). The average efficiencies against the logarithmic loop area are depicted by crosses. The average efficiencies $\bar{\epsilon}$ over the simulation period Δt_{tot} are shown in magenta, the efficiency of the last accreted loop $\langle\epsilon\rangle$ for each model in black, a quadratic fit function is depicted by a respective line.

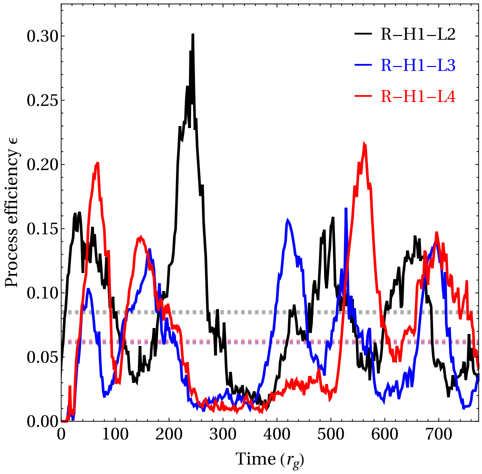

Figure 5. Same as Fig. 3 but for the co-rotating models of series C in Table 1. Both, the instantaneous and average efficiencies are notably smaller than in the case of counter-rotating discs.

show significantly lower process efficiencies (with $\bar{\epsilon} \approx 0.06$–$0.09$) than the setups of series A. Like in many counter-rotating models, the pulse pattern shows complex substructures and different peak heights. Though the loop length l can be recognized in the overall periodicity, the average efficiency $\langle\epsilon\rangle$ decreases for the models with the larger loop length R-H1-L3 and R-H1-L4. This happens because of the existence of longer *quiescent* periods between some of the peaks, where the instantaneous efficiency nearly drops to zero (e.g. between $\simeq 250 r_g$ and $\simeq 500 r_g$ for model R-H1-L4). Fig. 5 also shows that each accretion cycle for these models has two peaks of $\epsilon_P \approx 0.2$ with a drop in efficiency in between them.

Due to the large BH spin, the location of r_{ISCO} is very close to the BH horizon in case of co-rotating ADs. We are, hence, faced with two important challenges: (i) The disc height h has to be chosen such that the disc does not become excessively thick in the vicinity of the BH. Comparatively, the disc height-to-cylindrical radius ratio, h/r_{ISCO} is appreciably smaller for counter-rotating discs ($r_{\mathrm{ISCO}} \simeq 8.7 r_g$) than for co-rotating discs ($r_{\mathrm{ISCO}} \simeq 2.3 r_g$) with the same height. In practice, this fact introduces a strong distortion of the loop shape in co-rotating models. This distortion blurs the measurement of the process efficiency. (ii) Our ad hoc setup induces an additional far-field energy flow into our domain (see appendix C). The models of series C (Fig. 5) are chosen such that these caveats do not affect the energy flows at the BH horizon.

3.3 Field structure

3.3.1 Counter-rotating accretion disc

Once a magnetic loop reaches the inner disc boundary, part of it will start to free-fall on to the BH. This results in the development of structures resembling a *hairpin* (using the naming convention of Beckwith et al. 2009) in the plunging region, effectively connecting the BH horizon with the AD by twisted magnetic field lines (see panels a and d of Fig. 6). The emerging field structure shows a well-ordered dipole component, the growth and decrease of which are linked to the energy pulses as depicted in Fig. 3. At the same time, the action of strong differential shear in the plunging region (between the ISCO and the BH horizon) opens up magnetic field lines of the previously accreted loop, forming an ordered magnetic field of a parabola-like shape in the jet launching regions above the poles of the central BH (panel d). Though the accretion system supplies tubes of zero net magnetic flux, this structure of ordered magnetic fields is maintained over significant lengths compared both to the loop size and the plunging time-scale induced by r_{ISCO}.

Once a magnetic flux tube fully disconnects from the AD, several events occur in order to rearrange the magnetic field configuration with the accretion of a new magnetic tube of opposite polarity. During these processes, there is no efficient Poynting induced energy extraction across the BH horizon:

i) Establishment of quadrupole and higher multipoles (i.e. emergence of closed loops on either side of the equator, cf. Beckwith et al. 2008) small-scale structures resembling turbulence in the boundary between regions of different magnetic polarity (see Figs 6b and c). This process comes along with the relaxation of the parabola-like shape in the *jet launching* region, i.e. a biconic region with an approximate half-opening angle ~30°–45° (see Figs 6a and d).

ii) Expelling of large-scale flux structures from the jet launching region and replacing by the opposite polarity fields of the newly accreting tube opening up from the AD (see Fig. 6c).

iii) Evacuation of plasmoids with strong toroidal field dominance along the interface of opposite polarities into the jet launching region and away from the central object (see Fig. 6c).

During the phase of continuous accretion, the magnetic flux through the equatorial plane builds up spiral patterns (Fig. 7). Such perturbations reflect a loss of both, equatorial and axial symmetry along the equatorial current sheet, while the extended magnetic configuration may still exhibit ordered fields. The loss of symmetry in our perfectly axisymetric intial models is due to both numerical and physical reasons. The hierarchy of nested Cartesian

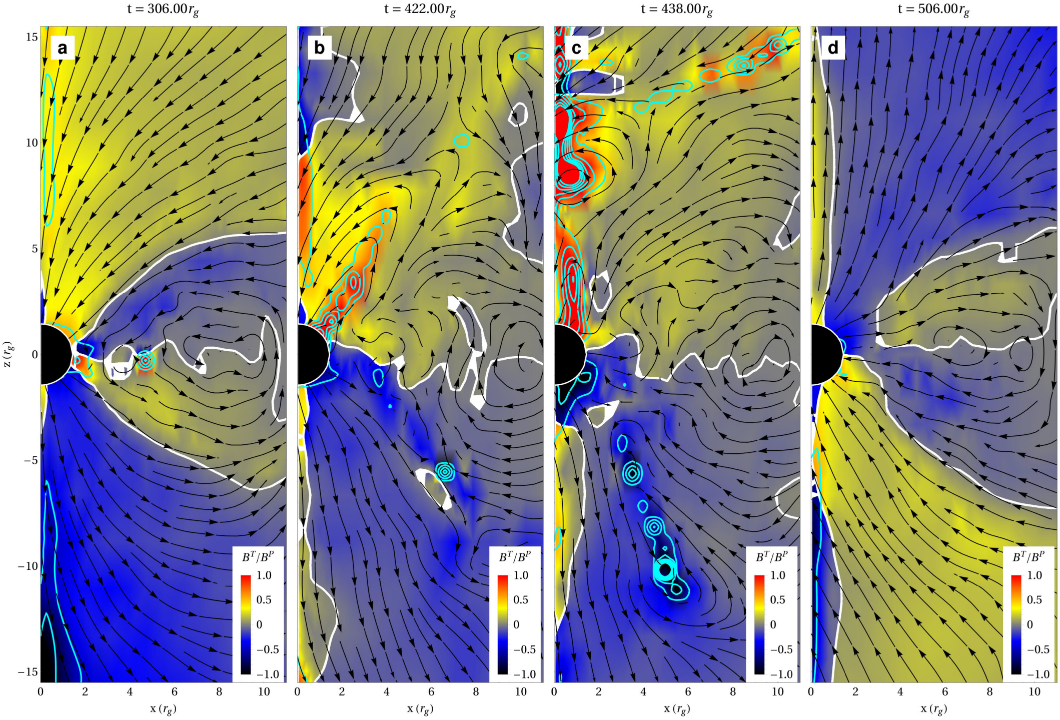

Figure 6. Evolution of the toroidal magnetic field dominance between two subsequent peaks of efficient energy extraction (model C-H4-L2). The colour scaling represents the strength of the toroidal magnetic field (including its sign) scaled by the magnitude of the poloidal magnetic field. The white lines indicate a change in polarity of the toroidal magnetic field. Cyan contours indicate very strong toroidal field dominance, e.g. as found in plasmoids. The shown data include refinement levels of resolutions $\Delta_{x,\,y,\,z} \leq 0.5r_g$. Episodes of efficient energy extraction (a and d) show recurring, ordered field structures. During the detachment of a magnetic loop from the AD and the change of overall polarization (b and c plots), simulations show small-scale, disordered structures (resembling turbulence) and plasmoids with strong toroidal field dominance.

grids mapping an axisymmetric setup may imprint small numerical perturbations on the plunging region, specially, at the boundary between the free-falling plasma and the AD. Episodic reconnection events drive physical perturbations along the equatorial plane also in the plunging region. Remarkably, qualitatively similar reconnection episodes may also break the equatorial symmetry in axisymmetric particle-in-cell simulations (Parfrey et al. 2019). Similar 3D effects have been observed by Beckwith et al. (2009, cf. Fig. 15) in the context of disconnecting magnetic loops in the accretion funnel of a large-scale magnetic flux system. During phases of efficient energy extraction from the central object (Fig. 3), extended helical structures of (outgoing) Poynting flux are formed in the polar regions. Fig. 8 shows such structures for the C-H4-L2 model at the moment of peak efficiency.

3.3.2 *Co-rotating accretion disc*

A *stationary*, *axisymmetric* force-free magnetospheres of a rotating BH including both open and closed (co-rotating) field lines anchored in a thin disc was discussed, e.g. by Uzdensky (2005), Mahlmann et al. (2018), and Yuan et al. (2019a, 2019b). In their equilibrium solutions all closed field lines connect the BH horizon to the inner regions of an equatorial (thin) disc up to a cylindrical radius $r_{\rm close} > r_{\rm ISCO}$. The disc also supports open field lines beyond $r_{\rm close}$. The foot-points of both open and closed field lines anchored in the disc rotate with the corresponding angular velocity (see equation 30). Closed field lines in this kind of magnetosperic topology allow for the exchange of angular momentum between the BH and the AD, but they do not efficiently extract energy to infinity. Uzdensky (2005) further identifies the possibility of a combination of these closed field lines and open field lines extending to a region far away from the central object in BH/AD systems, effectively extracting part of the energy by the BZ process (see also Contopoulos 2019, on the coexistence of electromagnetic accretion and ejection flows). Parfrey et al. (2015) argue that, since magnetic field lines can remain closed only up to $r_{\rm close}$ in axisymmetric magnetospheres, magnetic topologies composed by flux tubes with lengths $l < l_{\rm crit} = r_{\rm close} - r_{\rm ISCO} \sim O(r_g)$ will not produce jets. According to Uzdensky (2005), the exact location of $r_{\rm close}$ sensitively depends on the problem setup, e.g. the BH spin parameter, and the magnetic flux distribution on the disc. Thus, we also expect that $l_{\rm crit}$ depends on similar factors, in addition, e.g. to the disc's thickness and conductivity, and the radial distribution of the flux tubes in the disc. In the conducted simulations of co-rotating disc models, (series C, Table 1) we find closed magnetic flux tubes connecting the inner regions of the AD with the BH. These configurations are forming repeatedly, but they are neither axisymmetric nor steady. Due to the limitations of the

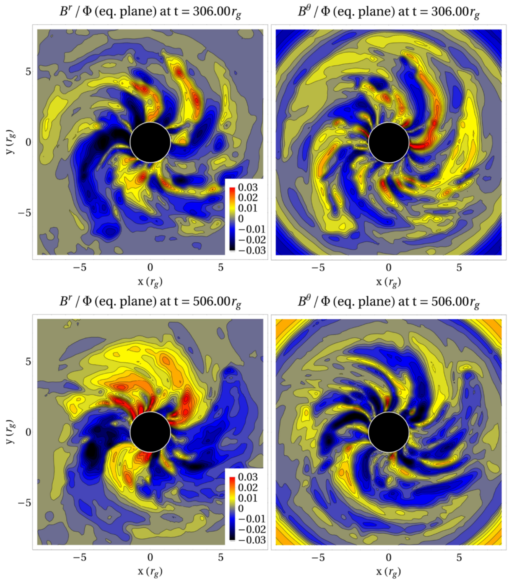

Figure 7. The B^r and B^θ components in the equatorial plane (model C-H4-L2) show periodic in-spiraling of magnetic flux on to the central BH during two subsequent episodes of efficient energy extraction. The shown data have a grid resolution of $\Delta_{x,\,y,\,z} \le 0.25 r_g$. The emerging spiral patterns show 3D effects in the plunging region, which break the axial symmetry.

Figure 8. 3D impression of the accretion of one magnetic flux tube on to a rapidly spinning BH ($a^* = 0.9$) in the C-L4-L2 model. The (outgoing) Poynting flux emerging from the BH horizon is visualized by ribbons coloured according to the strength of the associated radial energy flow (CGS units; see the colour scale). The radial magnetic flux (absolute value) is depicted by the density plot, indicating 3D non-axisymmetric effects in the plunging region. During peak outflow, extended helical structures of energy flow build up above the polar regions. Their confinement and strength decrease after peak efficiency. *Click* for animation (only Adobe Reader).

idealized setup for prograde AD models (appendix C), we cannot reliably separate the contribution of the BZ process from that of the AD in the overall electromagnetic luminosity far away from the BH. It is beyond the scope of this paper to asses the exact value of the critical loop length for various reasons: It would require modifying the AD setup in co-rotating models, so that the disc height be much smaller than $r_{\rm ISCO}$ (as required for thin ADs). Also, our simplified setup for co-rotating ADs is not optimally suited to explore models with larger values of a^* (appendix C). Finally, due to the numerical diffusion far away from the BH we would need to increase our resolution significantly in these regions to properly track energy flows towards infinity. These facts have, indeed, limited the numerically explored range of loop widths for prograde discs to values $2\,r_g \le l \le 4\,r_g$ (note that the smallest significant value of the loop width would be $l \approx r_{\rm ISCO} - r_+ \approx 0.9\,r_g$ for $a^* = 0.9$). Since our model setup differs slightly from that of Parfrey et al. (2015) – e.g. in the smaller value of a^* and in the larger accretion speed – we find that energy extraction is still efficient for $l = 2\,r_g$ (see also Section 4.2). Our results are compatible with the existence of a critical loop length, which manifests in our models as a reduction of the efficiency of the energy extraction for our prograde AD models compared to their retrograde counterparts. Another reason explaining the smaller efficiency of the BZ process in our prograde discs is of numerical origin. In general, maintaining the structural integrity of the AD model proves to be much harder for the co-rotating disc models. Especially in the UAL, the loop structure smears out in the course of the simulations. However, the time evolution shows the following sequence of reoccurring structures:

(i) Connection of the majority of field lines emerging from the BH to the innermost region of the AD with a vanishing overall energy extraction (see Fig. 9a).

(ii) Opening up of the accreted loop and gradual extension of field lines linking the polar regions to larger scale heights (Fig. 9b).

(iii) Complete opening of the accreted loop and initialization of the rearrangement of the jet launching region. In this phase, the peak energy extraction efficiency is attained. This comes along with the formation of larger scale flux structures above the polar regions, development of plasmoids with strong toroidal field dominance at the interface of different polarizations (Fig. 9c).

(iv) Rearrangement of the fields in the plunging region ensuing the development of extended regions of strong toroidal dominance along the axis of rotation. Decrease in process efficiency (Fig. 9d).

4 DISCUSSION

4.1 Reconnection sites

The development of regions with relatively sharp transitions of polarity in the magnetic field (current sheets) is enhanced in 3D compared to axisymmetry. 3D dynamics yield both, a growth of the surface where the magnetic field changes its polarity, and small-scale structures where the magnetic field folds into itself. Thus, they enhance the prospects for (physical) resistive reconnection compared to axisymmetric models. In our numerical method, both of these effects result into (numerical) dissipation of the magnetic field (see e.g. Rembiasz et al. 2017, for a deep discussion on the similarities of numerical and physical resistive effects), in qualitative agreement with recently presented simulations by Bromberg et al. (2019) and Davelaar et al. (2019). A relevant difference between the 2D models of Parfrey et al. (2015) and ours originates from the geometry and surface area of the current sheets between consecutive

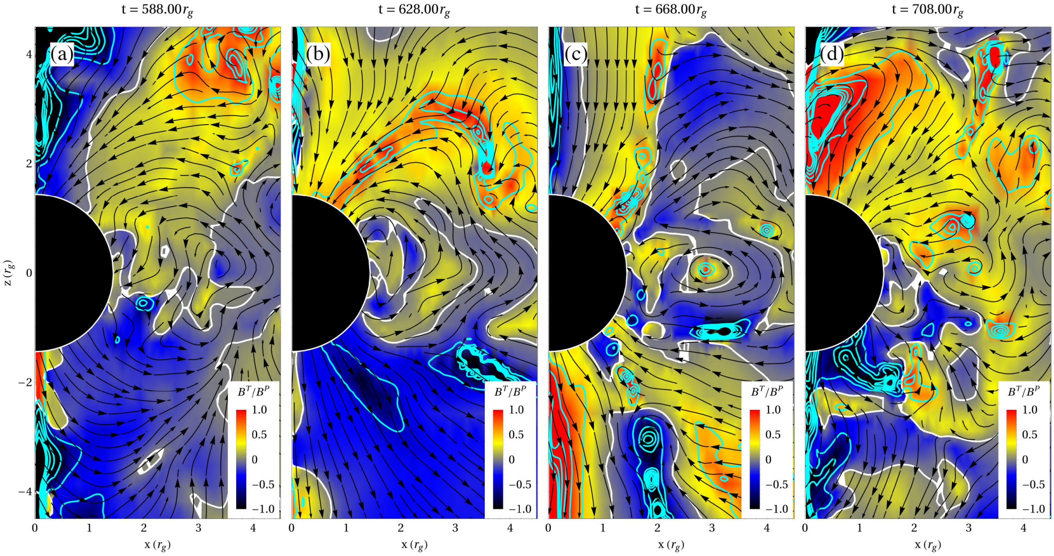

Figure 9. As Fig. 6, evolution of the toroidal magnetic field dominance across one peak of efficient energy extraction (model R-H1-L2). The shown data have a refinement resolution of $\Delta_{x,\,y,\,z} \leq 0.25 r_g$. Episodes of efficient energy extraction (b and c) follow the opening of magnetic loops and the transient development of larger scale flux structures in the jet launching region. Global rearrangements in the disc's funnel trigger the development of plasmoids at the interface of opposing polarities. The connection of the majority of magnetic field lines emerging from the BH to the AD (a) as well as the development of small-scale magnetic fields (d) are paralleled by a vanishing efficiency in the energy extraction.

loops of alternate polarity. When loops plunge into the BH, the shape their common interface is paraboloidal and axial-symmetric, with a surface $S_{2\mathrm{D}}$. In contrast, in 3D it is a wound up paraboloid whose projection on the equatorial plane resembles a helical structure (Fig. 7). The surface of these wound up structures is (roughly) $S_{3\mathrm{D}} \sim N S_{2\mathrm{D}}$, where $N \sim \Omega_{\mathrm{BH}}/(2\Omega_{\mathrm{ISCO}})$, and $\Omega_{\mathrm{ISCO}} = (a \pm r_{c,\mathrm{ISCO}}^{3/2}/\sqrt{M})^{-1}$ is the rotational frequency at the ISCO (30). For counter-rotating AD models, $N \simeq 4$ ($N \simeq 1$ in the co-rotating case).

The quasy-concentric layers where the magnetic field alternates polarity are potentially well suited to develop *ideal* resistive tearing modes on parallel current layers. The term *ideal* was introduced by Pucci & Velli (2014), who showed that current sheets with appropriate thickness $a = S^{-1/3} L$, are unstable against a tearing mode growing on an Alfvén (*ideal*) time-scale in classical resistive MHD (here L is a characteristic macroscopic length of the current sheet, and S is the Lundquist number; $S \gg 1$ in astrophysical environments, e.g. $S \sim 10^{12}$ in the solar corona). This result has been later confirmed numerically in (special) relativistic resistive MHD (Del Zanna et al. 2016; Miranda-Aranguren, Aloy & Rembiasz 2018). An extension of this result to multiple-layered systems in resistive relativistic MHD suggests that the growth rate of the tearing mode instability can be even faster than for single current layers (Baty, Petri & Zenitani 2013), even explosive (Baty 2017; Miranda-Aranguren 2018). Producing the development of these violent reconnection events with 3D global numerical simulations is, so far, not possible because of the extreme computational resources such problem demands.[7] However, it remains to be seen that explosive reconnection may be produced if the simplifications introduced in local numerical simulations are removed. Among the most striking differences between the idealized setup of local numerical models and our global models we single out two. First, the multidimensional geometry of the non-perfectly parallel layers of alternate polarity. Secondly, the non-stationary dynamics of our current sheets. As such, they are advected, bent, and distorted by local dynamics, i.e. they are strongly perturbed with respect to the optimal configurations for the growth of the ideal resistive tearing mode instability.

Plasmoids emerge following the current sheet that sets limits to the jet launching region around the rotational axis of the BH during the magnetospheric rearrangement between subsequent efficiency peaks (Fig. 6b). While such instabilities are likely to be sensitive to the imposed accretion model and numerical resolution, the fact that the presented simulations have peak and average efficiencies that are comparable to those obtained by other authors (Parfrey et al. 2015) is remarkable. The average efficiencies of our models (see Fig. 4 for counter-rotating disc models) deviate by ∼ 15 per cent from the ones derived by Parfrey et al. (2015), confirming that the accretion of zero net magnetic flux on to fast spinning BHs may also produce intermittent and efficient outflows in 3D. We stress again that our 3D models are resolution limited. Thus, the exact values of the BZ efficiency may change (likely within less than a factor of a few) if larger numerical resolutions (smaller dissipation) were employed.

---

[7] In order to properly resolve the non-linear growth of the fastest growing tearing mode in the explosive phase, one needs, at least 100 zones per current sheet width ($\Delta x \gtrsim a/100$; Miranda-Aranguren 2018). In our models, the typical length of the current sheets is $L \sim 1$–$10 r_g$. Hence, we estimate a typical number of numerical zones per dimension of $[10^6$–$10^7] \times (S/10^{12})^{1/3}$ for producing explosive reconnection events resulting from the relativistic ideal tearing mode instability.

Ball, Sironi & Özel (2019) show numerically the importance of X-points in reconnection layers for the relativistic acceleration of charged particles. Guo et al. (2019) conclude that such acceleration points are subdominant to the Fermi-type process in reconnection layers, while Petropoulou et al. (2019) recently confirmed the role of X-points in elongated current sheets. Both Ball et al. (2019) and Petropoulou et al. (2019) stress the important role of non-ideal (violating the force-free condition 23) electric fields (and, more recently, Kilian et al. 2020). Such violations are numerically corrected by the our GRFFE scheme (discussed in Section 2.2), but are likely to occur in regions where the magnetic field rearranges through the formation of small-scale structures that eventually reach the grid scale. Since we are resolution limited, we cannot follow the process of turbulent dissipation of these structures below the grid scale and the numerical scheme reacts by restructuring the electric fields in regions where condition (23) needs to be numerically enforced. Customary, this numerical process is considered as an indication of a (potentially turbulent) magnetic field reconnection and is identified with the development of plasmoids along current sheets. Fig. 6 shows a well developed chain of plasmoids at the current sheet flanking the outflow formation region, which are, thus, potential locations of strong particle acceleration and hard X-ray flares (Beloborodov 2017; Sironi & Beloborodov 2019). As mentioned above, the topology of the magnetic field in the previous current sheet is not axisymmetric, but helicoidal (see the 3D topology of the Poynting flux in Fig. 8). Thus, the 2D poloidal maps displayed in Fig. 6 do not show all the small-scale plasmoids developing in that current sheet. This main site for reconnection outside of the AD (turbulent reconnection very likely takes place inside the AD, but this is not included in our simplified model) may host particle acceleration and, hence, time-dependent high-energy processes. As Yuan et al. (2019a, b) point out, these reconnection sites relatively close to supermassive BHs in Seyfert galaxies, may produce the hard X-rays responsible for the observed fluorescent emission.

The opposite polarity of subsequently accreted magnetic flux tubes triggers the launching of transient jets with opposite polarity of both the toroidal and the poloidal field. Globally, the magnetic topology of the polar outflows resembles that of an *striped jet*. Jet stripes (cf. Drenkhahn 2002; Drenkhahn & Spruit 2002; Levinson & Globus 2016; Giannios & Uzdensky 2019) propagate through the magnetosphere at nearly the speed of light (Fig. 10) and with a typical stripe length $l_S \simeq c\Delta t_{\rm acc} \simeq lc/v_0$. Striped jets provide additional locations for energy dissipation through reconnection at layers of polarity changes, driving both the jet bulk acceleration and particle energization, though likely at larger scales than we have considered here (Giannios & Uzdensky 2019, and references therein).

4.2 Ideal loop efficiency

Uzdensky & Goodman (2008) propose that the formation of loop structures with sizes significantly larger than the AD height is possible by reconnection in the disc corona, supporting our (simplified) setup. Our analysis suggests a broad range of loop areas around $l \times h \approx 7.4\, r_g^2$ for an optimal process efficiency during the accretion of magnetic loops from a counter-rotating AD (see Fig. 4). We also find indications of a significant decrease of the process efficiency for both very small ($\simeq l \times h \approx 1.7\, r_g^2$) and large ($\simeq l \times h \approx 32.1\, r_g^2$) loop cross-sectional areas.

The accretion of magnetic flux tubes from co-rotating AD models extracts energy from the central BH much less efficiently. The time-evolution of magnetic fields recurrently establishes configurations in which all field lines emerging from the BH connect to the AD (as in the equilibrium solutions of, e.g. Uzdensky 2005; Mahlmann et al. 2018; Yuan et al. 2019a, b). The resulting transport of angular momentum from the BH to the AD combined with the (artificial) magneto-rotational energy extraction from our (simple) disc model (Appendix C) gradually distorts the UAL of the disc throughout the simulations. However, besides the negative feedback of these effects on the transport of energy from the BH to infinity, when field lines open up in the polar regions (cf. Fig. 9), peak efficiencies of $\epsilon \approx 0.2$ are reached.

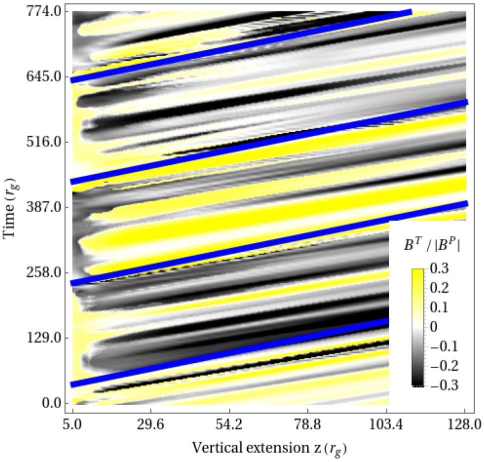

Figure 10. Time evolution of the toroidal dominance $B^T/|B^P|$ (in a cone enclosing an angle of $\theta = 7.5°$, averaged) around the central axis in the C-L4-L2-F model. The stripes of alternate polarity propagate through the magnetosphere with the speed of light (slope of the blue lines) carrying opposing polarity of B^T. These structures define what we denominate striped jet. A new jet stripe is launched with every new accreted flux-tube after a typical time $t_{\rm acc}$ (separation of the blue lines).

Yuan et al. (2019a, b) relate the emergence of open field lines in BH/AD systems to the ratio between the magnetic flux of the inner loop to the outer one. In their toy-model, consisting of two flux tubes of length $l \approx 2.5 r_g$ (appendix B), they use a current similar to ours (32) but adding the possibility that the current decays radially as $r^{-(\alpha+1)}$. In practice, they mimic the effect of frame dragging (or rigid rotation) by imposing an appropriate surface resistivity to a central disc-shaped membrane in a special relativistic simulation. These BH/AD toy-models show a strong dependency of the field line topology on the decay parameter α. The stronger the interior flux tube compared to the outer one, the more (and the faster) inclined the field lines emerge until they eventually open up. In other words, if stronger magnetic fields connect the tip of the AD to the BH in the plunging region, it is more likely to open up the magnetic field lines or to develop vertical, ordered magnetic structures. In order to validate our own results, we have reproduced the numerical setup suggested by Yuan et al. (2019a) in appendix B, and elaborate on it employing our GRFFE code. For that, we have run a set of ancillary models in which we use an AD setup that combines the essential magnetospheric structure of Yuan et al. (2019a) with our co-rotating models (Fig. 11). Especially, we have focused on the establishment of an equilibrium of loops for $\alpha = 2$ with different loop-length l. These loop lengths have been chosen to bracket the critical loop

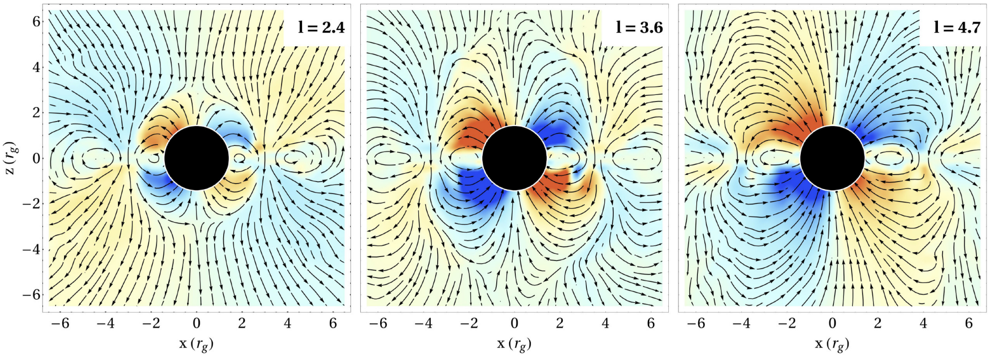

Figure 11. Toroidal field B^T (blue negative, red positive) for selected tests of a co-rotating AD with ($\alpha = 2$, $r_1 = r_{\rm ISCO}$, and $v^r = 0$) and a completely force-free plunging region. The loop length l is varied. Poloidal magnetic field lines are overlaid. The BH and AD rotation are set up as in our models (see Section 3.1). These ancillary models are a GR extension to the ones of Yuan et al. (2019b) with the notable difference that Yuan et al. (2019b) do prescribe boundary conditions on the electromagnetic fields at the BH horizon (employing a membrane description of the BH). The presented snapshots are taken at ∼9 revolutions of the BH (∼$180r_g$) after initialization and correspond roughly to the variability time-scales $\Delta t_{\rm acc}$ present in our slowly accreting models (series A). We observe the progressive twisting of the magnetic field close to the BH, manifesting itself as a pair of growing lobes with a butterfly shape in the poloidal plane.

length $l_{\rm crit} = 3.2r_g$ obtained by Parfrey et al. (2015). We find that a radially outwards Poynting flux occurs even for $l = 2.4\,r_g < l_{\rm crit}$ for these ancillary models. However, the lobes growing around the central BH have a finite size and do not efficiently connect to infinity (except, perhaps, along a bundle around the rotational axis of the system with a tiny radius). Thus, models with such a small loop width (below $l_{\rm crit}$) are not expected to produce outflows. We observe the growth of a pair of lobes around the BH with a *butterfly* shape in the poloidal plane in Fig. 11. These lobes become larger with increasing l, optimizing the prospects for the emanation of Poynting flux to infinity. The ancillary models shown in Fig. 11 cross-validate our results in several ways. First, we find that the BZ process is activated even for loop lengths below $l_{\rm crit}$. Secondly, they qualitatively reproduce the results of Yuan et al. (2019b), employing a resolution similar to the models of this paper. Thirdly, larger loop lengths yield poloidal fields that make a smaller angle to the vertical direction, hence improving the available efficiency of the BZ process. Finally, we find that with a different current distribution on the AD (with different radial dependence, see Appendix B), the previous conclusions still hold. The combination of the AD setup in Yuan et al. (2019b) with the full GR capacities of our method is well suited to analyse the influence of the rotation of an idealized disc on the activation of the BZ mechanism. This is because the effects of rotation are gauged by both, a suitable choice of the electric fields on the equatorial membrane mimicking the AD, and frame dragging of the space–time itself. By construction, the latter is not included in Yuan et al. (2019b). Furthermore, only field lines connecting to the central membrane can contribute to the magnetospheric energy flows in their default model of no AD rotation. While such idealized models provide a clean picture for the magnetospheric dynamics induced by BH/AD differential rotation, the setup from Yuan et al. (2019b) cannot straightforwardly be extended to account for the full *accretion* dynamics (i.e. for the radial displacement of the magnetic field lines). This is one of the most distinctive elements of our models compared to the ancillary setups we have considered above.

With a shorter accretion time $\Delta t_{\rm acc}$ (i.e. larger accretion speed v_0), field lines connecting the BH to the AD have less time to be twisted by differential rotation. In case of our co-rotating models, the central object completes ∼1.4 revolutions per each rotation of the tip of the AD at $r_{\rm ISCO}$. In case of the counter-rotating models, the BH spins ∼7.8 times in the opposite direction during one turn of the field lines located at $r_{\rm ISCO}$. Flux tubes which accrete without being sufficiently twisted by differential rotation may fail to develop sufficiently vertically elongated poloidal magnetic field lines. This vertical structure of the magnetic field (optimally connecting the BH to infinity) is required to drive an outflow (see Figs 6 and 10) under ideal conditions for operation of the BZ process (appendix A2). However, closed magnetic field lines linking the BH and the AD may transport energy and angular momentum between them, as in case of co-rotating AD models.[8] The dynamics of these closed magnetic field lines is very important to set the efficiency of the BZ process, and we observe a contrasting behaviour in co- and counter-rotating AD models. We find that some of the closed field lines connecting the BH to the AD experience a premature detachment from the AD due to 3D instabilities. These (kink-like) instabilities manifest in some models as, e.g. the *fall-down* of an incipient *magnetic tower* (i.e. a vertical thick flux tube along the symmetry axis threaded by helicoidal magnetic field lines; the basis of the magnetic tower emerges as helical patterns in the movie associated with Fig. 7; see also Lynden-Bell 1996). The development of kinks due to non-axisymmetric effects has also been noticed by Yuan et al. (2019b), who estimated that the time-scale for the growth of these kinks in the outflow is

$$t_{\rm kink} \simeq (\hat{h}/\hat{k} + 1)^2 r_{\rm LC}, \tag{42}$$

where $r_{\rm LC} \simeq 1/\Omega_{\rm BH} \simeq 3.2\,M$ is an estimation of the radius of the light cylinder. $\hat{h} = z/r_{\rm LC}$ and $\hat{k} = z/(r_c - r_{\rm LC})$ are the vertical height of the outflow in units of $r_{\rm LC}$ and a constant characterizing

---

[8] In our models, the feedback on the BH of the transport of energy and angular momentum from the AD is not included, since we do not feed the space–time evolution with the dynamics of the magnetic field (Cowling approximation; see Section 3). Likewise, since the *velocity* in the AD is imposed numerically, instead of being the result of a self-consistent MHD calculation, the transport of energy and angular momentum from the BH to the AD does not result into a braking or speeding up of the latter.

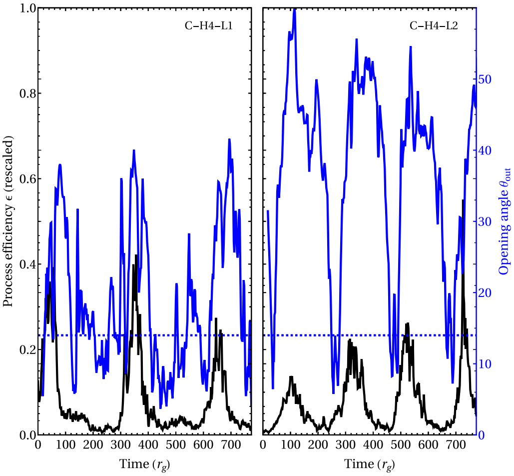

Figure 12. Evolution of the process efficiency (black curves, rescaled by a factor of 5) and the opening angle $\theta_{\rm out}$ (blue solid lines) for selected models of series A. The horizontal blue dashed line marks the value $\theta_{\rm kink} \approx 14^\circ$. C-H4-L1 (left) shows smaller outflow opening angles (on average) than C-H4-L2 (right). For C-H4-L1, values $\theta_{\rm out} < \theta_{\rm kink}$ are observed in clear correlation with periods of low-BZ efficiency, during time-scales comparable to $\Delta t_{\rm acc}$. In case of the efficiently working reference model C-H4-L2 (right), the flow develops significant opening angles of $\theta_{\rm out} \sim 50^\circ$ and extending before and after any of the high-efficiency BZ peaks. Short episodes of $\theta_{\rm out} \sim \theta_{\rm kink}$ are transient events and happen in association with the change of polarity throughout the magnetosphere (see Section 3.3).

the opening angle of the outflow, $\theta_{\rm out} \sim \arctan{(1/\hat{k})}$, respectively. Kink instabilities may grow in a steady, expanding, and collimated outflow if their characteristic growth time (42) is shorter than the expansion time-scale of the flow

$$t_{\rm flow} \simeq \hat{h}\sqrt{1/\hat{k}^2 + 1}\, r_{\rm LC}, \qquad (43)$$

i.e. if $t_{\rm kink}/t_{\rm flow} < 1$ (Yuan et al. 2019b). In our models, the outflow opening angle is not easy to compute. One possibility we have adopted is to evaluate the angular location, measured from the vertical axis, where the (radial) Poynting flux changes sign on a spherical surface with radius $r_{\rm P}$. Certainly, the opening angle is a function of the radial distance to the BH. Hence, to quantify our results, we measure the opening angle relatively close to the BH, namely, at $r_{\rm P} = 16\,M$. We pick this value because we observe that kinks in the magnetic tower can already develop at smaller values of r. We cautiously point out that $r_{\rm P}/r_{\rm LC} \gg 1$ to ensure that the approximations employed to derive (42) and (43) hold. We note, however, that in our case $r_{\rm P}/r_{\rm LC} \gtrsim 5$ and, more importantly, the outflow is not stationary. Hence, the estimates (42) and (43) are only crude approximations.

The values of $\theta_{\rm out}$ measured at $r = r_{\rm P}$ are extremely time dependent. They change from nearly zero to $\lesssim 60^\circ$ on time-scales that are shorter than $\Delta t_{\rm acc}$ (see Figs 12 and 13). Kink instabilities may only set in when the outflow opening angle is sufficiently small, i.e. when $\theta_{\rm out} \le \theta_{\rm kink} \simeq 14^\circ$; corresponding to $\hat{k} \simeq 4$. Values of the outflow opening angle smaller than $\theta_{\rm kink}$ happen before and after the peaks of efficient BZ energy extraction. When $\theta_{\rm out} \sim \theta_{\rm kink}$, the ratio $t_{\rm kink}/T_{\rm ISCO} \simeq 1$, i.e. the kink growth time-scale roughly coincides with the orbital period at the ISCO ($T_{\rm ISCO} = 2\pi/|\Omega_K(r_{\rm ISCO})|$).

For models with short loop length (see Fig. 12) or faster accretion speeds (see Fig. 13), i.e. shorter accretion times, the opening angle tends to be smaller than for wider loops or smaller values of v_0 (with extended periods of $\theta_{\rm out} \lesssim \theta_{\rm kink}$). In our simple estimate of the typical accretion speed in a Shakura–Sunyaev disc (31), both cases are disjoint. Larger values of l are connected to larger values of the disc half-thickness in our model and, hence to larger values of h/r, which make the accretion speed ($v_0 \simeq \alpha_{\rm SS}(h/r)^2 v_{\rm K}$) grow. Conversely, smaller accretion speeds are linked to a smaller disc half-thickness, which in our model setup imply smaller values of l.

Analysing the time evolution of the periodogram of the vertical magnetic field on a slim ring of radius $2M$, we find the growth of modes with wavelength comparable or a few times shorter than the length of the ISCO orbit ($L_{\rm ISCO} \simeq 55\,M$) during the periods of efficient BZ energy extraction. These wavelengths correspond to time-scales a few times shorter than $T_{\rm ISCO}$. Conversely, in between of high efficiency peaks, modes with shorter wavelengths appear. The length and time-scales of these structures are correlated with the loop length: larger values of l develop longer wavelengths and shorter time-scales. The alternation of shorter and longer dominant modes in the equatorial plane corresponds to the formation of spiral structures in the plunging region during the luminosity bursts and their disappearance in periods of low efficiency ϵ. While we have observed such indicators of a loss in equatorial and axial symmetry for different mesh resolutions (and distributions), detailed field dynamics in the plunging and jet regions will be probed with high-resolution simulations in the near future.

The counter-rotating reference model C-H4-L2 develops dynamics comparable to the axisymmetric model of Parfrey et al. (2015), hence minimizing the role of 3D instabilities in the efficiency of the BZ process. In contrast, the counter-rotating models C-H4-L1 and C-H4-L2-02 show alternations between very efficient extraction cycles due to the accretion of one AD magnetic flux tube and a subsequent, significantly less efficient period. In these models, the hairpin structures developing in the plunging region do not sufficiently extend vertically and only drive a partial change in the polarity of the magnetosphere in the vicinity of the BH. The energy extraction by the BZ process is suppressed for these *insufficiently stretched* magnetic structures. We note that in axial symmetry, the differential rotation between the disc and the BH inevitably yields to increasing the toroidal twist and, eventually, to open up the field lines to infinity (Uzdensky, Konigl & Litwin 2002). This is a consequence of the relativistic Ferraro's Law of isorotation (cf. Yuan et al. 2019b), which states that the angular velocity along a field line must be constant. Without imposing axial symmetry, this is not necessarily the case. Thus, the prospects to open up magnetic field lines leading to an efficient energy extraction are smaller in 3D than in 2D.

In the case of co-rotating BH/AD models, the decay of the magnetic field strength in the accretion funnel due to 3D instabilities (see above), may greatly impair the development of strong BZ type outflows. Fig. 9 and Section 3.3 identify this interplay between the tendency to connect the BH and the AD by closed magnetic field lines in a (short-term) quasi-equilibrium structure (akin to the magnetostatic configurations of Uzdensky 2005), and short periods in which open (or insufficiently stretched) field lines drive relatively low-power outflows.

Our numerical models, backed up by the ancillary simulations employed to compare to Yuan et al. (2019a), suggest that it is necessary to allow for several tens of rotational periods of the central object in order to build up inclined structures of twisted magnetic field lines (see Figs 11 and B2). Thus, there exists an additional

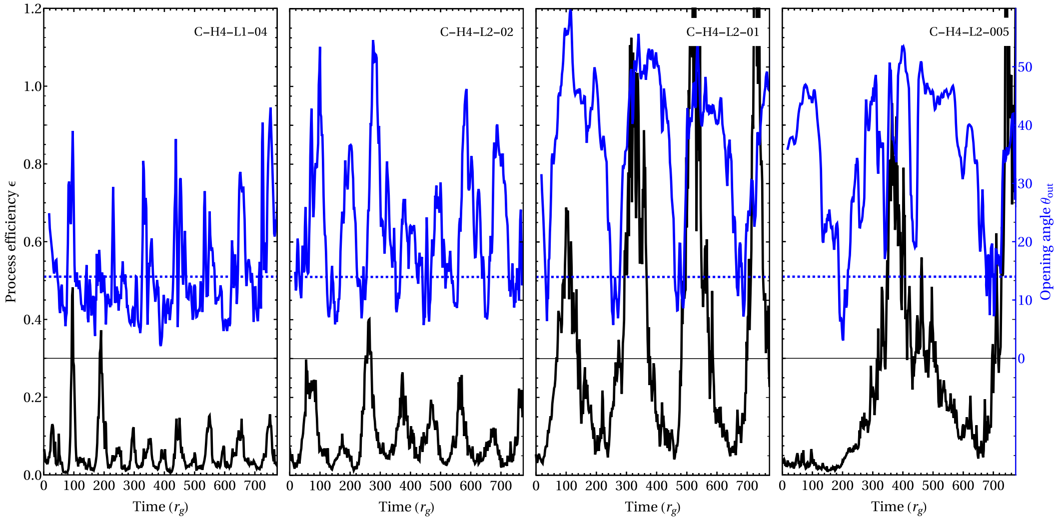

Figure 13. Instantaneous efficiency ϵ (equation 40) of the BZ process and opening angle $\theta_{\rm out}$ during the evolution of the counter-rotating disc reference model C-H4-L2 with different accretion speeds (series B, cf. Table 1). The pulse periodicity changes according to the accretion velocity $v_0 = [0.005, 0.01, 0.02, 0.04]$. We employ the same colours than in Fig. 12. Our results suggest a roughly linear dependence of the time-averaged outflow opening angle and the accretion speed for the models of the figure $\langle\theta_{\rm out}\rangle \simeq 0.7\text{–}11 \times v_0/c$.

relevant time-scale to set the efficiency of the BZ process in our setup. This is the time required to sufficiently and uniformly twist the magnetic loops connecting the BH to the AD. We can estimate this time-scale as

$$t_{\rm w} = \frac{2\pi}{0.5\Omega_{\rm BH} - \Omega_{\rm ISCO}}, \tag{44}$$

where we compare the rotational frequency at the ISCO to half the rotational frequency of the BH (as this is the optimal value of the field-line angular velocity to drive an efficient BZ process, see Appendix A3). Our models have values of $t_{\rm w} \simeq 91\,M$ and $t_{\rm w} \simeq 32\,M$ for co- and counter-rotating discs, respectively.

A thorough understanding of the role of the loop size and the loop magnetic field strength for the development of dissipative regions (by either kink instabilities or by reconnection processes) or relativistic outflows (BZ jets) will be studied in a subsequent work.

4.3 Variability time-scales of the BZ luminosity

The presented simulations are conducted in a system of units scaling with the BH mass $M_{\rm BH}$. Especially, time-scales are directly proportional to the mass of the central object. For relatively small values of the accretion speed (see below), the accretion time-scale $\Delta t_{\rm acc} \simeq l/v_0$ determines the overall duration of a single luminosity burst or pulse $T_{\rm Pulse}$

$$T_{\rm Pulse} = 1.37 \times \left(\frac{c}{v_0}\right)\left(\frac{l}{r_g}\right)\left(\frac{M_{\rm BH}}{M_9}\right)\ {\rm h}. \tag{45}$$

Here, we employ $M_9 = 10^9\,{\rm M}_\odot$. For a loop length of $l = 2r_g$, $v_0 = 0.01c$ (corresponding, e.g. to our reference counter-rotating model C-H2-L2) and a BH of $M_{\rm BH} = 6.5M_9$ this yields an approximate pulse duration of 74 d. We would like to stress that the accretion velocity, $v_0 = 0.01$ for the principal set of simulations (series A), has been chosen for numerical convenience and approximate comparability to the results of Parfrey et al. (2015). On the basis of a crude estimation, we have argued that we expect finding typical values $v_0 \lesssim 0.02c$ (31). Hence, series B (see Table 1) assembles variations of the reference model C-H4-L2 ($v_0 = 0.01$) with different accretion speeds $v_0 = [0.005, 0.02, 0.04]$. The pulse duration $T_{\rm Pulse}$ scales well with the chosen accretion speed, as we show in Fig. 13. However, the faster accretion speed counteracts the necessary spinning up of field lines connecting the BH to the AD and may cause insufficiently stretched magnetic structures (see previous section) in between energy peaks. Thus, the pulse duration estimated by (45) should be taken with care, due to the non-linear nature of our results, and due to the fact that the process efficiency does not linearly depend on the loop length (Section 3.2.1). It could be that in case of fast accretion speeds a larger efficiency may be obtained for larger loop lengths (at the cost of lengthening the duration of pulses from equation 45). Understanding in detail how the output power and variability time-scale changes with v_0 and l requires considering different models of ADs and initialization of the magnetic flux tubes inside them, something beyond the scope of this paper. Forcing the estimate in (45) to its limit of validity ($v_0 \simeq 0.04$, $l \simeq 1r_g$), one ends up with $T_{\rm Pulse} \simeq 9$ d for a BH mass like that of M87. Such time-scales are somewhat longer than the shortest variability time-scales observed in the TeV radiation of M87 (Aharonian et al. 2003; Acciari et al. 2009) and part of the data from the radio galaxy IC310 (Aleksić et al. 2014). However, the shortest variability time-scales in these AGNs correspond to extreme flaring events, which may require special conditions to develop.

Besides the most evident variability time-scales, roughly corresponding to $\Delta t_{\rm acc}$, smaller variability time-scales are present within each pulse. A spectral analysis of the data in, e.g. Fig. 3 (assembling models with $v_0 = 0.01c$) reveals that there is significant power at time-scales of up to ∼4 times smaller than $\Delta t_{\rm acc}$. In our counter-rotating models the period at the ISCO is $T_{\rm ISCO} = 158\,r_g \sim \Delta t_{\rm acc}/2$ (Table 2), hence, we identify the spectral power observed at

Table 2. Time-scales. The columns represent from left to right, the identifier, the values of h and l in units of r_g, the ratio of the accretion time-scale $\Delta t_{\rm acc} \simeq l/v_0$ to the Keplerian orbital period at the ISCO, $T_{\rm ISCO} = 2\pi/|\Omega_{\rm ISCO}|$, and the orbital period at the ISCO (in units of the BH mass).

Model	h	l	$\Delta t_{\rm acc}/T_{\rm ISCO}$	$T_{\rm ISCO}$
C-H4-L2-005	4.0	2.0	3.68	158
C-H4-L2-01	4.0	2.0	1.84	158
C-H4-L2-02	4.0	2.0	0.92	158
C-H4-L2-04	4.0	2.0	0.46	158
R-H1-L2	1.0	2.0	10.3	32.4
R-H1-L3	1.0	3.0	15.5	32.4
R-H1-L4	1.0	4.0	20.6	32.4

frequencies $\simeq 2/\Delta t_{\rm acc}$ with the dynamics of the loops as they are released from the ISCO. Certainly, the ratio $\Delta t_{\rm acc}/T_{\rm ISCO}$ depends on the imposed accretion speed and we foresee that variability time-scales associated with the location of the ISCO are longer than $\Delta t_{\rm acc}$ for $v_0 \gtrsim 0.02c$ (see Table 2). The amplitude of the variability at time-scales below $\sim\Delta t_{\rm acc}/2$ is nearly two orders of magnitude smaller than that corresponding to $\Delta t_{\rm acc}$. Both, the amplitude of these variations and, consistently, their spectral power depend on the numerical resolution since they are linked to resistive effects. Running the complete set of models at higher resolution than we have done so far demands extremely large computational resources. Besides, it is not justified to employ only a force-free model that does not account for the mass-loading of the magnetosphere and other non-ideal MHD effects. Thus, we cannot robustly assess the variability at time-scales below $\sim\Delta t_{\rm acc}/4$ with our models.

5 CONCLUSIONS

We have conducted a set of simulations of a simplified model advecting tubes of zero net magnetic flux in a thin ad hoc AD towards a rapidly spinning central BH. In total, we have probed 16 different BH/AD parameter setups plus three ancillary models for benchmarking. Our results show that powerful, intermittent outflows, driven by the BZ mechanism can form in 3D from magnetic structures having scales a few times larger than the AD height. Admittedly, our setup is a simplification of an actual AD, which does not allow for any torque from the BH on to the disc. Our AD toy-model is better suited for counter-rotating than for co-rotating ADs. In the latter case, there is a flux of energy resulting from the fact that our simplified setup makes the AD behave as a Faraday disc that is both accelerated and loaded with a current (appendix C). In spite of this artificial effect, our prograde AD models are still adequate to understand the energy flows at the horizon and in the immediate vicinity of the central BH for values of $a^* \lesssim 0.9$.

The average efficiency of the BZ process is very significant, $\bar{\epsilon} \sim 0.4$ for counter-rotating AD and $\bar{\epsilon} \sim 0.1$ for co-rotating ADs. Episodes of efficient energy extraction are linked to ordered magnetic fields structured by a dipolar component in the plunging region, as well as field lines emerging from the BH and extending to a significant distance. This effectively creates ideal conditions comparable to those of Blandford & Znajek (1977) for a short period of time. Even without imposing large-scale magnetic flux structures, our models develop an outgoing Poynting flux at the BH horizon in broad accordance with the BZ mechanism. At the same time, 3D *dynamical* evolution also triggers complicated field structures and field reversals, which cannot be described by the equations of *stationary*, *axisymmetric* GRFFE. In these regions, the efficiency of the BZ process is reduced or breaks down completely.

We have made a study over a range and combinations of parameters defining the accretion disc structure. They confirm and extend the work by Parfrey et al. (2015), especially in characterizing the Poynting outflow efficiency during periods of energy extraction. In line with Parfrey et al. (2015), our results also suggest that jets may be quenched in prograde accretion flows if there is no large-scale magnetic field threading the BH/AD system. Since our model setup is not exactly the same, we find a slightly smaller value of the critical loop length than Parfrey et al. (2015) did. A more careful modelling of the conditions in different environments, where there may exist prograde accretion flows around rapidly spinning BHs, is needed to more robustly assess the generality of a jet quenching mechanism which depends upon the ability of the turbulent AD to create magnetic flux tubes with sufficiently large sizes. Some of these systems are found, e.g. in Seyfert galaxies (Risaliti et al. 2013), intrinsically X-ray weak intermediate-mass BHs (e.g. in PL 1811 Dong et al. 2012), where the small variability time-scales indicate that the X-ray source is rather compact, or in X-ray binaries during the soft state (e.g. Plant et al. 2014).

Our models are resolution limited, since we aimed to run a relative large number of full-fledged 3D simulations. This means that resistive effects may be (numerically) overestimated. We have, however, benchmarked our results again, the (simpler) setup of Yuan et al. (2019b), employing a numerical resolution similar to the one employed in the rest of the models of this paper. We have found a remarkably good qualitative agreement with the results of these authors. In particular, ancillary models set up to reproduce a different radial distribution of the current in the AD (akin to that of Yuan et al. 2019b), cross-validate our result that efficiency is tightly linked to the loop length in prograde ADs. This comparison also serves for the purpose of assessing that our findings are not exclusively valid for the (simple) current setup employed here.

Future studies demand higher numerical resolution in a broad wedge around the rotational axis of the BH in order to accurately describe the dynamics of the generated outflows and the expelled plasmoids, as well as their interactions with flows directed along the jet axis. Understanding the detailed structure and the overall dynamics of plasmoids in reconnection regions may allow for links to recent results from first-principle simulations and the interpretation of their radiative imprints (cf. Christie et al. 2020). The viability of our ad hoc AD setup should be probed in GRMHD simulations, for example starting off at the flux tube structures considered by Beckwith et al. (2008, 2009) or the plasmoid formation modelled in 2D GRMHD by Nathanail et al. (2020).

The accretion of zero net magnetic flux structures with opposing polarity triggers quasi-periodic phenomena, most significantly, on a variability time-scale given by the accretion time $\Delta t_{\rm acc} \sim l/v_0$, but also on smaller time-scales (see below). For supermassive BHs at the core of AGNs like M87, these time-scales are days-to-months, while for stellar mass BHs in X-ray binaries, they may be as small as $\sim 0.01\,(M_{\rm BH}/10\,{\rm M}_{\odot})$ s, and for intermediate mass BHs $\sim 100\,(M_{\rm BH}/10^5\,{\rm M}_{\odot})$ s. Shorter time-scales ($\gtrsim \Delta t_{\rm acc}/4$–2 d to 2 weeks for supermassive BHs) are also reliably observed in our models. They result from the loop dynamics close to the inner edge of the AD and from genuinely 3D (kink-like) instabilities (they are not observable in axisymmetry, Parfrey et al. 2015). For supermassive BHs, these variability time-scales are comparable to the longest time-scales observed, e.g., in the TeV radiation of M87. However, a thorough comparison of our results to observations requires a post-processing step. Namely, computing the emission and radiation transfer from our models to the observer, effectively accounting for lensing effects, caustics, etc. induced during radiation propagation by the BH. This is beyond the scope of this paper, and we will address it elsewhere.

Resistivity is of numerical origin in our models. Hence, it is dependent on the (limited) numerical resolution of 3D models. However, we observe the standard phenomenology induced by the resistive dissipation of the magnetic field when current sheets develop as a result of the gravito-magnetic coupling between the BH and the AD plasma. Specifically

(i) Due to the polarity change of the accreted magnetic flux, the outflow developing over large distances along the central axis has a striped structure. In between of each of the jet stripes, additional reconnection sites may form. This structure gives qualitative support to the so-called striped jet model (e.g. Giannios & Uzdensky 2019), or models where reconnection is responsible for blazars' gamma-ray emission (Giannios 2013).

(ii) Extended current sheets form during the reordering of magnetospheric field polarization. These current sheets are prone to develop magnetic islands (plasmoids) that are potential locations for relativistic particle acceleration.

(iii) Closely connected to the previous current sheets, we identify sheets of alternate polarity in the plunging region and extending vertically above and below the equator. They arise naturally as a result of the differential rotation acting on diametrically opposed ends of the AD loops. Their projection on the equatorial plane resembles an $m = 1$ or $m = 2$ spiral structure. In planes parallel to the equator, these structures form a set of similarly thick spiral arms of alternate polarity. Such structures bear a topological similarity with sets of parallel current sheets with alternate polarity in which the relativistic *ideal* tearing mode instability may develop. We speculate with the possibility that these locations might develop explosive reconnection events. However, due to the stringent numerical resolution demanded to observe the violent non-linear phase of the relativistic ideal tearing mode instability, it is unlikely that global 3D simulations may unveil it in the very near future.

Magnetic reconnection converts magnetic energy into thermal and kinetic energy. The results of our idealized setups support models where reconnection may take place at very different scales, including scales of the order of a few gravitational radii ($\lesssim 10 r_g$) in BH/AD systems, independent of the BH mass (e.g. Beloborodov 1999, in the case of X-ray binaries). Reconnection can be the source of the X-ray coronae not only in X-ray binaries, but also in AGNs as well as in intermediate-mass BHs. Also fast magnetic reconnection between the magnetic field lines of the inner disc region and those that are anchored in the BH has been suggested to produce the radio flares in galactic microquasars such as GRS 1905+105 (de Gouveia dal Pino & Lazarian 2005), as well as in AGNs (de Gouveia Dal Pino et al. 2010).

Although the simulations we have carried out are 3D, the initial setup is axisymmetric. Likely, the azimuthal extension of loops produced in the disc as a result of the magneto-rotational instability may be $\Delta\phi \gtrsim H/r$, as argued by Parfrey et al. (2015). We obtain, however, that the dynamics of the loops as they detach from the AD are non-axisymmetric. This is due to genuine 3D instabilities in the outflow, where magnetic towers are kinked until they tip over the magnetic flux tubes in the plunging region. Indeed, reconnection combined with the effect of the fall-down of the magnetic towers create extended perturbations in the azimuthal direction. As a result, parts of the same (initially axisymmetric) flux tube at different azimuthal angles interact with the BH asynchronously. Each of these angular sectors contributes to the overall large-scale jet incoherently and, hence they produce the substructure observed in the BZ efficiency plots, within each large-scale outburst. We find that this substructure accounts for variations in the efficiency of the BZ process, one or two orders of magnitude smaller than the (ideal) overall accretion of each of the large-scale concentric flux tubes.

Once the magnetic field becomes strong enough in the vicinity of the BH, it may counteract totally or partially the in-fall, effectively breaking our ad hoc accretion flow. Thus, future work may go along improving the kinematic approximation used to impose the accretion velocity in the equatorial plane. The coincidence of small opening angles of the outflow (hence, prone to kink instabilities) at some distance from the BH and a non-efficient working of the BZ process at the BH horizon deserves special attention. With the correlation of large opening angles (hence, kink-stable flows) and efficient energy extraction also true in the presented simulations, we conclude that jet launching by gravitomagnetic coupling after all does require a stable magnetic structure extending over several r_g. Based on the presented analysis, we expect such structures to form preferentially when the length of the magnetic loops is large (hence, the disc half-thickness is large; $h/r \sim 0.5$), and when the accretion speed (and, likely, the mass accretion rate) is small.

ACKNOWLEDGEMENTS

We appreciate Kyle Parfrey's constructive review of our manuscript as well as his feedback during the development of this work. We thank Vassilios Mewes, Pablo Cerdá-Durán, Serguei Komissarov and Alejandro Torres for feedback (and hospitality) along many steps of this paper as well as fruitful discussions going deep into the details of their respective contributions. JM acknowledges a Ph.D. grant of the *Studienstiftung des Deutschen Volkes*. We acknowledge the support from the grants AYA2015-66899-C2-1-P, PGC2018-095984-B-I00, and PROMETEO-II-2014-069. We acknowledge the partial support of the PHAROS COST Action CA16214 and GWverse COST Action CA16104. The shown numerical simulations have been conducted on infrastructure of the *Red Española de Supercomputación* (AECT-2019-1-0004, AECT-2019-3-0017) as well as of the University of Valencia.

REFERENCES

Acciari V. A. et al., 2009, Science, 325, 444
Aharonian F. et al., 2003, A&A, 403, L1
Aleksić J. et al., 2014, Science, 346, 1080
Alic D., Moesta P., Rezzolla L., Zanotti O., Jaramillo J. L., 2012, ApJ, 754, 36
Aloy M. A., Mimica P., 2008, ApJ, 681, 84
Aloy M.-A., Gómez J.-L., Ibáñez J.-M., Martí J.-M., Müller E., 2000a, ApJ, 528, L85
Aloy M. A., Müller E., Ibáñez J. M., Martí J. M., MacFadyen A., 2000b, ApJ, 531, L119
Aloy M. A., Cuesta-Martínez C., Obergaulinger M., 2018, MNRAS, 478, 3576
Antón L., Zanotti O., Miralles J. A., Martí J. M., Ibáñez J. M., Font J. A., Pons J. A., 2006, ApJ, 637, 296
Ball D., Sironi L., Özel F., 2019, ApJ, 884, 57
Barkov M. V., Bosch-Ramon V., Aharonian F. A., 2012, ApJ, 755, 170
Baty H., 2017, ApJ, 837, 74
Baty H., Petri J., Zenitani S., 2013, MNRAS, 436, L20
Baumgarte T. W., Shapiro S. L., 2003, ApJ, 585, 921
Beckwith K., Hawley J. F., Krolik J. H., 2008, ApJ, 678, 1180

Beckwith K., Hawley J. F., Krolik J. H., 2009, ApJ, 707, 428
Beloborodov A. M., 1999, ApJ, 510, L123
Beloborodov A. M., 2017, ApJ, 850, 141
Beskin V. S., 2010, MHD Flows in Compact Astrophysical Objects. Springer-Verlag, Berlin, Heidelberg, New York
Bisnovatyi-Kogan G. S., Ruzmaikin A. A., 1976, Ap&SS, 42, 401
Blandford R. D., Payne D. G., 1982, MNRAS, 199, 883
Blandford R. D., Znajek R. L., 1977, MNRAS, 179, 433
Blandford R., Meier D., Readhead A., 2019, ARA&A, 57, 467
Bromberg O., Tchekhovskoy A., 2016, MNRAS, 456, 1739
Bromberg O., Singh C. B., Davelaar J., Philippov A. A., 2019, ApJ, 884, 39
Brown D., Diener P., Sarbach O., Schnetter E., Tiglio M., 2009, Phys. Rev. D, 79, 044023
Camenzind M., 2007, Compact Objects in Astrophysics: White Dwarfs, Neutron Stars, and Black Holes. Springer-Verlag, Berlin, Heidelberg, New York
Carrasco F. L., Reula O. A., 2016, Phys. Rev. D, 93, 085013
Carrasco F. L., Reula O. A., 2017, Phys. Rev. D, 96, 063006
Chatterjee K., Liska M., Tchekhovskoy A., Markoff S. B., 2019, MNRAS, 490, 2200
Chen A. Y., Yuan Y., 2019, preprint (arXiv:1908.06919)
Christie I. M., Petropoulou M., Sironi L., Giannios D., 2020, MNRAS, 492, 549
Chyba C. F., Hand K. P., Thomas P. J., 2015, Am. J. Phys., 83, 72
Collins D. C., Xu H., Norman M. L., Li H., Li S., 2010, ApJS, 186, 308
Contopoulos I., 2019, Galaxies, 7, 12
Contopoulos I., Kazanas D., Papadopoulos D. B., 2013, ApJ, 765, 113
Coroniti F. V., 1985, in Kundu M. R., Holman G. D., eds, Proc. IAU Symp. 107, Unstable Current Systems and Plasma Instabilities in Astrophysics. Kluwer, Dordrecht, p. 453
Davelaar J., Philippov A. A., Bromberg O., Singh C. B., 2019, preprint (arXiv:1910.13370)
de Gouveia dal Pino E. M., Lazarian A., 2005, A&A, 441, 845
de Gouveia Dal Pino E. M., Piovezan P. P., Kadowaki L. H. S., 2010, A&A, 518, A5
De Young D. S., 1993, ApJ, 405, L13
Dedner A., Kemm F., Kröner D., Munz C.-D., Schnitzer T., Wesenberg M., 2002, J. Comput. Phys., 175, 645
Del Zanna L., Papini E., Landi S., Bugli M., Bucciantini N., 2016, MNRAS, 460, 3753
Diener P., Dorband E. N., Schnetter E., Tiglio M., 2007, J. Sci. Comput., 32, 109
Di Matteo T., Celotti A., Fabian A. C., 1999, MNRAS, 304, 809
Dong R., Greene J. E., Ho L. C., 2012, ApJ, 761, 73
Drenkhahn G., 2002, A&A, 387, 714
Drenkhahn G., Spruit H., 2002, A&A, 391, 1141
Dreyer O., Krishnan B., Shoemaker D., Schnetter E., 2003, Phys. Rev. D, 67, 024018
Event Horizon Telescope Collaboration, 2019a, ApJ, 875, L1
Event Horizon Telescope Collaboration, 2019b, ApJ, 875, L5
Faber J. A., Baumgarte T. W., Etienne Z. B., Shapiro S. L., Taniguchi K., 2007, Phys. Rev. D, 76, 104021
Feynman R., Leighton R., Sands M., 2011, The Feynman Lectures on Physics, Vol. II: The New Millennium Edition: Mainly Electromagnetism and Matter. Basic Books, New York
Frolov V., Zelnikov A., 2011, Introduction to Black Hole Physics. OUP Oxford, Oxford
Giannios D., 2013, MNRAS, 431, 355
Giannios D., Uzdensky D. A., 2019, MNRAS, 484, 1378
Goodale T., Allen G., Lanfermann G., Massó J., Radke T., Seidel E., Shalf J., 2003, Vector and Parallel Processing – VECPAR'2002, 5th International Conference, Lecture Notes in Computer Science. Springer, Berlin
Gralla S. E., Jacobson T., 2014, MNRAS, 445, 2500
Guo F., Li X., Daughton W., Kilian P., Li H., Liu Y.-H., Yan W., Ma D., 2019, ApJ, 879, L23
Hawley J. F., Krolik J. H., 2006, ApJ, 641, 103
Hirotani K., Pu H.-Y., 2016, ApJ, 818, 50
Hirotani K., Pu H.-Y., Lin L. C.-C., Chang H.-K., Inoue M., Kong A. K. H., Matsushita S., Tam P.-H. T., 2016, ApJ, 833, 142
Hirotani K., Pu H.-Y., Lin L. C.-C., Kong A. K. H., Matsushita S., Asada K., Chang H.-K., Tam P.-H. T., 2017, ApJ, 845, 77
Hughes D., Paczuski M., Dendy R. O., Helander P., McClements K. G., 2003, Phys. Rev. Lett., 90, 131101
Igumenshchev I. V., 2008, ApJ, 677, 317
Jackson J. D., 1999, Classical Electrodynamics. AAPT, Maryland
Kilian P., Li X., Guo F., Li H., 2020, preprint (arXiv:2001.02732)
Kim J. Y. et al., 2018, A&A, 616, A188
Koide S., Meier D. L., Shibata K., Kudoh T., 2000, ApJ, 536, 668
Komissarov S. S., 2004, MNRAS, 350, 427
Komissarov S. S., 2011, MNRAS, 418, L94
Komissarov S. S., Barkov M. V., 2009, MNRAS, 397, 1153
LeVeque R., 2002, Finite Volume Methods for Hyperbolic Problems. Cambridge Texts in Applied Mathematics. Cambridge Univ. Press, Cambridge
Levinson A., 2000, Phys. Rev. D, 85, 912
Levinson A., Cerutti B., 2018, A&A, 616, A184
Levinson A., Globus N., 2016, MNRAS, 458, 2269
Levinson A., Rieger F., 2011, ApJ, 730, 123
Levinson A., Segev N., 2017, Phys. Rev. D, 96, 123006
Lin L. C.-C., Pu H.-Y., Hirotani K., Kong A. K. H., Matsushita S., Chang H.-K., Inoue M., Tam P.-H. T., 2017, ApJ, 845, 40
Liska M., Tchekhovskoy A., Ingram A., van der Klis M., 2019, MNRAS, 487, 550
Liu Y. T., Etienne Z. B., Shapiro S. L., 2009, Phys. Rev. D, 80
Löffler F. et al., 2012, Class. Quantum Gravity, 29, 115001
Lynden-Bell D., 1996, MNRAS, 279, 389
Lyutikov M., 2003, MNRAS, 346, 540
MacDonald D., Thorne K. S., 1982, MNRAS, 198, 345
Mahlmann J. F., Cerdá-Durán P., Aloy M. A., 2018, MNRAS, 477, 3927
Mahlmann J. F., Akgün T., Pons J. A., Aloy M. A., Cerdá-Durán P., 2019, MNRAS, 490, 4858
Martí J.-M., 2019, Galaxies, 7, 24
McKinney J. C., 2005, ApJ, 630, L5
McKinney J. C., 2006, MNRAS, 367, 1797
McKinney J. C., Gammie C. F., 2004, ApJ, 611, 977
McKinney J. C., Tchekhovskoy A., Blandford R. D., 2012, MNRAS, 423, 3083
McKinney J. C., Tchekhovskoy A., Sadowski A., Narayan R., 2014, MNRAS, 441, 3177
Mertens F., Lobanov A. P., Walker R. C., Hardee P. E., 2016, A&A, 595, A54
Mewes V., Font J. A., Galeazzi F., Montero P. J., Stergioulas N., 2016, Phys. Rev. D, 93, 064055
Mignone A., Tzeferacos P., 2010, J. Comput. Phys., 229, 2117
Miranda-Aranguren S. M., 2018, PhD thesis, Universitat de València
Miranda-Aranguren S., Aloy M. A., Rembiasz T., 2018, MNRAS, 476, 3837
Mizuno Y., Lyubarsky Y., Nishikawa K.-I., Hardee P. E., 2012, ApJ, 757, 16
Narayan R., Igumenshchev I. V., Abramowicz M. A., 2003, PASJ, 55, L69
Nathanail A., Contopoulos I., 2014, ApJ, 788, 186
Nathanail A., Fromm C. M., Porth O., Olivares H., Younsi Z., Mizuno Y., Rezzolla L., 2020, preprint (arXiv:2002.01777)
Neronov A., Aharonian F. A., 2007, ApJ, 671, 85
Obergaulinger M., Aloy M. Á., 2017, MNRAS, 469, L43
Okamoto I., 2006, PASJ, 58, 1047
Palenzuela C., Lehner L., Reula O., Rezzolla L., 2009, MNRAS, 394, 1727
Palenzuela C., Garrett T., Lehner L., Liebling S. L., 2010, Phys. Rev. D, 82, 044045
Parfrey K., Giannios D., Beloborodov A. M., 2015, MNRAS, 446, L61
Parfrey K., Spitkovsky A., Beloborodov A. M., 2017, MNRAS, 469, 3656
Parfrey K., Philippov A., Cerutti B., 2019, Phys. Rev. Lett., 122, 035101
Paschalidis V., Shapiro S. L., 2013, Phys. Rev. D, 88, 104031
Petropoulou M., Sironi L., Spitkovsky A., Giannios D., 2019, ApJ, 880, 37
Plant D. S., Fender R. P., Ponti G., Muñoz-Darias T., Coriat M., 2014, MNRAS, 442, 1767
Pucci F., Velli M., 2014, ApJ, 780, L19

Rembiasz T., Obergaulinger M., Cerdá-Durán P., Aloy M.-Á., Müller E., 2017, ApJS, 230, 18
Risaliti G. et al., 2013, Nature, 494, 449
Romanova M. M., Ustyugova G. V., Koldoba A. V., Chechetkin V. M., Lovelace R. V. E., 1998, ApJ, 500, 703
Schnetter E., 2010, Class. Quantum Gravity, 27, 167001
Shakura N. I., Sunyaev R. A., 1973, A&A, 500, 33
Shibata M., 2015, Numerical Relativity. 100 Years of General Relativity. World Scientific Publishing Company, Singapore
Sironi L., Beloborodov A. M., 2019, preprint (arXiv:1908.08138)
Sądowski A., Narayan R., 2016, MNRAS, 456, 3929
Tchekhovskoy A., Giannios D., 2015, MNRAS, 447, 327
Tchekhovskoy A., McKinney J. C., 2012, MNRAS, 423, L55
Tchekhovskoy A., Narayan R., McKinney J. C., 2010, ApJ, 711, 50
Tchekhovskoy A., Narayan R., McKinney J. C., 2011, MNRAS, 418, L79
Tchekhovskoy A., McKinney J. C., Narayan R., 2012, J. Phys.: Conf. Ser., 372, 012040
Thornburg J., 2004, Class. Quantum Gravity, 21, 743
Thorne K. S., Price R. H., MacDonald D. A., eds, 1986, Black Holes: The Membrane Paradigm. Yale University Press, New Haven
Tout C. A., Pringle J. E., 1992, MNRAS, 259, 604
Uzdensky D. A., 2005, ApJ, 620, 889
Uzdensky D. A., Goodman J., 2008, ApJ, 682, 608
Uzdensky D. A., Konigl A., Litwin C., 2002, ApJ, 565, 1191
Vourellis C., Fendt C., Qian Q., Noble S. C., 2019, ApJ, 882, 2
Wald R., 2010, General Relativity. University of Chicago Press, Chicago
Weber E. J., Davis Leverett J., 1967, ApJ, 148, 217
Yuan Y., Blandford R. D., Wilkins D. R., 2019a, MNRAS, 484, 4920
Yuan Y., Spitkovsky A., Blandford R. D., Wilkins D. R., 2019b, MNRAS, 487, 4114
Znajek R. L., 1977, MNRAS, 179, 457

APPENDIX A: NUMERICAL DETAILS

A1 The augmented system

The general relativistic evolution equations for force-free electrodynamics were developed, e.g. in Komissarov (2004), McKinney (2006), and reviewed in further detail by Paschalidis & Shapiro (2013). Their conservation laws may be written in its vector form

$$\partial_t\,\mathcal{C} + \partial_j\,\mathcal{F}^j = \left(\mathcal{S}_n + \mathcal{S}_s\right), \tag{A1}$$

where $\mathcal{C}$ denotes the conserved variables, $\mathcal{F}^j$ the flux vectors, $\mathcal{S}_n$ the geometrical and current induced source terms. Finally $\mathcal{S}_s$ are the potentially stiff (see e.g. LeVeque 2002) source terms. Note that each of these quantities consists of elements in a multidimensional space. In general, the conserved variables $\mathcal{C}$ are derived from the so-called primitive variables.

Besides other strategies, the evolution of the full set of Maxwell equations of the fields $\{\boldsymbol{B}, \boldsymbol{D}, \boldsymbol{H}, \boldsymbol{E}\}$ is introduced in the literature as a possibility to deal with electrodynamics in General Relativity by Komissarov (2004). In this case, an adaptation of equations (9) and (10) may be used as an evolutionary system. Following Palenzuela et al. (2009) as well as Mignone & Tzeferacos (2010), we suggest to study a suitably augmented system of Maxwell's equation

$$\nabla_\nu\left({}^*F^{\mu\nu} + s^{\mu\nu}\psi\right) = -\kappa_\psi k^\mu \psi \tag{A2}$$

$$\nabla_\nu\left(F^{\mu\nu} + g^{\mu\nu}\phi\right) = I^\mu - \kappa_\phi k^\mu \phi, \tag{A3}$$

Here, we employ $s^{\mu\nu} = c_h^2\gamma^{\mu\nu} - n^\mu n^\nu$. The functions ψ and ϕ are additional scalar potentials for the hyperbolic/parabolic cleaning of numerically induced divergence and charges, respectively (cf. Dedner et al. 2002; Palenzuela et al. 2009; Mignone & Tzeferacos 2010). κ_ψ, c_h, and κ_ϕ are the parameters controlling these cleaning terms. Contracting equation (A2) with ∇_μ yields

$$c_h^2\nabla_i\nabla^i\psi + \nabla_t\nabla^t\psi = -\kappa_\psi\nabla_t\psi, \tag{A4}$$

which compares to the telegraph equation. We stress the analogy of c_h with a finite propagation speed for divergence errors (Mignone & Tzeferacos 2010) and their decay according to the damping factor κ_ψ. For c_h equals to the speed of light, equation (A2) reduces to the evolution system given in Palenzuela et al. (2009). The covariant Mawell equations (A2) and (A3) may be written in terms of the conserved quantities

$$\mathcal{C} \equiv \begin{pmatrix} \mathcal{Q} \\ \mathcal{P} \\ b^i \\ d^i \end{pmatrix} = \sqrt{\gamma}\begin{pmatrix} \frac{\psi}{\alpha} \\ \frac{\phi}{\alpha} \\ B^i + \frac{\psi}{\alpha}\beta^i \\ D^i - \frac{\phi}{\alpha}\beta^i \end{pmatrix}, \tag{A5}$$

as well as the corresponding fluxes

$$\mathcal{F}^j \equiv \sqrt{\gamma}\begin{pmatrix} B^j - \frac{\psi}{\alpha}\beta^j \\ -\left(D^j + \frac{\phi}{\alpha}\beta^j\right) \\ e^{ijk}E_k + \alpha\left(c_h^2\gamma^{ij} - n^i n^j\right)\psi \\ -\left(e^{ijk}H_k + \alpha g^{ij}\phi\right) \end{pmatrix}. \tag{A6}$$

For the source terms, the split according to equation (A1) yields

$$\mathcal{S}_n \equiv \sqrt{\gamma}\begin{pmatrix} \alpha\psi\Gamma^t_{\mu\nu}s^{\mu\nu} \\ \alpha\phi\Gamma^t_{\mu\nu}g^{\mu\nu} - \rho \\ -\alpha\psi\Gamma^i_{\mu\nu}s^{\mu\nu} \\ \alpha\phi\Gamma^i_{\mu\nu}g^{\mu\nu} - J^i \end{pmatrix} \text{ and } \mathcal{S}_s \equiv \sqrt{\gamma}\begin{pmatrix} -\alpha\kappa_\psi\psi \\ -\alpha\kappa_\phi\phi \\ 0 \\ 0 \end{pmatrix}. \tag{A7}$$

In our practical implementation of the cleaning potential as potentially stiff source terms $\mathcal{S}_s$, we follow a Strang splitting approach (as employed, e.g. in Komissarov 2004), effectively solving part of the scalar equations (A5)–(A7) analytically. Prior (before `MoL_Step`) and after (before `MoL_PostStep`), the time integration of the Einstein Toolkit `thorn MoL` we evolve in time the equations

$$\mathcal{P}\left(t\right) = \mathcal{P}_0\exp\left[-\alpha^2\kappa_\phi t\right], \tag{A8}$$

$$\mathcal{Q}\left(t\right) = \mathcal{Q}_0\exp\left[-\alpha^2\kappa_\psi t\right], \tag{A9}$$

for a time $t = \Delta t/2$. The coefficients κ_ϕ and κ_ψ have to be chosen by optimization in accordance with the grid properties. We find it beneficial to choose a large value for κ_ϕ, effectively dissipating charge conservation errors on very short time-scales. As for the divergence cleaning, we conducted a series of tests, optimizing κ_ψ to yield stable and converging evolution for all shown resolutions, ultimately resorting to $\kappa_\psi = 0.125$. Numerical tests of the stability of force-free fields close to the BH horizon have shown that results improve significantly when advecting divergence cleaning errors ψ faster than with $c_h = 1$. In practice we, hence, employ $c_h = 2$.

A2 The BZ process in 3D time-dependent GRFFE

In the following, we present a detailed study of the relations between energy flow, magnetic field strengths, and field line angular velocity for the reference model (C-H4-L2). Blandford & Znajek (1977) quantify the energy extraction from (slowly) rotating BHs in

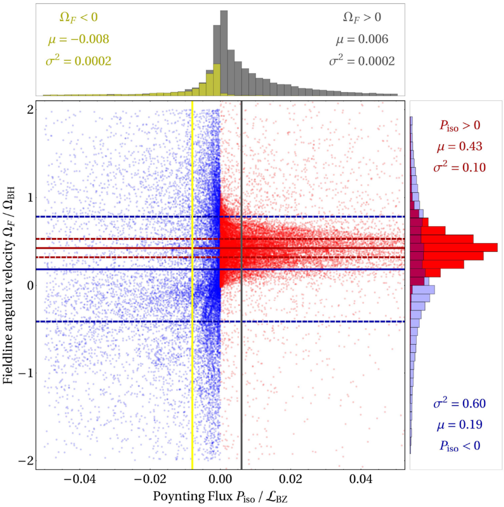

Figure A1. Statistical analysis of the relationship between the (approximate) field line angular velocity $\Omega_{\rm F}/\Omega_{\rm BH}$ and the isotropic Poynting flux (equation A11) normalized to the nominal BZ luminosity (equation 36) $P_{\rm iso}/\mathcal{L}_{\rm BZ}$. Sample points on the BH horizon have been extracted from the C-H4-L2-F model (414 time bins, 129 angular bins, 53 406 samples in total) and plotted individually in the graph. Basic statistical analysis is denoted by solid lines (mean μ), and dashed lines (variance σ^2 at $\mu \pm \sigma$) if applicable. The outgoing Poynting flux is found mainly at field line velocities along the rotational sense of the BH and clustred around a mean value of $\Omega_{\rm F}/\Omega_{\rm BH} \approx 0.43$. The ingoing Poynting flux seems to be related (with large variance) to more negative field line angular velocities.

stationary, *axisymmetric* force-free electrodynamics. The markers of BZ efficiency, like the field line angular velocity $\Omega_{\rm F}$ (A10), and the toroidal magnetic field B^T given by the Znajek condition (A12), do not need to be functions of the magnetic flux in 3D dynamical settings. The shown simulations accumulate points of inefficient or no energy extraction, where the ideal conditions described by Blandford & Znajek (1977) do not hold. Among the simulations that we present in this paper, we find many field lines for which the ideal conditions described by Blandford & Znajek (1977) do not hold and, hence, they are unable to efficiently extract energy out of the BH (or even extract energy at all). Fig. A2 points out combinations of reversed fields (with respect to the prescription in equation A12) which have an energy inflow across the BH horizon rather than an energy outflow. Such field reversals in time-dependent 3D models can greatly reduce the overall process luminosity (36). In the results at hand, such a breakdown of process efficiency is naturally observed between the accretion of two consecutive loops, where the magnetospheric fields rapidly rearrange to change their polarity (see Section 3.3, Fig. 6). We find, indeed, that in our simulations an outgoing Poynting flux at the BH horizon positively correlates with the fulfillment of conditions derived by Blandford & Znajek (1977), as we show in Figs A1 and A2. In case of the counter-rotating disc models (series A and B, Table 1) this outcome is especially noteworthy. Field lines depart with an angular velocity $\Omega_{\rm F}$ in the opposite direction to $\Omega_{\rm BH}$, but end up co-rotating under almost ideal conditions for the BZ process. For all models (co- and counter-rotating), we find the outflow of energy to be closely correlated to combinations of the magnetic fields B^r and B^ϕ allowed by the Znajek condition (A12).

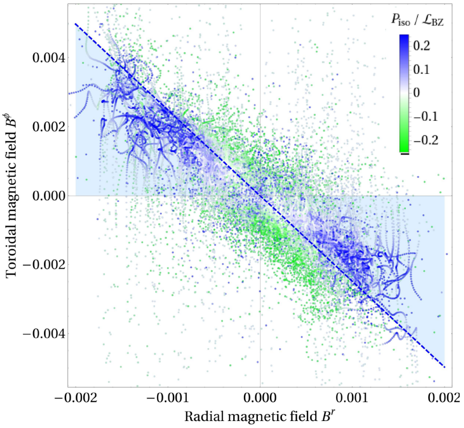

Figure A2. Statistical analysis of the relationship between the radial and toroidal magnetic fields B^r and B^ϕ. Sample points as in Fig. A1. The colour-scale indicates the respective ingoing (green) or outgoing (blue) Poynting flux. The combinations allowed by the Znajek condition (equation A12) for a field line angular velocity co-rotating with the BH (see Fig. A1) is denoted by the blue dashed line and the corresponding shading. An outgoing Poynting flux seems to be strongly correlated with a fulfillment of the Znajek condition, while an ingoing Poynting flux is arbitrarily scattered. The latter may occur especially for fields that are reversed in sign with respect to condition (A12).

A3 Field line angular velocity

The ratio between the angular velocity of the central object $\Omega_{\rm BH}$ and magnetic field lines threading the BH horizon $\Omega_{\rm F}$ is key for an efficient Poynting flux dominated energy extraction (see equation 4.5 in Blandford & Znajek 1977). More specifically, $\Omega_{\rm F} = \Omega_{\rm BH}/2$ is the optimal value and was used in the derivation of equation (36). In practice, studying more realistic (e.g. paraboloidally shaped) stationary and axisymmetric field lines in force-free Kerr magnetospheres, Nathanail & Contopoulos (2014) and Mahlmann et al. (2018) find $\Omega_{\rm F}$ to be smaller than this ideal value ($\sim 0.45\Omega_{\rm BH}$) for BHs with $M = 1$ and $a = 0.9$. In fact, Blandford & Znajek (1977) examine a paraboloidal field line configuration with $\Omega_{\rm F} \in [0.27\Omega_{\rm BH}, 0.5\Omega_{\rm BH}]$. In stationary, axisymmetric force-free electrodynamics, a field line angular velocity $\Omega_{\rm F}$ may be defined employing the relations given in Section 2.2 (Blandford & Znajek 1977; Carrasco & Reula 2017)

$$\Omega_{\rm F} = \frac{F_{t\theta}}{F_{\theta\phi}} = -\frac{E_\theta}{\sqrt{\gamma}\, B^r}. \tag{A10}$$

As the presented numerical simulations are *fully dynamic* and *3D*, equation (A10) will only have limited applicability. However, it was used, e.g. by Yuan et al. (2019b) in order to estimate $\Omega_{\rm F}$ during axisymmetric and relaxed episodes of BH force-free magnetospheric evolution. In the following, we will employ some basic statistical analysis in order to make statements about the correlation of field line angular velocity and energy extraction.

Fig. A1 displays a sample of combinations of an isotropic power emerging from an angular patch $\theta \in [\theta_-, \theta_+]$

$$P_{\rm iso}(\theta) = \frac{2\pi}{\cos\theta_+ - \cos\theta_-} \int_{\theta_-}^{\theta_+} S^r_+ \, \mathrm{d}A_r, \tag{A11}$$

and $\Omega_{\rm F}$ at different azimuthal positions and times throughout one of the conducted simulations. We observe clear trends in their correlation, for example examining model C-H4-L2 (see Fig. A1)

(i) Positive field line angular velocities ($\Omega_{\rm F} > 0$) on average correspond to outgoing energy flux. Conversely, $\Omega_{\rm F} < 0$ typically correlate with an ingoing, weaker Poynting flux.

(ii) The extraction of power ($P_{\rm iso} > 0$) is clearly clustred around $\Omega_{\rm F} \approx 0.43\Omega_{\rm BH}$, while its ingoing counterpart ($P_{\rm iso} < 0$) corresponds to mean values $\Omega_{\rm F} \approx 0.19\Omega_{\rm BH}$ and has a sixfold greater variance.

Qualitatively similar statistical results hold for all counter-rotating models (series A and B, Table 1). In the case of co-rotating ADs, however, there is no clear correlation between positive angular velocities and outgoing Poynting flux. The average field line angular velocity at the BH horizon for these models (series C) usually is $\Omega_{\rm F} > \Omega_{\rm BH}/2$, across both inward and outward flowing Poynting flux.

A4 Znajek condition

The so-called Znajek condition (Blandford & Znajek 1977; Znajek 1977) must be satisfied by the magnetic field at the BH horizon to enable a positive energy extraction in the BZ mechanism. The existence of asymptotic conditions for magnetic fields in stationary MHD was first posed by Weber & Davis (1967) and applied to Kerr BHs by Znajek (1977). In order to ensure finite field quantities at the BH horizon, the Znajek condition requires the following relationship between the radial and toroidal magnetic fields B^r and B^ϕ

$$B^\phi = \frac{\sin\theta}{\alpha} \frac{\Omega_{\rm F}\left(r_+^2 + a^2\right) - a^2}{r_+^2 + a^2\cos^2\theta} B^r. \tag{A12}$$

While Blandford & Znajek (1977) employ condition (A12) as a boundary condition at the BH horizon, it is nowadays understood as a regularity condition at the BH horizon (e.g. Komissarov 2004; Okamoto 2006; Beskin 2010; Contopoulos, Kazanas & Papadopoulos 2013). As such it is formulated in *stationary*, *axisymmetric* force-free electrodynamics, i.e. there is no intrinsic guarantee for its fulfillment in 3D time-dependent GRFFE. Fig. A2 shows that the presented simulations assemble an unrestricted range of possible combinations between B^r and B^ϕ. However, we find (for all employed models) that an outgoing Poynting flux is favoured by combinations allowed by the Znajek condition (A12) and stronger overall magnetic fields.

APPENDIX B: BENCHMARK TO SIMILAR RESEARCH

Yuan et al. (2019b) present a model to study 3D Minkowski dynamical force-free magnetospheres with field lines anchored to a central object and an extended AD. In order to include the electrodynamical effects of a BH on the AD, Yuan et al. (2019b) resort to the membrane paradigm to build a BH/AD analogue, where both the BH and the AD are replaced by thin, equatorial membranes. In their setup, Yuan et al. (2019b) assume that the BH is rotating with an angular velocity $\Omega_{\rm BH}$, while the AD may spin with an angular velocity $\Omega_{\rm D}$. Thus, field lines connecting the BH and the AD are differentially rotating. Prescribing the surface resistivity R of a disc-shaped central membrane (representing the BH) of radius r_1 and angular velocity $\Omega_{\rm BH}$, they are able to mimic different degrees of co-rotation of field lines of the BH/AD system. Following the membrane paradigm, the BH horizon has a surface resistivity of $R = 4\pi/c$(Gaussian) $= 1$(geom.) $\approx 377\Omega$(SI) (Thorne et al. 1986). The AD is set up as a perfect conductor with a surface resistivity $R = 0$. The field lines are dragged along rigidly with the AD angular velocity $\Omega_{\rm D}$. A structure of two tubes of zero-net magnetic flux is initialized by the following surface current in the (equatorial) AD

$$\sqrt{g_{\phi\phi}}\, J^\phi = \begin{cases} J_0 \cos\left(\dfrac{2\pi}{r_0}(r - r_2)\right)\left(\dfrac{r_2}{r}\right)^\alpha, & r_2 \le r \le r_2 + \dfrac{3}{4} r_0 \\ 0, & \text{else} \end{cases} \tag{B1}$$

where r_2 is the inner radius of the equatorial disc, r_0 is the centre of the current loop that generates a dipolar-shaped magnetic field in the disc, and the exponent α controls de radial decay of the boundary. J_0 is a normalization constant that we take equal to 0.1. This current is similar to the one employed in the presented simulations (cf. equation 32), differing mainly by a shift along the equatorial direction. After an initialization period, the resulting magnetic field is fixed as a boundary condition along the AD and the initialization current is replaced by suitable restrictions on the electric field (see Yuan et al. 2019b, for further details). In practice, the two membranes do not have zero thickness, but extend over a few cells of the numerical grid. We reset the space charge ρ and the numerical cleaning potentials to zero across all the numerical cells encompassing the membranes. We reproduce two exemplary series of setups from Yuan et al. (2019b) for a benchmark with the presented GRFFE method (Figs B1 and B2). Our results qualitatively reproduce those of Yuan et al. (2019b). A quantitative comparison is not possible since these authors do not provide enough information on the numerical grid and on the constants employed to setup their models. For a closer comparison with the BH/AD model described in Section 2.3, we repeat a similar test with appropriate changes to the setup in Section 4 (see Fig. 11). There, due to the full GR capacities of our method, we do not set further boundaries on the central BH (as our coordinates are horizon penetrating). Field lines rotate rigidly with the AD by enforcing zero space charge and the force-free electric field (cf. e.g. Camenzind 2007)

$$D^r = \frac{\sqrt{\gamma}}{\alpha}\gamma^{rr}\left(\Omega_{\rm D} + \beta^\phi\right) B^\theta, \tag{B2}$$

$$D^\theta = -\frac{\sqrt{\gamma}}{\alpha}\gamma^{\theta\theta}\left(\Omega_{\rm D} + \beta^\phi\right) B^r, \tag{B3}$$

$$D^\phi = 0. \tag{B4}$$

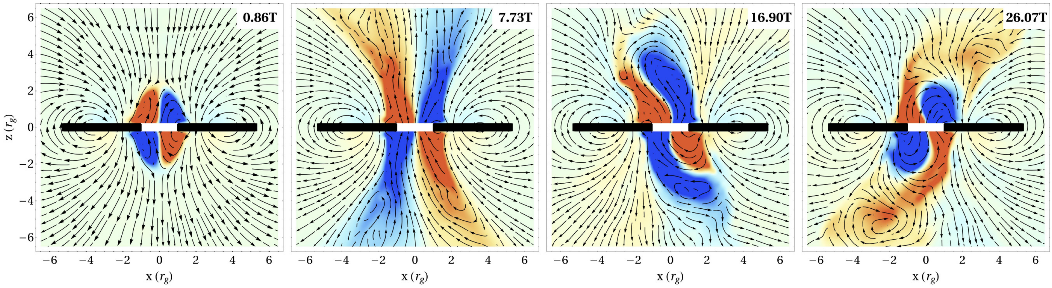

Figure B1. Snapshots from toy-models employed to compare our results to those of Yuan et al. (2019a). The models consist of disc-shaped membranes (located at $z = 0$) emulating both the central object (a BH or generically a star) surrounded by a thin disc. The colours represent the toroidal field B^{ϕ} component that is perpendicular to the displayed x–z plane (blue negative, red positive). Streamlines display the poloidal magnetic field (components in the x–z plane). The central membrane (thick white line) corresponds to a perfectly conducting object, $\eta = 0$, with cylindrical radius $r_1 = 1$, angular velocity $r_1 \Omega_{\rm BH} = 0.9$. The outer membrane (thick black line) is a truncated disc that is perfectly conducting ($\eta = 0$), non-rotating ($\Omega_{\rm D} = 0$), and extends outward from an inner radius $r_2 = 1.08 r_g$ with decay parameter $\alpha = 0.4$ (see equation B1). The dipolar-shaped magnetic field of the disc is driven by a current loop on the equatorial plane located at a distance $r_0 = 4.33 r_g$. Field lines connecting the central membrane to the disc are twisted up showing kink structures and stripes of reversed fields. The panels denote the simulation time after initialization in units of the rotational period $\mathrm{T} = 2\pi/\Omega_{\rm BH}$. The grid resolution on the finest refinement level is $\Delta_{x,\,y,\,z} = 0.125$. The colour scale is the same over all plots.

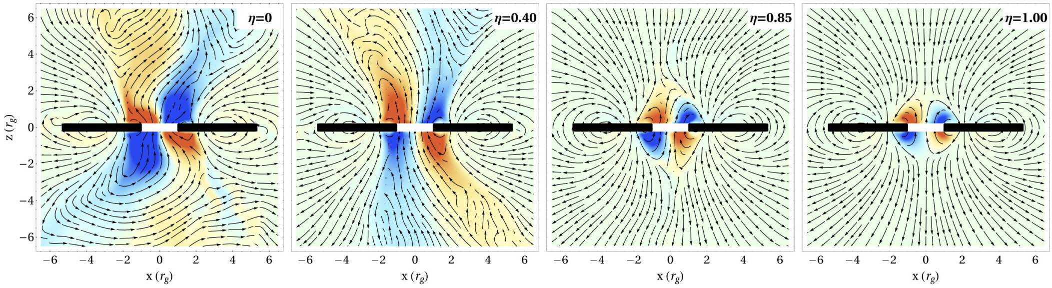

Figure B2. As in Fig. B1 but with decay parameter $\alpha = 0.9$ and varying surface resistivity η of the central membrane. Snapshots are shown for $t = 26.07$T.

APPENDIX C: ENERGY OUTFLOW FROM THE DISC

We find that our simplified AD model also artificially generates a radially outwards directed Poynting flux. The luminosity of the disc is very different in prograde and retrograde discs, being negligible for the latter cases, but significant for the former ones. An estimate of the flow of energy emerging from an isolated AD can be found in the so-called Faraday disc (e.g. Feynman et al. 2011; Chyba, Hand & Thomas 2015, and references therein). A disc-shaped electrical generator of height $h_{\rm F}$ rotating with angular velocity $\omega_{\rm F}$ in a uniform magnetic field $B_{\rm F}$ relies on the energy conversion from the magnetic field to the induced electric current $I_{\rm F}$ by the mechanical rotation. On the other hand, the current $I_{\rm F}$ brakes down the rotation the of the Faraday disc ensuring energy conservation. In our case we impose *both* disc rotation $\omega_{\rm F}$, and the disc current $I_{\rm F}$ in the ad hoc disc model (Fig. 1). Energy conservation, i.e. the interplay between induced electric current and magnetic braking, demands that energy $\mathcal{E}_{\rm F}$ be radiated from the disc. The amount of energy radiated can be roughly estimated as

$$\mathcal{E}_{\rm F} = \frac{\pi}{2} \sigma B_{\rm F}^2\, \omega_{\rm F}^2\, h_{\rm F}\, \left(b^4 - a^4\right). \tag{C1}$$

Here, a and b represent the inner and outer radius of the Faraday disc, respectively. For magnetic fields $B_{\rm F}^2 \propto 1/r^4$ and $\omega_{\rm F}^2 \propto 1/r^3$ (cf. equation 30) the energy radiated by a disc of finite length $|b - a|$ – corresponding, e.g. to $\sim l$ in one flux tube in our simulations – scales as $1/r^3$. Apart from the exact field geometry in the AD model, the power induced into the magnetosphere by this artificial process (equation C1) is greatly suppressed for counter-rotating discs due to the remote location of $r_{\rm ISCO}$ from the central object. Conversely, for prograde discs, in which $a \simeq r_{\rm ISCO} \sim r_+$, the AD luminosity of our models may even be larger than BZ luminosity. This is the case for large enough BH rapidity ($a^* \gtrsim 0.9$).

This paper has been typeset from a TEX/LATEX file prepared by the author.

Part III

Backmatter

Nomenclature

Abbreviations

AD	Accretion Disk
AGN	Active Galactic Nucleus
BH	Black Hole
BP	Blandford/Payne Process
BZ	Blandford/Znajek Process
ET	Einstein Toolkit
FFE	Force-Free Electrodynamics
GRB	Gamma-Ray-Burst
GRFFE	General Relativistic Force-Free Electrodynamics
GRMHD	General Relativistic Magnetohydrodynamics
GRPIC	General Relativistic Particle-In-Cell
GSE	Grad-Shafranov Equation
GW	Gravitational Wave
LC	Light Cylinder
MC	Magneto-Centrifugal
MHD	Magnetohydrodynamics
PDE	Partial Differential Equation
PIC	Particle-In-Cell

SGR	Soft Gamma Repeater
VLBA	Very Large Base-Line Array Telescope

Other Symbols

$\bar{\nabla}$	Covariant derivative with respect to the conformally related 3-metric
$\eta^{\mu\nu\lambda\zeta}$	Completely antisymmetric Levi-Civita symbol $\eta^{\mu\nu\lambda\zeta} = [\mu\nu\lambda\zeta]/\sqrt{-g}$
∇	Covariant derivative with respect to the four-metric $g_{\mu\nu}$
$\nabla^{(3)}$	Covariant derivative with respect to the three-metric γ_{ij}
$e^{\mu\nu\lambda\zeta}$	Completely antisymmetric four-pseudo-tensor $e^{\mu\nu\lambda\zeta} = -\eta^{\mu\nu\lambda\zeta}$
e^{ijk}	Completely three-antisymmetric pseudo-tensor $e^{ijk} = \alpha\eta^{0ijk}$
div	Divergence of a vector field

Physical Quantities

α	Lapse function ($3+1$ decomposition)
$\bar{\gamma}_{ij}$	Conformally related three-metric $\gamma_{ij} = e^{4\phi}\bar{\gamma}_{ij}$
γ_{ij}	Spacetime three-metric ($3+1$ decomposition)
κ_Φ	Damping constant for the cleaning of charge conservation errors
κ_Ψ	Damping constant for the cleaning of divergence errors
β	Shift vector ($3+1$ decomposition)
$\mathbf{B}$	Magnetic field measured by the local fiducial observer
$\mathbf{D}$	Electric field measured by the local fiducial observer
$\mathbf{E}$	Electric field measured by an observer at infinity
$\mathbf{H}$	Magnetic field measured by an observer at infinity
$\mathbf{S}$	Poynting flux $S^i \equiv -\alpha T^i_t$
Ω	Frame-dragging frequency
Ω_{BH}	BH angular velocity
Φ	Potential for hyperbolic/parabolic cleaning of charge conservation errors
ϕ	Conformal factor of BSSN formulation
Ψ	Potential for hyperbolic/parabolic cleaning of divergence errors
ρ	Charge density $\rho = \alpha I^t$
a	Specific BH angular momentum $a = J/M$
a^*	BH rotation rapidity $a = J/M^2$ (dimensionless)
c_h	Advection speed for the cleaning of divergence errors
e	(Electromagnetic) energy density
$F^{\mu\nu}$	Faraday tensor
$g_{\mu\nu}$	Spacetime four-metric
I^μ_{FF}	Force-free current conserving $\partial_t\left(\mathbf{D}\cdot\mathbf{B}\right) = 0$

I^μ	Electric current four-vector
J	BH angular momentum of the Kerr metric
J^i	Electric current three-vector $J^i = \alpha I^i$
K_{ij}	Extrinsic curvature tensor
M	BH mass of the Kerr metric
$r_\pm$	Location of the inner (−) and outer (+) BH horizon
$s^{\mu\nu}$	Adapted four-metric for accurate divergence-cleaning $s^{\mu\nu} = c_h^2 \gamma^{\mu\nu} - n^\mu n^\nu$
$T^\mu_{\ \nu}$	(Electromagnetic) stress-energy-tensor

Bibliography

B. P. Abbott et al. GW170817: Observation of gravitational waves from a binary neutron star inspiral. *PRL*, 119(16):161101, 2017. doi:10/cd8g.

V. A. Acciari et al. Radio imaging of the very-high-energy γ-ray emission region in the central engine of a radio galaxy. *Science*, 325:444, 2009. doi:10/bkmrx2.

F. Acero et al. Fermi large area telescope third source catalog. *ApJSS*, 218(2): 23, 2015. doi:10.1088/0067-0049/218/2/23.

R. X. Adhikari et al. Astrophysical science metrics for next-generation gravitational-wave detectors. *CQG*, 36(24):245010, 2019. doi:10.1088/1361-6382/ab3cff.

N. Aghanim et al. Planck 2018 results. I. Overview and the cosmological legacy of Planck. *A&A*, 2019. URL https://ui.adsabs.harvard.edu/abs/2018arXiv180706205P.

F. Aharonian et al. Is the giant radio galaxy M87 a TeV gamma-ray emitter? *A&A*, 403:L1–L5, 2003. doi:10.1051/0004-6361:20030372.

T. Akgün et al. Long-term evolution of the force-free twisted magnetosphere of a magnetar. *MNRAS*, 472:3914–3923, 2017. doi:10.1093/mnras/stx2235.

T. Akgün et al. The force-free twisted magnetosphere of a neutron star - II. Degeneracies of the Grad-Shafranov equation. *MNRAS*, 474:625–635, 2018. doi:10.1093/mnras/stx2814.

M. Alcubierre. *Introduction to 3+1 numerical relativity*. Oxford University Press, 2008. doi:10.1093/acprof:oso/9780199205677.001.0001.

M. Alcubierre et al. Symmetry without symmetry: Numerical simulation of axisymmetric systems using Cartesian grids. *IJMPD*, 10(03):273–289, 2001. doi:10.1142/S0218271801000834.

J. Aleksić et al. Black hole lightning due to particle acceleration at subhorizon scales. *Science*, 346:1080–1084, 2014. doi:10.1126/science.1256183.

D. Alexander and L. Fletcher. High-resolution observations of plasma jets in the solar corona. *SolP*, 190:167–184, 1999. doi:10.1023/A:1005213826793.

D. Alic et al. Accurate simulations of binary black hole mergers in force-free electrodynamics. *ApJ*, 754:36, 2012. doi:10.1088/0004-637X/754/1/36.

L. Antón et al. Relativistic magnetohydrodynamics: Renormalized eigenvectors and full wave decomposition Riemann solver. *ApJSS*, 188(1):1–31, 2010. doi:10.1088/0067-0049/188/1/1.

R. Arnowitt, S. Deser, and C. W. Misner. Dynamical structure and definition of energy in General Relativity. *PR*, 116(5):1322–1330, 1959. doi:10.1103/PhysRev.116.1322.

H. W. Babcock. The sun's magnetic field. *ARA&A*, 1(1):41–58, 1963. doi:10.1146/annurev.aa.01.090163.000353.

D. Ball, L. Sironi, and F. Özel. The mechanism of electron injection and acceleration in transrelativistic reconnection. *ApJ*, 884(1):57, 2019. doi:10.3847/1538-4357/ab3f2e.

R. Bandyopadhyay et al. Solar wind turbulence studies using MMS fast plasma investigation data. *ApJ*, 866(2):81, 2018. doi:10.3847/1538-4357/aade93.

T. W. Baumgarte and S. L. Shapiro. General relativistic magnetohydrodynamics for the numerical construction of dynamical spacetimes. *ApJ*, 585:921–929, 2003. doi:10.1086/346103.

T. W. Baumgarte et al. Equilibrium initial data for moving puncture simulations: The stationary 1 + log slicing. *CQG*, 26(8):085007, 2009. doi:10.1088/0264-9381/26/8/085007.

T. W. Baumgarte et al. Numerical relativity in spherical polar coordinates: Evolution calculations with the BSSN formulation. *PRD*, 87(4):044026, 2013. doi:10.1103/PhysRevD.87.044026.

K. Beckwith, J. F. Hawley, and J. H. Krolik. The influence of magnetic field geometry on the evolution of black hole accretion flows: Similar disks, drastically different jets. *ApJ*, 678:1180–1199, 2008. doi:10.1086/533492.

K. Beckwith, J. F. Hawley, and J. H. Krolik. Transport of large-scale poloidal flux in black hole accretion. *ApJ*, 707:428–445, 2009. doi:10.1088/0004-637X/707/1/428.

A. M. Beloborodov. Untwisting magnetospheres of neutron stars. *ApJ*, 703(1): 1044–1060, 2009. doi:10.1088/0004-637X/703/1/1044.

A. M. Beloborodov. Electron-positron flows around magnetars. *ApJ*, 777:114, 2013. doi:10.1088/0004-637X/777/2/114.

A. M. Beloborodov. A flaring magnetar in FRB 121102? *ApJL*, 843(2):L26, 2017. doi:10.3847/2041-8213/aa78f3.

A. M. Beloborodov and C. Thompson. Magnetar corona. *A&SSci*, 308(1-4): 631–639, 2007. doi:10.1007/s10509-007-9318-x.

B. Benneke et al. Water vapor and clouds on the habitable-zone sub-Neptune exoplanet K2-18B. *ApJL*, 887(1):L14, 2019. doi:10.3847/2041-8213/ab59dc.

V. S. Beskin. Reviews of topical problems: Axisymmetric stationary flows in compact astrophysical objects. *SovPU*, 40(7):659–688, 1997. doi:10.1070/PU1997v040n07ABEH000250.

G. S. Bisnovatyi-Kogan and A. A. Ruzmaikin. The accretion of matter by a collapsing star in the presence of a magnetic field. II: Self-consistent stationary picture. *A&SSci*, 42(2):401–424, 1976. doi:10.1007/BF01225967.

R. D. Blandford and M. C. Begelman. On the fate of gas accreting at a low rate on to a black hole. *MNRAS*, 303:L1–L5, 1999. doi:10.1046/j.1365-8711.1999.02358.x.

R. D. Blandford and D. G. Payne. Hydromagnetic flows from accretion disks and the production of radio jets. *MNRAS*, 199:883–903, 1982. doi:10.1093/mnras/199.4.883.

R. D. Blandford and R. L. Znajek. Electromagnetic extraction of energy from Kerr black holes. *MNRAS*, 179(3):433–456, 1977. doi:10.1093/mnras/179.3.433.

H. Bridge et al. The plasma experiment on the 1977 voyager mission. *SSRev*, 21 (3):259–287, 1977.

O. Bromberg et al. Kink instability: Evolution and energy dissipation in relativistic force-free nonrotating jets. *ApJ*, 884(1):39, 2019. doi:10.3847/1538-4357/ab3fa5.

D. Brown et al. Excision without excision. *PRD*, 76(8):081503, 2007. doi:10.1103/PhysRevD.76.081503.

D. Brown et al. Turduckening black holes: An analytical and computational study. *PRD*, 79(4):044023, 2009. doi:10.1103/PhysRevD.79.044023.

J. D. Brown. Conformal invariance and the conformal-traceless decomposition of the gravitational field. *PRD*, 71(10):104011, 2005.

M. Camenzind. Centrifugally driven MHD-winds in active galactic nuclei. *A&A*, 156(1-2):137–151, 1986.

M. Camenzind. *Compact objects in astrophysics: White dwarfs, neutron stars, and black holes*. Springer, 2007. doi:10.1007/978-3-540-49912-1.

C. Canuto et al. *Spectral methods: Evolution to complex geometries and applications to fluid dynamics*. Scientific Computation. Springer, 2007. ISBN 9783540307280. doi:10.1007/978-3-540-30728-0.

F. L. Carrasco and O. A. Reula. Covariant hyperbolization of force-free electrodynamics. *PRD*, 93(8):085013, 2016. doi:10.1103/PhysRevD.93.085013.

F. L. Carrasco and O. A. Reula. Novel scheme for simulating the force-free equations: Boundary conditions and the evolution of solutions towards stationarity. *PRD*, 96(6):063006, 2017. doi:10.1103/PhysRevD.96.063006.

P. Cerdá-Durán et al. A new general relativistic magnetohydrodynamics code for dynamical spacetimes. *A&A*, 492(3):937–953, 2008. doi:10.1051/0004-6361:200810086.

C. Chaston et al. Extreme ionospheric ion energization and electron heating in alfvén waves in the storm time inner magnetosphere. *GRL*, 42(24):10–531, 2015. doi:10.1002/2015GL066674.

K. Chatterjee et al. Accelerating AGN jets to parsec scales using general relativistic MHD simulations. *MNRAS*, 490(2):2200–2218, 2019. doi:10.1093/mnras/stz2626.

P. Chen. Coronal mass ejections: Models and their observational basis. *LRSolP*, 8(1):1, 2011. doi:10.12942/lrsp-2011-1.

C. Chiuderi and M. Velli. *Basics of plasma astrophysics*. Springer, 2015. doi:10.1007/978-88-470-5280-2.

D. Clery. Iter's $12 billion gamble. *Science*, 314(5797):238–242, 2006. ISSN 0036-8075. doi:10.1126/science.314.5797.238.

D. C. Collins et al. Cosmological adaptive mesh refinement magnetohydrodynamics with ENZO. *ApJSS*, 186:308–333, 2010. doi:10.1088/0067-0049/186/2/308.

I. Contopoulos, D. Kazanas, and C. Fendt. The axisymmetric pulsar magnetosphere. *ApJ*, 511(1):351–358, 1999. doi:10.1086/306652.

I. Contopoulos, D. Kazanas, and D. B. Papadopoulos. The force-free magnetosphere of a rotating black hole. *ApJ*, 765(2):113, 2013. doi:10.1088/0004-637x/765/2/113.

I. Cordero-Carrión et al. Mathematical issues in a fully constrained formulation of the Einstein equations. *PRD*, 77(8):084007, 2008. doi:10.1103/PhysRevD.77.084007.

R. Courant and D. Hilbert. *Methoden der mathematischen Physik*. Springer-Verlag, 1968.

R. Courant, K. Friedrichs, and H. Lewy. Über die partiellen Differenzengleichungen der mathematischen Physik. *Mathematische Annalen*, 100(1):32–74, 1928.

P. Damiano et al. Electron distributions in kinetic scale field line resonances: A comparison of simulations and observations. *GRL*, 45(12):5826–5835, 2018. doi:10.1029/2018GL077748.

M. de Naurois. H.E.S.S. - II - Gamma ray astronomy from 20 GeV to hundreds of TeV's. In *European Physical Journal Web of Conferences*, volume 136 of *European Physical Journal Web of Conferences*, page 03001, 2017. doi:10.1051/epjconf/201713603001.

A. Dedner et al. Hyperbolic divergence cleaning for the MHD equations. *JCP*, 175:645–673, 2002. doi:10.1006/jcph.2001.6961.

L. Del Zanna et al. Fast reconnection in relativistic plasmas: The magnetohydrodynamics tearing instability revisited. *MNRAS*, 460:3753–3765, 2016. doi:10.1093/mnras/stw1242.

L. Di Mascolo et al. An ALMA+ACA measurement of the shock in the bullet cluster. *A&A*, 628:A100, 2019. doi:10.1051/0004-6361/201936184.

P. Diener et al. Optimized high-order derivative and dissipation operators satisfying summation by parts, and applications in three-dimensional multi-block evolutions. *Journal of Scientific Computing*, 32(1):109–145, 2007. doi:10.1007/s10915-006-9123-7.

G. Drenkhahn and H. Spruit. Efficient acceleration and radiation in poynting flux powered GRB outflows. *A&A*, 391(3):1141–1153, 2002. doi:10.1051/0004-6361:20020839.

O. Dreyer et al. Introduction to isolated horizons in numerical relativity. *PRD*, 67(2):024018, 2003. doi:10.1103/PhysRevD.67.024018.

R. Eatough et al. A strong magnetic field around the supermassive black hole at the centre of the galaxy. *Nature*, 501(7467):391–394, 2013. doi:10.1038/nature12499.

A. Einstein. Die Grundlage der allgemeinen Relativitätstheorie. *Annalen der Physik*, 354(7):769–822, 1916. doi:10.1002/andp.19163540702.

Z. B. Etienne et al. Filling the holes: Evolving excised binary black hole initial data with puncture techniques. *PRD*, 76(10):101503, 2007. doi:10/bz29ks.

Z. B. Etienne et al. GiRaFFE: An open-source general relativistic force-free electrodynamics code. *CQG*, 34(21):215001, 2017. doi:10.1088/1361-6382/aa8ab3.

Event Horizon Telescope Collaboration et al. First M87 event horizon telescope results. I. The shadow of the supermassive black hole. *ApJL*, 875(1):L1, 2019a. doi:10/gfx8zm.

Event Horizon Telescope Collaboration et al. First M87 event horizon telescope results. v. physical origin of the asymmetric ring. *ApJL*, 875(1):L5, 2019b. doi:10/gfx8zp.

J. A. Faber et al. Relativistic hydrodynamics in the presence of puncture black holes. *PRD*, 76(10):104021, 2007. doi:10.1103/PhysRevD.76.104021.

H. P. Furth, J. Killeen, and M. N. Rosenbluth. Finite-resistivity instabilities of a sheet pinch. *Physics of Fluids*, 6:459–484, 1963. doi:10.1063/1.1706761.

C. F. Gammie, J. C. McKinney, and G. Tóth. HARM: A numerical scheme for General Relativistic magnetohydrodynamics. *ApJ*, 589(1):444–457, 2003. doi:10.1086/374594.

D. Garofalo, C. B. Singh, and A. Zack. The distribution and lifetime of powerful radio galaxies as a function of environment and redshift. *Scientific reports*, 8 (1):15097, 2018. doi:10.1038/s41598-018-33532-6.

I. M. George and A. C. Fabian. X-ray reflection from cold matter in active galactic nuclei and X-ray binaries. *MNRAS*, 249:352, 1991. doi:10.1093/mnras/249.2.352.

D. Giannios and H. C. Spruit. The role of kink instability in poynting-flux dominated jets. *A&A*, 450(3):887–898, 2006. doi:10.1051/0004-6361:20054107.

K. Glampedakis, S. K. Lander, and N. Andersson. The inside-out view on neutron-star magnetospheres. *MNRAS*, 437(1):2–8, 2014. doi:10.1093/mnras/stt1814.

J. P. H. Goedbloed and S. Poedts. *Principles of Magnetohydrodynamics*. Cambridge University Press, 2004. doi:10.1017/CBO9780511616945.

T. Gold. Motions in the magnetosphere of the earth. *JGS*, 64(9):1219–1224, 1959. doi:10.1029/JZ064i009p01219.

T. Goodale et al. The Cactus framework and toolkit: Design and applications. In *Vector and Parallel Processing – VECPAR'2002, 5th International Conference, Lecture Notes in Computer Science*, pages 197–227. Springer, 2003. doi:doi.org/10.1007/3-540-36569-9_13.

D. Gottlieb and S. Orszag. *Numerical analysis of spectral methods: Theory and applications*. CBMS-NSF Regional Conference Series in Applied Mathematics. Society for Industrial and Applied Mathematics, 1977. ISBN 9781611970425. doi:10.1137/1.9781611970425.

E. Gourgoulhon. *3+1 Formalism in General Relativity*. Springer, 2012. doi:10.1007/978-3-642-24525-1.

E. Gourgoulhon et al. Magnetohydrodynamics in stationary and axisymmetric spacetimes: A fully covariant approach. *PRD*, 83(10):104007, 2011. doi:10.1103/PhysRevD.83.104007.

H. Grad and H. Rubin. Hydromagnetic equilibria and force-free fields. In *Proceedings of the 2nd UN Conf. on the Peaceful Uses of Atomic Energy*, volume 2, pages 190–197, 1958. URL http://www-naweb.iaea.org/napc/physics/2ndgenconf/sets/46.html.

S. E. Gralla and T. Jacobson. Spacetime approach to force-free magnetospheres. *MNRAS*, 445(3):2500–2534, 2014. doi:10.1093/mnras/stu1690.

M. Grey et al. Europa pims prototype faraday cup development. In *2018 IEEE Aerospace Conference*, pages 1–15. IEEE, 2018. doi:10.1109/AERO.2018.8396522.

G. Grignani, T. Harmark, and M. Orselli. Existence of the Blandford-Znajek monopole for a slowly rotating Kerr black hole. *PRD*, 98(8):084056, 2018. doi:10.1103/PhysRevD.98.084056.

G. Grignani, T. Harmark, and M. Orselli. Force-free electrodynamics near rotation axis of a Kerr black hole. *arXiv e-prints*, 2019. URL https://ui.adsabs.harvard.edu/abs/2019arXiv190807227G.

X. Guan and C. F. Gammie. The turbulent magnetic prandtl number of MHD turbulence in disks. *ApJ*, 697(2):1901–1906, 2009. doi:10/c8fq89.

J. Guilet and G. I. Ogilvie. Transport of magnetic flux and the vertical structure of accretion discs - I. Uniform diffusion coefficients. *MNRAS*, 424:2097–2117, 2012. doi:10.1111/j.1365-2966.2012.21361.x.

F. Guo et al. Determining the dominant acceleration mechanism during relativistic magnetic reconnection in large-scale systems. *ApJL*, 879(2):L23, 2019. doi:10.3847/2041-8213/ab2a15.

L. Harra and K. Mason. *Space science.* Imperial College Press, 2004. doi:10.1142/p280.

J. F. Hawley and J. H. Krolik. Magnetically driven jets in the Kerr metric. *ApJ*, 641:103–116, 2006. doi:10.1086/500385.

M. Hesse and K. Schindler. A theoretical foundation of general magnetic reconnection. *JGS*, 93(A6):5559–5567, 1988. doi:10.1029/JA093iA06p05559.

J. Heyvaerts, E. R. Priest, and A. Bardou. Magnetic field diffusion in self-consistently turbulent accretion disks. *ApJ*, 473:403, 1996. doi:10.1086/178154.

I. Hinder, B. Wardell, and E. Bentivegna. Falloff of the Weyl scalars in binary black hole spacetimes. *PRD*, 84(2):024036, 2011. doi:10.1103/PhysRevD.84.024036.

N. Holtkamp et al. An overview of the iter project. *Fusion Engineering and Design*, 82(5-14):427–434, 2007.

G. G. Howes and K. D. Nielson. Alfvén wave collisions, the fundamental building block of plasma turbulence. II. Asymptotic solution. *PPl*, 20(7):072302, 2013. doi:10.1063/1.4812805.

L. Huang, Z. Pan, and C. Yu. Toward a full MHD jet model of spinning black holes. I. Framework and a split monopole example. *ApJ*, 880(2):93, 2019. doi:10/ggssd6.

P. Hugoniot. *Mémoire sur la propagation du mouvement dans un fluide indéfini*, volume 4. J. de Mathématiques, 1887.

P. Hugoniot. *Mémoire sur la propagation du mouvement dans les corps et spécialement dans les gaz parfaits*, volume 57. J. École Polytech., 1889.

A. Hull et al. The "alfvénic surge" at substorm onset/expansion and the formation of "inverted vs": Cluster and image observations. *JGS*, 121(5): 3978–4004, 2016. doi:10.1002/2015JA022000.

S. Husa, I. Hinder, and C. Lechner. KRANC: A mathematica package to generate numerical codes for tensorial evolution equations. *Computer Physics Communications*, 174(12):983–1004, 2006. doi:10.1016/j.cpc.2006.02.002.

IceCube Collaboration et al. Search for multimessenger sources of gravitational waves and high-energy neutrinos with advanced LIGO during its first observing run, ANTARES, and IceCube. *ApJ*, 870(2):134, 2019. doi:10.3847/1538-4357/aaf21d.

I. V. Igumenshchev. Magnetically arrested disks and the origin of poynting jets: A numerical study. *ApJ*, 677(1):317–326, 2008. doi:10.1086/529025.

J. D. Jackson. *Classical electrodynamics.* AAPT, 1999. ISBN 978-0-471-30932-1.

A. Jafari and E. T. Vishniac. Magnetic field transport in accretion disks. *ApJ*, 854(1):2, 2018. doi:10.3847/1538-4357/aaa75b.

V. M. Kaspi and A. M. Beloborodov. Magnetars. *ARA&A*, 55(1):261–301, 2017. doi:10.1146/annurev-astro-081915-023329.

C. Kennel and F. Coroniti. Confinement of the Crab pulsar's wind by its supernova remnant. *ApJ*, 283:694–709, 1984.

E. Khomenko and M. Collados. Heating of the magnetized solar chromosphere by partial ionization effects. *ApJ*, 747(2):87, 2012. doi:10.1088/0004-637X/747/2/87.

D. Kiramov and B. Breizman. Force-free motion of a cold plasma during the current quench. *PPl*, 25(9):092501, 2018. doi:10.1063/1.5046517.

S. Koide et al. General Relativistic simulations of early jet formation in a rapidly rotating black hole magnetosphere. *ApJ*, 536:668–674, 2000. doi:10.1086/308986.

Y. Kojima and S. Okamoto. Axisymmetric force-free magnetosphere in the exterior of a neutron star - II. Maximum storage and open field energies. *MNRAS*, 475(4):5290–5295, 2018. doi:10.1093/mnras/sty176.

S. S. Komissarov. Time-dependent, force-free, degenerate electrodynamics. *MNRAS*, 336(3):759–766, 2002. doi:10.1046/j.1365-8711.2002.05313.x.

S. S. Komissarov. Electrodynamics of black hole magnetospheres. *MNRAS*, 350 (2):427–448, 2004. doi:10.1111/j.1365-2966.2004.07598.x.

S. S. Komissarov. Multidimensional numerical scheme for resistive relativistic magnetohydrodynamics. *MNRAS*, 382(3):995–1004, 2007. doi:10.1111/j.1365-2966.2007.12448.x.

S. S. Komissarov. Blandford-Znajek mechanism versus Penrose process. *Journal of the Korean Physical Society*, 54(61):2503, 2009. doi:10.3938/jkps.54.2503.

S. S. Komissarov. 3+1 magnetodynamics. *MNRAS*, 418:L94–L98, 2011. doi:10.1111/j.1745-3933.2011.01150.x.

S. S. Komissarov and J. C. McKinney. The 'meissner effect' and the Blandford-Znajek mechanism in conductive black hole magnetospheres. *MNRAS*, 377: L49–L53, 2007. doi:10.1111/j.1745-3933.2007.00301.x.

S. S. Komissarov, M. Barkov, and M. Lyutikov. Tearing instability in relativistic magnetically dominated plasmas. *MNRAS*, 374(2):415–426, 2007. doi:10/dfvt3g.

R. Krasnopolsky, Z.-Y. Li, and R. Blandford. Magnetocentrifugal launching of jets from accretion disks. I. Cold axisymmetric flows. *ApJ*, 526(2):631–642, 1999. doi:10/dqxk59.

L. Landau et al. *Electrodynamics of continuous media*. Course of Theoretical Physics. Elsevier Science, 2013. ISBN 978-9333161527.

P. Lax. *Hyperbolic systems of conservation laws and the mathematical theory of shock waves*. Number 11-16 in CBMS-NSF Regional Conference Series in Applied Mathematics. Society for Industrial and Applied Mathematics, 1973. ISBN 9780898711776. doi:10.1137/1.9781611970562.

H. K. Lee, R. Wijers, and G. Brown. The Blandford-Znajek process as a central engine for a gamma-ray burst. *PRp*, 325(3):83–114, 2000. doi:10/dxbnkf.

R. LeVeque. *Finite difference methods for ordinary and partial differential equations: Steady-state and time-dependent problems*. Other Titles in Applied Mathematics. Society for Industrial and Applied Mathematics, 2007.

A. Levinson and B. Cerutti. Particle-in-cell simulations of pair discharges in a starved magnetosphere of a kerr black hole. *A&A*, 616:A184, 2018.

A. Levinson and F. Rieger. Variable tev emission as a manifestation of jet formation in M87? *ApJ*, 730(2):123, 2011. doi:10.1088/0004-637X/730/2/123.

X. Li and A. M. Beloborodov. Plastic damping of alfvén waves in magnetar flares and delayed afterglow emission. *ApJ*, 815(1):25, 2015. doi:10/ggssd7.

X. Li, J. Zrake, and A. M. Beloborodov. Dissipation of alfvén waves in relativistic magnetospheres of magnetars. *ApJ*, 881(1):13, 2019. doi:10/ggssd8.

M. Liska et al. Bardeen-petterson alignment, jets, and magnetic truncation in GRMHD simulations of tilted thin accretion discs. *MNRAS*, 487(1):550–561, 2019. doi:10.1093/mnras/stz834.

H. Liu et al. MMS observations of electron scale magnetic cavity embedded in proton scale magnetic cavity. *Nature Communications*, 10:1040, 2019. doi:10.1038/s41467-019-08971-y.

Y. T. Liu, Z. B. Etienne, and S. L. Shapiro. Evolution of near-extremal-spin black holes using the moving puncture technique. *PRD*, 80(12), 2009. doi:10/dqj6xk.

F. Löffler et al. The Einstein toolkit: A community computational infrastructure for relativistic astrophysics. *CQG*, 29(11):115001, 2012. doi:10.1088/0264-9381/29/11/115001.

S. H. Lubow, J. C. B. Papaloizou, and J. E. Pringle. Magnetic field dragging in accretion discs. *MNRAS*, 267:235–240, 1994. doi:10.1093/mnras/267.2.235.

R. Lüst and A. Schlüter. Kraftfreie magnetfelder. *ZfN*, 34:263, 1954. URL https://ui.adsabs.harvard.edu/abs/1954ZA.....34..263L/abstract.

R. Lüst and A. Schlüter. Axialsymmetrische magnetohydrodynamische gleichgewichtskonfigurationen. *ZfN*, A(12):850–854, 1957. doi:10.1515/zna-1957-1014.

M. Lyutikov. Explosive reconnection in magnetars. *MNRAS*, 346:540–554, 2003. doi:10/cvgfn6.

M. Lyutikov. Magnetocentrifugal launching of jets from discs around Kerr black holes. *MNRAS*, 396(3):1545–1552, 2009. doi:10/fbr5x6.

M. Lyutikov and K. N. Gourgouliatos. Coronal mass ejections as expanding force-free structures. *SolP*, 270(2):537–549, 2011. doi:10/bwr8fw.

M. Lyutikov et al. Explosive x-point collapse in relativistic magnetically dominated plasma. *Journal of Plasma Physics*, 83(6), 2017. doi:10/ggssd9.

D. MacDonald and K. S. Thorne. Black-hole electrodynamics: An absolute-space/universal-time formulation. *MNRAS*, 198(2):345–382, 1982. doi:10.1093/mnras/198.2.345.

D. A. Macdonald. Numerical models of force-free black-hole magnetospheres. *MNRAS*, 211(2):313–329, 1984. doi:10.1093/mnras/211.2.313.

M. Maggiore et al. Science case for the Einstein telescope. *JCAP*, 2020(3):050, 2020. doi:10.1088/1475-7516/2020/03/050.

J. Mahlmann, A. Levinson, and M. Aloy. Striped blandford/znajek jets from advection of small-scale magnetic field. *MNRAS*, 494(3):4203–4225, 2020.

J. F. Mahlmann, P. Cerdá-Durán, and M. A. Aloy. Numerically solving the relativistic grad-shafranov equation in Kerr spacetimes: Numerical techniques. *MNRAS*, 477:3927–3944, 2018. doi:10.1093/mnras/sty858.

J. F. Mahlmann et al. Instability of twisted magnetar magnetospheres. *MNRAS*, 490(4):4858–4876, 2019. doi:10.1093/mnras/stz2729.

B. Marcote et al. A repeating fast radio burst source localized to a nearby spiral galaxy. *Nature*, 577(7789):190–194, 2020. doi:10/dhwf.

G. E. Marsh. *Force-free magnetic fields: Solutions, topology and applications*. World Scientific, 1996. doi:10.1142/2965.

J. M. Martí and E. Müller. Numerical hydrodynamics in special relativity. *LRRel*, 6(1):7, 2003. doi:10.12942/lrr-2003-7.

A. Martocchia, V. Karas, and G. Matt. Effects of Kerr space-time on spectral features from X-ray illuminated accretion discs. *MNRAS*, 312(4):817–826, 2000. doi:10.1046/j.1365-8711.2000.03205.x.

D. McComas et al. The interstellar boundary explorer (ibex). In V. Florinski, N. V. Pogorelov, and G. P. Zank, editors, *Physics of the Outer Heliosphere*, volume 719 of *American Institute of Physics Conference Series*, pages 162–181, 2004. doi:10.1063/1.1809514.

J. C. McKinney. Total and jet Blandford-Znajek power in the presence of an accretion disk. *ApJL*, 630:L5–L8, 2005. doi:10.1086/468184.

J. C. McKinney. General Relativistic force-free electrodynamics: A new code and applications to black hole magnetospheres. *MNRAS*, 367:1797–1807, 2006. doi:10.1111/j.1365-2966.2006.10087.x.

J. C. McKinney and C. F. Gammie. A measurement of the electromagnetic luminosity of a Kerr black hole. *ApJ*, 611(2):977–995, 2004. doi:10.1086/422244.

S. Mereghetti, J. A. Pons, and A. Melatos. Magnetars: Properties, origin and evolution. *SSRev*, 191(1-4):315–338, 2015. doi:10.1007/s11214-015-0146-y.

V. Mewes et al. Numerical relativity simulations of thick accretion disks around tilted Kerr black holes. *PRD*, 93(6):064055, 2016. doi:10.1103/PhysRevD.93.064055.

V. Mewes et al. Numerical relativity in spherical coordinates with the Einstein Toolkit. *PRD*, 97(8):084059, 2018. doi:10.1103/PhysRevD.97.084059.

V. Mewes et al. Numerical relativity in spherical coordinates: A new dynamical spacetime and general relativistic mhd evolution framework for the einstein toolkit. *PRD*, 101(10):104007, 2020.

F. C. Michel. Rotating magnetospheres: An exact 3-D solution. *ApJ*, 180:L133, 1973. doi:10.1086/181169.

A. Mignone. High-order conservative reconstruction schemes for finite volume methods in cylindrical and spherical coordinates. *JCP*, 270:784–814, 2014. doi:10.1016/j.jcp.2014.04.001.

A. Mignone and P. Tzeferacos. A second-order unsplit godunov scheme for cell-centered MHD: The ctu-glm scheme. *JCP*, 229:2117–2138, 2010. doi:10.1016/j.jcp.2009.11.026.

I. Milch. Wendelstein 7-x im betrieb: Fusionsforschung mit stellaratoren. *Physik in unserer Zeit*, 50(1):16–23, 2019. doi:10.1002/piuz.201901524.

S. Miranda-Aranguren, M. A. Aloy, and T. Rembiasz. An HLLC Riemann solver for resistive relativistic magnetohydrodynamics. *MNRAS*, 476(3):3837–3860, 2018. doi:10.1093/mnras/sty419.

S. M. Miranda-Aranguren. *Numerical resistive relativistic magnetohydrodynamics*. PhD thesis, Universitat de València, 2018. URL http://roderic.uv.es/handle/10550/68071.

P. J. Montero, T. W. Baumgarte, and E. Müller. General Relativistic hydrodynamics in curvilinear coordinates. *PRD*, 89(8):084043, 2014. doi:10.1103/PhysRevD.89.084043.

F. Moreno-Insertis and K. Galsgaard. Plasma jets and eruptions in solar coronal holes: A three-dimensional flux emergence experiment. *ApJ*, 771(1):20, 2013. doi:10.1088/0004-637X/771/1/20.

P. Mösta et al. GRHydro: A new open-source General-Relativistic magnetohydrodynamics code for the Einstein Toolkit. *CQG*, 31(1):015005, 2013. doi:10.1088/0264-9381/31/1/015005.

C. Munz et al. Maxwell's equations when the charge conservation is not satisfied. *Academie des Sciences Paris Comptes Rendus Serie Sciences Mathematiques*, 328(5):431–436, 1999. doi:10.1016/S0764-4442(99)80185-2.

T. K. M. Nakamura et al. Measurement of the magnetic reconnection rate in the earth's magnetotail. *JGS*, 123(11):9150–9168, 2018. doi:10.1029/2018JA025713.

R. Narayan, I. V. Igumenshchev, and M. A. Abramowicz. Magnetically arrested disk: An energetically efficient accretion flow. *PASJ*, 55:L69–L72, 2003. doi:10.1093/pasj/55.6.L69.

A. Nathanail and I. Contopoulos. Black hole magnetospheres. *ApJ*, 788(2):186, 2014. doi:10.1088/0004-637x/788/2/186.

T. Neubert et al. A terrestrial gamma-ray flash and ionospheric ultraviolet emissions powered by lightning. *Science*, 367(6474):183–186, 2020.

K. D. Nielson, G. G. Howes, and W. Dorland. Alfvén wave collisions, the fundamental building block of plasma turbulence. II. Numerical solution. *PPl*, 20(7):072303, 2013. doi:10.1063/1.4812807.

C. Palenzuela. Modelling magnetized neutron stars using resistive magnetohydrodynamics. *MNRAS*, 431(2):1853–1865, 2013. doi:10.1093/mnras/stt311.

C. Palenzuela et al. Beyond ideal MHD: Towards a more realistic modelling of relativistic astrophysical plasmas. *MNRAS*, 394:1727–1740, 2009. doi:10.1111/j.1365-2966.2009.14454.x.

C. Palenzuela et al. Magnetospheres of black hole systems in force-free plasma. *PRD*, 82(4):044045, 2010. doi:10.1103/PhysRevD.82.044045.

C. Palenzuela et al. Robustness of the Blandford-Znajek mechanism. *CQG*, 28 (13):134007, 2011. doi:10.1088/0264-9381/28/13/134007.

Z. Pan. Magnetosphere structure of a Kerr black hole: Marginally force-free equatorial boundary condition. *PRD*, 98(4):043023, 2018. doi:10.1103/PhysRevD.98.043023.

B. P. Pandey and M. Wardle. Hall magnetohydrodynamics of partially ionized plasmas. *MNRAS*, 385(4):2269–2278, 2008. doi:10.1111/j.1365-2966.2008.12998.x.

K. Parfrey, A. M. Beloborodov, and L. Hui. Dynamics of strongly twisted relativistic magnetospheres. *ApJ*, 774(2):92, 2013. doi:10.1088/0004-637X/774/2/92.

K. Parfrey, D. Giannios, and A. M. Beloborodov. Black hole jets without large-scale net magnetic flux. *MNRAS*, 446:L61–L65, 2015. doi:10.1093/mnrasl/slu162.

K. Parfrey, A. Spitkovsky, and A. M. Beloborodov. Simulations of the magnetospheres of accreting millisecond pulsars. *MNRAS*, 469:3656–3669, 2017. doi:10.1093/mnras/stx950.

K. Parfrey, A. Philippov, and B. Cerutti. First-principles plasma simulations of black-hole jet launching. *PRL*, 122(3):035101, 2019. doi:10.1103/PhysRevLett.122.035101.

V. I. Pariev, S. A. Colgate, and J. M. Finn. A magnetic α-ω dynamo in AGN disks. II. Magnetic field generation, theories, and simulations. *ApJ*, 658(1): 129–160, 2007. doi:10.1086/510735.

S. J. Park. The transfield equation of the axisymmetric, nonstationary magnetosphere of a black hole. In C.-H. Lee and H.-Y. Chang, editors, *Current High-Energy Emission Around Black Holes*, pages 231–238, 2002. doi:10.1142/9789812777959_0017.

E. N. Parker. The origin of solar magnetic fields. *ARA&A*, 8:1, 1970. doi:10.1146/annurev.aa.08.090170.000245.

V. Paschalidis and S. L. Shapiro. A new scheme for matching general relativistic ideal magnetohydrodynamics to its force-free limit. *PRD*, 88(10):104031, 2013. doi:10.1103/PhysRevD.88.104031.

R. F. Penna, R. Narayan, and A. Sądowski. General Relativistic magnetohydrodynamic simulations of Blandford-Znajek jets and the membrane paradigm. *MNRAS*, 436:3741–3758, 2013. doi:10.1093/mnras/stt1860.

M. Petropoulou et al. Relativistic magnetic reconnection in electron–positron–proton plasmas: Implications for jets of active galactic nuclei. *ApJ*, 880(1):37, 2019. doi:10.3847/1538-4357/ab287a.

C. B. Phillips and R. T. Pappalardo. Europa clipper mission concept: Exploring jupiter's ocean moon. *Eos, Transactions American Geophysical Union*, 95(20): 165–167, 2014. doi:10.1002/2014EO200002.

A. Piel. *Plasma physics: An introduction to laboratory, space, and fusion plasmas*. Springer, 2017. doi:10.1007/978-3-642-10491-6.

A. G. Pili, N. Bucciantini, and L. Del Zanna. General Relativistic neutron stars with twisted magnetosphere. *MNRAS*, 447(3):2821–2835, 2015. doi:10.1093/mnras/stu2628.

J. Pons and D. Viganò. Magnetic, thermal and rotational evolution of isolated neutron stars. *LRRel*, 5(1):3, 2019. doi:10.1007/s41115-019-0006-7.

E. Priest and T. Forbes. *Magnetic Reconnection*. Cambridge University Press, 2000. doi:10.1017/CBO9780511525087.

R. E. Pudritz. Dynamo action in turbulent accretion discs around black holes. II. The mean magnetic field. *MNRAS*, 195:897, 1981a. doi:10.1093/mnras/195.4.897.

R. E. Pudritz. Dynamo action in turbulent accretion discs around black holes. I. The fluctuations. *MNRAS*, 195:881–914, 1981b. doi:10.1093/mnras/195.4.881.

B. Punsly. *Black hole gravitohydromagnetics*. Springer, 2001. doi:10.1007/978-3-662-04409-4_5.

B. Punsly. Force-free waves and black hole magnetospheric causality. *ApJ*, 583 (2):842–852, 2003. doi:10.1086/345422.

A. F. Rañada, M. Soler, and J. L. Trueba. Ball lightning as a force-free magnetic knot. *PRE*, 62(5):7181–7190, 2000. doi:10.1103/PhysRevE.62.7181.

W. J. M. Rankine. Xv. on the thermodynamic theory of waves of finite longitudinal disturbance. *Philosophical Transactions of the Royal Society of London*, pages 277–288, 1870.

A. Reinacher et al. The SOFIA telescope in full operation. *Journal of Astronomical Instrumentation*, 7(4):1840007, 2018. doi:10.1142/S225117171840007X.

C. Reisswig et al. Gravitational wave extraction in simulations of rotating stellar core collapse. *PRD*, 83(6):064008, 2011. doi:10.1103/PhysRevD.83.064008.

C. Reisswig et al. Three-dimensional General Relativistic hydrodynamic simulations of binary neutron star coalescence and stellar collapse with multipatch grids. *PRD*, 87(6):064023, 2013. doi:10.1103/PhysRevD.87.064023.

D. Reitze et al. Cosmic explorer: The U.S. contribution to gravitational-wave astronomy beyond LIGO. In *arXiv e-prints*, volume 51, page 35, 2019. URL https://ui.adsabs.harvard.edu/abs/2019BAAS...51g..35R.

T. Rembiasz et al. On the measurements of numerical viscosity and resistivity in eulerian MHD codes. *ApJSS*, 230(2):18, 2017. doi:10.3847/1538-4365/aa6254.

L. Rezzolla and O. Zanotti. *Relativistic hydrodynamics*. OUP Oxford, 2013. doi:10.1093/acprof:oso/9780198528906.001.0001.

P. J. Roache. Quantification of uncertainties in computational fluid dynamics. *ARFM*, 29(1):123–160, 1997. doi:10.1146/annurev.fluid.29.1.123.

D. M. Rothstein and R. V. E. Lovelace. Advection of magnetic fields in accretion disks: Not so difficult after all. *ApJ*, 677:1221–1232, 2008a. doi:10.1086/529128.

D. M. Rothstein and R. V. E. Lovelace. Assembling the ingredients for a jet: How do large-scale magnetic fields get there and what happens when they do? In R. M. Bandyopadhyay et al., editors, *A Population Explosion: The Nature & Evolution of X-ray Binaries in Diverse Environments*, volume 1010 of *American Institute of Physics Conference Series*, pages 35–39, 2008b. doi:10.1063/1.2945077.

M. A. Ruderman and P. G. Sutherland. Theory of pulsars - polar caps, sparks, and coherent microwave radiation. *ApJ*, 196:51, 1975. doi:10.1086/153393.

A. Sanna et al. NUSTAR and nicer reveal IGR J17591-2342 as a new accreting millisecond X-ray pulsar. *A&A*, 617:L8, 2018. doi:10.1051/0004-6361/201834160.

A. Savcheva et al. A study of polar jet parameters based on hinode xrt observations. *PASJ*, 59:S771, 2007. doi:10/ggssfb.

K. Schindler, M. Hesse, and J. Birn. General magnetic reconnection, parallel electric fields, and helicity. *JGS*, 93(A6):5547–5557, 1988. doi:10.1029/JA093iA06p05547.

E. Schnetter, B. Krishnan, and F. Beyer. Introduction to dynamical horizons in numerical relativity. *PRD*, 74(2):024028, 2006. doi:10.1103/PhysRevD.74.024028.

V. Shafranov. On magnetohydrodynamical equilibrium configurations. *SovPJ*, 33 (3):710–722, 1958. URL http://www.jetp.ac.ru/cgi-bin/dn/e_006_03_0545.pdf.

M. Shibata. *Numerical relativity.* 100 Years of General Relativity. World Scientific Publishing Company, 2015. ISBN 9789814699747. doi:10.1142/9692.

A. Sądowski and R. Narayan. Three-dimensional simulations of supercritical black hole accretion discs - luminosities, photon trapping and variability. *MNRAS*, 456(4):3929–3947, 2016. doi:10.1093/mnras/stv2941.

J. Spitzer, Lyman. History of the space telescope. *QJRAS*, 20:29, 1979.

H. C. Spruit and D. A. Uzdensky. Magnetic flux captured by an accretion disk. *ApJ*, 629:960–968, 2005. doi:10.1086/431454.

H. C. Spruit, T. Foglizzo, and R. Stehle. Collimation of magnetically driven jets from accretion discs. *MNRAS*, 288(2):333–342, 1997. doi:10.1093/mnras/288.2.333.

D. Stepanovs and C. Fendt. An extensive numerical survey of the correlation between outflow dynamics and accretion disk magnetization. *ApJ*, 825(1):14, 2016. doi:10.3847/0004-637X/825/1/14.

T. Sun et al. Soft X-ray imaging of the magnetosheath and cusps under different solar wind conditions: MHD simulations. *JGS*, 124(4):2435–2450, 2019. doi:10/ggssfc.

A. Suresh and H. T. Huynh. Accurate monotonicity-preserving schemes with Runge Kutta time stepping. *JCP*, 136:83–99, 1997. doi:10.1006/jcph.1997.5745.

M. Takahashi et al. Magnetohydrodynamic flows in Kerr geometry: Energy extraction from black holes. *ApJ*, 363:206, 1990. doi:10.1086/169331.

K. Tanabe and S. Nagataki. Extended monopole solution of the Blandford-Znajek mechanism: Higher order terms for a Kerr parameter. *PRD*, 78:024004, 2008. doi:10.1103/PhysRevD.78.024004.

Y. Tanaka et al. Gravitationally redshifted emission implying an accretion disk and massive black hole in the active galaxy MCG-6-30-15. *Nature*, 375(6533): 659–661, 1995. doi:10.1038/375659a0.

A. Tchekhovskoy, R. Narayan, and J. C. McKinney. Black hole spin and the radio loud/quiet dichotomy of active galactic nuclei. *ApJ*, 711:50–63, 2010. doi:10.1088/0004-637X/711/1/50.

J. Thomas. *Numerical partial differential equations: Finite difference methods.* Texts in Applied Mathematics. Springer New York, 2013. ISBN 9781489972781. doi:10.1007/978-1-4899-7278-1.

J. Thornburg. A fast apparent horizon finder for three-dimensional Cartesian grids in numerical relativity. *CQG*, 21:743–766, 2004. doi:10.1088/0264-9381/21/2/026.

K. S. Thorne, R. H. Price, and D. A. MacDonald, editors. *Black holes: The membrane paradigm.* Yale University Press, 1986. ISBN 978-0300037692.

N. Tomei et al. General Relativistic magnetohydrodynamic dynamo in thick accretion discs: Fully non-linear simulations. *MNRAS*, 491(2):2346–2359, 2020. doi:10.1093/mnras/stz3146.

P. Tondeur. *Geometry of foliations*, volume 90. Birkhäuser, 2012. doi:10.1007/978-3-0348-8914-8.

E. Toro. *Riemann solvers and numerical methods for fluid dynamics: A practical introduction*. Springer Berlin Heidelberg, 2013. doi:10.1007/b79761.

C. A. Tout and J. E. Pringle. Accretion disc viscosity - a simple model for a magnetic dynamo. *MNRAS*, 259:604–612, 1992. doi:10.1093/mnras/259.4.604.

D. Tskhakaya. *The particle-in-cell method*, volume 739, page 161. Springer, 2008. doi:10.1007/978-3-540-74686-7_6.

K. H. Tsui. Ball lightning as a magnetostatic spherical force-free field plasmoid. *PPl*, 10(10):4112–4117, 2003. doi:10.1063/1.1605949.

R. Turolla, S. Zane, and A. L. Watts. Magnetars: The physics behind observations. A review. *Reports on Progress in Physics*, 78(11):116901, 2015. doi:10.1088/0034-4885/78/11/116901.

P. Tzeferacos et al. On the magnetization of jet-launching discs. *MNRAS*, 400 (2):820–834, 2009. doi:10.1111/j.1365-2966.2009.15502.x.

T. Uchida. Theory of force-free electromagnetic fields. I. General theory. *PRE*, 56(2):2181–2197, 1997. doi:10.1103/physreve.56.2181.

D. A. Uzdensky. Force-free magnetosphere of an accretion disk - black hole system. I. Schwarzschild geometry. *ApJ*, 603(2):652–662, 2004. doi:10.1086/381543.

D. A. Uzdensky. Force-free magnetosphere of an accretion disk - black hole system. II. Kerr geometry. *ApJ*, 620:889–904, 2005. doi:10.1086/427180.

B. van Leer. Towards the ultimate conservative difference scheme III. Upstream-centered finite-difference schemes for ideal compressible flow. *JCP*, 23(3): 263–275, 1997. doi:10.1016/0021-9991(77)90094-8.

S. Vitale. Space-borne gravitational wave observatories. *General Relativity and Gravitation*, 46:1730, 2014. doi:10.1007/s10714-014-1730-2.

N. Vlahakis and A. Königl. Relativistic magnetohydrodynamics with application to gamma-ray burst outflows. II. Semianalytic super-alfvénic solutions. *ApJ*, 596(2):1104, 2003. doi:10.1086/378226.

A. A. Vlasov. Reviews of topical problems: The vibrational properties of an electron gas. *SovPU*, 10(6):721–733, 1968. doi:10.1070/PU1968v010n06ABEH003709.

C. Vourellis et al. GR-MHD disk winds and jets from black holes and resistive accretion disks. *ApJ*, 882(1):2, 2019. doi:10.3847/1538-4357/ab32e2.

R. Wald. *General Relativity*. University of Chicago Press, 2010.

R. M. Wald. Black hole in a uniform magnetic field. *PRD*, 10:1680–1685, 1974. doi:10.1103/PhysRevD.10.1680.

R. C. Walker et al. A VLBA movie of the jet launch region in M87. In *Journal of Physics Conference Series*, volume 131 of *Journal of Physics Conference Series*, page 012053, 2008. doi:10.1088/1742-6596/131/1/012053.

D. F. Webb and T. A. Howard. Coronal mass ejections: Observations. *LRSolP*, 9(1):3, 2012. doi:10.12942/lrsp-2012-3.

J. Wheeler. Geometrodynamics and the issue of final state. In *Relativité, Groupes et Topologie: Proceedings, Ecole d'été de Physique Théorique, Session XIII, Les Houches, France, Jul 1 - Aug 24, 1963*, pages 317–522, 1964.

D. R. Wilkins and A. C. Fabian. Understanding X-ray reflection emissivity profiles in AGN: Locating the X-ray source. *MNRAS*, 424(2):1284–1296, 2012. doi:10.1111/j.1365-2966.2012.21308.x.

C. Yu. A high-order WENO-based staggered Godunov-type scheme with constrained transport for force-free electrodynamics. *MNRAS*, 411(4):2461–2470, 2011. doi:10/bjbbcb.

Y. Yuan, R. D. Blandford, and D. R. Wilkins. Black hole magnetosphere with small-scale flux tubes. *MNRAS*, 484(4):4920–4932, 2019. doi:10/ggssfd.

Y. Yuan et al. Black hole magnetosphere with small-scale flux tubes - II. Stability and dynamics. *MNRAS*, 487(3):4114–4127, 2019. doi:10/ggssff.

R. L. Znajek. Black hole electrodynamics and the Carter tetrad. *MNRAS*, 179 (3):457–472, 1977. doi:10.1093/mnras/179.3.457.

This Ph.D. thesis has been funded by a grant of the **Studienstiftung des Deutschen Volkes**. Our research is supported by the **Spanish Ministry of Science and Education** (AYA2015-66899-C2-1-P, PGC2018- 095984-B-I00) as well as the **Valencian Regional Government** (GRISOLIAP/2016/097, PROMETEO-II-2014-069).

Committee: **Christian Fendt** (Max Planck Institut für Astronomie, Heidelberg), **Agnieszka Janiuk** (Centrum Fizyki Teoretycznej Polskiej Akademii Nauk), **Elena Khomenko** (Instituto de Astrofísica de Canarias), **Amir Levinson** (Tel Aviv University), **Susana Planelles Mira** (Universitat de València), **Jose A. Pons** (Universitat d'Alacant)

Chairperson: **Jose A. Pons** (Universitat d'Alacant)